EFFECTS OF SURFACE CONDITIONS ON NUCLEATION AND BOILING CHARACTERISTICS

by

Avtar Singh

B.E.(HONS.), Birla Institute of Tech. & Sci., Pilani, India

(1971)

S.M., Mechanical Engineering, M. I. T.

(1973)

SUBMITTED IN PARTIAL FULFILLMENT
OF THE REQUIREMENTS FOR THE
DEGREE OF

DOCTOR OF SCIENCE

at the

MASSACHUSETTS INSTITUTE OF TECHNOLOGY

September 9, 1974
i.e. February. 1975

Signature of Author ______________________
Department of Mechanical Engineering, September 9, 1974

Certified by ______________________
Thesis Supervisor

Accepted by ______________________
Chairman, Department Committee on Graduate Students

EFFECTS OF SURFACE CONDITIONS ON NUCLEATION AND BOILING CHARACTERISTICS

by

Avtar Singh

Submitted to the Department of Mechanical Engineering
on September 3, 1974 in partial fulfillment of the
requirements for the Degree of Doctor of Science.

ABSTRACT

Effects of cavity size, shape and their population on nucleation and boiling characteristics of a surface were studied. Dynamic effects on nucleation from a single isolated cavity in boiling were investigated both theoretically and experimentally. An analytical model has been developed for the stability of the cavity considering the effect of transient heat flux and inertial and viscous effects of the fluid. The model shows that dynamic effects are important in determining the required superheat for stable boiling from a single cylindrical cavity. Parameters such as cavity radius and depth (which are characteristic of the boiling surface), contact angle (which depends upon the fluid surface combination), and the dependent parameters (which are the consequence of the physical behavior of the considered phenomenon) e. g. the initial temperature and penetration velocity of liquid into the cavity, are found to be important in determining the required superheat for stable boiling from the cavity. A decrease in cavity depth, contact angle or the initial liquid temperature reduces the stability while a decrease in liquid penetration velocity enhances the cavity stability. For a cavity with large depth to diameter ratio, static model successfully predicts the required superheat and as this ratio decreases, higher superheats are required than predicted by the static model, as has been observed experimentally for artificially made cavities.

Attempt was made to produce very deep cavities (depth/diameter ratio of 4-6) on the boiling surface through laser drilling technique. A significant improvement in the cumulative site density and boiling heat-flux for a given superheat was observed for methanol in the isolated bubble region as compared to a natural surface having the same surface finish as employed on the laser surface. The frequency of bubble departure is observed to be a strong function of superheat (decreasing with decreasing superheat) for the deep laser cavities; the observed frequency behavior has been explained by a theoretical model which predicts the waiting time (time between the last bubble departure and appearance of the next one on the surface) and the bubble contact time for a given fluid as a function of superheat and cavity size.

Thesis Supervisor: Professor Borivoje B. Mikic
Title: Professor of Mechanical Engineering

ACKNOWLEDGEMENTS

The author is greatly indebted to Prof. B. B. Mikic, his thesis advisor, and Prof. W. M. Rohsenow for their guidance, valuable advice and inspiration throughout the course of this work. He wishes to express special thanks to Prof. Peter Griffith and Prof. N. H. Cook for their valuable suggestions, positive criticisms and encouragement.

The author is thankful to Mr. Dean Jorgenson of the Optimation Inc. for his co-operation in laser work and to Mr. Fred Johnson for his skilled help in building the apparatus.

Special thanks is expressed to all his colleagues at the M. I. T. Heat Transfer Laboratory and computing facility, who made useful contributions to various stages of this work.

Special gratitude also goes to Peggy Garlick for her careful and effective handling of the typing.

Finally, the author wishes to express a deep measure of gratitude to the U. S. Army Research Office for their financial support of this work.

TABLE OF CONTENTS

LIST OF SYMBOLS

A	surface area
C_{air}	concentration of air in liquid solution
C	specific heat, B/lbm°F
D	cavity depth, inches
D_b	bubble departure diameter
f	frequency of bubble departure, per second
F	Force, lbs.
g	acceleration of gravity, ft/sec^2
h	heat transfer coefficient
H	D-M, initial height of the interface from the bottom of the cavity, Fig. 8, inches
H_1	Maximum penetration, Fig. 8, inches.
H_2	Defined in Fig. 8
H_{fg}	Latent heat of vaporization, B/lbm
J	Joule's heat transfer coefficient, 778 ft. lbf/B
k	thermal conductivity, B/hr.ft^2°F
m	Henry's Law constant
M	initial penetration of liquid into the cavity, inches
N/A	number of active sites per unit area
P	Pressure, psi
P_{sat}	system pressure., psi
P_{vap}	pressure of vapor entrapped in cavity, psi
P_{vap}^{o}	$P_{sat} + \frac{2\sigma}{\rho_o}$, initial vapor pressure in cavity

q/A	total heat flux, B/hr.in^2
$(q/A)_b$	boiling component of the heat flux, B/hr.in^2
Q	Heat in Btu.
R_v	Universal Gas Constant
R_o	Cavity radius, inches
r_c	critical cavity radius, eqn. (5) and (6)
T_{sat}	saturated temperature corresponding to system pressure, °F
t	time, seconds
t_c	bubble contact time, seconds.
t_w	waiting time, seconds.
T	temperature, °F
ΔT, ΔT_w	wall superheat, $T_w - T_{sat}$, °F.
$(\Delta T)_{2\sigma/\rho}$	static superheat, eqn. (3), °F
$(\Delta T)_w^o$	ratio of actual superheat to static superheat as calculated by eqn. (16)
V	penetration velocity of liquid, inch/sec.
v	volume, in^3
v_{fg}	specific volume change of evaporation, ft^3/lbm.
v_{vap}	volume of vapor
W_g	mass of vapor in cavity, lbm.
W_g^o	initial mass of vapor in cavity, lbm.
z	distance coordinate for penetration, Fig. 8, inches
α	thermal diffusivity, ft^2/hr.
δ	thermal layer thickness, inches

μ	viscosity, lbm/ft-hr.
ρ	radius of curvature of liquid-vapor interface.
ρ_{eff}	value of ρ calculated from eqn. (4) with experimental ΔT value.
ρ_0	initial value of the radius of curvature of meniscus
ρ_ℓ	liquid density, lbm/ft^3
θ	contact angle
σ	surface tension, lbm/ft.
τ	bubble time period, seconds.
λ	area factor for the effective area of heat transfer at the meniscus.
γ	volumetric thermal expansion coefficient of fluid
ν	kinematic viscosity. ft^2/hr.

Subscripts

air	air
b	boiling
eq	equilibrium
g	gas
i	incipient
l, liq	liquid
nc	natural convection
o	initial condition
s, sat	saturation condition
v, vap	vapor
w	wall

LIST OF FIGURES AND TABLES

FIGURES:

I. INTRODUCTION

The effects of surface conditions in boiling have long been recognized. In nucleate boiling, bubbles usually form at specific discontinuities on the solid surface. Bankoff [1] presented theoretical arguments that likely nucleation sites are pits and scratches. Clark, Strenge and Westwater [2] photographed actual nucleation sites through a microscope; pits and scratches and not the grain boundaries in the metal surface were found to provide most of the nucleation sites. Courty and Foust [3], from their study, established that the size and shape distribution of the microroughness in heat-transfer surface and contact angle of bubbles were important variables determining the number of nucleation sites and heat flux characreristics in nucleate boiling. Kurihara and Myers [4] meassured the effects of liquid superheat and surface roughness on active site density and boiling heat transfer coefficient. Their experiments revealed that the number of active boiling centers on the plate increased with increasing surface roughness and calculated boiling coefficients were proportional to the one third power of the number of bubble columns rising from the surface.

The importance of the number of active sites in predicting the nucleate boiling heat-flux has been well studied, both theoretically and experimentally [5, 6, 7]. The surface conditions principally, can be related to the boiling characteristics by (i) relating surface finish to the cavity size distribution, (ii) relating a cavity size to conditions required for its activation, (iii) relating the overall boiling heat flux to conditions existing at the surface and active site population.

The last part follows from the considerations of the mechanism of nucleate boiling. The net boiling heat flux rate is seen to be directly dependent upon the number of active sites existing on the surface and frequency and size of bubble departure [7]. A successful prediction of the number of active sites in boiling requires a precise understanding of the nucleation phenomenon. In spite of the varied research work having been done to understand the nucleation phenomenon in boiling, there is no simple theory that satisfactorily accounts for all the parameters involved. Analytical models of the criteria for incipience of boiling and prediction of the size range of active sites have been made [8, 9, 10, 11]. None of these theories has successfully predicted the experimental data, as observed in investigations [11] and [12] (Figs. 1 and 2). The analysis of the incipience criteria by Hsu [9] and Han and Griffith [10] are both based on the assumption that there exists a semispherical vapor bubble nucleus over a cavity and this nucleus grows when the thermal layer adjacent to heating surface is of sufficient thickness. The incipience criteria proposed by Howell and Siegel [11] considered evaporation at the bubble nucleus surface within the thermal layer and condensation over the remainder of the nucleus surface. Nucleation criteria used by Griffith and Wallis [8], was verified in Reference [8] for uniformly superheated systems, however, the predicted superheat was too small for saturated pool boiling.

Bankoff [13] first considered dynamic effects in his approximate analysis for predicting superheat required for initiation of ebullition at low pressures. Neglecting inertia of the liquid and heat transfer for cavity walls, he formulated the cavity stability problem as one dimensional capillary penetration by condensation, and obtained a limiting real solution of the equations for the rate of penetration of the liquid into cavity. Later Marto and Rohsenow [14] and Shai and Rohsenow [15] considered the problem of cavity stability in boiling with liquid metals, and in their study, they realized the significance of nucleation site depth in determining the nucleation superheat.

The intent of this study is to undertake an analytical and experimental investigation of the fluid and surface parameters which affect the nucleation site stability. Once the pertinent fluid and surface parameters are known, boiling surfaces with enhanced nucleation characteristics could be developed by artificially controlling the surface parameters. This will have significant application by allowing for substantial reduction in wall superheat for a given boiling heat flux, i.e. enhancement of boiling heat transfer coefficient. As mentioned earlier, the boiling heat flux depends not only upon the active site density, but also the frequency and size of bubble departure. A qualitative study of the effect of surface parameters on bubble departure frequency has been made in the present investigation.

II. NUCLEATION IN BOILING

II.1 A Review Of Existing Nucleation Criteria

The nucleation phenomenon in boiling has been the subject of numerous research work over the past few years. Ample experimental evidence [16] suggest that boiling nuclei are pockets of vapor or gas trapped in small crevices in a solid surface. Initiation of boiling from a nucleation site has been normally considered in terms of a critical radius of nucleation site. For the static equilibrium of a spherical vapor nucleus of radius ρ, the force balance gives the following relation,

$$\Delta P = P_v - P_\ell = \frac{2\sigma}{\rho} \tag{1}$$

The pressure difference ΔP can be approximated by using Clausius-Clapeyron equation. Assuming that the vapor inside the nucleus is saturated, and making a perfect gas approximation, the following relation can be obtained,

$$\frac{dP}{dT} \approx \frac{P_v - P_\ell}{T_v - T_{sat}} \approx \frac{H_{fg}}{T_v\, v_{fg}} \approx \frac{H_{fg}\, P_v}{R_v\, T_v^2} \tag{2}$$

Since, $T_w \approx T_v$ at equilibrium, equations (1) and (2) may be combined to give,

$$(\Delta T)_{\frac{2\sigma}{\rho}} = T_w - T_{sat} \cong \frac{2R_v\, T_{sat}^2\, \sigma}{H_{fg}\, P_\ell\, \rho} \approx \frac{2\sigma T_{sat}\, v_{fg}}{H_{fg}\, \rho} \tag{3}$$

or alternatively,

$$\rho = \frac{2\sigma\, T_{sat}\, v_{fg}}{H_{fg}\,(T_w - T_{sat})} \tag{4}$$

Griffith and Wallis [8], observed in their study that equation (3) predicted the superheat required for nucleation in uniformly superheated systems. But, it predicted too low a superheat for non-uniformly heated systems, as is the case of boiling over a heated surface when the bulk is saturated or subcooled. Griffith and Wallis found that boiling from a cavity of $2\text{x}10^{-3}$ inch diameter started at 3°F superheat in a uniformly superheated liquid, but did not start from a heated strip inside a saturated liquid until the superheat attained a value of 20°F.

Hsu [9] and Han and Griffith [10] attempted to provide theoretical explanation for the experimental observations mentioned above. In their theories, the nucleus for bubble growth is assumed to exist at the cavity mouth and to have been formed by the residual vapor from the preceding bubble. The hypothesis presumes that the cavity meets the geometric requirements for the entrapment of gas or vapor and that the bulk liquid penetrating into the cavity is sufficiently hot that the nucleus does not condense into the cavity. Just following the bubble departure, nucleus is surrounded by liquid at saturation temperature from the bulk (at the time $t = 0$); as times goes on the temperature of the liquid rises due to heat transfer from the surface and the nucleus begins to grow when the liquid temperature exceeds the vapor temperature over the entire liquid-vapor interface. The series of events is shown in Fig. 3. For the saturated liquid boiling over a surface with constant superheat, Hsu [9] obtained the following relation:

$$(r_c)_{\max,\,\min} = \frac{\delta}{2C_1}\left[1 \pm \left(1 - \frac{8C_2\,\sigma\,T_{sat}}{H_{fg}\,P_v\,\delta\Delta T}\right)^{1/2}\right] \qquad (5)$$

where constants C_1 and C_2 depend upon the contact angle of the fluid and the slope of cavity walls at its mouth. The "limiting thermal layer thickness", δ , is defined as the size of the superheated liquid layer. Similarly, Han and Griffith [10] assume a hemispherical nucleus existing over the cavity mouth and give the relation:

$$(r_c)_{\text{max, min}} = \frac{\delta}{3}\left[1 \pm \left(1 - \frac{12\,\sigma\,T_{sat}}{H_{fg}\,P_v\,\delta\Delta T}\right)^{1/2}\right] \qquad (6)$$

Howell and Siegel [11] proposed a modified incipience criteria for sites of such a size that their attached nuclei extend through the thermal layer, $r_c > \delta$ as shown in Fig. 4a. They assumed evaporation to occur through that portion of the nucleus surface within the thermal layer and condensation over the remainder of the nucleus area. For a saturated bulk, and assuming a linear temperature profile in the thermal layer, they obtained the following equations for incipience superheat.

$$T_w - T_{sat} = \Delta T > \frac{4\,\sigma\,T_{sat}}{H_{fg}\,P_v\,\delta}\ ;\ r_c \geq \delta \qquad (7)$$

and,

$$\Delta T > \frac{2\,\sigma\,T_{sat}}{H_{fg}\,\rho_v\,r_c} \quad \frac{1}{\left(1 - \frac{r_c}{2\delta}\right)};\ r_c \leq \delta \qquad (8)$$

None of the forementioned criteria were able to predict successfully the experimental data as observed in References [11] and [12]. Fig. 1 taken from Ref. [12] and Fig. 2 from Ref. [11], show the comparison between the predicted and observed superheats for artificial cavities of known sizes. From Fig. 1 it could be seen that predicted superheats from equations (3), (5) and (6) differ greatly from the observed superheat values, the prediction being much worse for organics as compared to water.

The following reasons may be stated for the observed discrepancies between the predictions of the forementioned theories and the observed data:

(1) The criteria mentioned thus far assumed the existence of a vapor nucleus at the cavity mouth. In the case of actual boiling on a surface, as the bubble departs, the liquid in the vicinity of the cavity rushes towards the cavity mouth and penetrates into the cavity as observed in Reference [17]. Conditions for the incomplete displacement of vapor from the cavity by an advancing liquid front, has been discussed by Bankoff [1]. Significant parameters affecting the entrapment of vapor within a cavity, as shown by Bankoff [1] are liquid density, surface tension, contact angle, and geometry (radius and depth) of cavity. Therefore, a given cavity depending upon its geometry may not entrap enough vapor to form a vapor nucleus at its mouth, while boiling with a known fluid. In such a case, the assumption of the forementioned nucleation criteria become invalid, and thus leading to the discrepancy in predicted and observed superheat values.

(2) The hypothesis in the nucleation theories above presumes that the bulk liquid is sufficiently hot so that the vapor nucleus does not condense into the cavity, this may not be true. If the bulk is saturated or subcooled, there is a possibility of initial condensation of vapor trapped inside the cavity.

(3) In all the above criteria, liquid motion and inertial effects after the bubble departure have been neglected which might affect the penetration of liquid inside the cavity.

From the discussion above, it is apparent that the liquid motion after the previous bubble departure and resulting penetration, and condensation of entrapped vapor inside the cavity may be important in determining the required superheat of nucleation. The nucleation model considering dynamic effects, presented in the next section takes into account these factors, and the observed behavior of water and organics in boiling has been explained with the help of this model.

II.2. Dynamic Effects On Nucleation From An Isolated Cavity in Boiling

II.2-1 Entrapment Of Vapor In A Cavity At Bubble Departure

As the growing bubble departs from a cavity in boiling, the liquid in the vicinity of the cavity moves into the cavity mouth. Due to slight asymmetry in bubble departure, presumably caused by existing convection currents in the nucleate pool boiling, it may be assumed that liquid spreads over the cavity from a favored direction. Bankoff [1] has shown, Fig. 5a, that for a wedge shaped groove vapor will not be removed completely by an advancing liquid front if $\theta > \phi$. In the present analysis the advancing liquid front has been assumed to be a plane surface as it penetrates into the cavity, and trapping is completed as the front intersects the opposite edge of the cavity as shown in Figs. 5b and 6a. As noted in Ref. [17] the assumption of flat liquid front does not correspond to the actual shape of liquid interface, which must be determined by hydrodynamic and surface effects. Fig. 7 reproduced from Ref. [18] shows this more complicated mechanism in detail.

The volume of trapped vapor can be calculated from geometrical considerations. Clearly, this is a function of cavity radius R_0, cavity depth D and advancing contact angle θ of fluid, Although, the data for advancing contact angles of organics is relatively scarce, a few references [8, 19, 20, 21, 22] are available for water; data for the contact angle scattered over a wide range from 30° - 100°. In the present work, $\theta = 45°$ was used for water and for organics θ was chosen in the range 8° - 15°. As is apparent, organics penetrate deeper into the cavity and thus entrap less volume of vapor than water. It should be pointed out that in the present analysis any evaporation or condensation at the liquid-vapor interface has been neglected during the vapor entrapment process and the volume of trapped vapor is determined by the contact angle and geometrical considerations only.

It should be noticed that the liquid which penetrated into the cavity may have a penetration velocity V_o and depending upon the temperatures of liquid and vapor, condensation or evaporation may occur at the liquid vapor interface causing liquid motion inside the cavity. In the next section, initial conditions existing in the cavity at the completion of liquid penetration have been discussed.

II.2-2 Initial Conditions

At the completion of the entrapment process, as described in the previous section, it is assumed the liquid vapor interface has a spherical shape, such that the interface makes an angle θ at cavity walls, Fig. 5c and 6b. It is assumed that during this transition the volume of the entrapped vapor remains unchanged, which may not be precisely true since the surface tension of liquid might cause a little compression of the vapor. The present analysis assumes that this compression is small.

The position of the liquid vapor interface just after transition, will be referred to as the initial position ($z = 0$) at time $t = 0$, as shown in Fig. 8. Initial radius of curvature of the liquid vapor interface, ρ_o , is given by the expression,

$$\rho_o = \frac{R_o}{\cos\theta} \tag{9}$$

The initial vapor pressure of the trapped vapor, P^o_{vap} is calculated by the force-balance accross the meniseus, e.g.

$$P^o_{vap} = P_\ell + \frac{2\sigma}{\rho_o} \tag{10}$$

where P_ℓ represents the pressure in the liquid inside cavity and in the vicinity of liquid-vapor interface. The initial value of P_ℓ is taken to be equal to P_{sat}, the system pressure and the trapped vapor is assumed to be saturated at P^o_{vap} , given by equation (10).

The initial temperature of the liquid, having penetrated into the cavity, may be subcooled, saturated or slightly superheated depending upon the system conditions, cavity size and thickness of the superheated liquid layer near the vicinity of the cavity. In the present analysis, saturated bulk conditions were considered and the initial liquid temperature was calculated using the following expression.

$$T_\ell^o = T_{sat} + A_1 \, (T_w - T_{sat}) \qquad (11)$$

where A_1 is a fixed constant for a known fluid and cavity size. For saturated bulk conditions, it is clear that A_1 can have values such that $0 \leqslant A_1 \leqslant 1$. An approximate model given in Appendix B, gives an estimate for A_1. It has been shown that if the thickness of the superheated liquid layer in the vicinity of the cavity at the time of bubble departure is small as compared to the cavity diameter, then A_1 varies linearly with δ. The value of A_1 for water was determined empirically on the basis of the experimental fact that dynamic effects for water are small for cavities having dimensions of the size of a typical natural cavity. This value was used as the base value to calculate A_1 for other fluids, using the following relation,

$$A_{1\ \mathrm{fluid}} = A_{1\ \mathrm{water}} \left(\frac{\delta_{\mathrm{fluid}}}{\delta_{\mathrm{water}}} \right) = A_{1\ \mathrm{water}} \left(\frac{\alpha_{\mathrm{fluid}}}{\alpha_{\mathrm{water}}} \right)^{1/2} \qquad (12)$$

In general the liquid that penetrates into the cavity may have an initial velocity, V_o. Experiments were conducted by Anton and Veka's [23], on two different glass-made artificial nucleation sites, recording the liquid penetration and liquid-vapor interface evolution inside the nucleation sites. From their observations, the initial liquid penetration velocities for water are found to be approximately in the range of 5-20 inch/sec for the two artificial cavities tested. In general, the entering velocity of the fluid may be a function of the bubble departure size, fluid properties, contact angle and mouth diameter of the cavity. In the following analysis values of V_o ranging from zero to 40 inch/sec. will be considered.

Next, we will derive the governing equations for the motion of the liquid-vapor interface and stability of the cavity in boiling.

II.2-3. Analysis For The Motion Of Liquid-Vapor Interface

Depending upon the initial conditions, the initial temperature of the liquid inside the cavity may be higher or lower than the initial vapor temperature. If the vapor temperature is higher than the liquid temperature, vapor will start condensing on the interface. Due to condensation, the pressure of vapor inside the cavity will decrease and the interface will move down into the cavity. As the liquid-vapor interface recedes into the cavity, temperature of the liquid rises due to the heat received from conduction at the cavity walls and condensation at the meniscus. The rise in the temperature of the liquid depends upon the rate at which latent heat of vaporization is supplied at the meniscus (due to vapor condensation) and the rate at which it is conducted away by the liquid. Rise in liquid-temperature, will decrease the rate of condensation, causing slower rate of liquid penetration. If the cavity is deep enough, then at some point where the liquid temperature equals the vapor temperature, the condensation will stop. Ahead of this point, liquid temperature will become higher than the vapor temperature due to heat transfer from cavity walls and vaporization will occur causing cavity to remain stable in boiling. On the other hand, if the cavity is not deep enough, the liquid may quench the cavity completely before the bulk liquid in the vicinity of the meniscus could attain a temperature equal to that of the vapor, and thus causing deactivation of the cavity.

A stationary one dimensional co-ordinate system, with origin at the initial position of the interface has been selected to represent the position of the interface at any time t, as shown in Fig. 8. For the purpose of applying momentum theorem, a control volume, whose upper boundary is fixed and lower boundary moves with the liquid-vapor interface, has been selected as shown in Fig. 8. The system forces acting on this control volume in z direction are sketched in Fig. 9; these include the shear force at the cavity walls and an unbalanced pressure force in z direction. The pressure of vapor inside the cavity is determined by the net effect of condensation or evaporation and compression or expansion due to the interface motion. Convection effects have been neglected. On account of the radial heat flux at cavity walls and the axial heat flux due to condensation or evaporation at the liquid-vapor interface, the actual temperature field is two dimensional. But an order of magnitude analysis shows that for a cavity in the size range of natural cavities existing on ordinary surfaces, the effective thermal layer thickness for fluids like water and organics, near cavity walls due to radial heat flux, is at least an order of magnitude smaller than the diameter of the cavity. Therefore, the effect of heat transfer to the liquid from cavity walls is small and hence insignificant. However, in the present analysis it has been approximated by a uniformly distributed heat source within the liquid. A one dimensional analysis has been performed to calculate the heat flux in the axial direction. The amount of condensation or evaporation and hence the pressure of vapor inside cavity depends upon the net heat flux at the liquid-vapor interface. Details of analysis for a cylindrical cavity have been given in Appendix A.

The analysis is based upon the following assumptions:

1. The liquid-vapor interface retains a semispherical shape during its motion within the cavity, and makes an angle θ at the cavity walls.

2. Pressure at the cavity mouth is constant at the system pressure.

3. Conductivity of the vapor is negligible.

4. The temperature of cavity walls remains constant during the motion of the interface within the cavity.

5. Velocity field in the liquid inside cavity is parabolic being a function of radius r and time only.

6. Momentum change of vapor during condensation or evaporation at the interface is negligible.

7. No thermal or pressure gradients exist within the vapor present in the cavity. So the liquid-vapor interface temperature is assumed to be equal to the temperature of vapor.

8. The pressure of vapor at any time being known, its temperature can be approximated using Clausius - Clyapeyron equation.

9. Vapor is assumed to satisfy the ideal gal law, PV = MRT.

Application of momentum theorem to the system, leads to the following second order non-linear equation for a cylindrical cavity (Appendix A).

$$\rho_\ell \ (M + z) \ (H - z) \ \frac{d^2z}{dt^2} + 8\mu \ (M + z) \ (H - z) \frac{dz}{dt} - (\frac{2\sigma + P}{\rho}{}_s) \ (H-z)$$

$$+ H \ P_v^o \left[1 + \frac{\lambda \ K \ \pi \ R_o^2}{H_{fg} \ W_g^o} \int_o^t q \ dt \right] = 0 \qquad (13a)$$

Applying Clausius-Claypeyron equation gives the following governing equation for the system:

$$(T_i - T_{sat})\ (H-z) + \frac{P_s\ (H-z)\ v_{fg}\ T_{sat}}{J\ H_{fg}} = \frac{v_{fg}\ H\ P_v^o\ T_{sat}}{J\ H_{fg}} \left[1 + \frac{\lambda\ K\ \pi\ R_o^2}{H_{fg}\ W_g^o} \int_o^t q\ dt \right] \qquad (13b)$$

In equation 13a and 13b, the quantity $\int_o^t q\ dt$ denotes the net amount of heat transferred from vapor to liquid at the interface between time t = 0 and t = t. This is also equal to the net latent heat released by the condensation of vapor.

Initial conditions as described in Section II.2-2, can now be written as:

At time t = 0

a. $z = 0$

b. $\frac{dz}{dt} = V_o$

c. $P^o_{vap} = P_s + \frac{2\sigma}{\rho_o}$

d. $T^o_{interface} = T^o_i$ = Saturated temperature of vapor at P^o_{vap}

e. $T^o_{liq} = T_{sat} + A_1\ (T_w - T_{sat})$

Equations 13a and 13b can be solved simultaneously for z and T_i with the above initial conditions. The input values are fluid properties and cavity geometry. Before we discuss the numerical results, it might be helpful to describe experimental observations and then show how the analytical model can be used to explain the observed results.

II. 2-4 Experimental Observations And Results

In order to study the dynamic effects in boiling two kinds of experiments were carried out - boiling experiments and gas diffusion experiments. In the gas diffusion system, the test surface is immersed in a supersaturated solution of air in the test fluid. As the dissolved gas diffuses out of the liquid it nucleates at the cavities on the test surface. Due to slower rates of gas diffusion through the liquid, the nucleation process is slow and hence, the dynamic effects in the gas diffusion system can be assumed to be negligible as compared to that in boiling.

Boiling Experiments:

The apparatus and procedure for boiling experiments have been described in Appendix (C). Six artificial cavities of arbitrary shape and size were made on the surface of a copper test section by hitting the surface with a sharp pointed object. Fluids used were water and ethanol. Heat flux was first raised to about one half the critical heat flux value, so that most of the surface was in active boiling. Heat flux was then reduced slowly until the isolated bubble region reached so that each active site could be identified easily. Heat flux was further decreased gradually and the surface superheat was recorded for each of the artificial cavities, when it ceased bubble production. Although, as mentioned earlier in Section II.1, ρ calculated from eqn. (4) represents the radius of nucleation ρ_{eff} , where the value used for ΔT in eqn. (4) is the observed value of superheat in boiling experiments. For each of the six cavities, ρ_{eff} for water and ethanol was calculated using eqn. (4).

Gas Diffusion Experiments:

In order to isolate dynamic effects due to liquid motion, gas diffusion experiments were carried out to measure the effective radius of nucleation for the six artificial cavities. If the gas concentration in the liquid near the surface is uniform, as is approximately true when the liquid is sufficiently stirred, the system will behave similar to a uniformly superheated system in boiling and the following expression describes the equilibrium of a nucleus of critical size,

$$\rho_{eff} = \frac{2\sigma}{P_v + P_g - P_\ell} \tag{14}$$

where P_g depends upon the concentration of gas in the liquid.

The test surface was immersed in the supersaturated solution of air in liquid and nucleation was observed from the cavities on the surface. Gas concentration in the liquid decreased slowly, since the solution was opened to atmosphere and being stirred. P_g was recorded from each cavity when the nucleation seized from it and the corresponding ρ_{eff} was calculated from eqn. (14).

If the dynamic effects due to liquid motion in boiling are negligible, ρ_{eff} for a particular cavity and a known fluid should be same from both the gas diffusion and boiling experiments. Gas diffusion experiments could not be carried out successfully with organics, presumably due to fast-depletion rates of gas concentration in organics and experimental difficulty to maintain high gas concentration in the liquid solution at the surface. In particular, none of the sites were found active with ethanol at $\rho_{eff} \simeq 0.46 \times 10^{-4}$ inches, which corresponds to the maximum gas concentration that could be attained.

In addition to the data for isolated artificial cavities, gas diffusion and boiling experiments with water were also carried out on a prepared copper surface (4-0 finish) with decreasing gas concentration and heat-flux respectively. The cumulative active site density N/A and the corresponding superheat ΔT were recorded for various heat-flux values in the isolated bubble region during boiling. Similarly, in the gas diffusion experiment, N/A and corresponding P_g were recorded at different gas concentrations from these data N/A vs. ρ_{eff} characteristics of the surface were obtained.

Experimental Results:

Fig. 10 shows the results of boiling and gas diffusion experiments for the six artificial cavities. All the cavities were active in gas-diffusion with water at ρ_{eff} values between 1.2×10^{-4} and 2.1×10^{-4} inches. In boiling with water all cavities except #2 and #3 were seen active in the isolated bubble region. Apparently #2 and #3 require higher superheats, which corresponds to lower ρ_{eff} values. But for superheat values higher that ΔT corresponding to $\rho_{eff} \approx 1 \times 10^{-4}$ inches, nucleation took place from adjacent natural sites and the isolated bubble region did not exist making it difficult to identify the individual cavities. Higher superheats required by cavities #2 and #3 may be attributed to the presence of dynamic effects in boiling. ρ_{eff} for cavities #1, #4, #5 and #6 was observed to be about 15% - 40% smaller in boiling with water than gas diffusion, suggesting that the dynamic effects may depend upon the cavity shape and size which may differ from one cavity to another.

The importance of dynamic effects is further emphasized by the results plotted in Fig. 11, which shows N/A vs. ρ_{eff} characteristics of a prepared copper surface (4-0 finish) as observed in gas diffusion and boiling experiments with water, comparatively larger number of active sites were observed in gas diffusion than boiling for the same value of ρ_{eff}.

With ethanol, cavities #1, #3 and #5 were not seen to be active in the isolated bubble region in boiling. ρ_{eff} for cavities #2, #4 and #6 was observed to be about 2 to 10 times smaller in boiling with ethanol than with water. Cavity #3 which has the smallest ρ_{eff} in the gas diffusion experiment with water was not active in boiling with either of the fluids.

Fig. 12, taken from Ref. [18] gives similar data for single natural cavities and a comparison of the effective radius as calculated in the boiling and gas diffusion experiments. Again it could be noted that ρ_{eff} for organics is two to six times smaller than for water in boiling.

In the next section, the analytical model described in Section II.2-3 will be used to explain the observed behavior of water and organics on the basis of dynamic effects by modeling the cavity as a smooth walled cylindrical cavity. In Ref. [18], natural boiling cavities were modelled as conical cavities, and it was concluded that the observed relative behavior of water and organics in boiling, could be explained on the basis of a static model. It was argued in Ref. [18], that organics having lower contact angles penetrate deeper than water, and thus nucleate at smaller ρ (radius of curvature of vapor nucleus). Bankoff [1] has shown, Fig. 3a, that for a wedge shaped groove, vapor will not be removed completely by an advancing liquid front if $\theta > \phi$. Hence, for organics like methanol, ethanel, benzene etc. which have very small advancing contact angles, the conical cavity has to be sufficiently deep for incomplete displacement of vapor. For example for $\theta = 8°$, the conical cavity must be at least seven times as deep as its diameter for entrapment of vapor to occur. Such cavity configurations are not typical of the natural cavities existing on ordinary surfaces prepared by ordinary preparation techniques, as could be seen from the photomicrographs in Fig. 13, of some individual cavities taken on a surface finished by Silicon Carbide Grit Paper #320. By modelling the nucleation site as a cylindrical cavity, configurations closer to those of natural sites could be maintained. For a cylindrical cavity, the value of ρ does not depend upon the initial penetration so far as the liquid-vapor interface does not reach the bottom. Therefore, had the dynamic effects been negligible, water and organics should nucleate at the same ρ_{eff} value, predicted by the analytical model. As will be shown in the next section, the model predicts that dynamic effects are in fact important.

II.2-5 Analytical Results And Discussion

A microscopic examination of an ordinary boiling surface reveals that the pits and cavities existing on the surface have dimensions (depth and diameter) of the order of 10^{-4} inches, Fig. 13. For our analytical study of dynamic effects, we arbitrarily select a smooth walled cylindrical cavity of mouth radius $R_o = 1\mathrm{x}10^{-4}$ inches and a depth/diameter ratio of 2.5. The effect of varying R_o and depth will also be discussed separately.

ΔT_w^o has been defined as the ratio of the actual value of ΔT_w that has been imposed on cavity walls to the static superheat $(\Delta T)_{\frac{2\sigma}{R_o}}$ (eqn. (3)) that would be required for nucleation from the cavity, had the dynamic effects been negligible. It is to be noted in Figs. 1 and 2 that predictions of eqns. (3), (5), (6) and (8) merge together as cavity radius decreases. Therefore for natural cavities, which have small radii of the order of 10^{-4} inches, the superheat predicted by these equations will almost be equal and is referred to as $(\Delta T)_{\frac{2\sigma}{R_o}}$ in the present work, e.g.,

$$(\Delta T)_{\frac{2\sigma}{R_o}} = \frac{2\sigma\, T_{sat}\, v_{fg}}{h_{fg}\, R_o} \tag{15}$$

Since ρ is inversely proportional to ΔT, eqn. (4), ΔT_w^o also represents the ratio of the critical radius of nucleation, R_o and ρ_{eff}, e.g.

$$\Delta T_w^o = \frac{\Delta T_w}{(\Delta T)_{2\sigma/R_o}} = \frac{R_o}{\rho_{eff}} \tag{16}$$

The numerical solution to eqns. (13a) and (13b) has been obtained using a fourth order Runge-Kutta integration technique, with the initial conditions described in Section II.2-3.

Fig. 14 shows the relative behavior of water and ethanol, as obtained from the analytical model, in boiling from a single cylindrical cavity. Values of contact angle θ, used for water and ethanol were 45° and 10° respectively, with initial liquid velocity chosen to be zero. A_1 for (eqn. (11)) water is taken to be 0.35 and 0.23 for ethanol as discussed in Appendix B. The ordinate in Fig. 14 represents percent penetration (z/H_1). Initially at $t = 0$, z is zero and as the liquid interface moves into the cavity, percent penetration increases. When liquid penetration is 100%, the cavity is assumed to be deactivated; this happens with ethanol, Fig. 14, when $\Delta T_w^o = 2.5$. As ΔT_w^o is increased to 3, evaporation starts and the liquid interface recedes back before the penetration is 100%. Thus the model predicts that for the cavity to be stable in boiling with ethanol, a wall superheat ΔT_w between 2.5 to 3 times of the static superheat $(\Delta T)_{\frac{2\sigma}{R_o}}$ is required. For water the required ΔT_w^o is slightly less than 1. In other words, using eqn. (16) it could be seen that the predicted ρ_{eff} for ethanol is about 2.5 to 3 times smaller than that for water, a trend similar to that observed in the boiling experiments, Figs. 10 and 12. In the next section, we will examine the effects of different parameters on the superheat ΔT_w required for the stability of the cavity.

Effect of Different Parameters Used in the Analytical Model:

The analytical model contains the following different parameters, 1. The surface parameters e.g. cavity radius and depth, 2. contact angle (which depends upon the fluid-surface combination) and, 3. Initial temperature and penetration velocity of liquid (which are the consequence of the physical behavior of the considered phenomenon). We shall discuss the effects of varying these parameters on the required superheat for stable boiling and the sensitivity of analytical results to their chosen values.

a. Effect of Wall Superheat:

A change in the wall superheat ΔT_w affects the cavity stability in two ways - firstly by altering the initial liquid temperature, eqn. (11) and secondly by changing the rate of heat transfer to the liquid from cavity walls. For higher superheats, the initial temperature of the liquid is higher, hence the rate of condensation is lower due to smaller temperature gradient in the liquid near the interface. In the extreme case when the superheat is high enough such that the initial temperature of liquid is higher than the vapor temperature, condensation does not take place at all and the interface recedes back due to evaporation. Fig. 15a shows the effect of superheat for ethanol ($\theta = 8°$). As could be seen from Fig. 15a, a superheat as high as $\Delta T_w^o = 3.5$ is not enough for the cavity to remain active, the liquid penetration being 100%. When the superheat is increased to $\Delta T_w^o = 4$, evaporation starts and the interface recedes back. Effect of superheat for water is shown in Fig. 14.

b. Effect Of Contact Angle Of The Fluid

Contact angle seems to be one of the most important parameters determining cavity stability. Given a cavity size, the initial penetration of liquid into the cavity depends upon the contact angle of the fluid. Lower the contact angle, deeper is the initial penetration and smaller is the distance (H_1) which the interface has to travel before it reaches the cavity bottom. During condensation, the liquid temperature rises due to the latent heat transferred through the liquid-vapor interface and the heat transferred from cavity walls. If sufficient amount of heat is transferred to the liquid so that its temperature rises above the interface temperature corresponding to the vapor pressure, evaporation will start and the interface will recede back towards cavity mouth. For small contact angle, however, the amount of trapped vapor is small and the heat trnasferred to the liquid due to complete condensation of this small amount of vapor may not be enough to raise the liquid temperature to a level when evaporation could start and the cavity may thus be deactivated. The effect of contact angle has been plotted in Fig. 16a for ethanol and in Fig. 16b for water. A wall superheat corresponding to $\Delta T_w^o = 2.38$ was imposed on cavity walls for ethanol. As shown in Fig. 16a, when θ has values 10° and 13°, evaporation takes place and interface recedes back. When θ is reduced to 8°, cavity is deactivated as the liquid interface reaches the cavity bottom.

Apparently, higher wall superheat ΔT_w will be required for the cavity to remain active for $\theta = 8°$. It could be seen from Fig. 16b that the cavity stability is not much affected when θ for water is changed by small amounts $(\Delta\theta \simeq 5°)$, since for larger contact angles, H_1 is not very sensitive to small changes in the contact angle as is shown in Table I which gives the values of V^o_{vap} and H_1 for different values of θ for a cylindrical cavity having $R_o = 1x10^{-4}$ inches and $D = 5x10^{-4}$ inches. $A_1 = 0.35$ was used both for water and ethanol in Fig. 16.

Fig. 17 shows the effect of contact angle on the required superheat for stable boiling for methanol. A cavity with $R_o = 1x10^{-4}$ inches and $D = 7x10^{-4}$ inches was considered for calculation and for values of θ between 4° - 14°, minimum value of ΔT_w required for incomplete penetration was determined from analysis. As could be seen for Fig. 17, when θ is large $(\theta \gtrsim 12°)$ a wall superheat ΔT_w equal to $\Delta T_{\frac{2\sigma}{R_o}}$ is enough for cavity stability. As θ is decreased, higher ΔT_w is required, the liquid penetration being complete when θ is reduced to 4° and sufficiently large superheats may be required for nucleation.

TABLE I

VALUES OF V^{o}_{vap} AND H_1 vs. θ FOR A CYLINDRICAL CAVITY ($R_o = 1 \times 10^{-4}$ INCHES, D = 5×10^{-4} INCHES):

θ	V^{o}_{vap} (IN^3)	H_1 (IN)
8°	2.04×10^{-12}	1.07×10^{-5}
10°	2.8×10^{-12}	3.74×10^{-5}
13°	4.03×10^{-12}	8.04×10^{-5}
40°	12.05×10^{-12}	3.58×10^{-4}
45°	12.56×10^{-12}	3.78×10^{-4}
50°	13.1×10^{-2}	3.98×10^{-4}

c. Effect of Initial Liquid Temperature:

The initial liquid temperature of the liquid is determined by eqn. (11),

$$T^o_{liq} = T_{sat} + A_1 (T_w - T_{sat})$$

Higher the initial liquid temperature, lower will be rate of condensation and greater the cavity stability. Effect of varying A_1 on cavity stability in boiling with water has been presented in Fig. 18a and Fig. 18b. Fig. 18a shows that small changes in A_1 do not have much effect on the liquid penetration for water. For example, when $A_1 = 0$, a superheat corresponding to $\Delta T^o_w \simeq 1.5$ is required for incomplete penetration, as shown in Fig. 18b. The effect of A_1 is more pronounced on methanol, specially when A_1 is small, as shown in Fig. 19. For $A_1 = 0$, a superheat as high as $\Delta T^o_w \simeq 5.5$ is required and when A_1 is increased ΔT^o_w decreases. Results of calculation for three different values of A_1 (A_1 = 0.0, 0.23, 0.35) have been presented in Fig. 20a, b, and c.

d. Effect of Initial Liquid Velocity:

An increase in the initial liquid velocity decreases the cavity stability because of greater penetration caused not only by enhanced inertial effects but also due to the additional condensation caused by internal compression which tends to increase the vapor pressure and the corresponding interface temperature. Thus higher superheats are required for greater initial liquid velocities, the effeet being more pronounced for ethanol than water as demonstrated in Figs. 21 and 22. A superheat value $\Delta T^o_w \simeq 4.5$ is just enough for the cavity to sustain boiling with ethanol for V_o = 10 inches/sec, Fig. 21a; for V_o = 25 inch/sec a higher superheat, $\Delta T_w^o = 6$ must be imposed on cavity walls, Fig. 21b. The effect of an increase in the initial velocity for water is small, as shown in Fig. 22, since H_1 is comparatively large and ample time is available for liquid temperature to rise and evaporation to take place counteracting the effect of increased liquid inertia, before the interface could penetrate enough into the cavity.

e. Effect of Cavity Depth:

For a given mouth radius R_o as the depth decreases, comparatively less amount of vapor is trapped for the same contact angle of the fluid and H_1 becomes smaller. Thus the effect of a reduction in depth is somewhat similar to a decrease in contact angle θ; both reduce the cavity stability. As shown in Fig. 23, even water ($\theta = 45°$) is quite sensitive to cavity depth. The cavity having $R_o = 1 \times 10^{-4}$ inches remains no more stable with water at $\Delta T_w^o = 1$, as depth is decreased from 4×10^{-4} inches to 3×10^{-4} inches. Evidently, higher superheats are required for the shallower cavities. Similar effect for methanol has been shown in Fig. 24; it should be noted that for large depth ($D > .0012$), $\Delta T_w^o \approx 1$ is enough for the cavity to remain stable in boiling. The effect of cavity depth and initial liquid velocity on the required superheat for water and methanol has been plotted in Fig. 25 for a cavity with $R_o = 0.0001$ inch. For large depths the required superheat ΔT_w^o is approximately 1, both for water and methanol. As the depth decreases ΔT_w^o increases almost exponentially. For a given R_o and θ, the penetration is complete when depth attains a certain minimum value, as denoted by (*) in Fig. 25, and substantially higher superheats may be required for nucleation to occur. An increase in velocity further increases the value of required superheat, as seen in Fig. 25.

The effect of varying cavity size (R_o and D) on nucleation superheat for methanol is shown in Fig. 26. For a given cavity depth, (for example curve 1 in Fig. 26) when R_o is small, the required superheat is predicted by $(\Delta T)_{\frac{2\sigma}{R_o}}$ and as R_o is increased, the value of required ΔT_w first decreases and attains an optimum value before it starts increasing again (point A' on curve 1). At some value of R_o (for a given depth) the penetration becomes complete (point B on curve 1) as shown by the sign (*) in Fig. 26. The values of input parameters considered for calculation were $\theta = 8°$, $V_o = 0$ and $A_1 = 0.23$.

Fig. 26 can be used to determine the size range of active cavities with methanol for a given superheat. In the following, the conceptual approach is discussed qualitatively. Let the given wall superheat be ΔT_1 as shown by a horizontal line in Fig. 26. The corresponding minimum value of R_o is given by R_1, where the horizontal line ΔT_1 intersects the curve $(\Delta T)_{2\sigma/R_o}$ (Point F in Fig. 26). All those cavities which have a size corresponding to the region contained between the ΔT_1 line and the $(\Delta T)_{2\sigma/R_o}$ curve will be active nucleation sites; this has been shown in Fig. 27a on cavity radius vs. depth plot. Curve O'G in Fig. 27a denotes the dimensions (R_o and D) of cavities for which total initial penetration occurs and these will be considered as inactive sites. All cavities corresponding to the region on the right of the curve O'G entrap sufficient vapor to become potential nucleation sites. Point F on Fig. 27a corresponds to the minimum radius of active cavity, R_1, in Fig. 26. None of the cavities having mouth radius R_0 less than R_1, as denoted by the region above the line R_1FP in Fig. 27a will be active at superheat ΔT_1. Moving towards the right (increasing R_0) on ΔT_1 line in Fig. 26, larger active cavity depth is incurred at point A (Fig. 26) where the curve 1 intersects ΔT_1 line. Increasing R_0 further, depth also increases - point C in Figs. 26 and 27a. At point D in Fig. 26 line ΔT_1 passes through a cavity size for which penetration is complete and hence point D also lies on the curve O'G in Fig. 27a. By similar arguments it is apparent that point E which is to the right of point D in Fig. 26 also lies on the curve O'G in Fig. 27a. The size range of cavities which will be active nucleation sites at superheat ΔT_1 is shown by the shaded region to the right of the curve FACDEG. Cavities belonging to the region FNKDCAF do entrap sufficient amount of vapor to be potential nucleation sites as well as the wall superheat ΔT_1 does satisfy the static criteria of nucleation i.e. ΔT_1 is equal to or greater than $(\Delta T)_{\frac{2\sigma}{R_0}}$; but these cavities are not deep enough so that dynamic effects require a superheat larger than ΔT_1 for their activation. The region of inactive sites in Fig. 27a has been resketched in Fig. 28b and represented by three different shaded regions. Region 1 consists of those inactive cavities which do not entrap sufficient amount of vapor to become potential nucleation sites. The shape of this region in R_0 - D plane depends upon the contact angle θ of the fluid.

For larger contact angle, the boundary of Region 1 shifts downward left, since smaller depth is enough for a given R_0 to entrap vapor, and vice versa. Cavities in Region 2 are good vapor traps but have their mouth radii smaller than R_1, which is the minimum value of R_0 that could be activated at a superheat ΔT_1 as governed by $\Delta T_{2\sigma/R_0}$ criteria, eqn. (15). For higher wall superheats line R_1NFP moves up as described in Fig. 27a and Region 2 becomes smaller. Cavities in Region 3 entrap sufficient amount of vapor and also satisfy the static criteria of nucleation, i.e. $\Delta T_1 > \Delta T_{2\sigma/R_0}$; but their depth being small, they entrap only small amounts of vapor which results in lower stability of such a cavity and a wall superheat greater than ΔT_1 is required for its activation. The right hand side boundary FACD of region 3 represents those cavities which have their sizes such that the superheat ΔT_1 is just enough to overcome dynamic effects and cause nucleation. For a higher superheat ($\Delta T_2 > \Delta T_1$), even smaller cavities become active and region 3 assumes a new boundary as denoted by IJKNQ in Fig. 27a. It is evident now that, as ΔT_w increases, Regions 2 and 3 become smaller and when ΔT_w becomes very large Regions 2 and 3 vanish and all cavities except those in Region 1 become active nucleation sites. Similar arguments could be provided for the effects of decreasing wall superheat on the sizes and shapes of Regions 2 and 3. Region 4 which includes all the cavities excluding Regions 1, 2 and 3, is the region of active sites, and its shape depends upon the shape of Regions 1, 2 and 3.

All the above regions have been presented in a three dimensional plot of Fig. 28a. The three co-ordinates used in Fig. 28a are wall superheat ΔT_w , cavity mouth radius R_o and cavity depth D. The vertical surface 01230 represents the boundary of the region containing all those cavities which entrap sufficient amount of vapor; cavities belonging to the region between the vertical plane $R_o = 0$ and the surface 01230 will be good vapor traps and potential nucleation sites. Surface 45674 represents the $(\Delta T)_{2\sigma/R_o}$ surface and all cavities in the region above this surface satisfy the static criterion of superheat i.e. $\Delta T_w > \Delta T_{2\sigma/R_o}$. Surface 45674 intersects the surface 01230 along the curve iQNG. Thus all cavities in the region enclosed by these two surfaces and to the right of the curve iQNG entrap sufficient vapor and satisfy the static nucleation criterion, however some of these cavities will not be active because of dynamic effects. Regions of active nucleation sites at superheats ΔT_1 and ΔT_2 as shown in Figs. 27a and 27b, have been shown as shaded regions in planes ΔT_1 and ΔT_2 in Fig. 28a. The region where dynamic effects are important is enclosed by surfaces iQNG2i; iQNGP5i and a twisted curved surface whose intersecting curves with planes ΔT_1 and ΔT_2 are FACD and IJK respectively. Thus the regions FACDNF and IJKQI represent those cavities for which dynamic effects are important at superheats ΔT_1 and ΔT_2 respectively, as described earlier in Fig. 27a and 27b. The region of dynamic effects becomes narrower and includes cavities of smaller size as ΔT_w is increased in Fig. 28a.

The static criteria of nucleation based on "limiting thermal boundary layer" thickness δ, were mentioned in Section II.1. Eqns. (5) and (6) describe these criteria and give the minimum and maximum cavity nucleation radius R_o in terms of δ and superheat, ΔT. Such criteria could qualitatively be combined with other criteria discussed earlier in this section, to predict the size range of active cavities at different values of superheat. This has been demonstrated in Figs. 28b, c and d. In Fig. 28b, curve $4\ P_2'\ P_2\ Q_2 6$ in the $\Delta T_w - R_o$ plane qualitatively presents one such criteria (similar to eqn. (5) or eqn. (6)). Size range of active cavities under the influence of three different criteria - vapor entrapment, limiting thermal layer δ and the dynamic effects have been shown by shaded regions in two different superheat planes ΔT_1 and ΔT_2 ($\Delta T_2 > \Delta T_1$) in Figs. 28b, c and d. It should be noted that the region of active sites at a given superheat in Fig. 28b, c and d is bounded by a maximum value of R_o (R_1', denoted by line G_1G_2 in Fig. 28c and R_2' , denoted by line $G_1'\ G_2'$ in Fig. 28d) due to the existing thermal layer δ , while such upper limit does not exist in Fig. 28a, where $\Delta T_{2\sigma/R_o}$ was used instead. The analytical expressions governing the location and shapes of the boundary surfaces enclosing the region of active sites have been given in Appendix G.

Using the concepts discussed above, the size range of active sites on a given surface which has a known cavity size distribution, could be predicted at a given superheat. In Fig. 28e, the cavity size distribution of a given boiling surface has been described by a curved surface 12341 in the N-R_o-D space,where N is the number of cavities of a certain size R_o and D. (The boiling surface described by the smooth curved surface 12341 in the N - R_o - D space of Fig. 28e has been assumed to have a continuous size distribution (mouth radius and depth) of cavities. Thus N denotes the total number of all those cavities whose radius lies between R_o and $R_o + dR_o$, and depth between D and D + dD, where both dR_o and dD are assumed to be infinitesimal. In general, a real surface may not have a continuous size distribution of cavities and hence, the surface 12341 may be discontinuous consisting of population N_i in the discrete size range $(R_o)_i$ and $(R_o + \Delta R_o)_i$, and D_i and $(D + \Delta D)_i$). The region of active sites (in terms of R_o and D) as obtained from Figs. 28a or b could be plotted in Fig. 28e in the R_o and D plane, as shown by the shaded region 5675 in Fig. 28e. When this region is projected vertically up, it intersects the surface 12341 in a segment bounded by the curve 5875, which gives the population distribution of active cavities on the given surface at the particular superheat. As superheat is increased more cavities of smaller sizes are added to the active site population the increase in total population depending upon the shape of the surface 12431. Total active site population is given by:

$$N_{total} = \frac{\iint_{\text{area } 5675} N\,(R_o, D)\, dR_o d_D}{\iint_{\text{area } 5675} dR_o\, d_D}$$

If the given surface does not have a continuous size distribution of cavities, then letting $N_i(R_o, D)$ be the population of cavities existing between radius $(R_o)_i$ and $(R_o + \Delta R_o)_i$ and depth D_i and $(D + \Delta D)_i$, the total active site population is given by:

$$N_{total} = \sum_{\text{area } 5675} N_i\,(R_o, D)$$

f. Effect of R_o and Depth/Diameter Ratio:

In the previous section, we discussed the effect of varying cavity depth and concluded that for small depth to diameter ratio, the required superheat for nucleation is higher than the static superheat, i.e. $\Delta T_w^o > 1$, due to the dynamic effects. In this section, we consider the cavities in the region of dynamic effects and study the effect of varying the cavity size R_o on the required superheat ratio, ΔT_w^o.

As R_o increases, the value of static superheat $(\Delta T)_{\frac{2\sigma}{R_o}}$ as predicted by eqn. (15) decreases. However, in the present analysis, the following factors tend to make the cavity unstable, thus resulting in higher values of ΔT_w^o, as R_o increases for a given cavity depth:

1. Initial penetration of liquid into the cavity is larger, hence H_1 becomes smaller and as discussed before (the effect of cavity depth), the stability of the cavity decreases.
2. Initial liquid temperature might be lower, since more liquid from the saturated bulk may penetrate into the cavity as R_o increases. The approximate analysis in Appendix (B), to predict A_1 shows that A_1 varies inversely with the diameter of cavity. Therefore, larger the diameter of cavity, smaller will be the value of A_1 and lower will be the initial liquid temperature as predicted by eqn. (11).
3. Although the exact mechanism to predict V_o is not known, V_o may depend upon the mouth radius of the cavity.

The effect of varying R_o for a given cavity depth ($4x10^{-4}$inches) can be seen in Fig. 23 and 29c. Fig. 23 shows that for $R_o = 1x10^{-4}$inches, a superheat $\Delta T_w^o \simeq 2.0$ is required, showing that for larger R_o, the cavity is less stable as stated before.

Figs. 29a, b and c show the effect of varying R_o and depth such that depth to diameter ratio of the cavity is kept constant (equal to unity). A superheat corresponding to $\Delta T_w^o \approx 1.3$ is enough for the cavity with $R_o = 1x10^{-4}$ inches, to remain active in boiling with water for zero initial velocity ($V_o = 0$), Fig. 29a. When R_o is increased to $1.5 x10^{-4}$ and $2.0x10^{-4}$ inches higher ratios, $\Delta T_w^o \simeq 1.75$ and 2.0 respectively (Figs. 18b and c) are required, suggesting that for a given depth/diameter ratio (equal to unity) the stability of cavity is decreased for larger R_o.

g. Relative Behavior of Organics in Boiling:

Fig. 30 shows how different organics can exhibit similar behavior under the effect of the initial velocity V_o, assuming they have the same contact angle. Since for small values of θ, the cavity stability is very sensitive to θ, A_1 and the initial liquid velocity, all of these factors may affect the behavior of organics considerably. Since the exact values of θ are not known precisely, $\theta = 8°$ has been assumed for the three liquids - ethanol, benzene and heptane, in Fig. 30. For a $\Delta T_w^o = 4.5$ being imposed on cavity walls, Fig. 30 shows that for $V_o = 25$ in/sec., the three fluids do not behave much differently. When $V_o = 30$ in/sec. is used for benzene and heptane, the three fluids behave almost alike.

(It should be noted that the effect of presence of non-condensible gas inside the cavity was not included in the present analysis and care was taken during the boiling experiments to remove the non-condensible gas by boiling the liquid for sufficient time at high heat flux before the boiling data were taken. However, the presence of a non-condensible gas does effect the cavity stability, as discussed in Ref. [16], and the present model could be modified to include this effect.)

II.3 Boiling Data With Laser Drilled Cavities And Comparison With Analytical Results:

Results of theoretical model, as discussed in previous sections, indicate that the cavity size (R_o and D), contact angle θ of the fluid, initial liquid velocity and the initial liquid temperature are important parameters which determine the cavity stability. For deep initial liquid penetration, as for ethanol and methanol, the required superheat for stable boiling is a strong function of θ, V_o and T^o_{liq}. The relative behavior of water and organics with regard to the value of ρ_{eff} as obtained from the theoretical model depends upon the cavity size. Thus for a given set of cavities having different sizes, the ratio $(\rho_{eff})_{water}/(\rho_{eff})_{organics}$ as calculated from the model may vary from one cavity to another and for a cavity having dimensions of the order of natural cavities on a boiling surface ($R_o = 1\text{x}10^{-4}$ inches, $D = 5\text{x}10^{-4}$ inches), this ratio is shown to be much larger than 1. The observed ρ_{eff} data for individual cavities in Figs. (11) and (12) for water, ethanol and methanol is qualitatively similar to that predicted by the model; i.e. the ratio $(\rho_{eff})_{water}/(\rho_{eff})_{organics}$ as observed in these experiments is observed to be much larger (2 to 10 times) than 1.

The results of the theoretical model in the previous section indicated that the required superheat for stable boiling decreases as the depth increases and for large depths, the superheat approaches the value predicted by the static model, eqn. (15). In order to investigate the effect of cavity depth, boiling experiments were carried out on deep artificial cavities made with laser. The test surface was polished with alumina powder suspension (0.3μ) in liquid and a rotating polishing cloth, so that the surface had a mirror smooth finish. Laser cavities were then drilled on this surface using a high power laser. About 40 to 200 cavities were drilled on different surfaces and care was taken to distribute them uniformly over the surface. Mouth diameter of these cavities was observed to vary from 2×10^{-4} inches to 1×10^{-3} inches and depth to diameter ratio between 1 and 7. Figs. 31 and 32 show photographs of some typical laser cavities taken before boiling with an optical microscope at x1000 magnification.

Methanol and distilled water were boiled respectively on the test surfaces having laser cavities using the apparatus and procedure as described in earlier boiling experiments. At large heat flux values, approximately 50% of the critical heat flux, almost all the laser cavities were found active; however, the active site population decreased as the heat flux was lowered gradually in small steps. At each step, heat flux, surface superheat and number of active sites were recorded. For some cavities, the value of surface superheat at which the individual cavity ceased bubble production was also recorded. ρ_{eff} was calculated using eqn. (4) both for water and methanol.

The observed N/A vs. ρ_{eff} characteristics of a typical boiling surface I, having laser distilled cavities have been shown in Fig. 33. This surface had about 40 laser drilled cavities with R_o ranging from 1.5×10^{-4} inches to 3.5×10^{-4} inches and depth to diameter ration between 1.4 and 4. n/A - ρ_{eff} behavior of an ordinary 0.3μ surface without laser cavities has been included in Fig. 33 for comparison. It could be seen that for the same active site population of methanol, higher (as high as 10 times) ρ_{eff} is observed with the laser drilled surface than the ordinary 0.3μ surface without laser cavities. In other words for the same active site population, the laser drilled surface requires smaller superheat for methanol than the ordinary surface. This could be explained qualitatively on the basis of the theoretical model in the following way. Most of the natural cavities existing on the ordinary surface have their depth to diameter ratio of about 1 and thus are not good vapor traps for wetting fluids like methanol. However, some of these cavities which are able to entrap (depending upon their shape and size) sufficient amount of vapor to nucleate are not deep enough for dynamic effects to be negligible and require high superheat ratio, $\Delta T_w^o > 1$. For the same reason, smaller ρ_{eff} is observed for such cavities on ordinary surfaces during boiling with organics. The laser cavities having their mouth radius of the same order of magnitude (10^{-4} inches) as the natural cavities existing on an ordinary 0.3μ surface, have comparatively larger (1.5 to 4 times) depths. The laser cavities are, hence, good vapor traps and more stable in boiling with methanol as compared to the natural cavities and require much smaller superheats. It should be mentioned here that, although the laser cavities are not strictly cylindrical, as seen in the photomicrographs of some of the cavities in Figs. 35a, b, c and d (taken after boiling with water), the results of the theoretical model which is based on a cylindrical cavity could be qualitatively applied to predict the effect of different parameters. At a given N/A, the observed increase in ρ_{eff} for the laser surface over the ordinary 0.3μ surface is much smaller for water as compared to methanol, the reason being that the natural cavities on the ordinary surface are deep enough for water (the contact angle being large) so that the dynamic effects are small. Hence, the presence of deeper laser cavities on the surface has only marginal effect on the required superheat or ρ_{eff}.

Boiling data for some individual laser cavities have been plotted in Fig. 34. The observed $(\rho_{eff})_{water}/(\rho_{eff})_{methanol}$ ratio varies from 1.3 to 2.1 for these cavities and is much smaller than the same observed for natural cavities, Fig. 12, where it varied from 2 to 6. This agrees with the earlier conclusion from the theoretical model that for large depth, the dynamic effects are small and the static theory, eqn. (15), predicts the required superheat. Magnified photomicrographs were taken of these laser cavities (Fig. 35a, b, c and d) on an optical microscope and the minimum value of R_0 was measured from these photomicrograph for each of these cavities. These values of R_0 have been plotted on Fig. 34 and are found to be in good agreement with the ρ_{eff} observed for water for most of the cavities. Table II gives a listing of the observed ρ_{eff} values and dimensions of the laser cavities.

Thus on the basis of the forementioned analytical and experimental evidence, it could be concluded that laser cavities having large depths to diameter ratio are much more stable in boiling with methanol as compared to natural cavities existing on an ordinary surface. Consequently, a surface having such laser cavities exhibits enhanced nucleation characteristics (larger population of active sites) with methanol at a given superheat than the ordinary surface. Some more of boiling data have been presented in Figs. 36 and 37, for four different boiling surfaces having laser cavities. Surface II and III had about 40 laser cavities each, having R_0 ranging from $2x10^{-4}$ to $7.5x10^{-4}$ inches and depth/diameter ratio varying from 0.5 to 3, as shown in the photomicrographs (taken after boiling with water) of two typical cavities in Fig. 38. Since the laser cavities on surface I on the average had larger R_0 than the laser cavities on surface II, ρ_{eff} with water is larger for surface II than for surface I as could be noted in Figs. 33 and 36. On the other hand, since the average depth/diameter ratio of the laser cavities on surface II is smaller than

TABLE II

OBSERVED DATA FOR LASER CAVITIES:

Cavity #	Mouth Rad. R_o, (D/2)	depth L	L/D	$(\rho_{eff})_{water}$	$(\rho_{eff})_{methanol}$	$\frac{(\rho_{eff})_{water}}{(\rho_{eff})_{methanol}}$
7	2.0×10^{-4}	14.6×10^{-4}	3.65	1.76×10^{-4}	1.34×10^{-4}	1.32
6	1.75×10^{-4}	12.6×10^{-4}	3.6	1.84×10^{-4}	1.12×10^{-4}	1.65
5	2.3×10^{-4}	Large (black hole)	large	2.09×10^{-4}	1.06×10^{-4}	2.0
4	2.5×10^{-4}	18×10^{-4}	2.6	1.4×10^{-4}	1.06×10^{-4}	1.32
3	2.5×10^{-4}	13.8×10^{-4}	2.75	1.61×10^{-4}	0.882×10^{-4}	1.8
2	2×10^{-4}	7.9×10^{-4}	1.9	1.84×10^{-4}	0.882×10^{-4}	2.1
1	2.25×10^{-4}	8.0×10^{-4}	1.78	1.5×10^{-4}	0.845×10^{-4}	1.8

than the cavities on surface I, dynamic effects are more significant and smaller ρ_{eff} is observed with methanol for surface II as compared to surface I.

Surface IV had about 200 laser drilled cavities and surface V had about 140, with R_o ranging from $1.5\text{x}10^{-4}$ to $4\text{x}10^{-4}$ and a depth/diameter ratio varying between 1 and 7. Surface V had qualitatively larger population of laser cavities with higher depth to diameter ratio and hence exhibited higher ρ_{eff} with methanol, as shown in Fig. 37. It should be noted that ρ_{eff} for surface V is almost 10 times larger than that for the ordinary 0.3μ surface, at low active site densities, n/A (i.e. at low heat flux values).

II.4 Comparison With Data From Other Sources

In Ref. [12], data for the incipience superheat were taken on artificial cylindrical cavities of known size with water, ethanol, benzene and n-heptane at atmospheric pressure. Fig. 1 shows these data and a comparison with the prediction of different static theories. As described earlier in Section II.1, none of these theories could successfully predict the observed data.

Table III gives a qualitative comparison between the observed values of superheat for regular bubble production and calculated from the present analysis for a cavity having $R_o = 0.6 \times 10^{-4}$ ft. and depth/diameter ratio equal to 2.5. $\theta = 9°$ was assumed for the three fluids - ethanol, benzene and n-heptane, and V_o was taken in the range 20-26 in/sec. (Bubble nucleation was studied on different glass made artificial cavities and the liquid vapor interface evolution inside the nucleation sites was photographically recorded, in Ref. [17] and [29]. Initial penetration velocity ranging approximately from 6 to 40 in/sec is observed from the experimental data taken for water in these studies.)

TABLE III

COMPARISON WITH DATA FROM REF. [12]:

Fluid	Measured $(T_w - T_{sat})$, F°	Predicted $(T_w - T_{sat})$, F°	Value of V_o used for calculation (inch/sec.)
Ethanol	8	9	20
		12	25
Benzene	14	19	22
		25	26
n-Heptane	10	10	22
		13	26

Denny [24] investigated the effect of the cavity shape and size on pool boiling heat transfer to saturated CCl_4, boiling on a surface in which some artificial cavities of known dimensions were made. Table IV lists some of his data for cylindrical cavities as quoted in Ref. [24]. ΔT represents the temperature at which the onset of ebullition was observed. A comparison has been shown with the analytical results, θ being taken equal to 12° for carbon tetrachloride. It is interesting to note from Table IV that cavities 2a and 7 have the same depth/diameter ratio, but cavity 2a which is 5 times larger than cavity 7, required virtually the same superheat. The static superheat as predicted by eqn. (15) will be 5 times smaller for cavity 2a as compared to cavity 7. In other words, required ΔT_w^o for cavity 2a is 5 times larger than for cavity 7. This is consistent with the prediction of the present model as discussed in Section II.2-5f.

TABLE IV.

COMPARISON WITH DATA FROM REF. [24]:

Cavity	Diameter Inches	Depth Inches	Measured ΔT, F°	Predicted ΔT, F°	V_o used in the analysis in/sec.
(Saturated pressure = 1 atmos.)					
2a	1×10^{-3}	2×10^{-3}	34.7	38 45	20 25
2b	1×10^{-3}	2×10^{-3}	34.6	38 45	20 25
7	2×10^{-4}	4×10^{-4}	35.4	30	25
(Saturated pressure = 1.5 atmos.)					
2a	1×10^{-3}	2×10^{-3}	27.4	23	20
7	2×10^{-4}	4×10^{-4}	27.0	20	25

II.5 DISCUSSION:

The conceptual approach based on the theoretical model for cavity stability, to determine the size range of active cavities was described earlier in Section II.2-5 (Figs. 28a, b, c. d and e). In the following, the effect of varying wall superheat, contact angle and cavity depth respectively on the population distribution of active cavities on a given surface having a prescribed cavity size (R_o) distribution, has been discussed. Fig. 58 shows the cavity size (mouth radius, R_o) distribution on a typical boiling surface. n/A represents the population per unit area, $f(R_o)$, of a certain size R_o and $(N/A)_{Total}$ represents the total population of cavities having a size greater than R_o, e.g.

$$(N/A)_{Total} = \int_{R_o}^{R_{max}} f(R_o) dR_o = F(R_o)$$

In general, N/A denotes the net active site population between size R_1 and R_2,

$$N/A = \int_{R_1}^{R_2} f(R_o)\, dR_o$$

a. Effect of varying wall superheat, ΔT_w:

The effect of varying ΔT_w for a given fluid (contact angle = θ_1) on the size range (R_o and D) of active cavities has been shown in Fig. 59, where the boundary of the region of active sites for five different (progressively increasing) superheats ΔT_1 . . . . . ., ΔT_5 , is described respectively by five different curves. Let us assume that all cavities on the surface have a uniform depth D_1, then the size range of active sites at a superheat ΔT_i is determined by the intersection of the constant depth line $D = D_1$ and the boundary curve of the region of active sites corresponding to ΔT_i. For example, at ΔT_3, all cavities between sizes R_3 and $R_3^{'}$ will be active and the corresponding n/A distribution is shown in Fig. 59a. It is clear that at ΔT_1 none of the sites will be active and as the superheat is increased to ΔT_2, incipience of boiling starts when line $D = D_1$ just touches the boundary of the active site region (point i , $R_o = R_i$). Increasing the superheat further, enlarges the size range and the cumulative active site density (N/A) increases as shown in Fig. 59b. Each of the (N/A) curves in Fig. 59b is described by:

$$N/A = \int_{R_o}^{R^{'}} f(R_o)\, dR_o$$

where, $R^{'}$ is the upper limit on the active cavity size at ΔT_i. These curves terminate at the sign (*) (points F, G. H etc.), where $R_o = R_{min}$ or the lower limit on the active cavity size. The maximum active cavity size is given by $R_o = R_A$ where the curve oG representing the limiting vapor entrapment criterion, intersects line $D = D_1$. Thus the N/A curve starting at $R = R_A$, represents an asymptote for higher superheats and the maximum cumulative active site density corresponding to the minimum active cavity size R_o , increases along this curve as denoted by points G and H respectively for superheats ΔT_4 and ΔT_5. It should be noted that for the case selected, the maximum cumulative site density is less than $(N/A)_{Total}$, since the cavities between size R_A and R_{max} are never active because they do not satisfy the vapor entrapment criterion (Curve OG in in Fig. 59a). Curve R_1FGH represents the cumulative site density vs. R_{min}, as determined by the static criteria given by eqn. (4). The N/A vs. ρ_{eff} data taken on different surfaces during the boiling experiments are equivalent to the curve R_1FGH, since ρ_{eff} has been calculated using eqn. (4) and corresponds to R_{min}.

The effect of wall superheat on N/A, for a different cavity depth D_2 ($D_2 > D_1$, uniform for all the cavities), contact angle θ_1 and the same n/A distribution, has been shown in Fig. 59c. As shown in Fig. 59a, the new incipient point i_1 occurs at superheat ΔT_1 and $R_o = R_{i1}$ ($\Delta T_1 < \Delta T_2$, and $R_{i1} > R_i$). Note that depth D_2 was selected such that the maximum active cavity size, determined by the limiting vapor entrapment criterion (curve OG) is equal to R_{max} (point B), the size of largest cavity existing on the surface. Hence, the new asymptote for N/A with increasing ΔT, coincides with the curve $(N/A)_{Total}$ as shown in Fig. 59c and if the superheat is increased indefinitely, all cavities on the surface become active. For larger depths ($D > D_2$), the point of incipience occurs at greater R_o until it reaches R_{max} when N/A distribution concides with $(N/A)_{Total}$ curve throughout the size range $0 < R_o < R_{max}$. The results of Fig. 59b and c have been summarized in Fig. 59d, which shows an increase in N/A for increased depth at a given superheat.

The effect of superheat on N/A for a different contact angle θ_2 ($\theta_2 > \theta_1$), the same n/A distribution and depth D_1, has been shown in Fig. 60. For larger contact angle θ_2, curve OG representing the limiting vapor entrapment criterion shifts downward on R_o - D plot and encloses cavities of larger R_o. Also the boundary of the region of active sites at a given superheat moves leftwards and encloses cavities of smaller depths. As is clear, the incipience now occurs at smaller superheat ΔT_0 ($\Delta T_0 < \Delta T_2$, Fig. 59a) and larger $R_o = R_{i2}$ ($R_{i2} > R_i$, Fig. 59a). Note that for contact angle θ_2 and depth D_1, the maximum active cavity size as determined by the limiting vapor entrapment criterion is greater than R_{max}, hence the asymptote N/A for increasing ΔT_w coincides with $(N/A)_{Total}$ (Fig. 60b). The results of Fig. 59b and Fig. 60b have been summarized in Fig. 60c, which shows an increase in N/A for increased contact angle at a given superheat.

b. Effect of varying cavity depth, D:

The effect of the cavity depth (assumed to be uniform for all cavities) on N/A for a given contact angle θ and superheat ΔT_w has been shown in Fig. 61. Curve E1i2345 represents the boundary of the region of active sites at ΔT_1 and R_i is incipient size at depth D_1. As the cavity depth D is increased the size range of active sites enlarges as determined by the intersection of different constant depth lines $D_1, \ldots\ldots, D_5$ with curve E1i2345. At a certain depth D_5 the maximum active cavity size (R_5) reaches a value R_{max}, which is the size of the largest cavity existing on the surface, the minimum size (R_1) being determined by eqn. (4) and the value of ΔT_w. For this value of depth (D_5), the N/A distribution coincides with the asymptote $(N/A)_{Total}$ as shown in Fig. 61b. For depths between D_1 and D_5, the maximum active cavity size is less than R_{max} (R_2, R_3, R_4 etc.) and the corresponding N/A is smaller than $(N/A)_{Total}$. An increase in the cavity depth beyond D_5 does not alter the population, N/A.

c. Effect of varying contact angle, θ:

The effect of varying θ on N/A distribution for a constant superheat ΔT_1 and depth D_1 is shown in Fig. 62. As θ is progressively increased from θ_1 to θ_5, curve OG, representing the vapor entrapment criterion moves downward (curves OG_1, OG_2, OG_3, OG_4 and OG_5 respectively in Fig. 62a). The boundary of the region of active sites correspondingly moves to the left, since the increase in contact angle causes cavities of smaller depths to become active. As is clear from Fig. 62a, for $\theta = \theta_1$, none of the cavities are active. Incipience starts at $\theta = \theta_2$ and at $R_o = R_1$, and with an increase in θ, the size range of active cavities grows, with a corresponding increase in the population N/A, as shown in Fig. 62b. For a certain $\theta = \theta_5$, the maximum active cavity size attains a value $R_5 = R_{max}$, the size of the biggest cavity existing on the surface, and N/A distribution coincides with the asymptote $(N/A)_{Total}$. The minimum active cavity size is determined by eqn. (4) based on ΔT_w, as before.

III. Effect Of Surface Conditions On The Boiling Heat-Flux

III.1 Heat Flux Model

In the present work, the transient heat flux model developed by Mikic and Rohsenow [7] has been used to predict the boiling heat flux. Considering the transient conduction to and subsequent replacement of the superheated liquid layer in contact with the heating surface as the single predominant mechanism of heat transfer in nucleate boiling, Mikic and Rohsenow derived an expression for $(q/A)_b$ in terms of liquid properties, average bubble frequency f, bubble departure diameter D_b, active site density N/A and wall superheat ΔT, as given by the following expression:

$$(q/A)_b = 2\sqrt{\Pi\ (k\rho c)_\ell}\ \sqrt{f}\ D_b^2\ (N/A)\ \Delta T \qquad (17)$$

The above relation is strictly valid for the isolated bubble region only, when the individual areas of influence of active sites do not overlap. The total heat flux from the boiling surface can be expressed as

$$q/A = \frac{A_{nc}}{A_{total}}\ (q/A)_{nc} + (q/A)_b \qquad (18)$$

where $(q/A)_{nc}$, the natural convection component of heat flux, can be estimated by the following.

For laminar range, i.e. for $10^4 < R_a < 10^7$, where, $R_a = \dfrac{\gamma\ g\ \Delta T\ (A_{nc})^{3/2}}{\alpha\ \gamma}$,

$(q/A)_{nc}$ is given by:

$$(q/A)_{nc} = 0.54\ (\rho c)_\ell \left[\frac{g\ \gamma\ \Delta T^5\ \alpha^3}{\sqrt{A_{nc}}\ \nu}\right]^{1/4} \tag{19}$$

and for Turbulent Range: $2x10^5 < R_a < 3x10^{10}$

$$(q/A)_{nc} = 0.14\ (\rho c)_\ell \left[\frac{g\ \gamma\ \Delta T^4\ \alpha^2}{\nu}\right]^{1/3} \tag{20}$$

$\dfrac{A_{nc}}{A_{total}}$ is given in terms of n/A as follows:

$$\frac{A_{nc}}{A_{total}} = 1 - \frac{N}{A}\ \Pi D_b^2 \tag{21}$$

where A_{total} is the total area of the heating surface.

Values of f and D_b, required in eqn. (17) can be estimated by the following [24, 25]:

$$D_b = C_2 \left[\frac{\sigma\ g_o}{g\ (\rho_\ell - \rho_v)}\right]^{1/2} [Ja]^{*\ 5/4} \tag{22}$$

where, $C_2 = 1.5x10^{-4}$ for water and $4.65x10^{-4}$ for organics and

$$\overset{*}{Ja} = \frac{\rho_\ell\ c_\ell\ T_s}{\rho_v\ H_{fg}} \tag{23}$$

and,

$$f\ D_b = 0.6 \left[\frac{\sigma\ g_o\ g\ (\rho_\ell - \rho_v)}{\rho_\ell^2}\right]^{1/4} \tag{24}$$

Thus, for a given surface and fluid, if N/A vs. ΔT distribution, which depends upon the surface characteristics and fluid properties, is known, $(q/A)_b$ vs. ΔT can be estimated from eqn. (17).

III.2 Experimental Results

Boiling data with water and methanol were taken on four different copper surfaces with varying degrees of roughness and prepared by different preparation techniques as discussed in Appendix C. q/A vs. ΔT were taken with decreasing heat flux and active site density, N/A vs. ΔT was visually recorded in the isolated bubble region. Heat flux was then lowered to a value when all nucleation sites disappeared and h_{nc} was estimated from the corresponding q/A vs. ΔT values. Using this value of h_{nc} , $(q/A)_{nc}$ was estimated at other ΔT values, $(q/A)_b$ was then calculated using eqns. (18) and (21).

Figs. 39a, 40a, 41a and 42a show the observed cumulative site density distribution for the four different copper surfaces. ρ_{eff}, plotted on abscissa was calculated from the observed ΔT values using eqn. (4).

Figs. 39b, 40b, 41b and 42b show the comparison between the observed $(q/A)_b$ as mentioned above and the predicted $(q/A)_b$ from eqn. (17) for the four different surfaces respectively. A close prediction can easily be noted. The value of f and D_b for water and methanol, used in eqn. (17) were taken from Ref. [27] and [28], where f and D_b were measured experimentally for the two fluids. It can be noted that the extrapolation of $(q/A)_b$ vs. ΔT behavior in the isolated bubble region, successfully predicts the behavior in the higher heat flux region. As noted earlier in Ref. [18], the good agreement in the higher heat flux is fortuitous, since eqn. (17) is strictly valid at the isolated bubble region only. This fortuitous agreement may in part be due to the enhanced natural convection due to bubble generation compensating for bubble overlap.

The effect of surface roughness on the cumulative site density and boiling heat flux is summarized in Figs. 43 and 44, which are replots of Figs. 39, 40, 41 and 42. As the rms surface roughness increases, both N/A and $(q/A)_b$ increase for a given ΔT_w. Relative behavior of different fluids boiling on the same surface have been discussed in Appendix E.

Effect of Laser Cavities on Boiling Heat Flux:

Fig. 45 to Fig. 48 show $(q/A)_b$ (as defined in eqn. (18) vs. ΔT_w behavior as observed in boiling on four different laser drilled surfaces. Higher boiling heat flux is observed for the same ΔT_w, on a laser drilled surface as compared to a similar surface without laser cavities. The increase in the boiling heat flux occurs, according to eqn. (17) by an increase in the active site population at a given superheat due to the presence of deep laser cavities. However, the boiling heat flux predicted by eqn. (17) using the observed N/A and ΔT values, is found to be higher than the observed $(q/A)_b$ defined by eqn. (18), as seen in Figs. 45 and 46. As mentioned earlier in this section, the values of f and D_b for water and methanol, used in eqn. (17) were taken from Ref. [27] and [28], where f and D_b were measured experimentally during boiling on heated cylindrical test elements having ordinary smooth surface. Some crude experimental measurements were made in the present study to measure the frequency of bubble departure from laser cavities, using a variable frequency stroboscope. Data taken on laser surface III for water has been presented in Fig. 49; much lower values of frequency are observed as compared to that measured in Ref. [27] for a smooth surface. Moreover, frequency is found to vary with wall superheat, increasing with increasing superheat. It is suspected that the observed changes in the departure frequency may also affect the bubble departure diameter and thus f and D_b values used in eqn. (17) for the prediction of $(q/A)_b$ may be in error, causing a discrepency in the prediction of $(q/A)_b$ for laser surfaces as observed in Figs. 45 and 46. In order to provide a complete understanding of the effect of the presence of deep cavities on heated surfaces on boiling behavior, one has to know not only the superheat for their activation and with it the whole active site distribution but also the eventual changes in bubble frequency and departure size due to the presence of such cavities. No precise measurements on the bubble frequency and departure size have been made in the present investigation and further experimental work is required to explain the observed heat flux behavior of boiling surfaces having deep cavities. A theoretical analysis, presented in Appendix F, considers the effect of cavity size and superheat on frequency by considering the effect on waiting time (time between the last bubble departure and appearance of the next one on the surface) and bubble growth time. The observed frequency behavior of laser drilled surfaces, e.g. comparatively lower departure frequency than ordinary surfaces in the low heat flux region and the observed increase in frequency with increasing superheat, has been explained qualitatively by the theoretical model, presented in Appendix F. An increase in the cavity size or decrease in the surface superheat ΔT_w, results in longer waiting time and bubble contact time, thus causing a lower frequency, as observed for deep laser cavities.

IV. SUMMARY AND CONCLUSIONS:

Several nucleation theories [8, 9, 10, 11] have been proposed in the past to predict the size range of active sites in boiling. These theories did not account for all the important parameters involved and hence, could not successfully predict the observed nucleation behavior of some artificial cavities of known size and shape [11, 12]. The present investigation was undertaken to study the pertinent parameters affecting nucleation in boiling.

A theoretical model for the stability of boiling nucleation from a cavity, has been developed considering the liquid penetration, the effects of transient heat flux and, the inertial and viscous effects of liquid moving inside the cavity. Parameters such as cavity radius and depth (which are characteristic of the boiling surface), contact angle (which depends upon the fluid-surface combination), and the dependent parameters (which are the consequence of the physical behavior of the considered pheomenon) e.g. the initial temperature and penetration velocity of liquid into the cavity are found to be important in determining the required superheat for stable boiling from the cavity. A decrease in cavity depth or contact angle decreases the amount of trapped vapor and the stability of cavity, thus increasing the required superheat for stable boiling. A lower initial liquid temperature enhances the condensation of vapor in the cavity, thus causing lower stability and increasing the required superheat. A lower initial penetration velocity of the liquid enhances cavity stability and decreases the superheat due to smaller inertial effects.

Gas diffusion and boiling experiments carried out with ethanol, methanol and water on individual cavities, revealed that cavities which have small depth to diameter ratio (of the order of 1) require much higher (2 to 10 times) superheats than predicted by the static theory when boiled with ethanol and methanol, but the observed superheats for boiling with water were closely predicted by the static theory. For laser cavities having large depth to diameter ratio (as large as 7) the static model closely predicts the observed superheat for stable boiling both for methanol and water. The observed experimental results have been explained qualitatively by the analytical model. All boiling experiments were carried out at atmospheric pressure and saturated bulk conditions.

The following three different criteria are found to be important in determining the required superheat for stable boiling from a cavity:

1. Vapor entrapment in the cavity at bubble departure.
2. Dynamic effects caused by the inertia and viscous effects of moving liquid and transient heat transfer effects due to the evaporation and condensation of vapor inside the cavity.
3. Static equilibrium criterion which governs the necessary conditions for the growth of the vapor nucleus emerging out of the cavity mouth.

For a given surface in boiling with a known fluid and wall superheat, all those cavities which have their dimensions such that they entrap sufficient amount of vapor and that ΔT is large enough to satisfy criteria 2 and 3 above, will be active. The size range of active cavities at different superheats as determined by the three criteria above, have been depicted by a three dimensional region in the $\Delta T - R_o - D$ space.

Boiling data were taken with methanol and water on five different surfaces having laser drilled cavities. These surfaces contained about 40 to 200 laser cavities with their mouth diameter varying from 2×10^{-4} inches to 1×10^{-3} inches and depth to diameter ratio from 1 to 7.

Since the laser cavities having large depth to diameter ratio are more stable in boiling than the natural cavities which have small depth to diameter ratio (of the order of 1), higher active site population and boiling heat flux are observed at a given superheat for surfaces having laser drilled cavities than the ordinary surfaces without such artificial cavities. The bubble departure frequency, which plays an important role in determining the boiling heat flux, is observed to decrease with decreasing wall superheat for the laser cavities. The observed effect of the cavity size and wall superheat on frequency has been explained qualitatively by a theoretical model, which estimates the waiting time and the bubble contact time when the bubble breaks away from the surface.

V. RECOMMENDATIONS:

The present analytical model explains the qualitative behavior of water and organics as regard to their stability in boiling from a cavity; nevertheless, the model contains several oversimplifications and the following improvements could be considered:

1. The postulated vapor trapping mechanism requires modifications to account for condensation or evaporation effects at the liquid vapor interface during entrapment, the effect of the liquid motion on contact angle and other transient fluid dynamic effects which effect the interface motion into the cavity. Evaporation at the interface during the vapor entrapment may cause smaller liquid penetration and similarly the condensation might result in deeper penetration into the cavity. As described earlier in the discussion of the effect of contact angle, the initial liquid penetration has strong effect on cavity stability.

2. No definitive data are available in literature for the magnitude of the initial liquid penetration velocity, V_o, of different fluids after the bubble departure from a cavity in boiling, as mentioned earlier in Section II.2-5. Since V_o is an important input parameter in the present theoretical analysis of dynamic effects, its experimental measurement for different cavity sizes and fluids might be helpful to enhance the utility of the present model.

3. In the present analysis of cavity stability, the cavity is assumed to become inactive when liquid-vapor interface reaches the cavity bottom as sketched in Fig. 8. The volume of vapor contained, in this situation, between the interface and cavity bottom is v_{crit}. If the initial volume of trapped vapor which depends upon the cavity size and θ, is less than this volume, the cavity is not considered to be a potential nucleation site. However, the entrapped vapor may form a small nucleus near to the bottom of the cavity which may grow by evaporation under certain conditions of wall superheat. Further analysis is required to predict nucleation under such conditions.

4. In the present theory, a smooth walled cylindrical cavity was considered. The natural cavities existing on a boiling surface are observed to have arbitrary shapes and a microroughness on walls. These factors must be considered to predict the behavior of a natural boiling surface.

As mentioned earlier in the Section III.2, in order to provide a complete understanding of the effect of the presence of deep cavities on heated surfaces on boiling behavior, one has to know the eventual changes in bubble frequency and departure size due to the presence of such cavities. Only preliminary experimental measurements were made on bubble frequency in the present investigation, and the observed frequency behavior (f vs. ΔT) was explained qualitatively by a theoretical model. Further experimental and theoretical work is recommended to predict the effects of cavity size on bubble frequency and departure size, so that the overall heat flux behavior of the surface having deep artificial cavities could be determined more precisely.

BIBLIOGRAPHY

1. Bankoff, S. G.; "Entrapment of Gas in the Spreading of a Liquid over a Rough Surface." A.I.Ch.E. Journal, Vol. 4, 1958, pp. 24-26.

2. Clark, H. B., Strenge, P. S., and Westwater, J. W.; "Active Sites for Nucleate Boiling." Chem. Eng. Prog. Symp. Series, Vol. 55, 1959, pp. 103-110.

3. Corty, C. and Foust, A. S.; "Surface Variables in Nucleate Boiling." Chem. Eng. Prog. Symp. Series, Vol. 51, No. 17, p. 1 (1955).

4. Kurihara, H. M. and Myres, J. E.; "The Effect of Superheat and Surface Roughness on Boiling Coefficients." A.I.Ch.E. Journal, Vol. 6, 1960, pp. 83-91.

5. Tien, C. L.; "A Hydrodynamic Model for Nucleate Pool Boiling." Intl. J. of Heat and Mass Transfer, Vol. 5, 1962, pp. 533-540.

6. Zuber, N.; "Nucleate Boiling: The Region of Isolated Bubbles and the Similarity with Natural Convection." Intl. J. of Heat and Mass Transfer, Vol. 6, 1963, pp. 53-78.

7. Mikic, B. B. and Rohsenow, W. M.; "A New Correlation of Pool Boiling Data including the Effect of Heating Surface Characteristics." Journal of Heat Transfer, Vol. 91, 1969, pp. 245-250.

8. Griffith, P. and Wallis, J. D.; "The Role of Surface Conditions in Nucleate Boiling." Chem. Eng. Progress Symp. Series, Vol. 56, No. 30, pp. 49-63, 1960.

9. Hsu, Y. Y.; "On the Size Range of Active Nucleation Cavities on a Heating Surface." J. of Heat Transfer, Vol. 84, No. 3, August 1962, pp. 207-216.

10. Han, C. Y. and Griffith, P.; "The Mechanism of Heat Transfer in Nucleate Pool Boiling." Intl. J. of Heat and Mass Transfer, Vol. 8, No. 6, June 1965, pp. 887-904.

11. Howell, J. R. and Siegel, R.; "Incipience, Growth and Detachment of Boiling Bubbles in Saturated Water from Artificial Sites of Known Geometry." Third Intl. Heat-Transfer Converence, Chicago, Vol. 4, 1966, p. 12.

12. Hatton, A. P., James, D. D. and Liew, T. L.; "Measurement of Bubble Characteristics for Pool Boiling from Single Cylindrical Cavities." Heat Transfer 1970, Elsevier Publishing Co., Amsterdam, Vol. V, p. B1.2.

13. Bankoff, S. G.; "The Prediction of Surface Temperatures at Incipient Boiling." Chem. Eng. Progress Symposium Series, Vol. 55, No. 29, pp. 87-99, 1959.

14. Marto, P. J. and Rohsenow, W. M.; "The Effect of Surface Conditions on Nucleate Pool Boiling Heat Transfer to Sodium." Journal of Heat Transfer, May 1966, pp. 183-195.

15. Shai, I. and Rohsenow, W. M.; "The Mechanism of Nucleate Pool Boiling." M. I. T. Engineering Projects Lab. Report No.-DSR 76303-45 (1967).

16. Cole, Robert; "Boiling Nucleation." Reprints from Advances In Heat Transfer, Vol. 10, c 1974, Academic Press Inc., pp. 85-165.

17. Kosky, P. G.; "Nucleation Site Instability In Nucleate Boiling." Intl. J. of Heat Mass Transfer, Vol. 11, 1968, pp. 929-932.

18. Lorenz, J. J.; "The Effects of Surface Conditions on Boiling Characteristics." Ph.D. Thesis, Dept. of Mech. Eng., M. I. T., December 1971.

19. Simon, F. F. and Hsu, Y. Y.; "Effect of Contact Angle Hysteresis on Moving Liquid Film Integrity." Technical Paper proposed for presentation at Seventy-third National Meeting of the A.I.Ch. E., Minneapolis, Minnesota, Aug. 27-30, 1972.

20. Davies, J. T. and Rideal, E. K.; "Interfacial Phenomenon." Academic Press, 1961.

21. Adam, N.; "Physics and Chemistry of Surfaces." London, Oxford, University Press, Third Edition, 1941.

22. Gregg, S. J.; "The Surface Chemistry of Solids." Chapman and Hall, 1951.

23. Denny, V. E.; "Some Effects of Surface Microgemetry on Natural Convection and Pool Boiling Heat Transfer to CCl_4." Ph.D. Thesis, University of Minnesota, 1961.

24. Fabic Stanislav; "Vapor Nucleation on Surfaces subjected to Transient Heating", Ph.D. Thesis, University of California, Berkeley, Aug. 1964.

25. Cole, R. and Rohsenow, W. M.; "Correlation of Bubble Departure Diameters for Nucleate Boiling," presented at the 10th National Heat Transfer Conference, A.I.Ch.E., August 1968.

26. Cole, R.; "Bubble Frequencies and Departure Volumes at Subatmospheric Pressures." A.I.Ch.E. Journal, Vol. 13, No. 4, 1967, pp. 779-783.

27. Tolubinsky, V. I. and Ostrovsky, J. N.; "On the Mechanism of Boiling Heat Transfer (Vapor Bubbles Growth Rate in the Process of Boiling of Liquids, Solutions and Binary Mixtures)", Intl. J. of Heat and Mass Transfer, Vol. 9, 1966, pp. 1463-70.

28. Perkins, A. S. and Westwater, J. W.; "Measurements of Bubbles Formed in Boiling Methanol", A.I.Ch.E. Journal, Vol. 2, No. 4, Dec. 1956, pp. 471-475.

29. Anton, I. and Vékaś, L.; "A Study on the Cavitation Bubble Formation Process", Rev. Roum Sci. Tech-Me'c. Appl., Tome 18, No. 6, p. 1113-1129, Bucarest, 1973.

30. Mikic, B. B., Rohsenow, W. M. and Griffith, P.; "On Bubble Growth Rates", Intl. J. of Heat Mass Transfer, Vol. 13, pp. 657-666, Pergamon Press 1970.

31. "Conduction Heat Transfer" by V. S. Arpaci, University of Michigan Addison-Werley Publishing Co., pp. 231-236.

32. Staniszowski, B. E.; "Nucleate Boiling Growth and Departure:, Tech. Report No. 16, DSR 7673, ONR Contract No. 1841 (39), Heat Transfer Lab., M. I. T. (Aug. 1959).

33. Hatsopoulous, G. N. and Keenan, J. H.; "Principles of General Thermodynamics", John Wiley and Sons. (1965).

APPENDIX A. Analysis For Liquid Motion Inside A Cylindrical Cavity Considering Dynamic Effects:

General momentum theorem, when applied to a control volume of fluid, leads to the following relation in z direction:

$$\Sigma \vec{F}_z = \frac{\partial}{\partial t} \iiint_{c.v.} \vec{V}_z \, \rho_\ell \, dv + \oint\!\!\oint_{c.s.} \vec{V}_z \, (\rho_\ell \vec{V}_z \cdot d\vec{s}) \qquad (A.1)$$

where $\vec{F}_z$ represents **net** force and $\vec{V}_z$, the velocity in z direction.

As shown in Figs. 8 and 9, in the present analysis, the positive z direction has been chosen pointing towards the bottom of the cavity. The average velocity of the liquid column, V has been assumed to be a function of time only e.g.

$$V = \frac{dz}{dt}$$

In terms of V, equation (A.1) could be written as follows:

$$\oint\!\!\oint_{c.s.} \vec{V}_z \cdot (\rho_\ell \vec{V}_z \cdot d\vec{s}) = -\rho_\ell V^2 \pi R_o^2 \qquad (A.2)$$

$$\frac{\delta}{\delta t} \iiint_{c.v} \vec{V}_z \cdot \rho_\ell \, dv = \pi R_o^2 \, \rho_\ell \, (M + Z) \, \frac{dV}{dt} + \rho_\ell V^2 \pi R_o^2 \qquad (A.3)$$

Substituting the above in equation (A.1) gives:

$$\Sigma \vec{F}_z = \pi R_o^2 \, \rho_\ell \, (M + z) \, \frac{dV}{dt} \qquad (A.4)$$

Fig. 9 shows the forces acting on the control volume in z direction. We will now evaluate each of these forces as follows:

Wall shear stress on liquid is given by (assuming a laminar fully developed velocity profile),

$$\tau_z = \mu\left(\frac{dV_z}{dr}\right)_{r=R_o} \tag{A.5}$$

In order to estimate the shear stress the following velocity distributions has been assumed:

$$V_z = 2V\left[1 - \left(\frac{r}{R_o}\right)^2\right] \tag{A.6}$$

where, V is the average velocity of the liquid column as defined earlier. Substituting V_z from equation (A.6) into (A.5) gives:

$$\tau_z = -\mu\,\frac{4V}{R_o} \tag{A.7}$$

Net shear force on liquid in z direction,

$$F_{sh} = -2\pi R_o\,(M + z)\,\frac{4\mu V}{R_o} = -8\pi\mu\,V\,(M + Z) \tag{A.8}$$

Pressure force in z direction,

$$F_p = -\left[\left(P_{vap} - \frac{2\sigma}{\rho}\right) - P_s\right]\pi R_o^2 \tag{A.9}$$

where P_{vap} is the pressure of vapor inside the cavity at time t, when the interface is at z.

At time t = 0, pressure of vapor satisfies the relation:

$$P^o_{vap} = \frac{W^o_g \; RT_o}{v^o_{vap}}$$

At t > 0,

$$P_{vap_z} = \frac{P^o_{vap} \; W_g \; v^o_{vap} \; T}{W^o_g \; v_{vap} \; T_o}$$

where, v_{vap} is the volume of vapor at time t.

Assuming $T \simeq T_o$,

$$P_{vap_z} = \frac{P^o_{vap} \; W_g \; v^o_{vap}}{W^o_g \; v_{vap}} \tag{A.10}$$

Mass of vapor inside the cavity at any time t > 0,

$$W_g = W^o_g + \frac{\lambda \pi R_o^2}{h_{fg}} \left[\int_0^t q \, d \, t \right] \tag{A.11}$$

where $\int_0^t$ qdt represents total amount of heat transferred from liquid to vapor through the interface, this is also equal to the latent heat required for evaporation at the interface. λ is the area correction factor due to the curvature of the interface.

Total volume of vapor is given by:

$$v_{vap} \simeq v^o_{vap} + \Delta v = v^o_{vap} - \frac{Z}{H} \; v^o_{vap} \tag{A.12}$$

Substituting (A.11) and (A.12) in (A.10) gives:

$$P_{vap_z} = \frac{P^o_{vap}\left[W^o_g + \frac{\lambda\pi R_o^2}{H_{fg}} \int_0^t q\,d\,t\right]}{W^o_g\ (1 - Z/H)} \qquad (A.13)$$

From (A.9) and (A.13),

$$F_p = -\left[\frac{P^o_{vap}\left[W^o_g + \frac{\lambda\pi R_o^2}{H_{fg}} \int_0^t q\,d\,t\right]}{W^o_g\ (1 - Z/H)} - P_s - \frac{2\sigma}{\rho} \quad \pi R_o^2\right] \qquad (A.14)$$

Substituting (A.8) and (A.14) in (A.4), the momentum equation reduces to:

$$\left[\frac{P^o_{vap}\left[W^o_g + \frac{\lambda\pi R_o^2}{H_{fg}} \int_0^t q\,d\,t\right]}{W^o_g\ (1 - Z/H)} - P_s - \frac{2\sigma}{p}\right] \Pi R_o^2 + 8\pi\mu\ (M + Z)$$

$$+\pi R_o^2\ \rho_\ell\ (M + Z)\ \frac{dV}{dt} = 0 \qquad (A.15)$$

Rearranging equation (A.15), and noting that $\frac{dV}{dt} = \frac{d^2z}{dt^2}$, we get,

$$H\ P^o_{vap}\left[1 + \frac{\lambda\pi R_o^2}{H_{fg}\ W^o_g} \int_0^t q\,d\,t\right] + \frac{8\ \mu\ (M + Z)\ (H-Z)}{R_o^2}\ \frac{dz}{dt}$$

$$+ \rho_\ell\ (M + Z)\ (H-Z)\ \frac{d^2z}{dt^2} - \left(P_s + \frac{2\sigma}{\rho}\right)(H-Z) = 0 \qquad (A.16)$$

Assuming that the interface temperature T_i is equal to the vapor temperature, which can be estimated by Clausius-Clapeyron equation with the perfect gas approximation as follows:

$$P_{vap_z} - P_s = \frac{J\, H_{fg}}{v_{fg} T_{sat}} \quad (T_i - T_{sat})$$

or,

$$T_i - T_{sat} = \frac{v_{fg}\; T_{sat}}{J\, H_{fg}} \; (P_{vap_z} - P_s) \qquad \text{(A.17)}$$

substituting for P_{vap_z} from equation (A.13), (A.17) reduces to

$$T_i - T_{sat} = \frac{v_{fg}\; T_{sat}}{J\, H_{fg}} \left[P^o_{vap} \; \frac{\left[W^o_g + \frac{\lambda \pi R_o^2}{H_{fg}} \int_0^t q\, dt \right]}{W^o_g \quad (1 - Z/H)} \quad - P_s \right] \qquad \text{(A.18)}$$

Rearranging equation (A.18) one gets -

$$(T_i - T_{sat})\; (H-Z) + \frac{P_s \;\; (H-Z)\; v_{fg}\; T_{sat}}{J\, H_{fg}} = \frac{v_{fg}\; H\, P^o_{vap}\; T_{sat}}{J\, H_{fg}} \left[1 + \frac{\lambda \pi\, R_o^2}{H_{fg}\; W^o_g} \int_0^t q\, dt \right] \qquad \text{(A.19)}$$

Equations (A.16) and (A.19) represents the governing equations that can be solved simultaneously for z and T_i with the initial conditions described in Sections II.2-2 and II. 2-3.

APPENDIX B. Estimation Of The Initial Liquid Temperature:

As the bubble departs from a cavity, liquid from the vicinity of the cavity mouth moves into the cavity. The liquid that penetrates into the cavity may come partly from the thermal boundary layer in the liquid adjacent to the heating surface. In the present analysis the initial liquid temperature has been estimated by equation (11), e.g.

$$T^o_{liq} = T_{sat} + A_1(T_w - T_{sat})$$

Had all the liquid, that penetrated into the cavity, come from the bulk, T^o_{liq} would have been equal to T_{sat}, thus A_1 being zero. Clearly, A_1 can assume values between 0 and 1, depending upon the relative portions of liquid that come from the bulk and from thermal boundary layer. Due to slight asymmetry in bubble departure, the liquid may move into the cavity from a preferential direction. This has been sketched in Fig. 51, where the liquid has been shown to be moving from the right into a cylindrical cavity of the mouth radius R_o. θ represents the contact angle of the liquid and δ the thermal layer thickness at the time of penetration. It has been assumed that of all the liquid that penetrated into the cavity, a liquid volume corresponding to a thickness equal to δ comes from the thermal layer, as shown in Fig. 51. So the volume of liquid that comes from the thermal layer can be approximated (for small δ) by,

$$v_{t\ell} \; \alpha \; R_o^2 \; \delta \cot \theta$$

or,

$$v_{t\ell} = C_1 R_o^2 \delta \cot\theta, \quad \text{where } C_1 \text{ is a constant.}$$

Total volume of liquid that penetrated into the cavity can be written as:

$$v_{total} \; \alpha \; R_o^3 \cot\theta$$

or,

$$v_{total} = C_2 R_o^3 \cot\theta, \quad \text{where } C_2 \text{ is another constant.}$$

Assuming that the liquid that comes from the thermal layer has an average temperature equal to $(T_{sat} + \frac{\Delta T}{2})$, the overall liquid temperature can be calculated by energy balance as follows:

$$C_2 R_o^3 \cot\theta \, T^o_{liq} = (C_2 R_o^3 \cot\theta - C_1 R_o^2 \delta \cot\theta) T_{sat} + \left[C_1 R_o^2 \delta \cot\theta \left(T_{sat} + \frac{\Delta T}{2}\right) \right] = C_2 R_o^3 \cot\theta \, T_{sat} + C_1 R_o^2 \delta \cot\theta \left(\frac{\Delta T}{2}\right)$$

or,

$$T^o_{liq} = T_{sat} + \frac{C_1 R_o^2 \delta \cot\theta}{C_2 R_o^3 \cot\theta} \frac{\Delta T}{2}$$

$$= T_{sat} + \frac{C_1}{2C_2} \frac{\delta}{R_o} \Delta T$$

comparing with equation (11), we see that

$$A_1 \; \alpha \; \delta / R_o$$

As a growing bubble departs from a cavity, a liquid microlayer at the base of the bubble evaporates with it, and new liquid from the bulk takes its place. If we assume that the time elapsed between the bubble departure and initial liquid penetration is small, then δ will be small as has been assumed in the above analysis.

APPENDIX C. Boiling Apparatus and Procedure

APPARATUS

An apparatus similar to that described in Ref. [18] was used. Fig. 52 shows the sketch of the apparatus, which consisted of a rectangular brass chamber 4" x 4" x 6" in size and coated with FEP Teflon on inside and outside. The coating provided a good corrosion resistance. Through a 1-1/2" diameter hole in the bottom of this chamber, a cylindrical copper specimen of 1-1/4" diameter and 4: long, was fitted with the help of a 0.04" thick nickle steel flange and four 1/8" brass bolts. Teflon and rubber gaskets were used to provide proper sealing as well as insulation between the chamber bottom and the nickle steel flange of the specimen. The main heater used was 940 watt Hot Watt cartridge heater 5/8" diameter, 2" long fitted into a copper cylinder 1-1/8" diameter and 3" long. The copper cylinder was fastened to the bottom of the specimen with the help of flanges and 3 screws. For proper thermal contact between the specimen and the heated cylinder, 'Silver Goop' was applied between their mating surfaces. To keep the bulk of boiling liquid saturated two 400 watts chomalox annular shaped guard heaters were fastened to the two vertical sides of the chamber. To view the boiling surface, two 2" x 5" glass windows were provided on the front and back side of the chamber. Four 30 gage Copper-Constantan thermocouples were place in 0.025" diameter thermocouple holes located at 0.1", 0.6", 1.1", and 1.6" from the boiling surface and along the axis of the specimen. Two reflux condensers were provided at the top of the chamber to condense the vapor back into the chamber. A safety suction hood was located just above the boiling chamber to remove away the vapors escaping through condensers. A therometer was used to check the saturation temperature of the bulk.

SURFACE PREPARATION AND BOILING PROCEDURE:

Before each test run the proper surface technique was employed according to the required surface roughness of the test specimen. Wet grinding was used with silicon carbide grit papers having different grit sizes. For smoother surfaces (.3μ) alumina powder suspension in liquid was used with a rotating polishing cloth. Grinding was employed to obtain rougher surfaces. Finally the surface was washed with soap and rinsed with alcohol before it was dried in a draft of warm air. Laser cavities were drilled by Optimation, Inc., 358 Baker Avenue, Concord, Massachusetts.

Each liquid was degassed for about 45 minutes before actual observations were taken. Organics were degassed by boiling in the chamber at about 2/3 burn out heat flux. Water was first partially degassed in a separate container on a heater for about 1/2 hour and again in the chamber for about 30 minutes at about 1/2 burn out heat flux. Data with organics were taken prior to water, since they do not affect the boiling surface much as compared to distilled water which causes visual oxidation of the surface and formation of scales. If water were boiled first, the surface characteristics may change due to oxidation and comparison with organics with similar characteristics of the surface would be difficult.

Data were taken while traversing the boiling curve from higher to lower heat flux values. Sufficient time was allowed to reach equilibrium during each observation.

To minimize heat losses, the test specimen and the chamber were insulated using several layers of fiberglass insulation.

APPENDIX D. Gas Diffusion Experiment:

In order to predict the nucleation characteristics (N/A vs. ρ of a boiling surface with different liquids, an alternative technique - gas diffusion, was attempted at. In this experiment the test surface is imersed in a supersaturated solution of air in the liquid. As air diffuses out of the liquid, it causes nucleation to occur at various sites over the surface. The cumulative density of active nucleation sites depends in general, upon the surface characteristics, liquid properties and the concentration of gas in the liquid.

EQUILIBRIUM RADIUS OF CURVATURE

The thermodynamic equilibrium of a spherical air nucleus in a liquid x requires the following relations to be satisfsied:

$$(\mu_x)_{liq} = (\mu_x)_{gas} \qquad (D.1)$$

$$(\mu_{air})_{liq} = (\mu_{air})_{gas} \qquad (D.2)$$

$$T_{liq} = T_{gas} \qquad (D.3)$$

$$(P_{air} + P_{x_{vap}} - P_{\ell}) = \frac{2\sigma}{\rho_{eq}} \qquad (D.4)$$

where ρ_{eq} is the equilibrium radius of the interface and P_{air} and $P_{x_{vap}}$ represent the partial pressures of air and liquid vapor in the gas phase. Eqn. (D.1) leads to the result [33] that vapor states correspond approximately to the saturation states at the system temperature. For dilute solutions, condition (D.2) is described by

Henry's Law

$$P_{air} = m\ C_{air}$$

where C_{air} is the concentration of air in the liquid and m is Henry's Law constant, which is a function of temperature only for low partial pressures.

Equation (D.4) which results from the static equilibrium of the spherical nucleus can be written as -

$$\rho_{eq} = \frac{2\sigma}{P_{air} + P_{x_{vap}} - P_{\ell}} \qquad (D.5)$$

For a given system temperature and pressure and a fixed air concentration in liquid equation (D.5) gives unique equilibrium radius of curvature. If for a particular cavity, ρ_{eff} is larger than ρ_{eq} , the bubble will grow due to larger internal pressure and vice versa.

EXPERIMENTAL APPARATUS AND PROCEDURE

Two kinds of gas diffusion systems were used - open system and closed system, as described below:

1. OPEN GAS DIFFUSION SYSTEM:

Fig. 53 shows the sketch of the open gas diffusion system. The apparatus consists of a 15 gallon glass lined high pressure tank, 4" x 8 x 12" plexiglass vessel, an electric stirrer, an oxygen probe to measure air partial pressure in the solution and a potentiometric recorder.

The high pressure tank is filled with about 8 gallons of liquid (deionized water or ethanol) and air is bubbled through the water at 65 psig for about 12 hours. Due to the high pressure, air dissolves in liquid and its concentration increases approximately to a value corresponding to the saturated concentration at the tank pressure. This air-liquid solution is then throttled onto the test surface placed in the plexiglass vessel open to the atmospehric pressure. The solution is supersaturated with respect to the new condition (atmospheric pressure) and the gas diffuses out of the liquid causing growth of active nucleation sites on the surface. In order to avoid fast depletion of air in the liquid near to the test surface, a sufficiently high (10") column of liquid is maintained over the test surface. The supersaturated solution flows at a steady rate into the plexiglass vessel near the bottom and is drained out at the upper end. The liquid is stirred continuously in order to maintain a uniform concentration of air in the liquid bulk. Different values of air concentration can be maintained by adjusting the flow rate of supersaturated solution into the vessel. The pressure in the high pressure tank is kept at a constant level by attaching it to a high pressure air-cylinder. The oxygen probe kept near to the surface continuously monitors the air concentration, which is indicated by a potentiometer recorder. Ref. [18] gives the detailed description of the oxygen probe.

The data were taken while decreasing the air concentration from a higher initial value. At higher concentration P_{air} is larger and ρ is smaller, subsequently large number of active sites appear on the surface. The bubbles appear from all those cavities which have effective radii greater than or equal to the equilibrium radius. As the flow rate is decreased, the level of concentration is lowered and the cumulative site density becomes smaller. At each concentration the number of active sites is noted. Since the diffusion rate of air in water is very slow, the bubbles grow slowly. When the concentration reaches a steady value, the surface is wiped off with a teflon wiper at constant time intervals of about 2 minutes and each time the population of newly growing bubbles is counted. An average of these readings corresponds to the active site density at the particular air concentration. In this way $^N/A$ vs. ρ_{eff} characteristics of the surface can be obtained.

When the above experiment was repeated with ethanol, no active sites were seen on the same surface, presumably due to the large depletion rates of air concentration, when the supersaturated solution is expanded.

2. CLOSED GAS DIFFUSION SYSTEM:

One possible way of obtaining high gas concentrations is to increase the system pressure, since solubility of gas in a liquid increases with pressure. This was attempted in the closed system. Fig. 54 shows the sketch of the closed gas diffusion system, which consists of a 4" diameter cylindrical copper vessel of 1/8" wall thickness and 8" height. The vessel was provided with a 100 psi pressure gage, and two valves, one at the top and the other at the bottom. The vessel could be sealed with the help of a brass cap and rubber gasket using six quarter inch diameter steel bolts. The test specimen is fastened to inside wall of the cap, with the help of 3 small screws and the test surface could be observed through a 1/2" thick optical glass window. The vessel could be inverted on a two way tripod welded to the cap.

The vessel was first thoroughly cleaned and then rinsed with the liquid to be used for observations. The test surface was then prepared and fastened to the inside of the cap, which was subsequently bolted to the vessel using a rubber seal gasket. Top and bottom valves were opened and liquid was entered into the vessel through the bottom valve up to a height of about 4", so that the test surface was fully immersed in the liquid. Both valves were then closed and the vessel inverted. Since the specimen was about 3" long, the liquid level on inversion was about 1" below the test surface (note the total height of vessel was 8"). This was done in order to avoid the initial wetting of the surface by the liquid. Air was then bubbled through the top valve at a pressure of 100 psig for about 12 hrs. and at small flow rates so as to avoid violent motions of the liquid inside the vessel.

Both valves were then closed and the vessel inverted so that the surface was immersed in gas liquid solution. Top valve was then opened to reduce the pressure inside the vessel. The pressure gage and the top valve were then removed off the vessel and an oxygen probe and stirrer were inserted into the liquid through the two holes in the top. Rest of the procedure is similar to as described in the open gas diffusion system.

It was observed that with water the closed system behaves similar to the open system as described earlier, i.e. similar N/A vs. ρ_{eff} behavior is observed for a given surface with closed and open system. However, with ethanol, when the top valve was opened to reduce the system pressure, violent bubbling occurred over the test surface for a very short period time (fraction of a second) and no active site was observed on the surface afterwards. This behavior may be attributed to the fast transients of the gas concentration in liquid as the pressure is released.

APPENDIX E. Relative Behavior Of Different Fluids Boiling On The Same Surface

If the cumulative site distribution (N/A vs. ρ_{eff}) of a given boiling surface with two different fluids is known, then the relative superheats required by the two fluids at a fixed value of $(q/A)_b$ can be estimated as follows:

From equation (17), for the same $(q/A)_b$ for two fluids 1 and 2,

$$\frac{(\frac{N}{A}\ \Delta T)_1}{(\frac{N}{A}\ \Delta T)_2} = \frac{\left[(k\rho c)_\ell\ D_b\right]_2^{1/2}}{\left[(k\rho c)_\ell f\ D_b\right]_1^{1/2}} \left[\frac{D_{b_2}}{D_{b_1}}\right]^{3/2} \qquad (E.1)$$

A cumulative site distribution of the form $N/A = C\ \Delta T^m$, where C and m are constants, satisfies the observed behavior in Fig. 43. So we shall assume the following relations for the two fluids:

$$(N/A)_1 = C_1\ \ \Delta T_1^{m_1}$$

$$(N/A)_2 = C_2\ \ \Delta T_2^{m_2} \qquad (E.2)$$

where, $m_1 = m_2 = m$ since the slope of log N/A vs. log ρ are approximately equal.

From equations (E.1) and (E.2),

$$\frac{C_1\ \Delta T_1^{m+1}}{C_2\ \Delta T_2^{m+1}} = \frac{\left[(k\rho c)_\ell\ f\ D_b\right]_2^{1/2}}{\left[(k\rho c)_\ell\ f\ D_b\right]_1^{1/2}} \left[\frac{D_{b_2}}{D_{b_1}}\right]^{3/2} \qquad (E.3)$$

As given by equations (19) and (21), f and D_b are functions of fluid properties and do not vary much for ordinary surfaces over a wide range of heat flux. Therefore, equation (E.3) can be written as

$$\frac{\Delta T_1^{\,m+1}}{\Delta T_2} = A' \frac{C_2}{C_1} \tag{E.4}$$

where A' is a constant given by,

$$A' = \frac{\left[(k\rho c)_\ell \; f \; D_b\right]_2^{1/2}}{\left[(k\rho c)_\ell \; f \; D_b\right]_1^{1/2}} \left[\frac{D_{b_2}}{D_{b_1}}\right]^{3/2} \tag{E.5}$$

$\dfrac{C_2}{C_1}$ can be found from N/A vs. ρ_{eff} curves as follows:

for $(N/A)_1 = (N/A)_2$, equation (E.2) gives

$$\frac{C_2}{C_1} = \left[\frac{\Delta T_1}{\Delta T_2}\right]^m_{N/A\,=\,\text{constant}} \tag{E.6}$$

using equation (4),

$$\frac{C_2}{C_1} = \left(\frac{\rho_{eff_2}}{\rho_{eff_1}}\right)^m_{N/A\,=\,\text{constant}} \frac{\left[\dfrac{2\sigma \; T_{sat} \; v_{fg}}{H_{fg}}\right]_1^m}{\left[\dfrac{2\sigma \; T_{sat} \; v_{fg}}{H_{fg}}\right]_2^m} \tag{E.7}$$

Substituting equation (E.7) in equation (E.4) and rearranging:

$$\frac{\Delta T_1}{\Delta T_2} = A^{\frac{1}{m+1}} \left(\frac{\rho_{eff_2}}{\rho_{eff_1}}\right)^{\frac{m}{m+1}}_{N/A\,=\,const.} \left[\frac{\left(\frac{2\sigma\, T_{sat}\, v_{fg}}{H_{fg}}\right)_1}{\left(\frac{2\sigma\, T_{sat}\, v_{fg}}{H_{fg}}\right)_2}\right]^{m/m+1} \qquad (E.8)$$

Since m has values between 10-25, $\frac{m}{m+1} \approx 1$; and equation (E.8) can be written as:

$$\frac{\Delta T_1}{\Delta T_2} = A^{\frac{1}{m+1}} \left(\frac{\rho_{eff_2}}{\rho_{eff_1}}\right)_{\frac{N}{A}\,=\,constant} \left[\frac{\left(\frac{2\sigma\, T_{sat}\, v_{fg}}{H_{fg}}\right)_1}{\left(\frac{2\sigma\, T_{sat}\, v_{fg}}{H_{fg}}\right)_2}\right] \qquad (E.9)$$

where the $\left(\frac{\rho_{eff_2}}{\rho_{eff_1}}\right)_{N/A\,=\,const.}$ is to be taken from the N/A vs. ρ_{eff} characteristics, which are known for the two fluids.

Boiling data were taken with methanol and water on four different copper surfaces of varying degree of roughness prepared by ordinary preparation techniques like polishing and grinding etc., as described in Section III.2 and plotted in Fig. 43 (N/A vs. ρ_{eff}) and Fig. 44 ($(q/A)_b$ vs. ΔT).

A careful observation of Fig. 43 will reveal that, although the cumulative site density distribution changes with surface roughness, the ratio $(\rho_{eff})_{water}/ (\rho_{eff})_{methanol}$ for any known N/A remains almost constant or in other words log ($^N/A$) vs. log (ρ_{eff}) curves for the two fluids are approximately parallel for each of the different surface roughness used. Also the slopes $\frac{d \log (N/A)}{d \log (\rho_{eff})}$ of these curves, which are seen to be straight lines, are quite large and vary from about 10 to 25 as the surface roughness is increased from 0.65 (μ inch) rms to 58 (μ inch) rms. A similar trend can be seen for the $(q/A)_b$ vs. ΔT curves in Fig. 44, where the ratio $(\Delta T)_{methanol}/ (\Delta T)_{water}$ for a fixed $(q/A)_b$ remains almost constant for the two fluids, for surfaces of different roughnesses.

The above indicates that the relative behavior (ρ_{eff} vs. N/A) of the two fluids does not depend much upon the surface preparation technique or the value of surface roughness. In other words for any given surface (within the range of experiments), if N/A vs. ρ_{eff} characteristics for one fluid are known, then knowing the relative behavior of the two fluids for any arbitrary surface the cumulative site density distribution for the other fluid can be estimated. Once the N/A vs. ρ_{eff} behavior of the two fluids are known $(q/A)_b$ vs. ΔT curves can be predicted using equation (17). In particular, for a given $(q/A)_b$, the relative superheats required by two different fluids 1 and 2, can be estimated by equation (E.9):

$$\frac{\Delta T_1}{\Delta T_2} = A^{\frac{1}{m+1}} \left(\frac{\rho_{eff}}{\rho_{eff_1}}\right)_{\frac{N}{A} = \text{cont.}} \frac{\left[\frac{2\sigma\, T_{sat}\, v_{fg}}{H_{fg}}\right]_1}{\left[\frac{2\sigma\, T_{sat}\, v_{fg}}{H_{fg}}\right]_2} \qquad \text{(E.9)}$$

where,

$$A = \frac{\left[(k\rho c)_{\ell}\ f\ D_b\right]_2^{1/2}}{\left[(k\rho c)_{\ell}\ f\ D_b\right]_1^{1/2}} \left(\frac{D_{b_2}}{D_{b_1}}\right)^{3/2}$$

and m is the slope of log N/A vs. log ρ_{eff} curves for the two fluids, i.e.

$$m = \frac{\left[d\ \log\ (N/A)\right]}{\left[d\ \log\ (\rho_{eff})\right]}$$

Thus, if N/A vs. ρ distribution is known for the fluids with any arbitrary surface, $\frac{\rho_{eff_2}}{\rho_{eff_1}}$ can be known and equation (E.9) can be used to estimate $\frac{\Delta T_1}{\Delta T_2}$ for any given surface. Note that the above has been observed to be true for water and methanol, boiling on copper surfaces of different roughnesses. If the surface material is changed, then depending upon the relative change in wetting characteristics of the two fluids $\left(\frac{\rho_{eff_2}}{\rho_{eff_1}}\right)_{N/A = \text{cont.}}$ may change, subsequently changing the ratio

$\frac{\Delta T_1}{\Delta T_2}$. Also, since m is much larger than 1, a small change in m does not affect the value of $(A)^{\frac{1}{m+1}}$ appreciably and $A^{\frac{1}{m+1}} \simeq 1$.

We will now generalize the above results for other organics like freon-113, carbon-tetrachloride, acetone, benzene, carbon-disulphide, hexane, etc. Figs. 55a, b, c and d reproduced from Ref. [18] show N/A vs. ρ_{eff} data for water and organics boiled on different copper surfaces. It can be seen from Figs. 55a, b and c that benzene and freon-113 have almost similar cumulative site distribution as methanol. A similar behavior can also be noted for other organics, namely carbon disulphide, carbon tetrachloride, hexane and acetone in Fig. 55d, based on data taken from Ref. [4]. Thus equation (E.9) can be used to predict the relative superheats for these organics.

COMPARISON WITH DATA

For water and methanol equation (E.9) takes the form:

$$\frac{\Delta T_{water}}{\Delta T_{methanol}} = 0.258^{\frac{1}{m+1}} \quad 0.308 \quad \frac{(\rho_{eff})_{methanol}}{(\rho_{eff})_{water}}$$

From Fig. 43, $\frac{(\rho_{eff})_{methanol}}{(\rho_{eff})_{water}} \simeq 0.18$

so, $\frac{\Delta T_{water}}{\Delta T_{methanol}} = 0.56$, which agrees well with the boiling data in Fig. 44.

Fig. 55d shows N/A vs. ρ_{eff} data from Ref. [4]. For this data $\frac{(\rho_{eff})_{water}}{(\rho_{eff})_{CCl_4}} \simeq 5.5$, and using equation (E.9), $\frac{\Delta T_{CCl_4}}{\Delta T_{water}} \simeq 2.2$ can be calculated.

From Fig. 56 a and b reproduced from Ref. [4], a good agreement can be seen with the predicted relative superheats for the two fluids at the same $(q/A)_b$. Note that the curves in Fig. 56a and b represent total q/A given by equation (18). Since the prediction of equation (E.9) is valid for a constant $(q/A)_b$, $\frac{\Delta T_{CCl_4}}{\Delta T_{water}} = 2.2$ will strictly hold true only for large values of q/A, when the effect of $(q/A)_{nc}$ is small and $q/A \simeq (q/A)_b$.

APPENDIX F. Effect Of Cavity Size And Superheat On The Frequency Of Bubble Departure

During stable boiling of a liquid from a cavity on the surface, a continuous (periodic) stream of bubbles is emitted from the cavity. Time elapsed between two subsequent bubble departures is defined as the bubble time period, τ . When a bubble departs or collapses on a cavity, cold liquid from the bulk rushes to the cavity mouth and penetrates into the cavity, as explained earlier in Section II.2-1 and Fig. 6. If the cavity is in stable boiling, evaporation will eventually start at the meniscus which will recede towards the cavity mouth and finally come out of the cavity as depicted in Fig. 50a. The time elapsed between the departure of the previous bubble and the appearance of the new vapor nucleus on the surface (Fig. 50a) is defined as the waiting time, t_w in the present analysis (note that the time for penetration to occur has been assumed zero). Beyond this point, the bubble grows until it finally detaches from the heated surface; the time of bubble growth is defined as the bubble contact time, t_c . Thus, it is clear that the total bubble time period τ is equal to the sum $(t_w + t_c)$.

In order to determine the frequency of bubble departure, or the bubble time period τ, both t_w and t_c need to be determined. In the present discussion, an approximate theoretical model has been developed to predict t_w and t_c is estimated using the expression for bubble growth rates in Ref. [30].

Fig. 50a shows a cavity of diameter $2R_0$ and depth L, which is in stable boiling and is shown with a vapor nucleus sitting on its mouth. The region of influence, (Ref. [10]) of the bubble has been shown extending up to $2R_0$ from the centreline of the bubble . For analytical convenience, a length of liquid column equal to $8R_0$ extending from the surface into the saturated bulk of liquid (at T_{sat}) has been considered to be influenced by the transient heat transfer effects after the departure of the previous bubble. The pressure of vapor inside the cavity is assumed to remain constant at $P_{\frac{2\sigma}{R_0}} = P_{bulk} + \frac{2\sigma}{R_0}$ and the temperature of the liquid vapor interface at $T_{2\sigma/R_0}$, the saturation temperature at $P_{\frac{2\sigma}{R_0}}$. For mathematical simplicity the semispherical surface of the liquid-vapor meniscus has been stretched into a circular plane surface a b in Fig. 50b such that the surface area of the meniscus remains the same; thus the new radius of the meniscus takes a value $\sqrt{2}R_0$ as shown in Fig. 50b. The region of influence of the bubble is stretched out correspondingly extending to a radius $(1 + \sqrt{2})R_0$, where the liquid is assumed to be isolated from the heat transfer effects of the surrounding liquid (i.e. $\frac{\partial T}{\partial r} = 0$). The boundary conditions in terms of temperature T of the liquid body have been shown in Fig. 50b, T_{wall} being the temperature of the cavity walls. Just after the bubble departure, fresh liquid at T_{sat} rushes to the surface; this time is taken as $t = 0$ and $T = T_{sat}$ throughout the body of the liquid.

The formulation of the problem to predict waiting time t_w, has been presented in the discussion below.

Let T(r, z, t) describe the temperature field at any r, z and time t; then letting $\theta = T - T_{sat}$ and applying two dimensional transient energy eqn. in cylindrical co-ordinates leads to eqn.:

$$\frac{\partial\theta}{\partial t} = \alpha \left[\frac{1}{r} \frac{\partial}{\partial r} \left(r \frac{\partial\theta}{\partial r}\right) + \frac{\partial^2\theta}{\partial z^2}\right] \qquad \text{(F. 1)}$$

Initial Condition:

At $t = 0$, $\theta = 0$ at all r and z.

Boundary Conditions:

At $t > 0$,

1. $\frac{\partial\theta}{\partial r} = 0$ at $r = R_o \ (1 + \sqrt{2}\ )$
2. $\frac{\partial\theta}{\partial r} = 0$ at $r = 0$
3. θ = finite at $r = 0$
4. $\theta = 0$ at $z = 0$

At $z = 8R_o$,

5. $\theta = \theta_{2\sigma/R_o} = T_{2\sigma/R_o} - T_{sat}$ for $0 \leq r \leq \sqrt{2}\ R_o$

$\theta = \theta_w = T_w - T_{sat}$ for $\sqrt{2}R_o \leq r \leq (1 + \sqrt{2}\ ) R_o$

SOLUTION:

Let $\theta = \theta_s\ (r, z) + \theta_t\ (r, z, t)$ (F. 2)

be the solution of the problem defined above. Substituting into eqn. (F.1) and the initial and boundary conditions, the original problem could be broken into the following steady and unsteady parts:

a. Steady state solution θ_s (r,z) satisfies the following:

$$\frac{1}{r}\ \frac{\partial}{\partial r}\ \left(r\ \frac{\partial\theta_s}{\partial r}\right) + \frac{\partial^2\theta_s}{\partial r^2} = 0 \qquad \text{(F.3)}$$

Boundary Conditions:

1a. $\frac{\partial\theta_s}{\partial r} = 0$ at $r = R_o\ (1 + \sqrt{2}\ )$

2a. $\frac{\partial\theta_s}{\partial r} = 0$ at $r = 0$

3a. θ_s = finite at $r = 0$

4a. $\theta_s = 0$ at $z = 0$

At $z = 8R_o$,

$$\text{5a.}\quad \begin{bmatrix} \theta_s = \theta_{2\sigma/R_o} & \text{for}\quad 0 \leq r \leq \sqrt{2}\ R_o \\ \theta_s = \theta_\omega & \text{for}\ \sqrt{2}\ R_o \leq r \leq (1 + \sqrt{2})R_o \end{bmatrix}$$

b. Transient solution θ_t (r, z, t) satisfies the following

$$\frac{\partial\theta_t}{\partial t} = \alpha \left[\frac{1}{\gamma}\ \frac{\partial}{\partial r}\ \left(r\ \frac{\partial\theta_t}{\partial r}\right) + \frac{\partial^2\theta_t}{\partial z^2}\right] \qquad \text{(F.4)}$$

Initial Condition:

At $t = 0$, $\theta_t = -\theta_s$ at all r and z

Boundary Conditions:

At $t > 0$,

1b. $\frac{\partial \theta_t}{\partial r} = 0$ at $r = R_o \ (1 + \sqrt{2})$

2b. $\frac{\partial \theta_t}{\partial r} = 0$ ar $r = 0$

3b. θ_t = finite at $r = 0$

4b. $\theta_t = 0$ at $z = 0$

At $z = 8R_o$

5b. $\theta_t = 0$ for $0 \leq r \leq R_o \ (1 + \sqrt{2})$

SOLUTION TO THE STEADY STATE PROBLEM θ_s:

It can be shown (Ref. [31]) that θ_s has the following general form

$$\theta_s = bz + \left[C_1 J_o (\alpha_n r) + C_2 Y_o (\alpha_n r)\right]\left[C_3 \sinh (\alpha_n z) + C_4 \operatorname{Cosh} (\alpha_n z)\right] \qquad (F.5)$$

Applying boundary conditions 3a, eg. θ_s = finite at $r = 0$ gives $C_2 = 0$. Boundary condition 4a, $\theta_s = 0$ at $z = 0$ gives $C_4 = 0$. Hence the solution reduces to,

$$\theta_s = bz + C_1 \cdot C_3 \, J_o \, (\alpha_n r) \sinh (\alpha_n z)$$

or,

$$\theta_s = bz + C_5 \, J_o \, (\alpha_n r) \sinh (\alpha_n z) \text{ , where } C_5 = C_1 \, C_3$$

Boundary condition 1a gives

$$\left(\frac{\partial \theta_s}{\partial r}\right)_{r = R_o (1 + \sqrt{2})} = J_1 \left[\alpha_n R_o \; 1 + \sqrt{2} \;)\right] = 0 \qquad \text{(F. 6)}$$

The above equation determines the characteristic functions α_n, $n = 1, 2, \ldots\ldots$ Now the series solution to the steady problem could be written as

$$\theta_s \, (r, z) = bz + \sum_{n=1}^{\infty} a_n \, J_o \, (\alpha_n r) \sinh (\alpha_n z) \qquad \text{(F. 7)}$$

where a_n is a new constant used in place of C_5 and is evaluated below: Applying boundary conditions at $z = 8 \, R_o$,

$$\theta_s = \theta_{\frac{2\sigma}{R_o}} = 8b \, R_o + \sum_{n=0}^{\infty} a_n \, J_o \, (\alpha_n r) \sinh (8\alpha_n R_o) \text{ , for } 0 \leq r \leq \sqrt{2} \, R_o \qquad \text{(F. 8a)}$$

$$\theta_s = \theta_w = 8bR_o + \sum_{n=0}^{\infty} a_n \, J_o \, (\alpha_n r) \sinh (8\alpha_n R_o) \text{ , for } \sqrt{2} \, R_o \leq r \leq (1+\sqrt{2}\,)_{R_o} \qquad \text{(F. 8b)}$$

Now, from the properties of Fourier Bessel Series (p. 232, Ref. [31]), a_n could be determined as below:

$$a_n = \frac{\int_0^{\sqrt2 R_0} (\theta_{\frac{2\sigma}{R_0}} - 8bR_0)\, r\, J_0\,(\alpha_n r)dr + \int_{\sqrt2 R_0}^{(1+\sqrt2)R_0} (\theta_w - 8bR_0) r\, J_0\,(\alpha_n r)dr}{\sinh(8\alpha_n R_0) \int_0^{(1+\sqrt2)R_0} r\, J_0^2\,(\alpha_n r)dr}$$

$$= \frac{\left[\frac{1}{\alpha_n}\,(\theta_{\frac{2\sigma}{R_0}} - 8bR_0)\right]\left[(\sqrt2\, R_0)\, J_1\,(\sqrt2\, R_0\, \alpha_n)\right] + \left[\frac{1}{\alpha_n}\,(\theta_w - 8bR_0)\right] \mathrm{x} \left[(1 + \sqrt2)\, R_0\, \cancelto{=0}{J_1\left\{\alpha_n(1 + \sqrt2)R_0\right\}} - \sqrt2\, R_0\, J_1\,(\sqrt2\, R_0\, \alpha_n)\right]}{\sinh\,(8\,\alpha_n\, R_0)\, \frac{(1 + \sqrt2)^2 R_0^2}{2} \left[\left\{J_0\,(\alpha_n(1 + \sqrt2)R_0)\right\}^2 + \left\{\cancelto{=0}{J_1(\alpha_n(1+\sqrt2)R_0)}\right\}^2\right]}$$

$$= \frac{\frac{1}{\alpha_n}\, J_1\,(\alpha_n\, \sqrt2\, R_0)\quad \sqrt2\, R_0\quad \theta_{\frac{2\sigma}{R_0}} - \cancel{8bR_0} - \theta_w + \cancel{8bR_0}}{\frac{(1 + \sqrt2)^2\, R_0^2}{2} \left[J_0^2 \left\{\alpha_n\, (1 + \sqrt2)R_0\right\}\right] \sinh\,(8\alpha_n R_0)} \tag{F. 9}$$

Summing eqns. (F. 8a) and (F. 8b) and integrating between the limits, $r = 0$ and $r = (1 + \sqrt2)R_0$, yields

$$b = \frac{\theta_w + \theta_{2\sigma/R_0}}{16\, R_0}$$

SOLUTION TO THE TRANSIENT PROBELM (θ_t):

Let us assume solution of the form:

$$\theta_t = R(r)\ Z\ (z)\ \tau(t) \qquad \text{(F. 10)}$$

where R, Z and τ are functions of r, z and t respectively. Substituting the above in eqn. (F.4) gives final solution of the form (Ref. [31]) as below:

$$\theta_t = e^{-\alpha(\beta_n^2 + \gamma_m^2)t} \left[C_1\ J_o\ (\beta_n r) + C_2\ Y_0\ (\beta_n r)\right] \left[C_3 \sin(\gamma_m z) + C_4 \text{ Cos } (\gamma_m z)\right] \qquad \text{(F. 11)}$$

Applying boundary condition 3b, θ_t = finite at r = 0, gives $C_2 = 0$. Boundary condition 1b gives:

$$\left[\left(\frac{\partial\theta_t}{\partial r}\right)\right]_{r=(1+\sqrt{2})R_o} = J_1\ (\beta_n\ (1+\sqrt{2})R_o) = 0 \qquad \text{(F. 12)}$$

The above equation gives the characteristic roots β_n. Comparing with equation (F. 6), we see that $\alpha_n = \beta_n$.

Applying boundary condition 4b to equation (F. 11) further gives $C_4 = 0$, and solution now reduces to, in the form of a Fourier Sereis:

$$\theta_t = \sum_{m=0}^{\infty} \sum_{n=0}^{\infty} C_{nm}\ \ell^{-\alpha(\beta_n^2 + \gamma_m^2)t}\ J_o\ (\alpha_n r) \sin(\gamma_m z) \qquad \text{(F. 13)}$$

Applying boundary condition 5b to equation (F.13) gives

$\sin\ (8R_o\ \gamma_m) = 0$, and hence,

$$\gamma_m = \frac{m\,\pi}{8\,R_o} \quad , m = 0, 1, 2, \ldots\ldots$$

since $J_o\,(0) = 1$ and $\gamma_o = 0$, θ_t could also be written as,

$$\theta_t = \sum_{m=1}^{\infty} C_{om}\, e^{-\alpha\,\gamma_m^2\,t} \sin\,(\gamma_m z) + \sum_{n=1}^{\infty}\sum_{m=1}^{\infty} C_{nm}\, e^{-\alpha(\alpha_n^2 + \gamma_m^2)t} \Big[J_o\,(\alpha_n r)\,\sin\,(\gamma_m z) \Big] \qquad (F.\ 14)$$

Applying initial condition, $\theta_t = -\theta_s\,(r,z)$ at $t = 0$ to equation (F.14) gives:

$$-bz - \sum_{n=1}^{\infty} a_n \sinh\,(\alpha_n z)\, J_o\,(\alpha_n r) = \sum_{m=1}^{\infty} C_{om} \sin\,(\gamma_m z)$$

$$+ \sum_{n=1}^{\infty}\sum_{m=1}^{\infty} C_{nm}\, J_o\,(\alpha_n r)\,\sin\,(\gamma_m z) \qquad (F.\ 15)$$

Multiplying both sides of eqn. (F. 15) with r and integrating from $r = 0$ to $r = (1 + \sqrt{2})R_o$ gives,

$$-bz = \sum_{m=1}^{\infty} C_{om} \sin\,(\gamma_m z) \qquad (F.\ 16)$$

Multiplying both sides by $\sin\,(\gamma_m z)$ and integrating between $z = 0$ and $z = 8R_o$ yields:

$$-\int_0^{8R_o} bz \sin\,(\gamma_m z)\,dz = \int_0^{8R_o} C_{om} \sin^2\,(\gamma_m z)\,dz$$

$$C_{om} = \frac{\displaystyle\int_0^{8R_o} -bz \sin\,(\gamma_m z)\,dz}{\displaystyle\int_0^{8R_o} \sin^2\,(\gamma_m z)\,dz}$$

$$= \frac{-\frac{b}{\gamma_m^2}\left[\sin(\gamma_m z) - z\,\gamma_m \cos(\gamma_m z)\right]_0^{8R_o}}{\frac{1}{\gamma_m}\int_0^{8R_o\gamma_m} \sin^2 y\, dy}$$

$$= \frac{\frac{b}{\gamma_m^2}\left[-8R_0\gamma_m \cos(8R_o\gamma_m)\right]}{\frac{1}{\gamma_m}\left[\frac{1}{2}y - \frac{1}{4}\sin(2y)\right]_0^{8\gamma_m R_o}}$$

or,

$$C_{om} = \frac{-\frac{b}{\gamma_m^2}\left[-m\pi \cos(m\pi)\right]}{4R_o} \qquad (F.\ 17)$$

Combining equations (F. 15) and (F. 16) gives,

$$-\sum_{n=1}^{\infty} a_n \sinh(\alpha_n z)\, J_o(\alpha_n r) = \sum_{n=1}^{\infty}\sum_{m=1}^{\infty} c_{nm}\, J_o(\alpha_n r)\sin(\gamma_m z)$$

Mutliplying both sides by sin $(\gamma_m z)$ and integrating between $z=0$ and $z=8R_o$ leads to the following ;

$$C_{nm} = \frac{-a_n \int_0^{8R_o} \sinh(\alpha_n z)\sin(\gamma_m z)\, dz}{\int_0^{8R_o} \sin^2\left(\frac{m\pi z}{8R_o}\right) dz}$$

or,

$$C_{nm} = \frac{a_n r_m \cos(8R_o\gamma_m)\sinh(8R_o\alpha_n)}{4R_o(\alpha_n^2 + \gamma_m^2)} \qquad (F.18)$$

FINAL SOLUTION

The complete solution can be written in the following form:

$$\theta = \theta_s + \theta_t$$

or

$$\begin{aligned}\theta = {} & bz + \sum_{n=1}^{\infty} a_n \sinh(\alpha_n z)\, J_o(\alpha_n r) \\ & + \sum_{m=1}^{\infty} C_{om}\, e^{-\gamma_m^2 t} \sin(\gamma_m z) \\ & + \sum_{n=1}^{\infty} \sum_{m=1}^{\infty} C_{nm}\, e^{-\alpha(\alpha_n^2 + \gamma_m^2)t} J_o(\alpha_n r) \sin(\gamma_m z)\end{aligned} \qquad \text{(F. 19)}$$

where α_n's are the roots of equation, $J_1\left[\alpha_n (1 + \sqrt{2}) R_o\right] = 0$, for $n = 1, 2, 3, \ldots\ldots, \infty$;

$$\gamma_m = \frac{m\pi}{8R_o}, \quad m = 1, 2, \ldots\ldots, \infty$$

$$a_n = \frac{\dfrac{J_1(\sqrt{2}\, R_o \alpha_n)}{\alpha_n} \sqrt{2}\, R_o \left[\theta_{\frac{2\sigma}{R_o}} - \theta_w\right]}{\dfrac{(1 + \sqrt{2})^2}{2} R_o^2 \left[J_o^2 \left\{\alpha_n (1 + \sqrt{2}) R_o\right\}\right] \sinh(8\alpha_n R_o)}$$

$$\text{Com} = \frac{-b/\gamma_m^2 \left[-m\pi \cos(m\pi)\right]}{4 R_o}$$

$$C_{nm} = \frac{a_n \gamma_m \cos(8R_o \gamma_m) \sinh(8R_o \alpha_n)}{4R_o (\alpha_n^2 + \gamma_m^2)}$$

and,

$$b = \frac{\theta_w + \theta_{2\sigma/R_o}}{16R_o}$$

The temperature field being known, heat flux can now be calculated through the meniscus surface ($z = 8\ R_o,\ 0 \leq r \leq \sqrt{2}\ R_o$). The heat transferred to the meniscus causes evaporation and the net amount of vapor produced at the meniscus up to a time t could be estimated by calculating the total heat Q transferred to the meniscus and dividing by the latent heat of evaporation, h_{fg}. When sufficient amount of vaporization has occured to fill up the cavity with vapor, the vapor nucleus appears on the surface; time ($t = t_w$) taken for this to happen, depends upon the volume of the liquid that has penetrated into the cavity and which must be replaced by an equal volume of vapor generated at the meniscus. t_w could be determined as follows:

Heat flux to the meniscus (at $z = 8R_o$) from the liquid is given by:

$$(q/A)_{z=8R_o} = -k\left(\frac{\partial\theta}{\partial z}\right)_{z=8R_o} \quad \text{for } 0 \leq r \leq \sqrt{2}\ R_o$$

Total amount of heat transferred to the meniscus upto time t_w could be found by integrating the above:

$$\theta\ (t_w) = \int_0^{t_w} \int_0^{\sqrt{2}R_o} -\kappa \left(\frac{\partial\theta}{\partial z}\right)_{z=8R_o} 2\pi\ r\ dr\ dt \qquad (F.\ 20)$$

Differentiating equation (F. 19) ω. r. to z gives

$$\left(\frac{\partial\theta}{\partial z}\right)_{z=8R_o} = b + \sum_{n=1}^{\infty} a_n \alpha_n \cosh\,(8R_o\, \alpha_n)\, J_o(\alpha_n r)$$

$$+ \sum_{m=1}^{\infty} C_{om}\, \gamma_m \cos\,(m\pi)\, e^{-\alpha\,(\gamma_m^2)t}$$

$$+ \sum_{n=1}^{\infty} \sum_{m=1}^{\infty} C_{nm}\, J_o\,(\alpha_n r)\, \gamma_m \cos\,(m\pi)\, e^{-\alpha(\alpha_n^2 + \gamma_m{}^2)t} \tag{F. 21}$$

Substituting equation (F. 21) in (F. 20) and carrying out the integration, one obtains:

$$Q\,(t_w) = 2\pi\kappa R_o^2\, t_w\, b$$

$$+ 2\,\pi\kappa R_o^2 \sum_{m=1}^{\infty} C_{om}\, \gamma_m \cos\,(m\pi) \left[\frac{e^{-\alpha\,(\gamma_m^2)\,t_w} - 1}{\alpha\,\gamma_m^2}\right]$$

$$+ \int_0^{t_w} \left[- \sum_{n=1}^{\infty} 2\pi\kappa\; a_n \sqrt{2}\, R_o \cosh\,(8R_o\, \alpha_n)\, J_1\,(\alpha_n \sqrt{2}\, R_o)\right] dt$$

$$+ \int_0^{t_w} \left(\frac{-2\pi\kappa}{\alpha_n}\right) \sum_{n=1}^{\infty} \sum_{m=1}^{\infty} C_{nm}\, \gamma_m\, (\sqrt{2}\, R_o) \cos\,(m\pi)\, J_1\,(\alpha_n \sqrt{2} R_o) e^{-\alpha(\alpha_n^2+\gamma_m^2)t} dt$$

or,

$$Q\,(t_w) = -2\pi\kappa\, b\, R_o^2\, t_w$$

$$+ \frac{2\pi\kappa\, R_o^2}{\alpha} \sum_{m=1}^{\infty} C_{om}\, \gamma_m \cos\,(m\pi)\, \frac{e^{-\alpha\,\gamma_m^2\, t_w} - 1}{\gamma_m^2}$$

- (continued on the next page)

$$-2\pi\kappa\sqrt{2}\,R_o\left[\sum_{n=1}^{\infty} a_n \cosh(8R_o\alpha_n)\,J_1(\alpha_n\sqrt{2}\,R_o)\quad t_w\right]$$

$$+\frac{2\pi\kappa\sqrt{2}\,R_o}{\alpha_n}\left[\sum_{n=1}^{\infty}\sum_{m=1}^{\infty} C_{nm}\,\gamma_m\cos(m\pi)\,J_1(\alpha_n\sqrt{2}\,R_o)\,\frac{e^{-\alpha(\alpha_n^2+r_m^2)t_w}-1}{\alpha(\alpha_n^2+\gamma_m^2)}\right]$$

(F. 22)

Mass of vapor generated by heat $Q(t_w)$,

$$m_v = \frac{Q(t_w)}{h_{fg}} \qquad \text{(F. 23)}$$

where h_{fg} and other properties of vapor used ahead are evaluated for saturated vapor at pressure $P_{2\sigma/R_o}$. Volume of this vapor, v_{vap} is equal to $m_v\,v_g$. If the liquid penetrates into the cavity upto a distance M from the mouth (Fig.8) the vapor nucleus will appear on the surface when

$$m_v\,v_g = \left[\pi R_o^2 M + \frac{2}{3}\pi R_o^3\right]$$

, which is roughly the volume of liquid to be displaced by vapor for the vapor nucleus to appear at cavity mouth as shown in Fig. 50a. Hence, the equation

$$m_v\,v_g = \frac{Q(t_w)\,v_g}{h_{fg}} = \left[\pi R_o^3\, M + \frac{2}{3}\pi R_o^3\right] \qquad \text{(F. 24)}$$

gives t_w in terms of cavity geometry and wall superheat as contained in $Q(t_w)$.

ESTIMATION OF THE BUBBLE CONTACT TIME, t_c:

For a growing bubble on a heated surface at superheat $\Delta T_w = T_w - T_{sat}$ in a liquid at temperature T_b and pressure p_∞ (T_{sat} = sat. temp. at p_∞). Mikic, Rohsenow and Griffith [30] obtained the following expression for the later part of bubble growth ($t^+ >> 1$):

$$R^+ = (t^+)^{1/2} \left(1 - \theta \left[\left(1 + \frac{t_w^+}{t^+}\right)^{1/2} - \left(\frac{t_w^+}{t^+}\right)^{1/2} \right] \right) \qquad \text{(F. 25)}$$

where,

$R^+ = \frac{AR}{B^2}$, R = radius of bubble at time t.

$$A = \left(\frac{\pi}{7} \frac{h_{fg} \, \rho_v \, \Delta T_w}{\rho_\ell \, T_{sat}} \right)^{1/2}$$

$$B = \left(\frac{12}{\pi} \alpha_\ell\right)^{1/2} J_a \quad , \quad J_a = \frac{\Delta T \, \rho_\ell \, C_\ell}{h_{fg} \, \rho_v}$$

$$t^+ = \frac{A^2 t}{B^2}$$

$$t_w^+ = \frac{A^2 t_w}{B^2}$$

$$\theta = \frac{T_w - T_{bulk}}{T_w - T_{sat}}$$

when $t_w^+ >> t^+$, equation (F. 25) reduces to

$$R = B \sqrt{t}. \qquad \text{(F. 26)}$$

The condition $t_w^+ >> t^+$ strictly holds when ΔT_w is small as happens during nucleation from deep laser cavities having large depth/diameter ratio. (For example in Table F-I given ahead, at $\Delta T_w = 2.8°F$ for water, $t_w/t_c \simeq 3$). When ΔT_w is large, the previous **inequality** does not hold and time t predicted by equation (F. 26) for a given bubble radius R, is an underestimation of the real bubble growth time [Ref. 30]. However, equation (F. 26) will be used to estimate the bubble contact time and qualitative effect of wall superheat on frequency in the analysis below.

Staniszewski [32] suggests the following empirical equation for bubble departure radius, R_d , when breaking off the heating surface:

$$R_d = 0.4215 \; \theta \left(\frac{2\sigma}{g \; (\rho_\ell - \rho_v)}\right)^{1/2} \quad (1 + 5.4 \; \dot{R}) \qquad \text{(F. 27)}$$

where R_d is in ft., θ in radius and $\dot{R}$ in ft/sec.. Evaluating $\dot{R}$ from equation (F. 26) and substituting in (F. 27) leads to the following expression for the bubble contact time t_c ,

$$B \sqrt{t_c} = 0.4215 \; \theta \left(\frac{2\sigma}{g \; (\rho_\ell - \rho_v)}\right)^{1/2} \quad (1 + 5.4 \; \frac{B}{\sqrt{t_c}}) \qquad \text{(F. 28)}$$

Let $x = 0.4215 \; \theta \left(\frac{2\sigma}{g \; (\rho_\ell \quad \rho_v \;)}\right)^{1/2}$ be a function of the contact angle **and** fluid properties only. Substituting in (F. 28),

$$B \sqrt{t_c} = x + 5.4 \; x \; \frac{B}{\sqrt{t_c}}$$

or, $$t_c - \frac{x}{B}\sqrt{t_c} - 5.4\,x = 0 \qquad \text{(F. 29)}$$

Taking roots of the above equation:

$$\sqrt{t_c} = \frac{1}{2}\left[\frac{x}{B} \pm \sqrt{\left(\frac{x}{B}\right)^2 + 21.6\,x}\right] \qquad \text{(F. 30)}$$

For saturated water boiling at 1 atmos. and $\theta = 45°$, the above equation reduces to:

$$\sqrt{t_c} = \frac{0.45}{\Delta T} \pm \sqrt{\frac{0.21}{\Delta T^2} + 1.96 \times 10^{-2}} \qquad \text{(F. 31)}$$

where, t_c is in seconds and ΔT in F°.

Similarly, for methanol ($\theta = 10°$) one could obtain:

$$\sqrt{t_c} = \frac{0.158}{\Delta T} \pm \sqrt{\frac{.025}{\Delta T^2} + 0.268 \times 10^{-2}} \qquad \text{(F. 32)}$$

Thus, ΔT being given, t_c could be estimated using equations (F. 31) and (F. 32) for water and methanol respectively.

Results of some numerical calculation have been presented in Table F-1. A cavity with $R_o = 0.001''$ and depth $0.01''$ was selected and, t_w and t_c were calculated using equations (F. 24), (F. 31) and (F. 32). The strong effect of wall superheat ΔT_w on frequency is apparent from these results, which is qualitatively consistent with the observed frequency behavior during boiling from laser cavities (F. 49), e.g. the frequency decreases with decreasing wall superheat, and vice versa.

TABLE F-1

EFFECT OF WALL SUPERHEAT ON FREQUENCY

$R_o = 0.001''$

$L = 0.01''$

$(\Delta T)_{2\sigma/R_o}$, water $= 2.3°F$, $(\Delta T)_{\frac{2\sigma}{R_o}}$, methanol $= 0.7°F$

ΔT_w, °F	t_{wait}, sec.	t_c, sec.	$t_w + t_c$, sec.	f, 1/min
WATER				
10	0.007	0.0373	0.0443	1350
5	0.02	0.066	0.086	700
2.8	0.4	0.139	0.539	112
METHANOL				
10	0.006	0.00505	0.01105	5400
5	0.015	0.00855	0.02355	4250
2	0.07	0.0303	0.10	600

APPENDIX G. Analytical Presentation of the Boundary Surfaces Enclosing the Region of Active Sites In $\Delta T_w - R_o$-D Space:

As described in Section II.2-5, the following three criteria determine the required superheat for stable boiling from a cavity:

1. Vapor entrapment criterion.
2. Dynamic effects due to liquid motion inside the cavity.
3. Static criterion which governs the growth of vapor nucleus outside the cavity.

In the ΔT_w-R_o-D space (Figs. 28a and 28b) these criteria are represented by three different surfaces which can be described analytically as follows:

1. Limiting Criterion for Vapor Entrapment:

   (Surface 01230 in Figs. 28a and 28b)

The idealized vapor entrapment process was described earlier in Section II.2-1 (Fig. 6). The volume of trapped vapor for a given contact angle θ, can be calculated as below:

Case I, $D \geq \dfrac{2R_o}{\tan\theta}$ (Fig. 57a):

For this case, volume v^o_{vap} is clearly given by,

$$v^o_{vap} = \pi R_o^2 D - \frac{1}{2}\pi R_o^2\, h_1$$

or, $$v^o_{vap} = \pi R_o^2 D - \frac{1}{2}\pi R_o^2 \left(\frac{2R_o}{\tan\theta}\right)$$

or, $$v^o_{vap} = \pi R_o^2 \left(D - \frac{R_o}{\tan\theta} \right) \qquad \text{(G.1)}$$

Case II, $D < \frac{2R_o}{\tan\theta}$ (Fig. 57b, c):

From Fig. 57c, for a triangular volume element,

$$h = \frac{\sqrt{R_o^2 - y^2} - (R_o - D\tan\theta)}{\tan\theta}$$

where, (x, y) is any point on the circle, $x^2 + y^2 = R_o^2$

Hence, volume of the triangular element,

$$dv = \frac{1}{2} \frac{\left[\sqrt{R_o^2 - y^2} - (R_o - D\tan\theta)\right]^2}{\tan\theta} dy$$

Total volume of trapped vapor:

$$v^o_{vap} = \frac{1}{2\tan\theta} \int_{-y_1}^{+y_1} \left[\sqrt{R_o^2 - y^2} - (R_o - D\tan\theta)\right]^2 dy$$

or, $$v^o_{vap} = \frac{1}{\tan\theta} \int_0^{y_1} \left[\sqrt{R_o^2 - y^2} - (R_o - D\tan\theta)\right]^2 dy \qquad \text{(G.2)}$$

where, $y_1 = \sqrt{R_o^2 - (R_o - D\tan\theta)^2}$

After the entrapment of vapor the liquid-vapor interface takes a spherical shape as shown in Fig. 6, such that the volume of trapped vapor remains the same. The volume of vapor under the spherical interface could be written as:

$$v^o_{vap} = \pi R_o^2 H_2$$

$$+ \frac{\pi}{3} \left(\frac{R_o}{\cos \theta} \right)^3 \quad (2 - 3 \sin \theta + \sin^3 \theta) \qquad \text{(G.3)}$$

For the "limiting criterion for vapor entrapment", $H_2 = 0$, so that the liquid-vapor interface touches the cavity bottom (Fig. 6), hence

$$v^o_{vap} = \frac{\pi}{3} \left(\frac{R_o}{\cos \theta} \right)^3 \left(2 - 3 \sin \theta + \sin^3 \theta\right) \qquad \text{(G.4)}$$

gives the expression for the entrapment surface 01230 in Figs. 28a and 28b, in terms of R_o and D, where v^o_{vap} is given by eqn. (G.2).

2. Dynamic Effects:

The curved surface enclosing the region of dynamic effects in Figs. 28a and b and as described earlier in Section II.2-5 is obtained by solving eqns. (13a) and (13b) subject to the condition that $\frac{dz}{dt} = 0$ when $z = H_1$, which physically corresponds to the condition that evaporation starts and the liquid-vapor interface starts receding back as soon as it reaches the cavity bottom. The above solution gives the implicit relation between ΔT_w, R_o and D which represents the boundary surface of the region of dynamic effects.

3. Static criterion:

There are two kinds of static criterion considered in Figs. 28a and 28b, each of which is represented by a surface in the

ΔT-R_o-D space. Surface 45674 in Fig. 28a represents the criteria given by eqn. (15), e.g.,

$$(\Delta T)_{\frac{2\sigma}{R_o}} = \frac{2\sigma\ T_{sat}\ v_{fg}}{h_{fg}\ R_o}$$

and, surface $45Q_1\ 26Q_24$ in Fig. 28b describes the static criterion of eqn. (5) in Section II-1, which considers the effect of the 'limiting thermal layer' at the surface.

BIOGRAPHICAL NOTE

The author was born January 2, 1950 in Sakauti Tanda, India and passed his High School (1964) and Intermediate (1966) from Uttar Pradesh Board. In 1966, he was admitted to the Mechanical Engineering Department of Birla Institute of Technology and Science, Pilani, where he obtained his B.E.(HONS.) degree in May, 1971.

He joined the Mechanical Engineering Graduate School at M. I. T. as a Research Assistant in September 1971 and received his S.M. in February 1973. From June to September of 1973, he worked as a summer staff at Teledyne Materials Research, Waltham, Massachusetts.

In February, 1973 he entered the Ph.D. program in Mechanical Engineering at M.I.T. working on The Effects of Surface Conditions on Nucleation and Boiling Characteristics under the supervision of Professor B. B. Mikic.

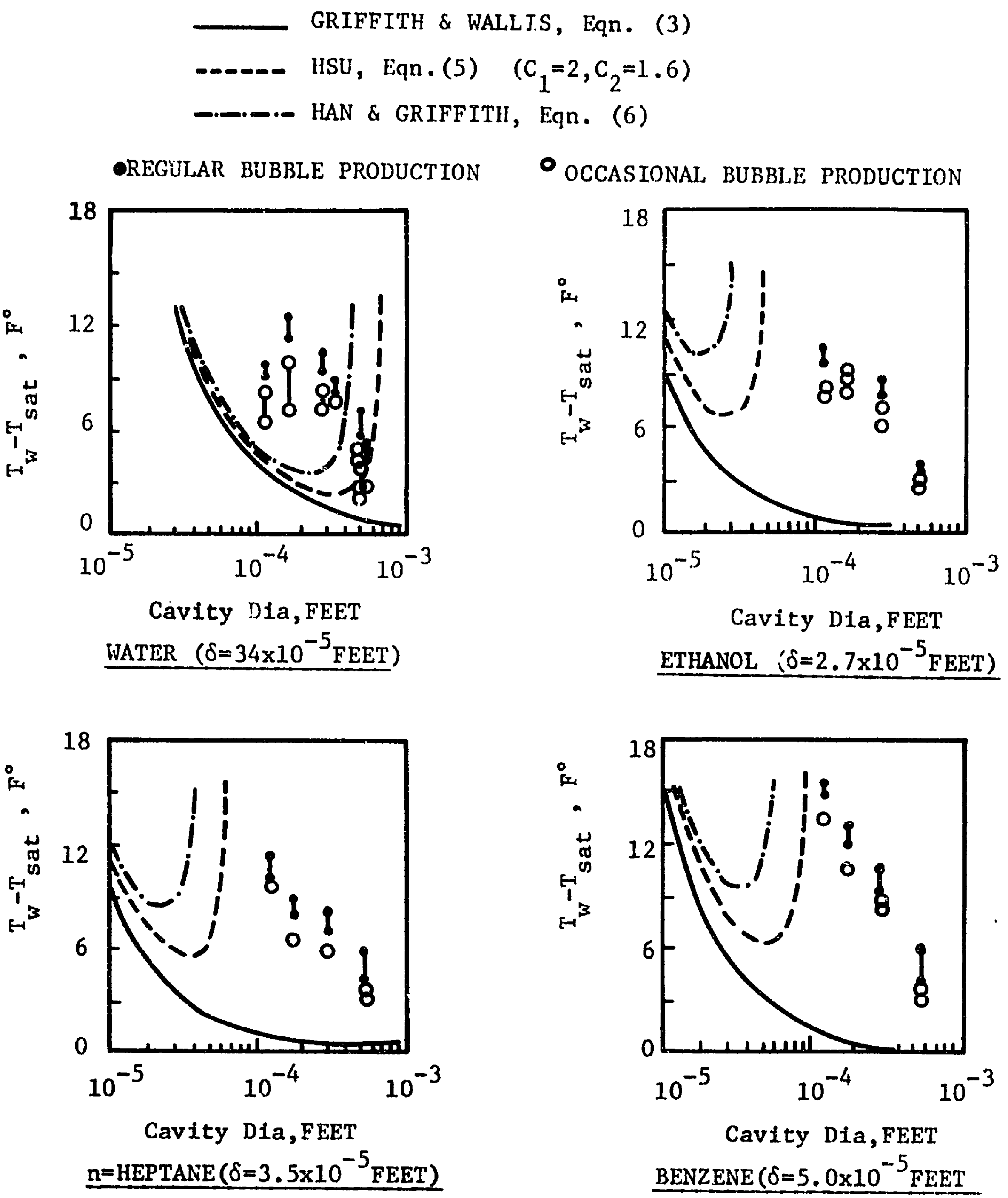

Fig. 1: Comparison between measured and predicted incipience temperature differences at atmospheric pressure, Ref.[12]

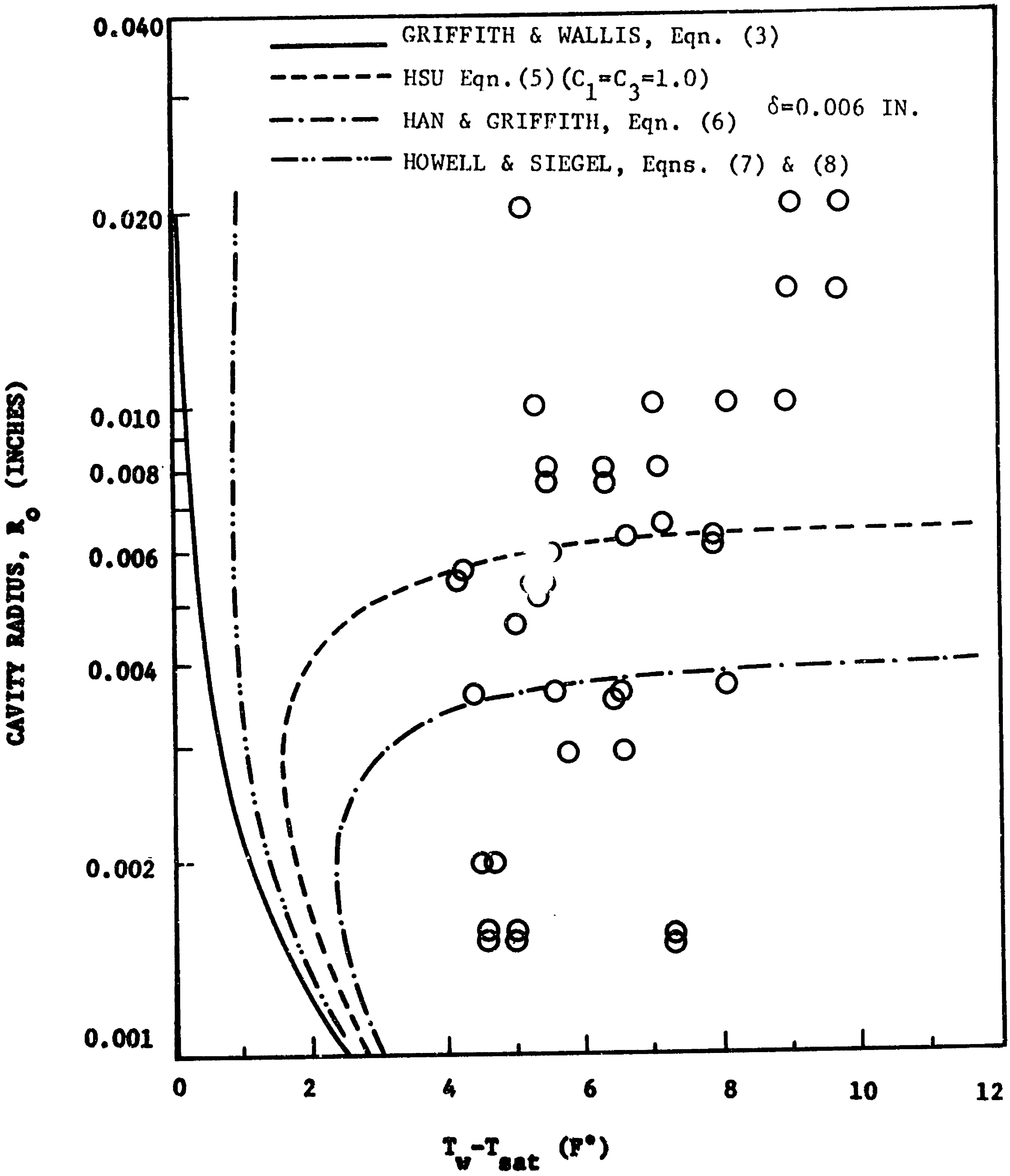

Fig.2: **Incipience temperature required for regular bubble production from machine drilled cylindrical cavities in boiling with water, Ref. [11].**

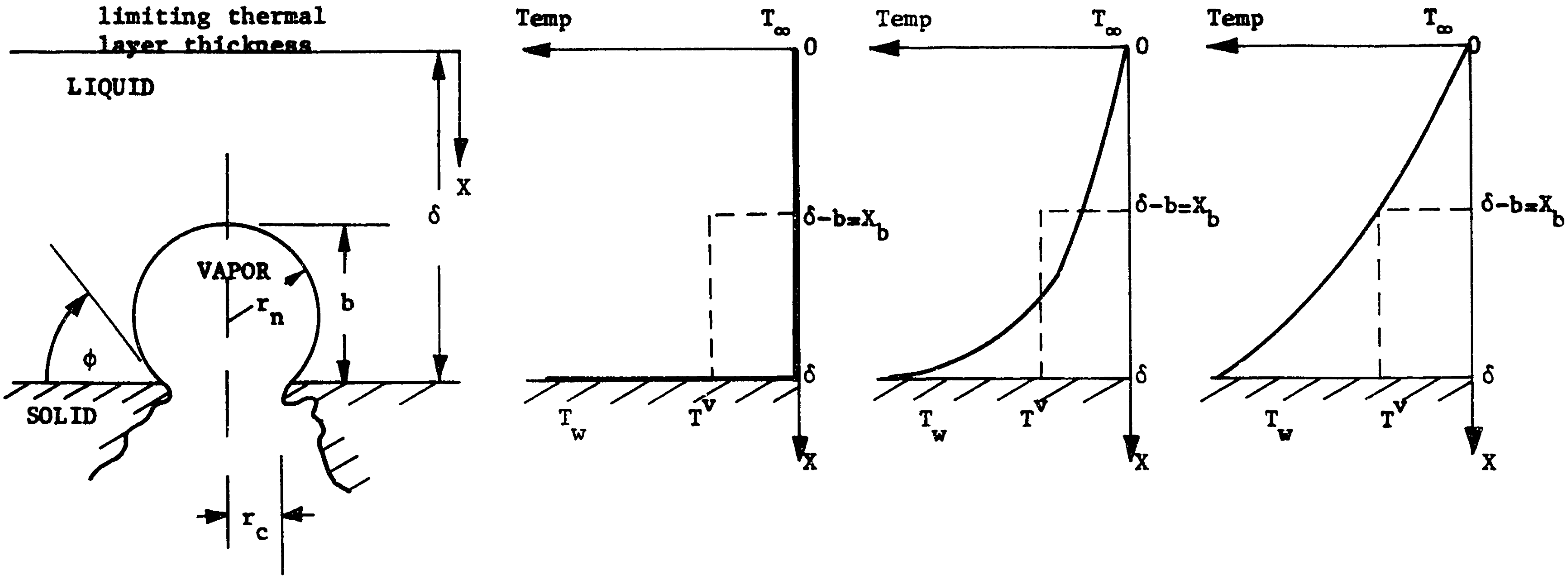

Fig. 3: Model for nucleation hypothesis (Hsu [9]).

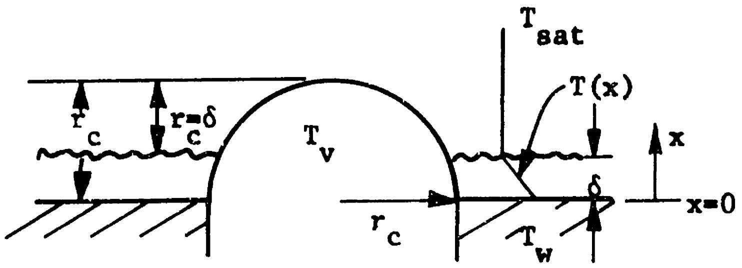

(a) Nucleus extending outside the thermal layer.

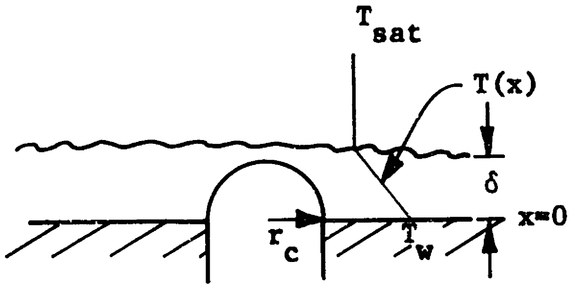

(b) Nucleus contained within the thermal layer.

Fig. 4: Criteria for growth of hemispherical bubble nucleus [11].

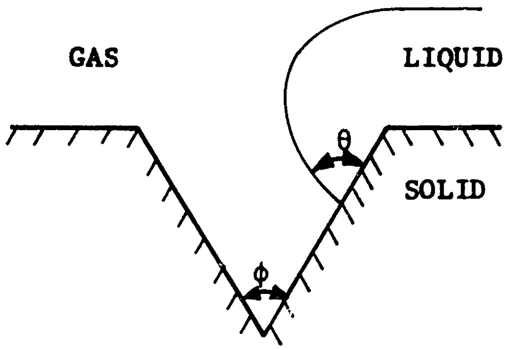

a. Conditions for the entrapment of gas in the advance of a semi-infinite liquid sheet across a grove, Ref. 1.

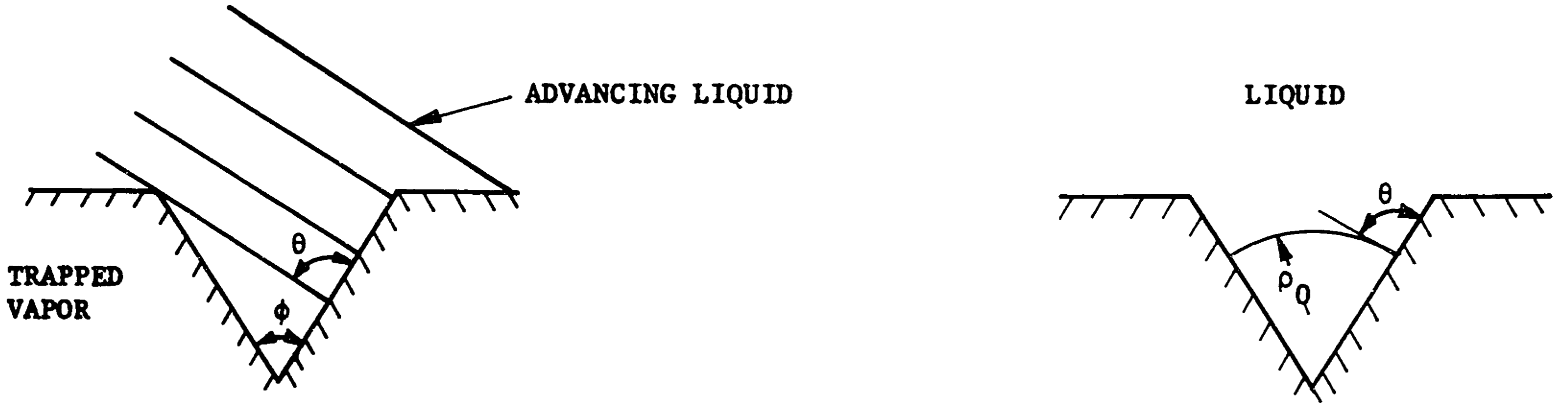

b. Postulated vapor trapping mechanism for a conical cavity.

c. Formation of spherical meniscus from the trapped vapor inside the conical cavity.

Fig. 5: Sketch of the postulated vapor trapping mechanism for a conical cavity.

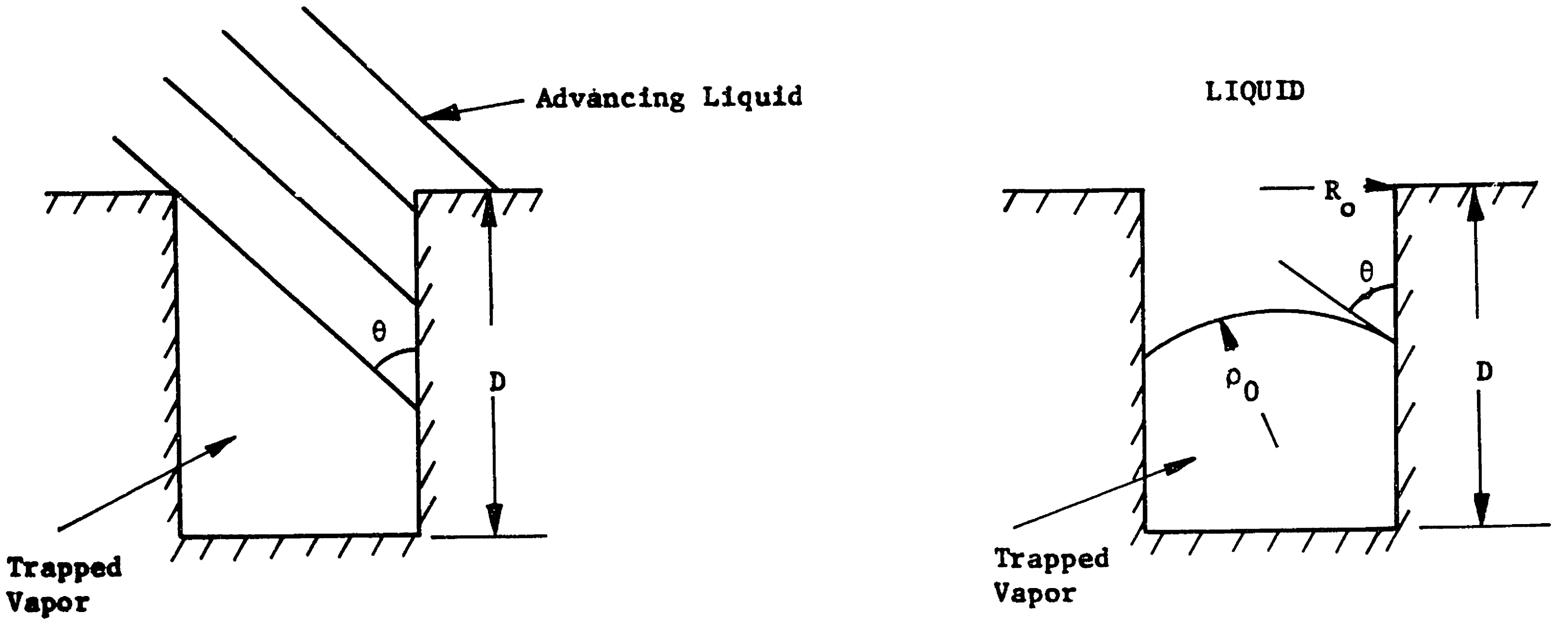

a. Postulated vapor trapping mechanism for a cylindrical cavity.

b. Formation of spherical meniscus from the trapped vapor inside the cylindrical cavity.

Fig. 6: Sketch of the postulated vapor trapping mechanism for a cylindrical cavity.

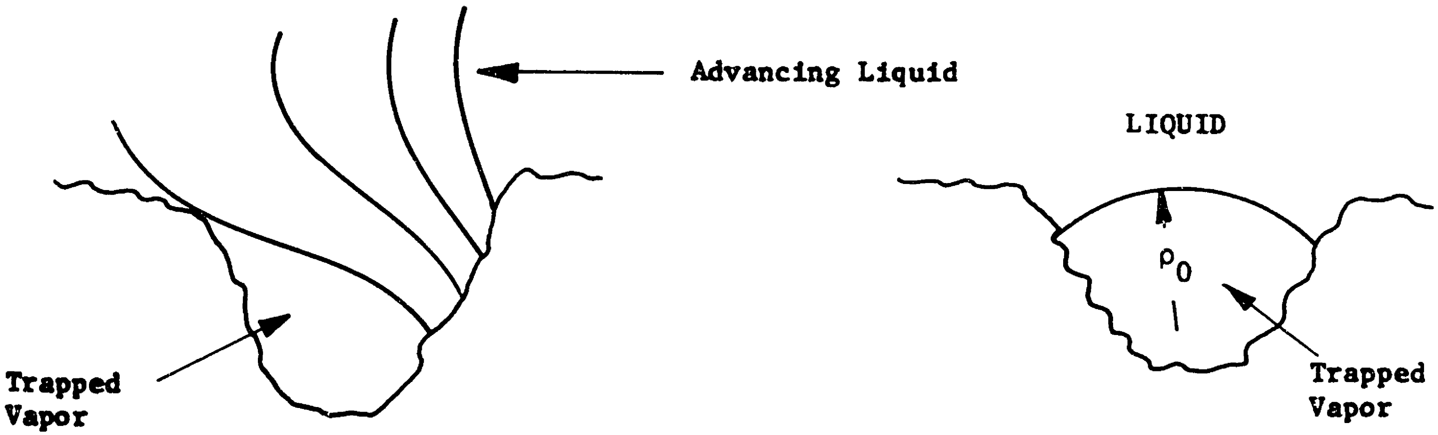

a. Trapping process for a natural cavity.

b. Formation of spherical meniscus from the trapped vapor.

Fig. 7: Sketch of the postulated vapor trapping process for a natural cavity.

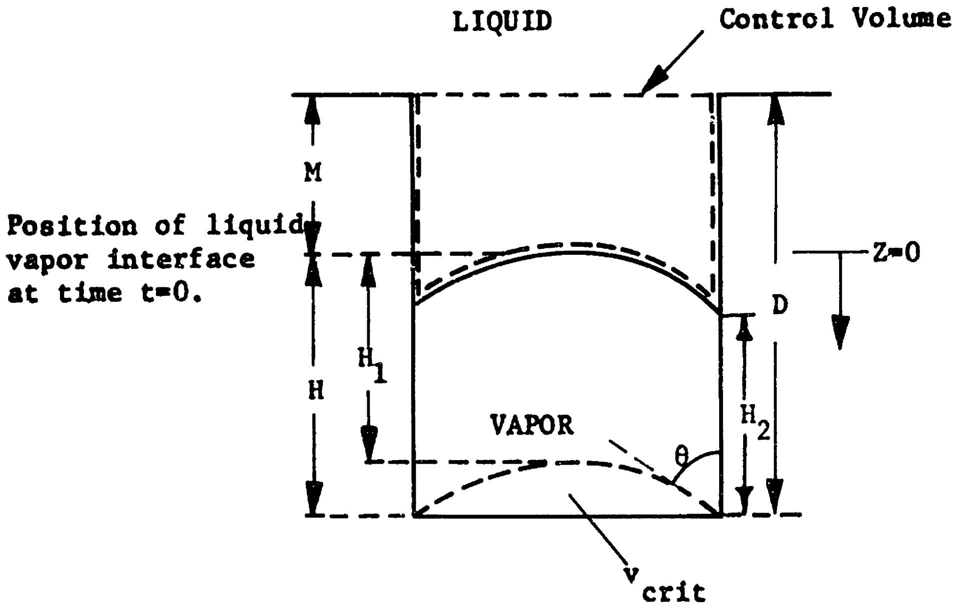

Fig. 8: Sketch showing the solution domain of dynamic effects on nucleation from an isolated cylindrical cavity in boiling.

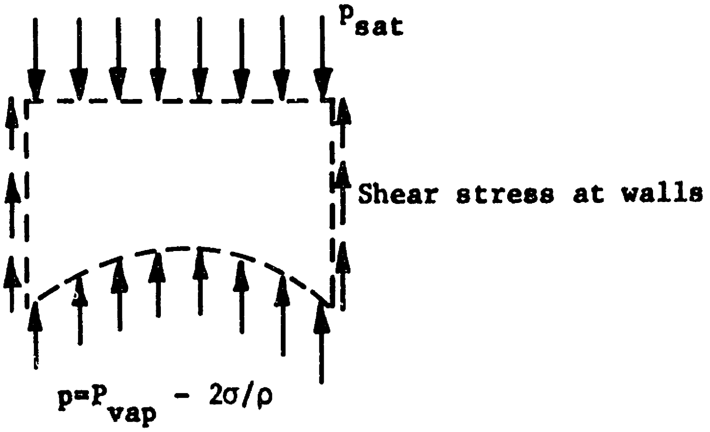

Fig. 9: External forces acting on the control volume, selected in Fig. 8, during motion of the interface in the positive Z-direction.

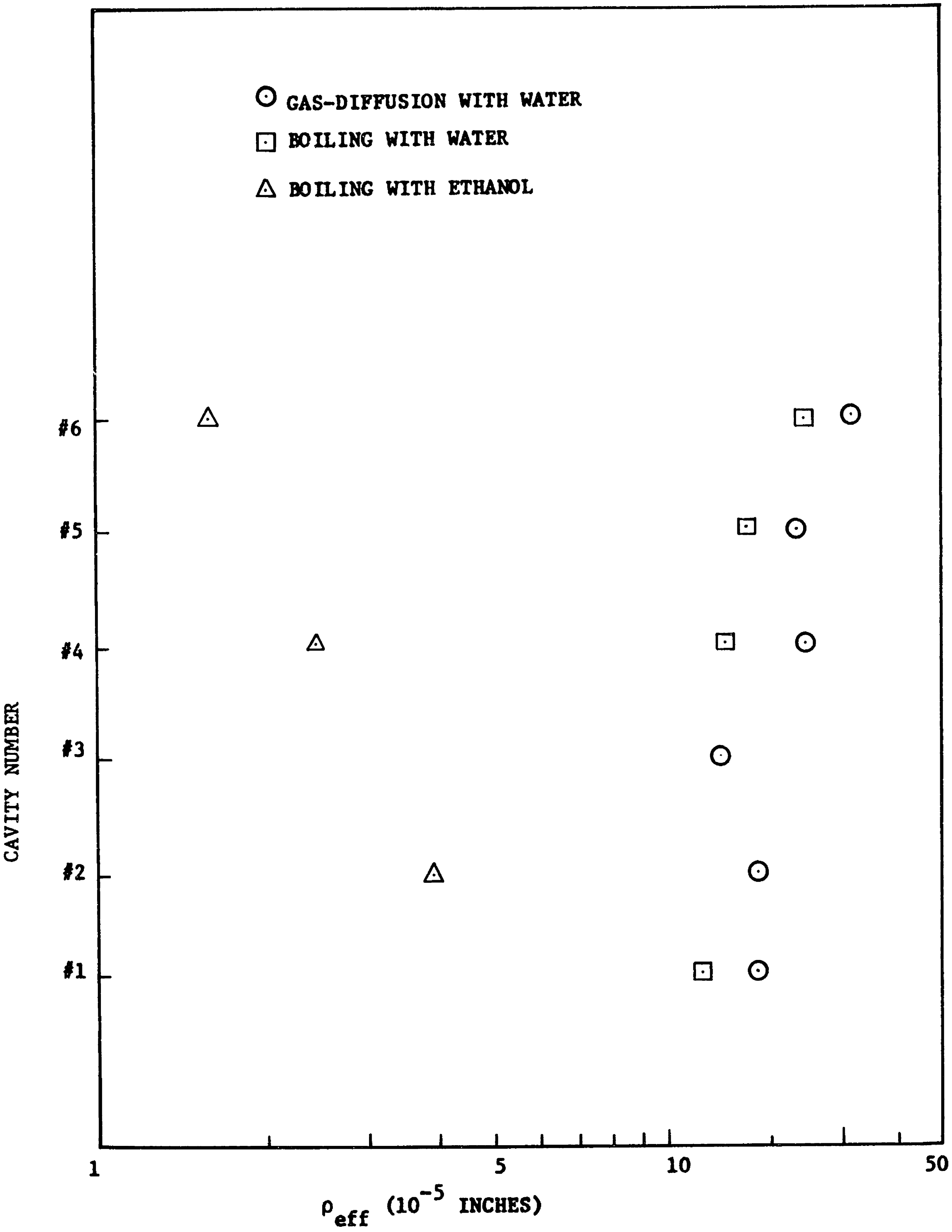

Fig. 10: Results of gas diffusion and boiling experiments for single artificial cavities.

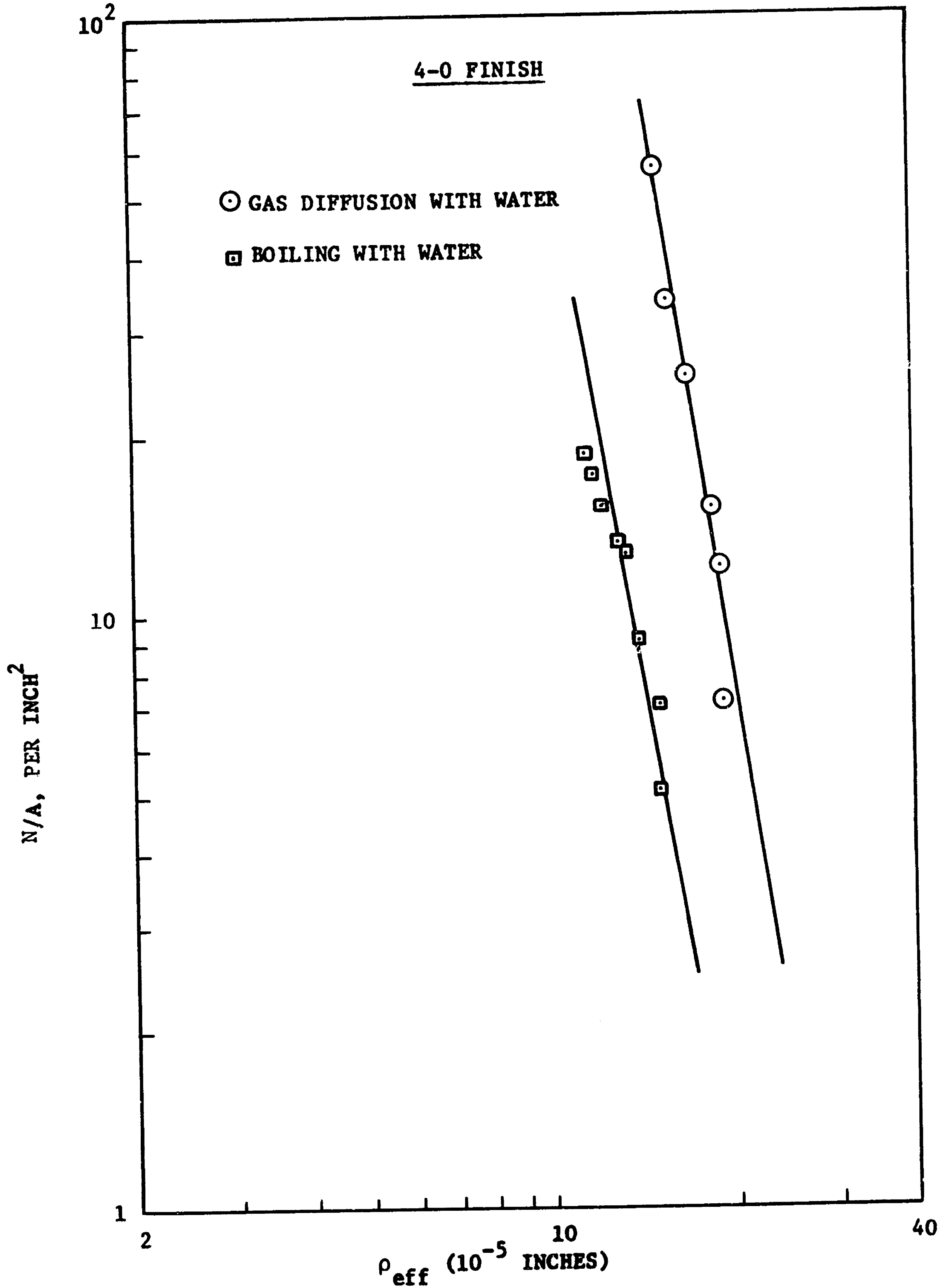

Fig. 11: N/A vs. ρ_{eff} characteristics of a prepared copper surface, observed during gas diffusion and boiling experiments.

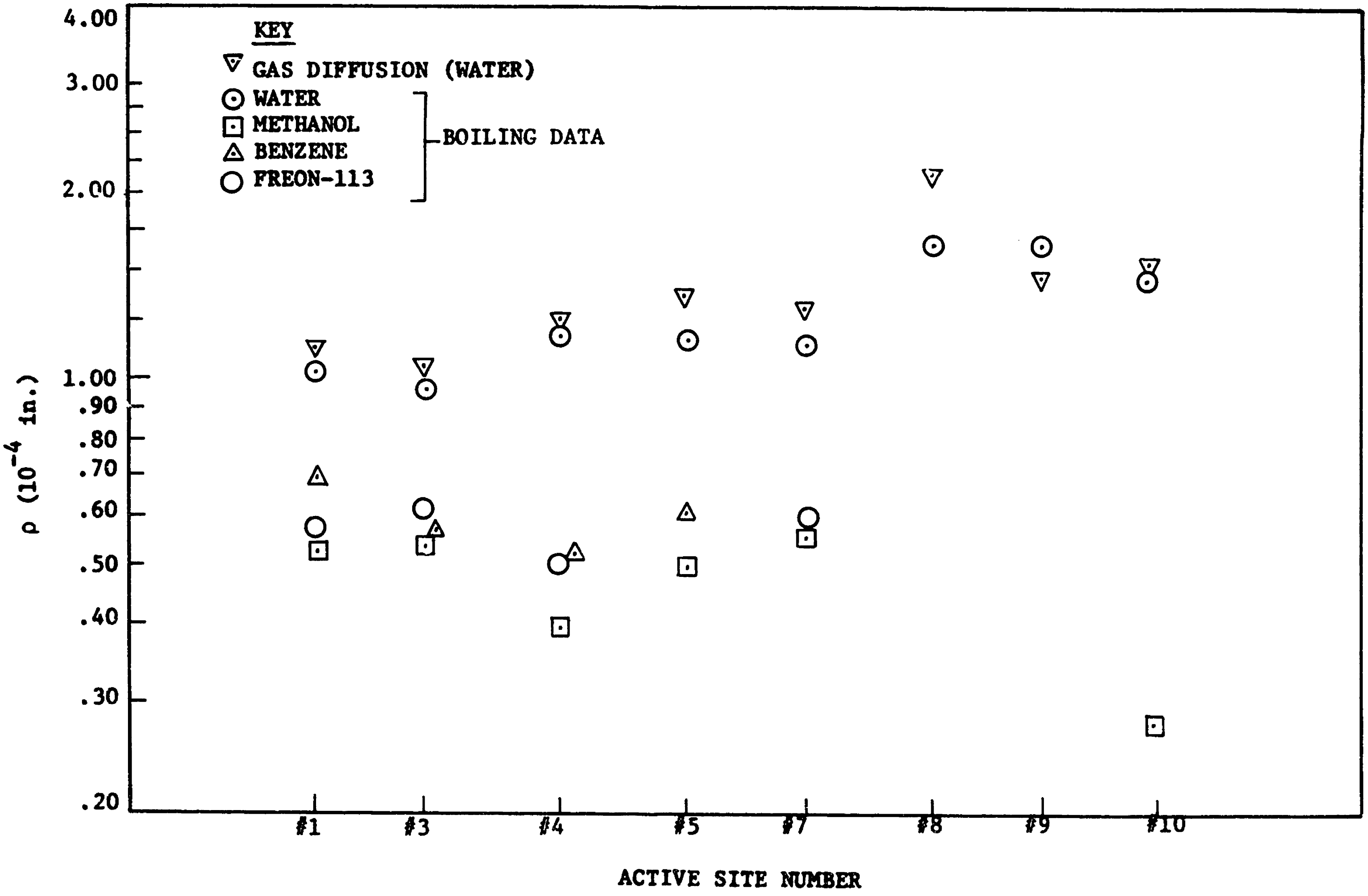

Fig. 12: Results of Gas Diffusion and Boiling Experiments for Indiviudal Cavities.

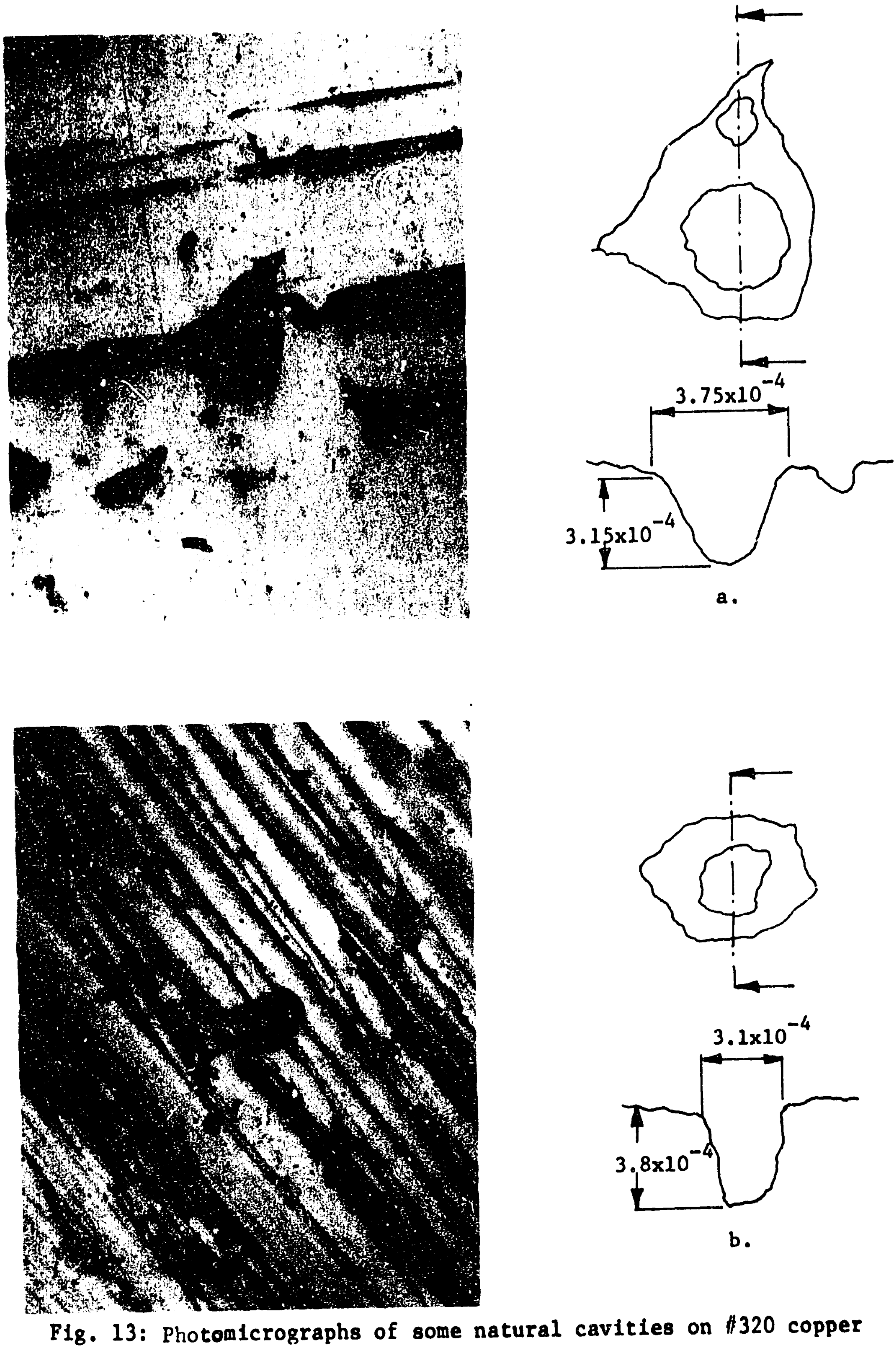

Fig. 13: Photomicrographs of some natural cavities on #320 copper surface at magnification x1000.

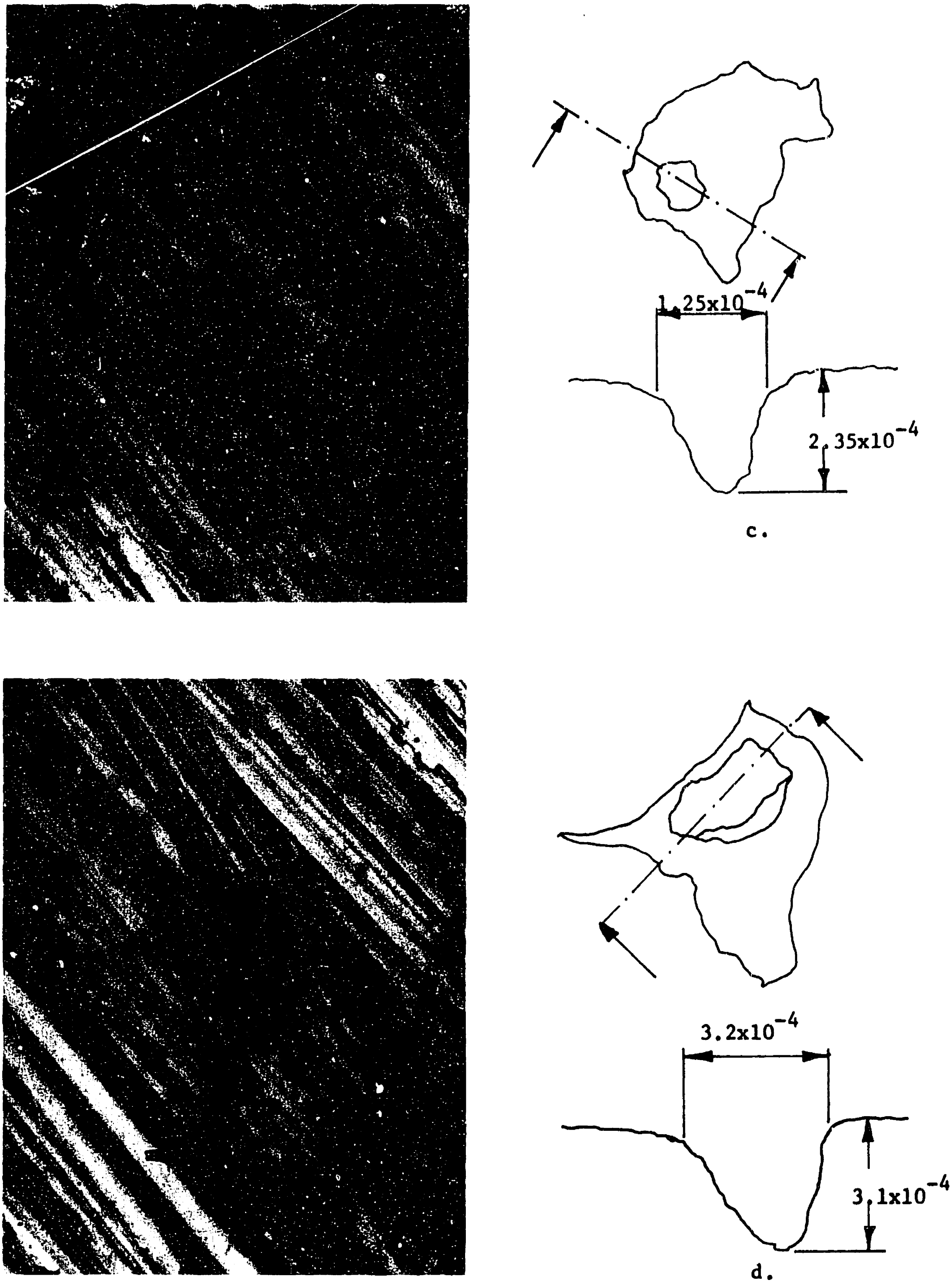

Fig. 13: Photomicrographs of some natural cavities on #320 copper surface at magnification x1000.

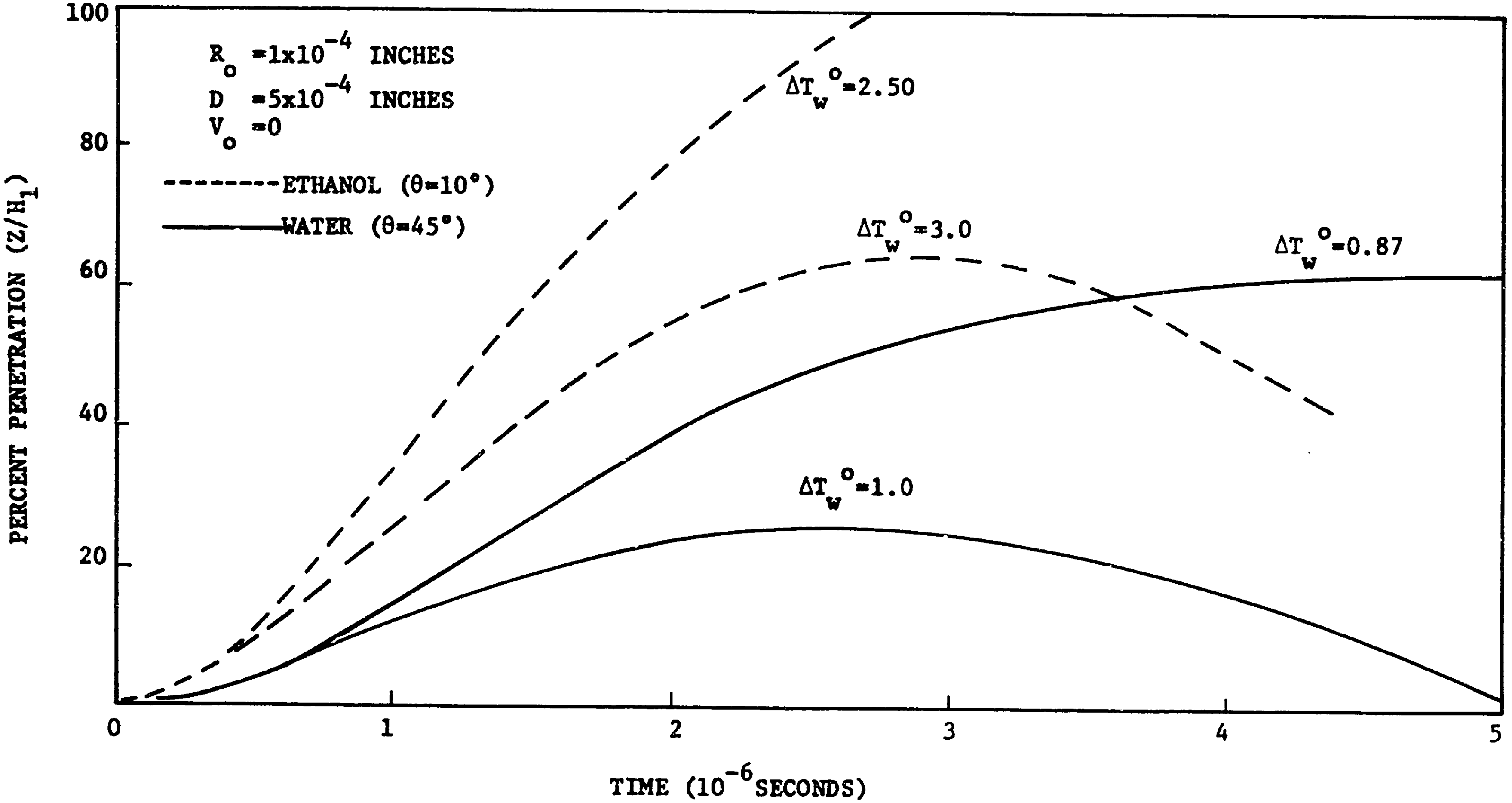

Fig. 14: Effect of fluid on cavity stability. Relative behavior of water and ethanol with a cylindrical cavity in boiling.

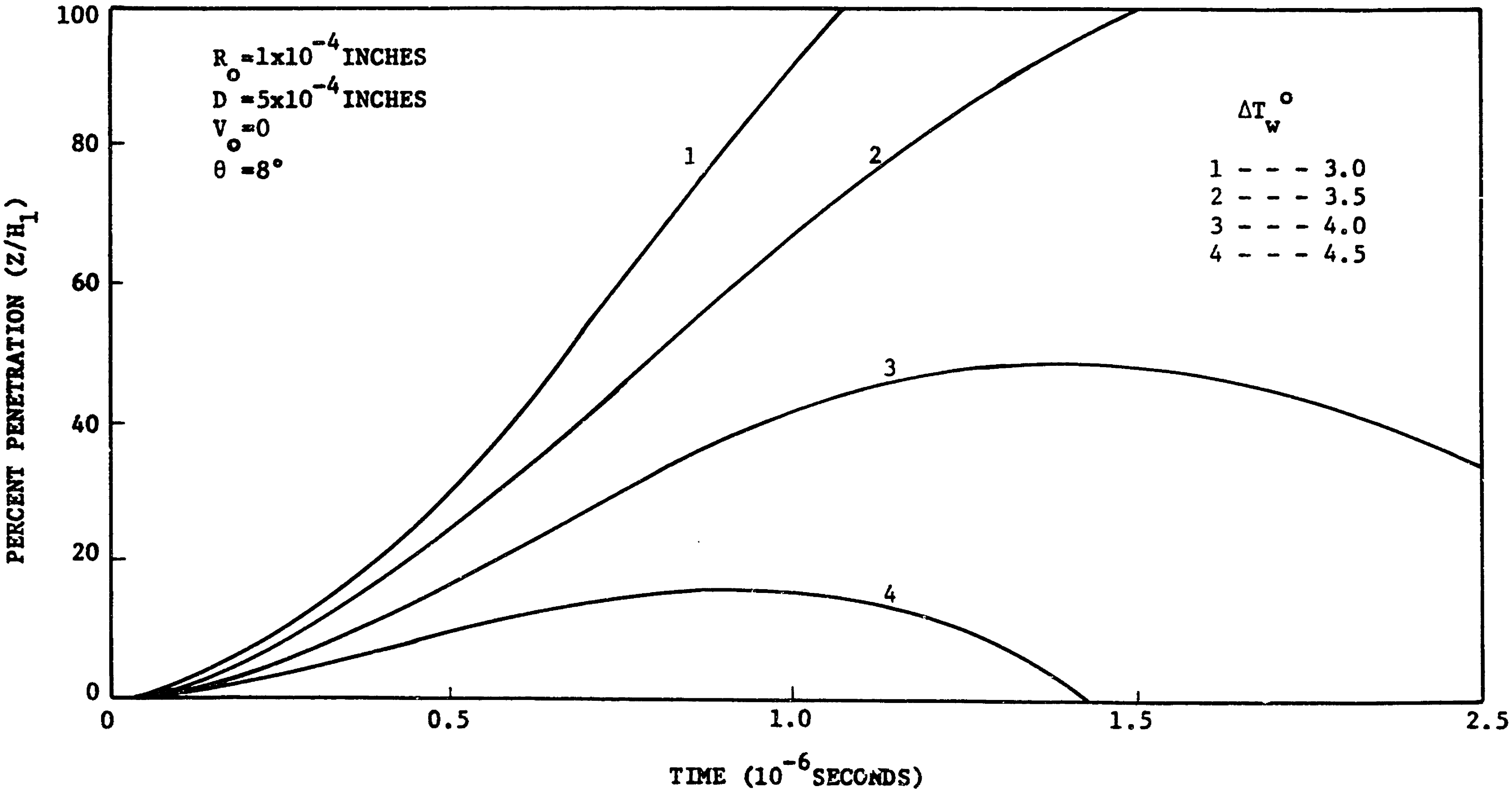

Fig. 15: Effect of superheat on cavity stability for ethanol.

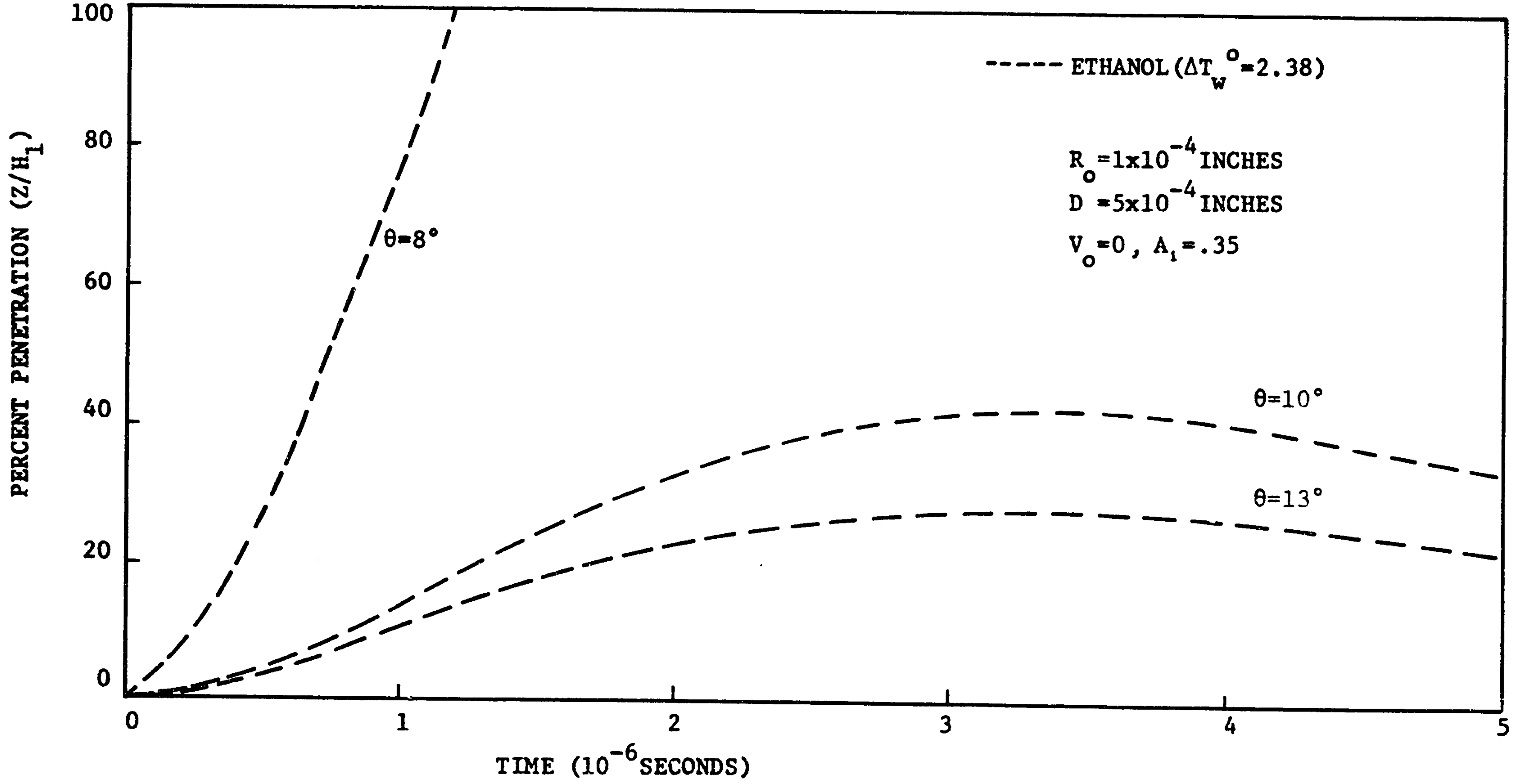

Fig. 16a: Effect of contact angle on the stability of cavity in boiling with ethanol.

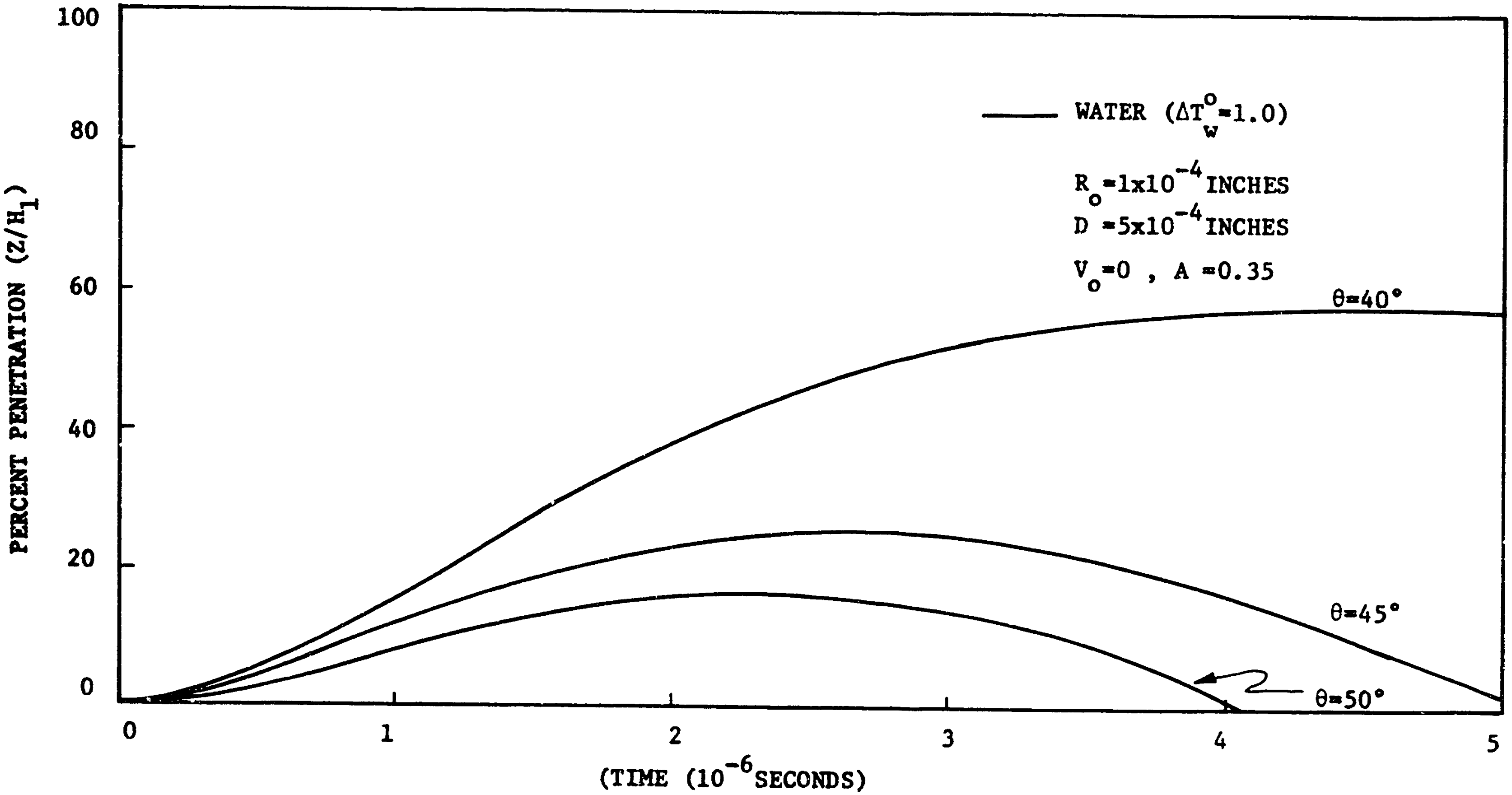

Fig.16b: Effect of contact angle on the stability of cavity in boiling with water.

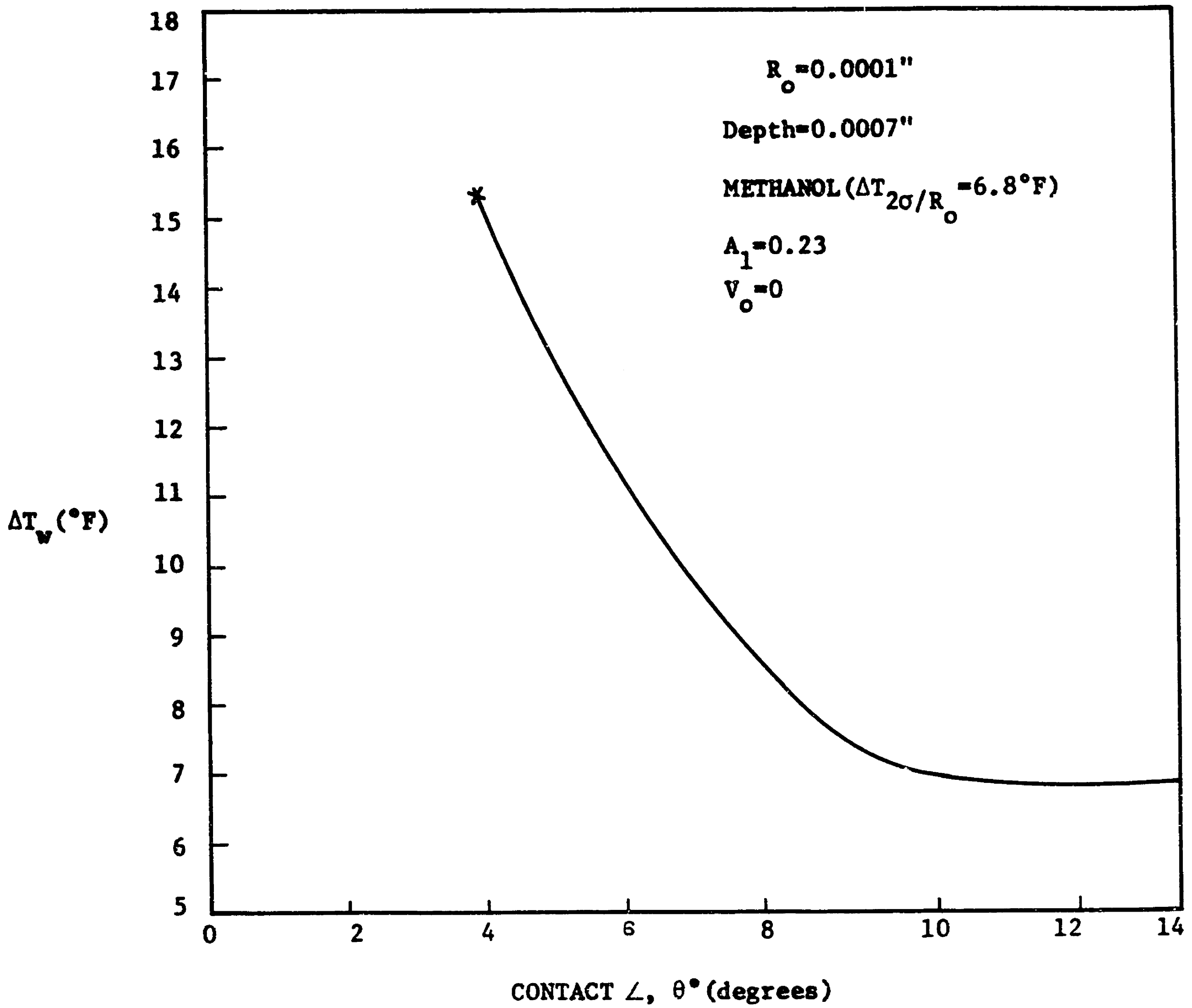

Fig. 17: Effect of Contact Angle on the superheat required for stability.

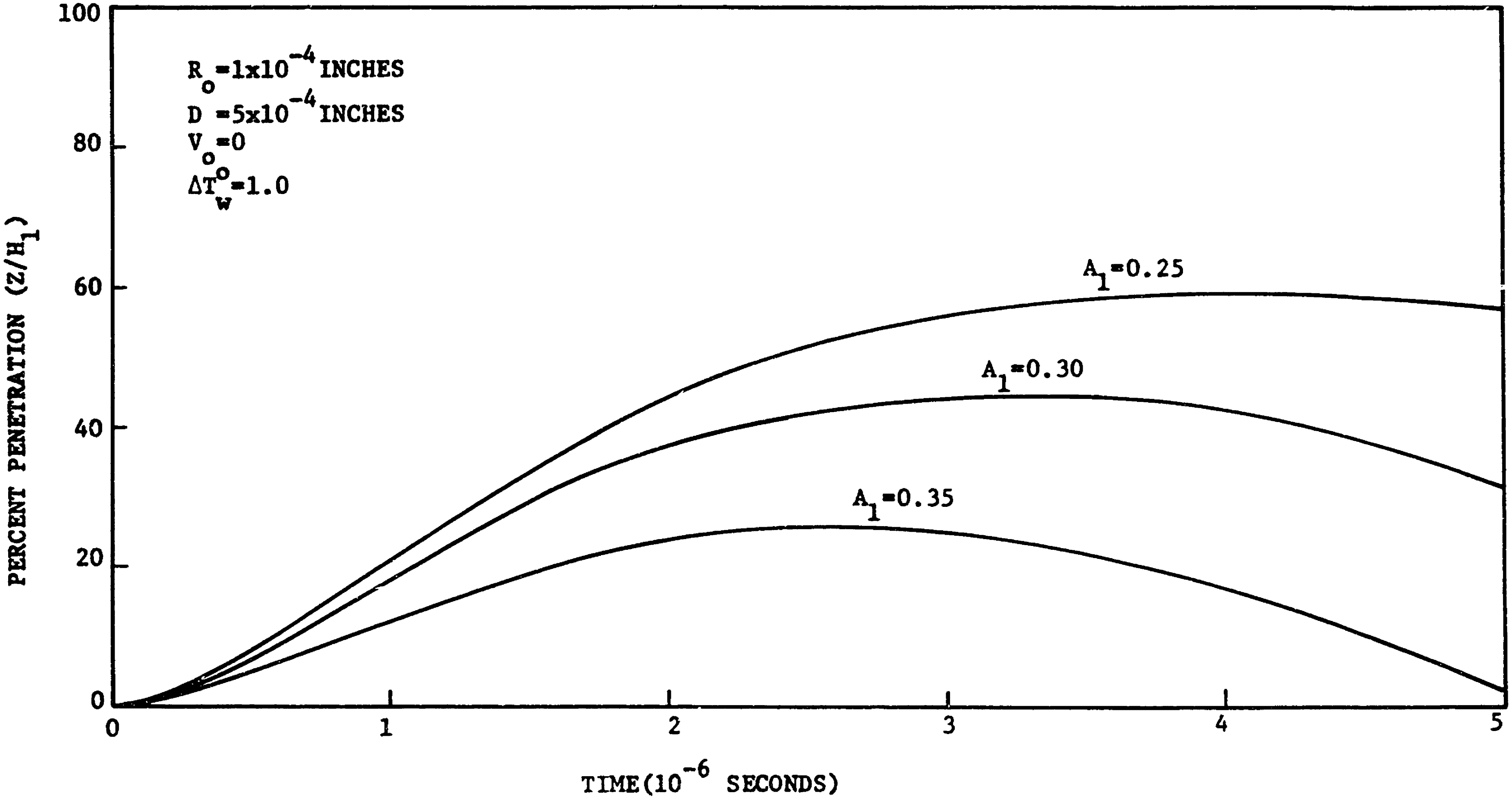

Fig. 18a: Effect of initial temperature of liquid on the stability of a cylindrical cavity in boiling with water.

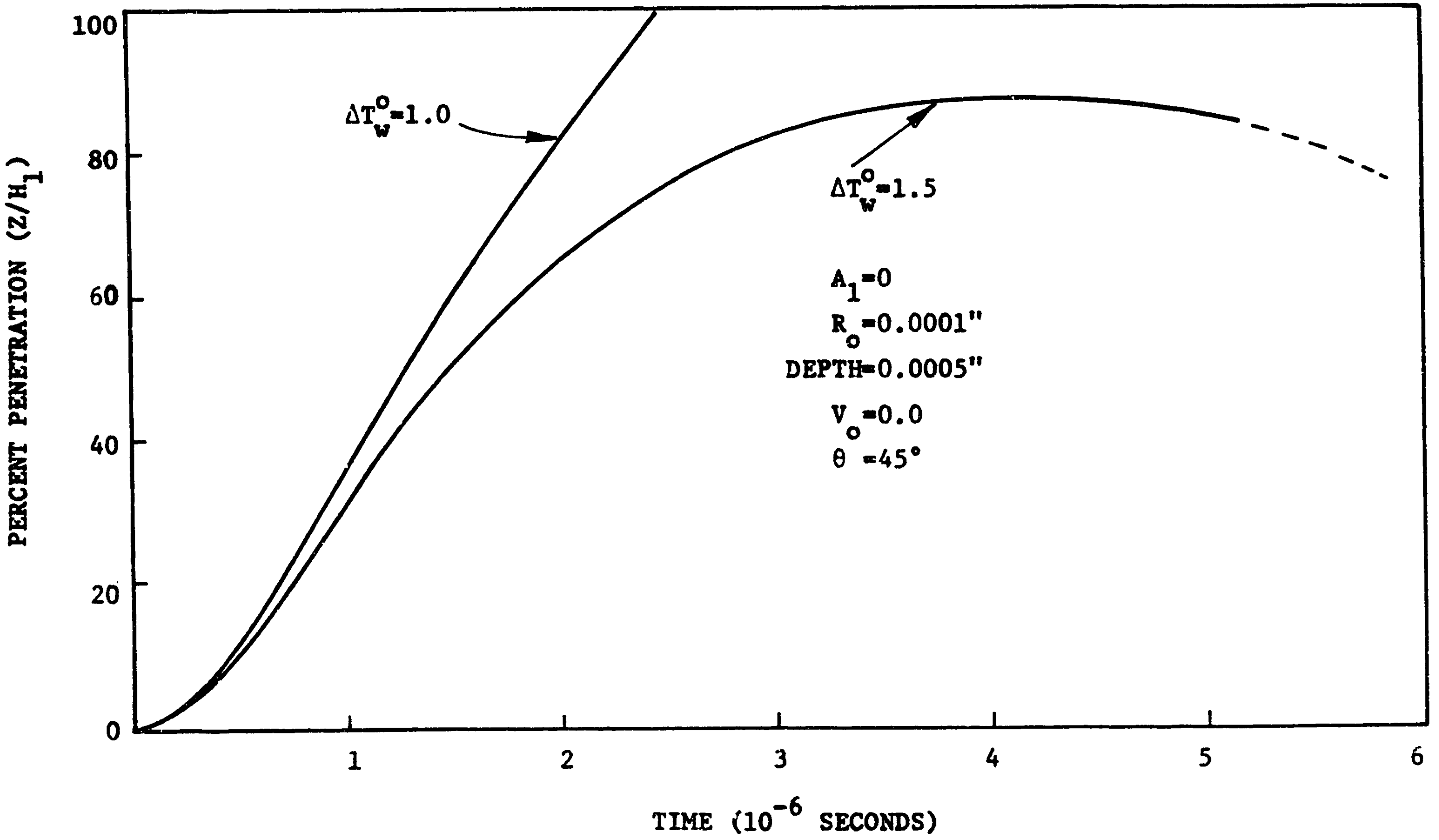

Fig. 18b: Effect of A_1 on water.

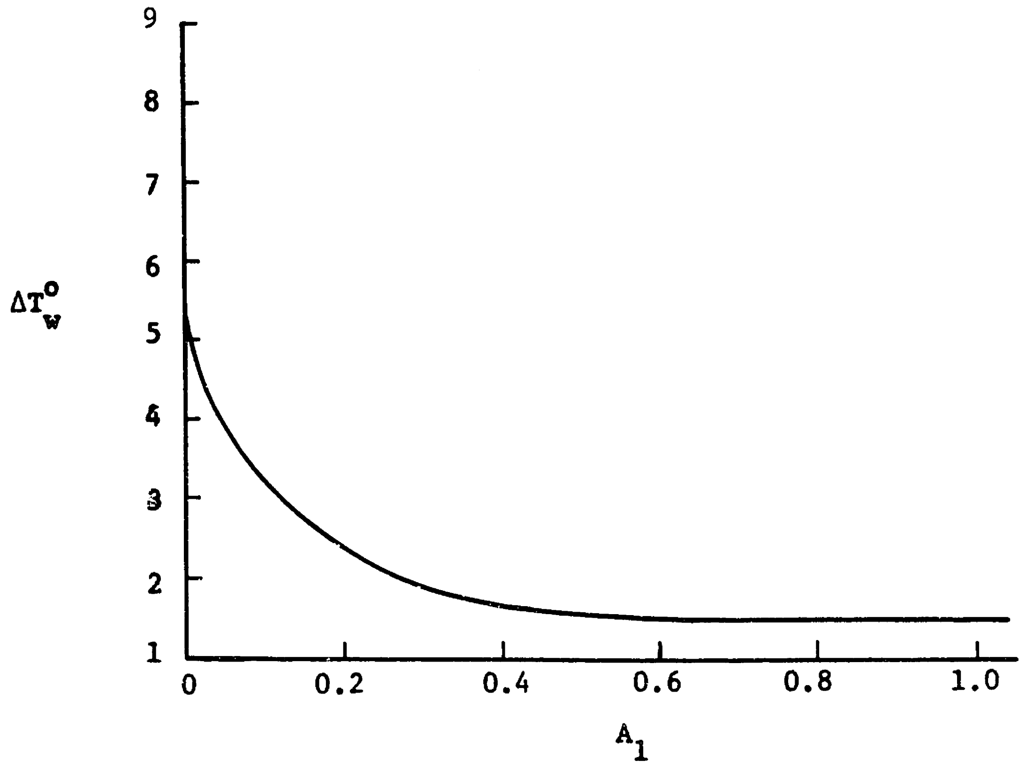

Fig. 19: Effect of A_1 on the required superheat for cavity stability in boiling with methanol.

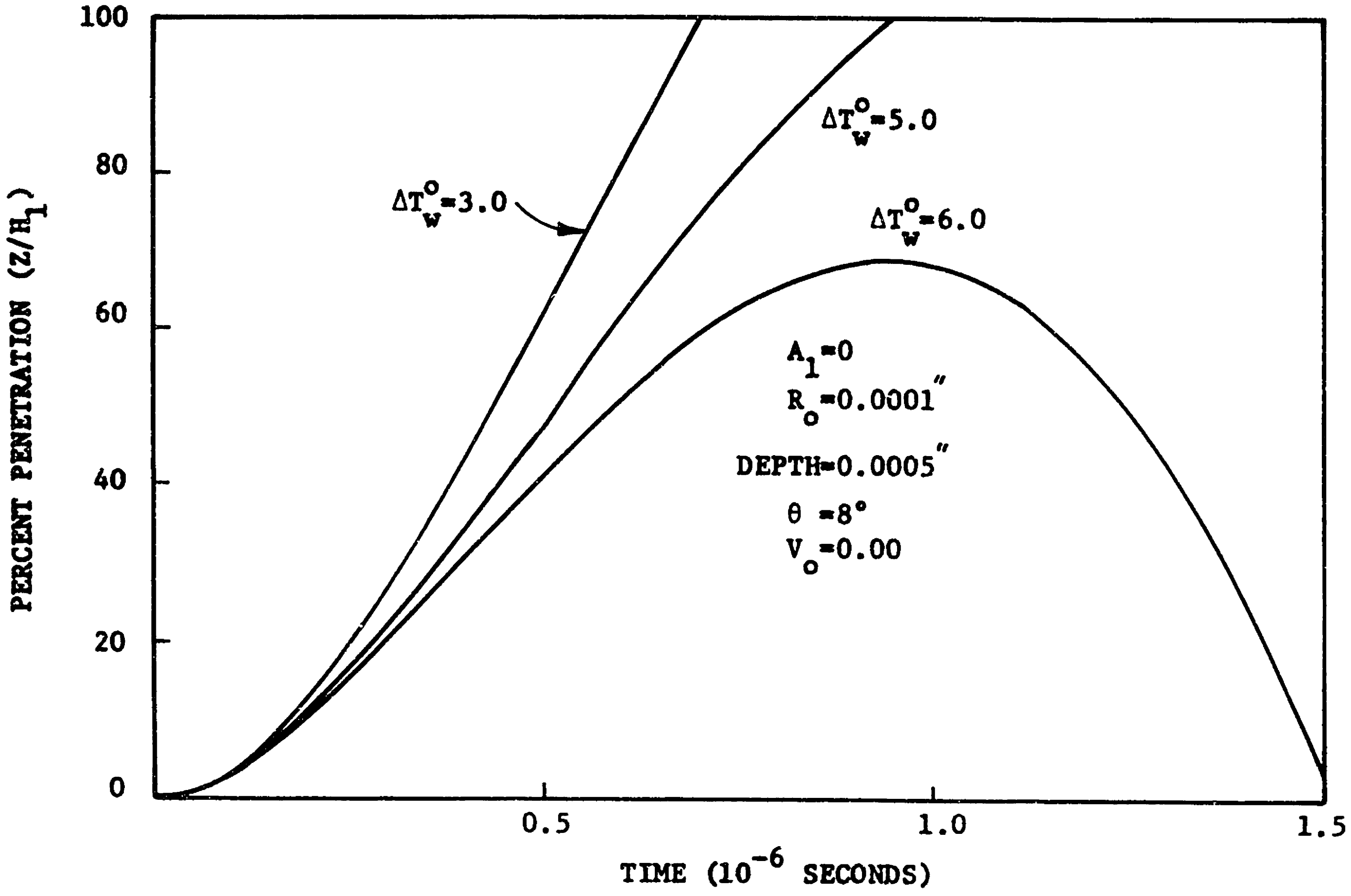

Fig. 20a: Effect of A_1 on the cavity stability in boiling with methanol ($A_1 = 0$).

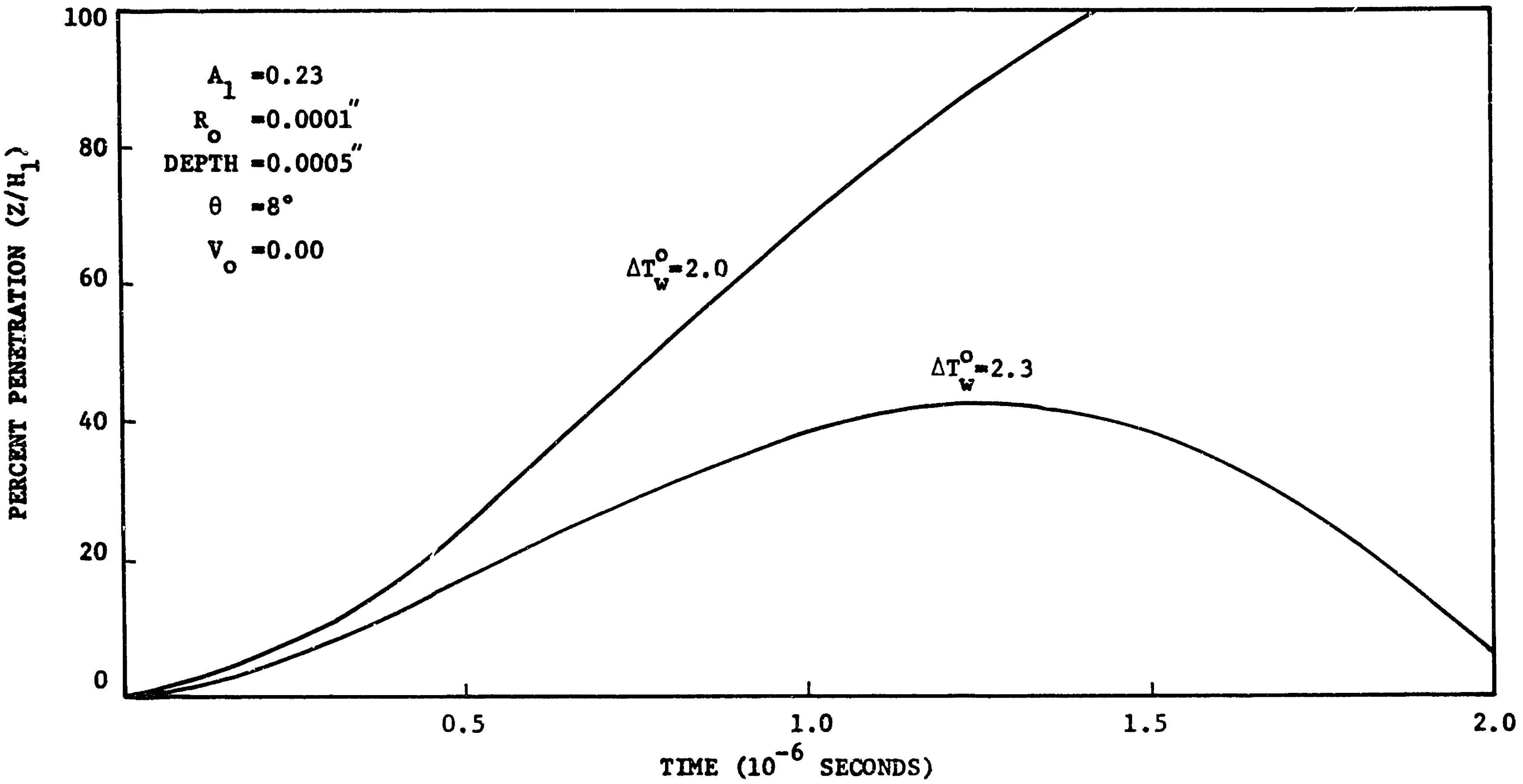

Fig. 20b: Effect of A_1 on the cavity stability in boiling with methanol (A_1=0.23).

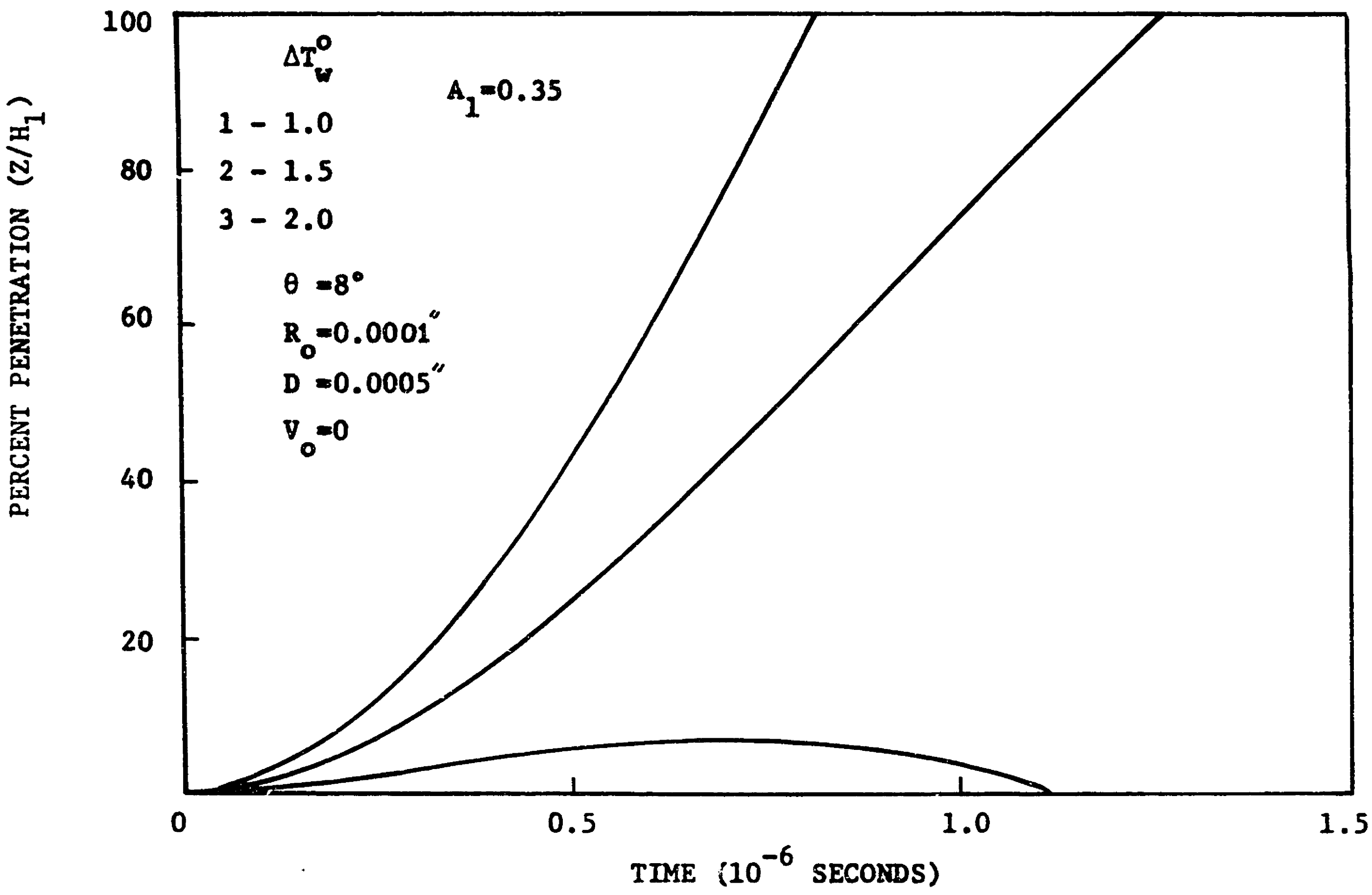

Fig. 20c: Effect of A_1 on cavity stability in boiling with methanol (A_1=0.35).

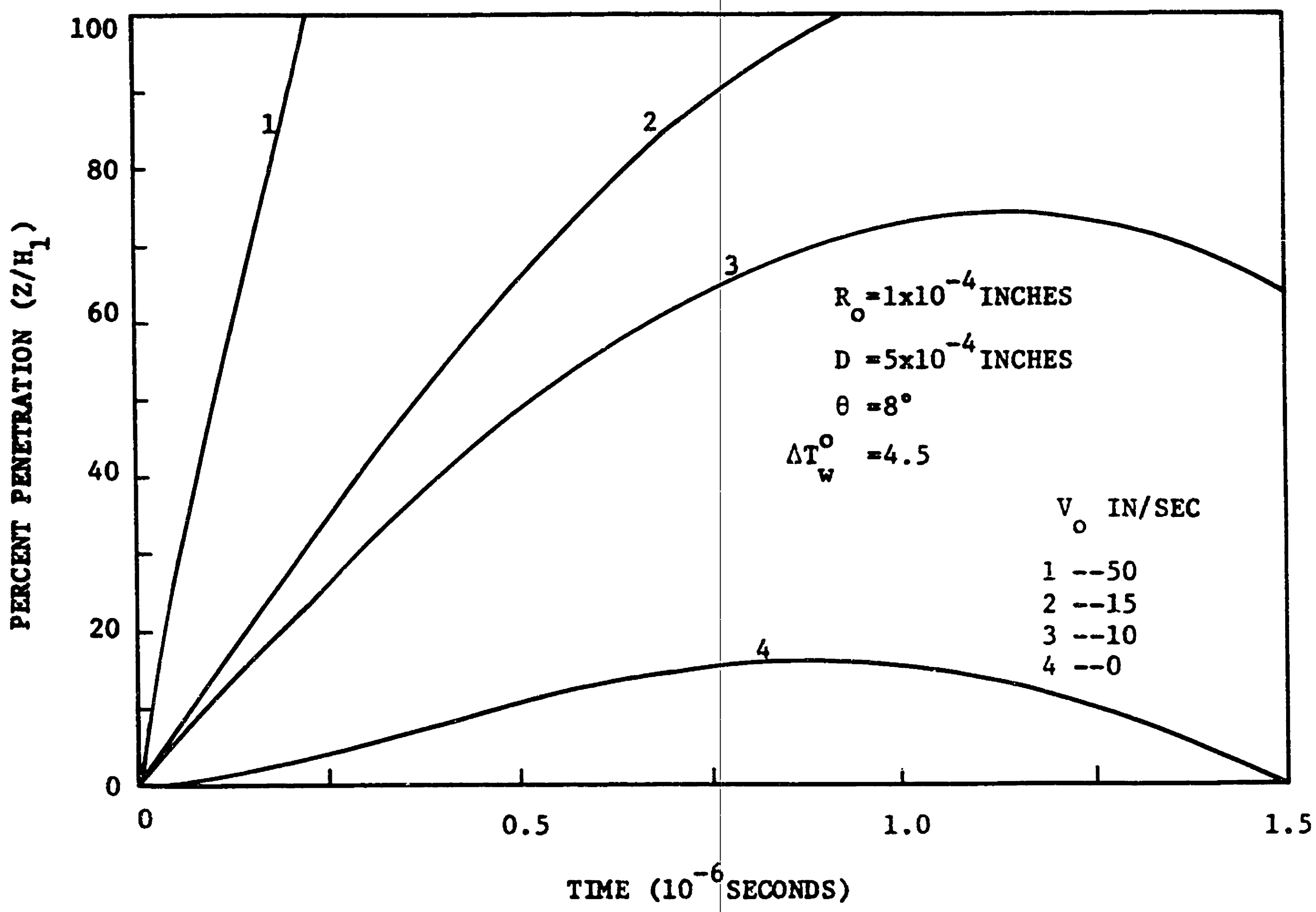

Fig. 21a: Effect of initial velocity on cavity stability for ethanol.

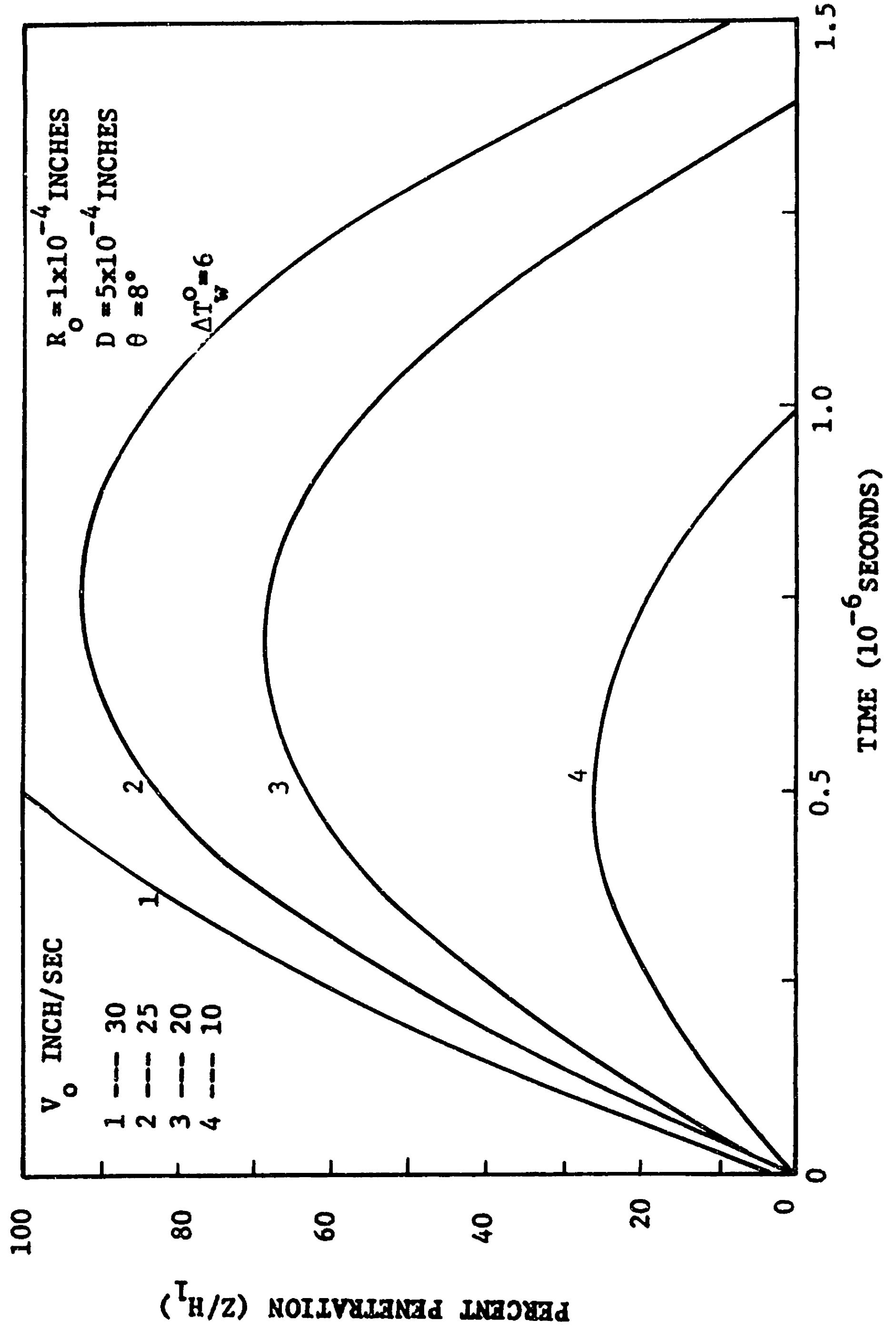

Fig. 21b: Effect of initial velocity on cavity stability for ethanol.

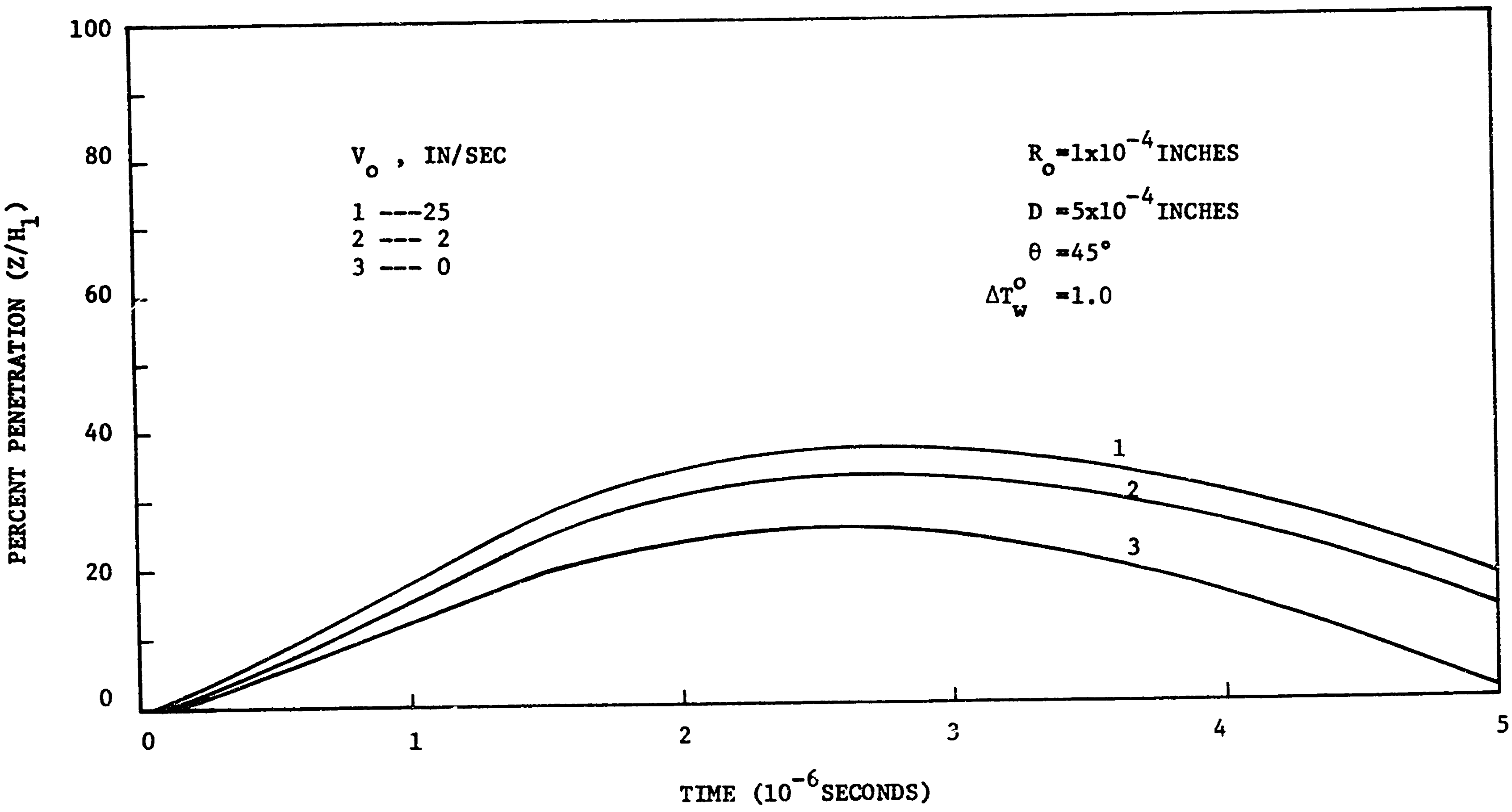

Fig. 22: Effect of initial velocity on cavity stability in boiling with water.

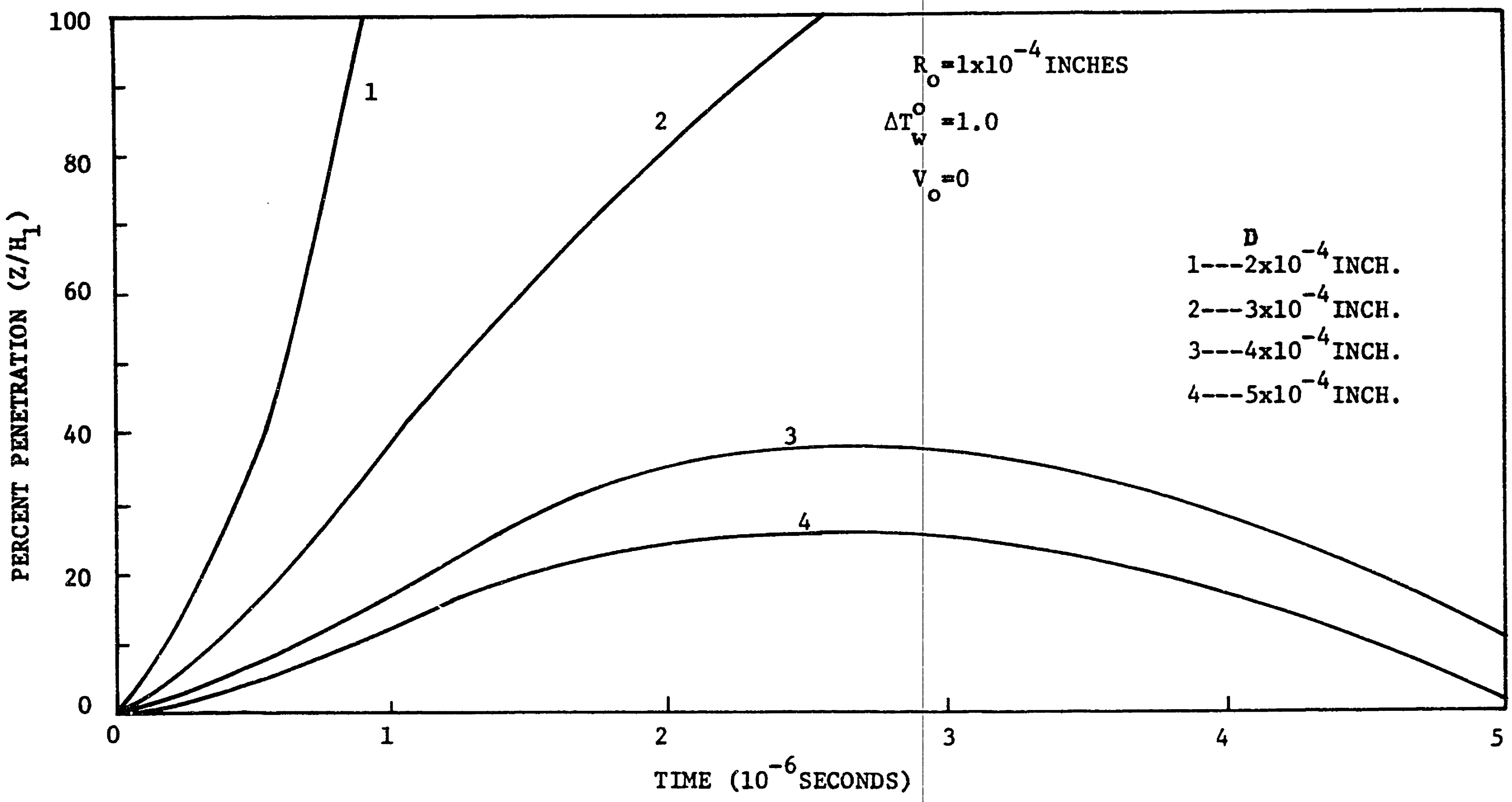

Fig. 23: Effect of cavity depth on the stability of a cavity in boiling with water.

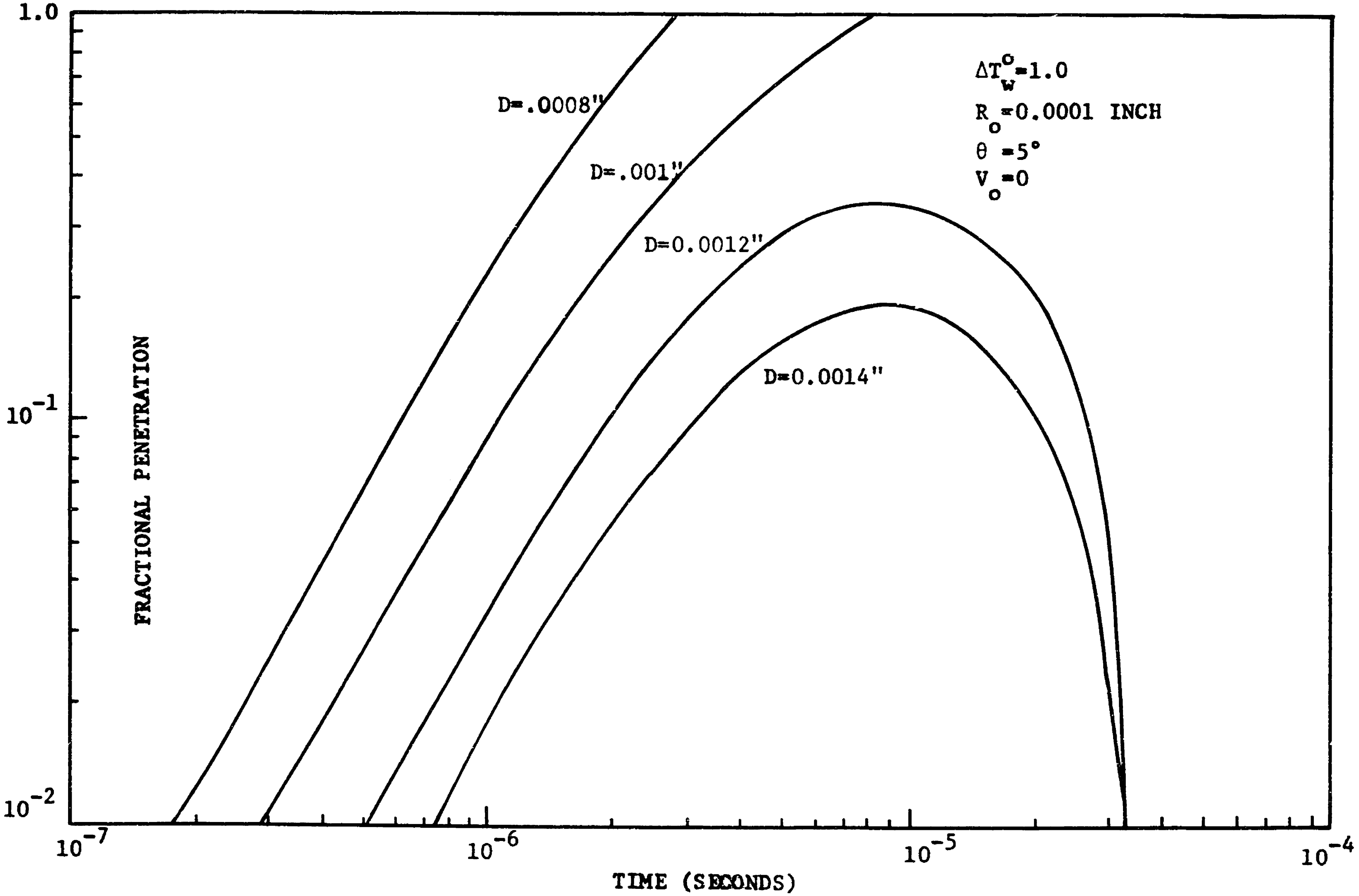

Fig. 24: Effect of cavity depth on cavity stability in boiling with methanol.

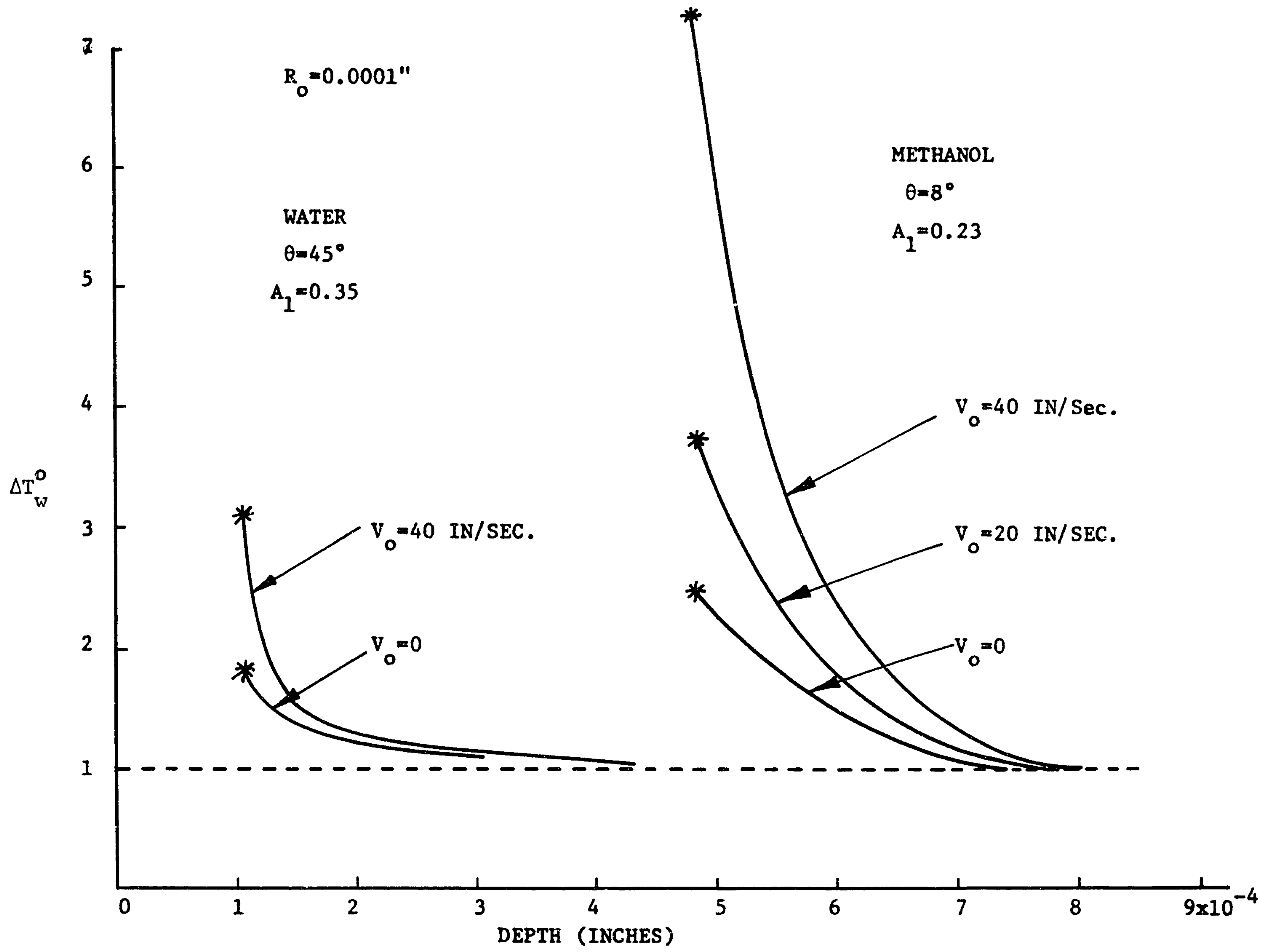

Fig. 25: Effect of cavity depth and velocity on superheat required for stable boiling.

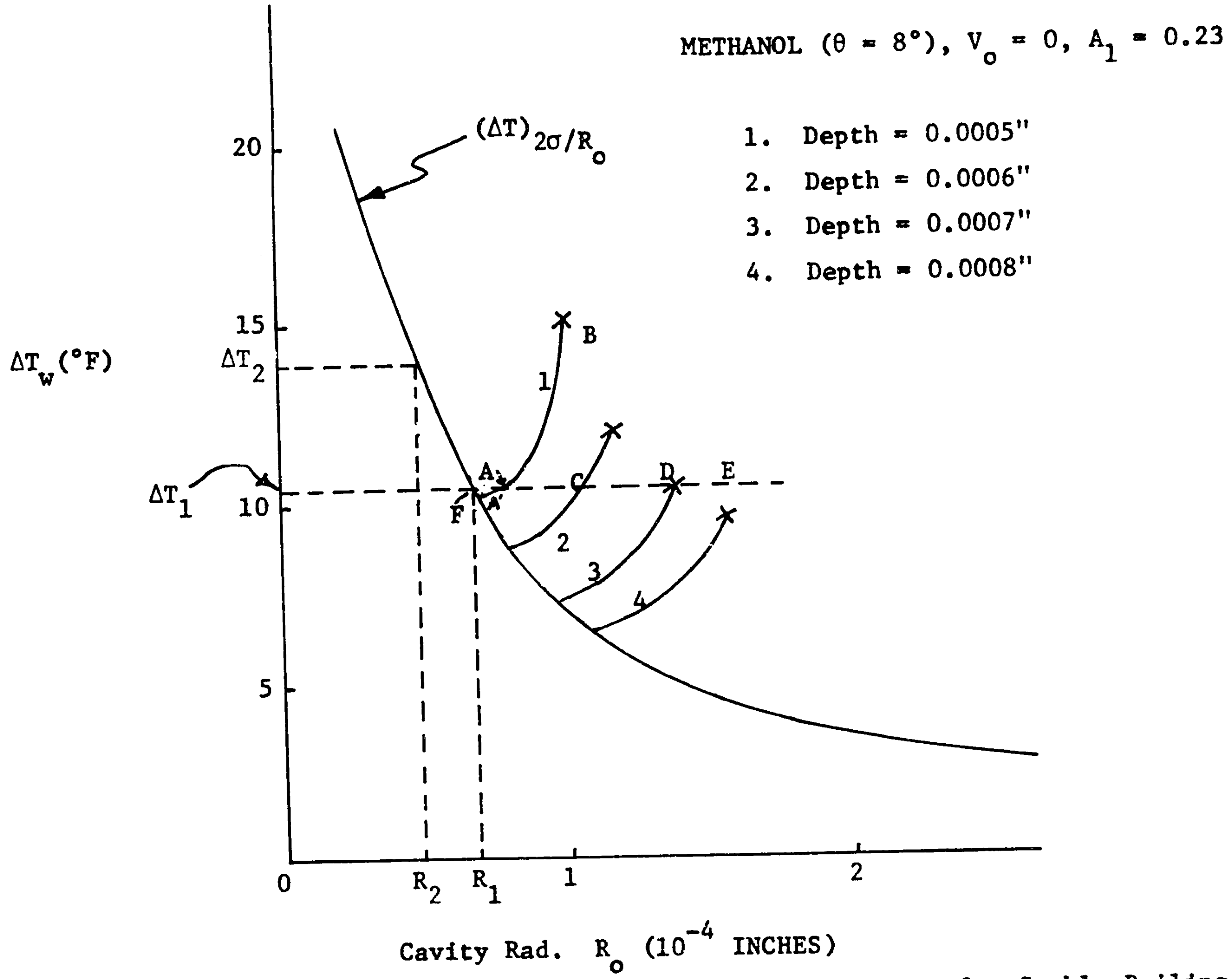

Fig. 26: Effect of Cavity Size on Superheat for Stable Boiling.

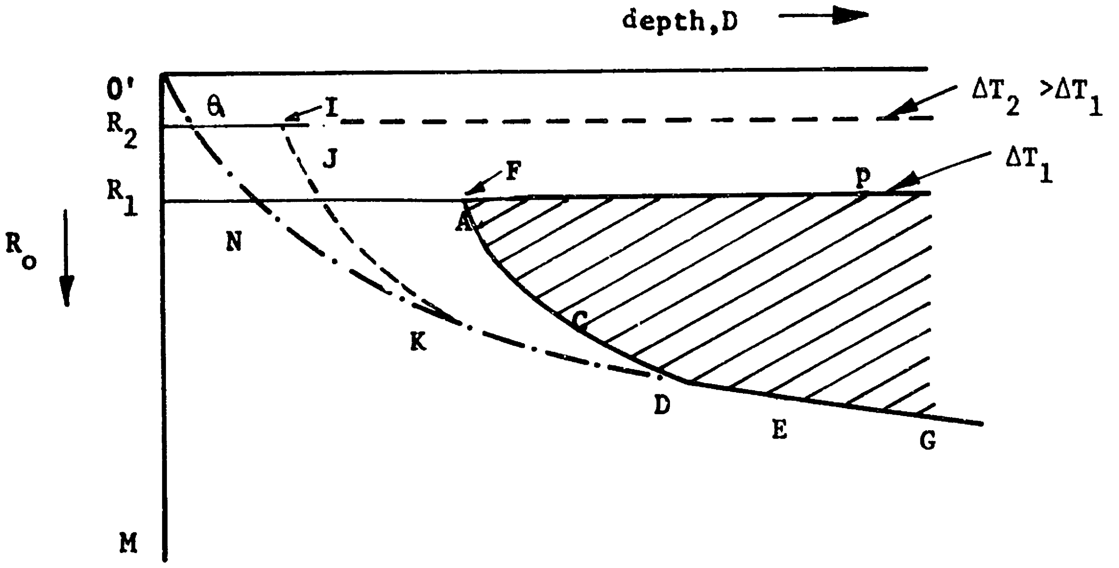

Fig. 27a: Size range of active sites at a given superheat ΔT_1 and contact angle θ.

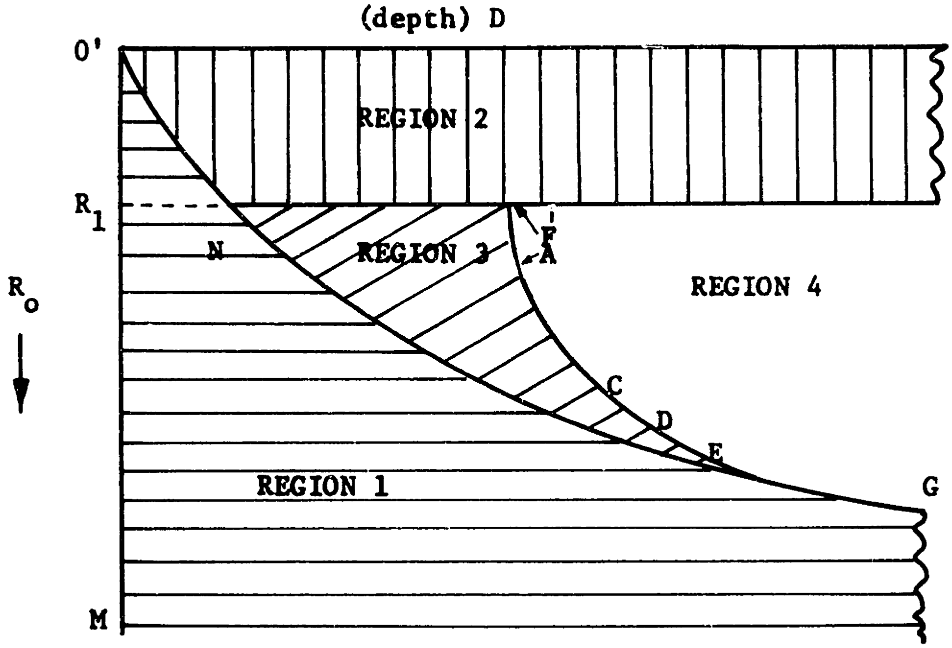

Fig. 27b: Regions of inactive and active sites, governed by three different criteria, at superheat ΔT_1 and given contact angle.

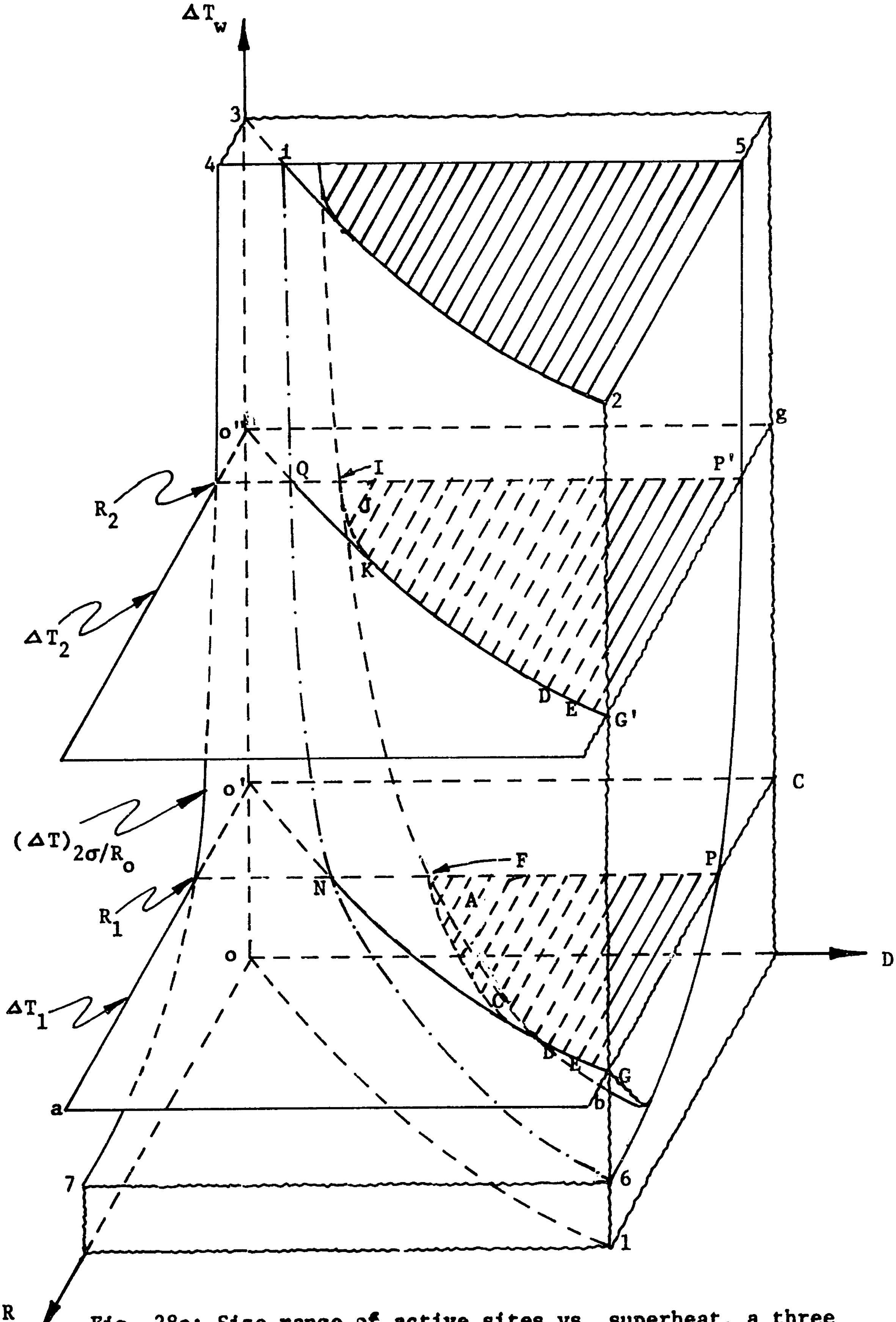

Fig. 28a: Size range of active sites vs. superheat, a three dimensional presentation.

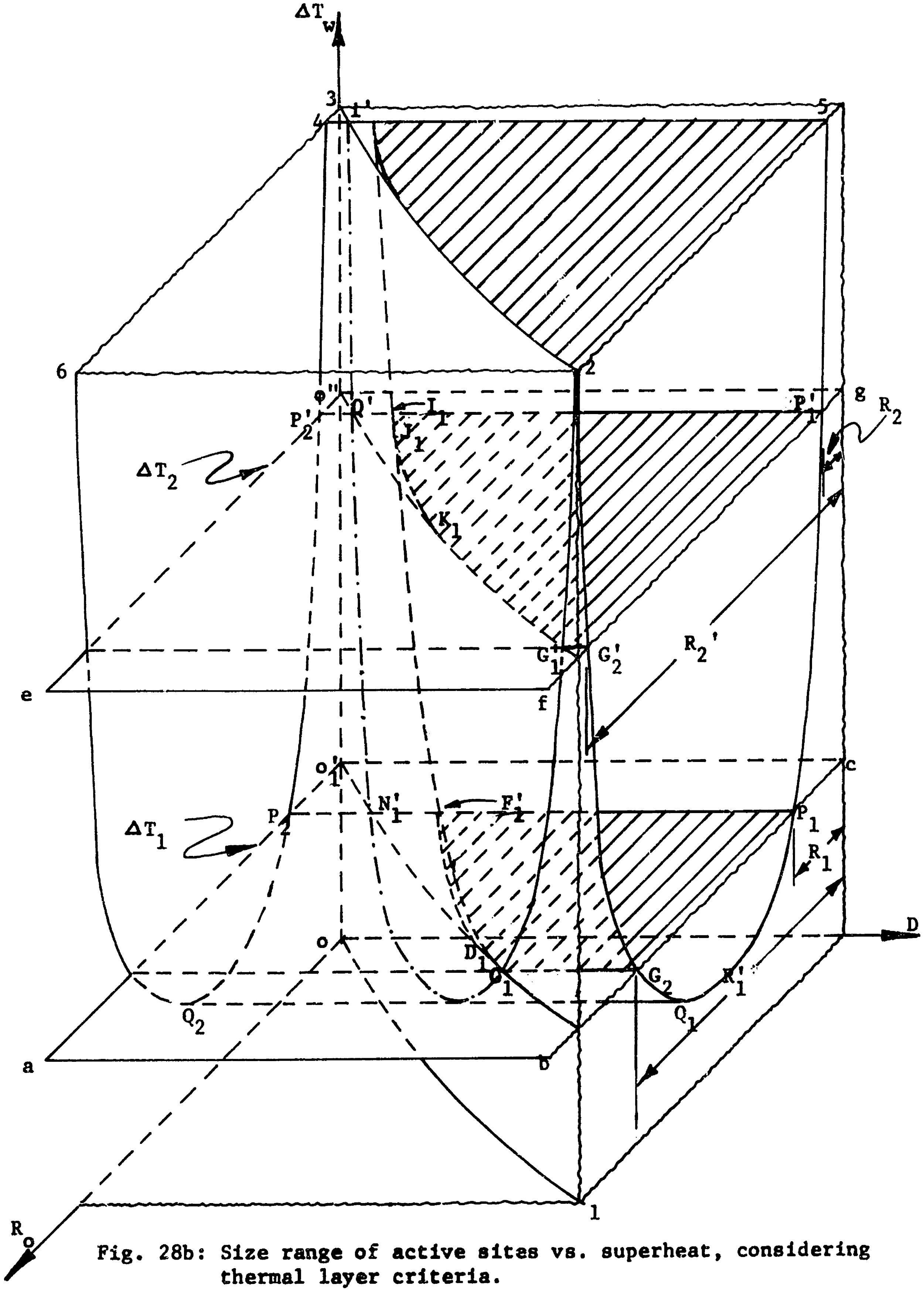

Fig. 28b: Size range of active sites vs. superheat, considering thermal layer criteria.

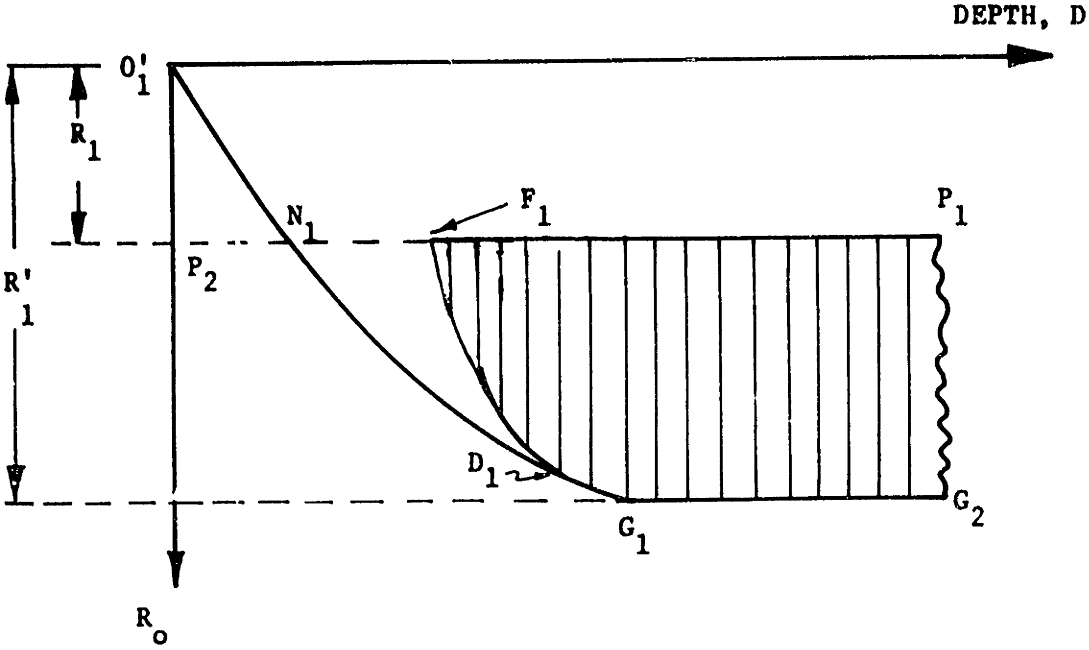

Fig. 28c: Region of active sites at supeheat ΔT_1, considering thermal layer criteria.

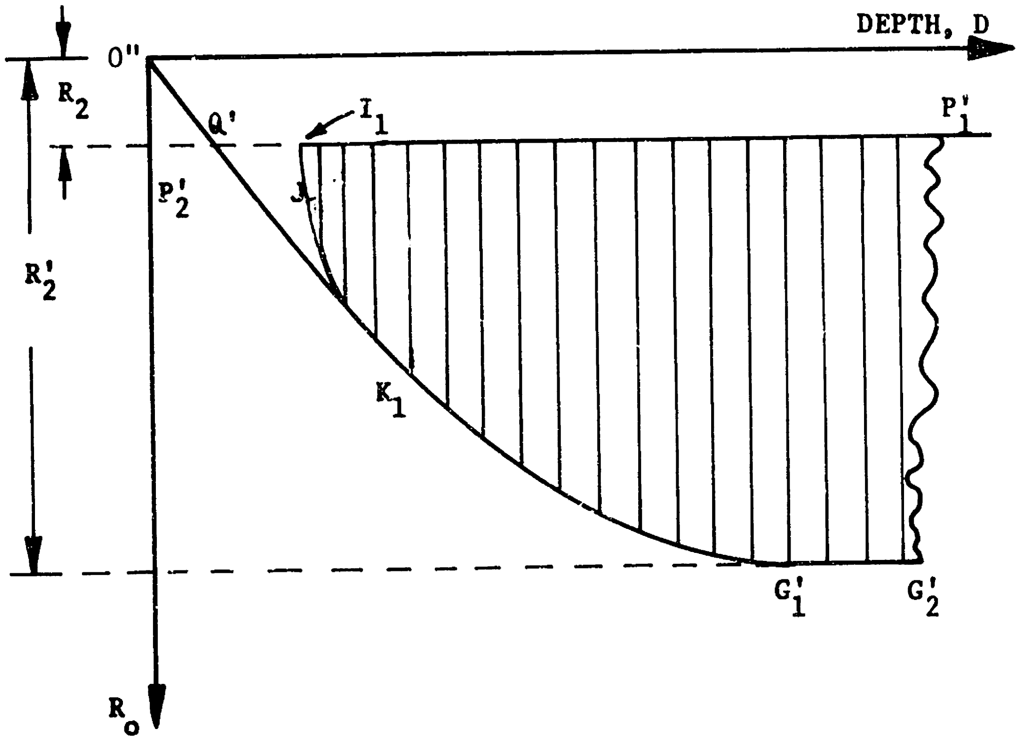

Fig. 28d: Region of active sites at superheat ΔT_2, ($\Delta T_2 > \Delta T_1$) considering thermal layer criteria.

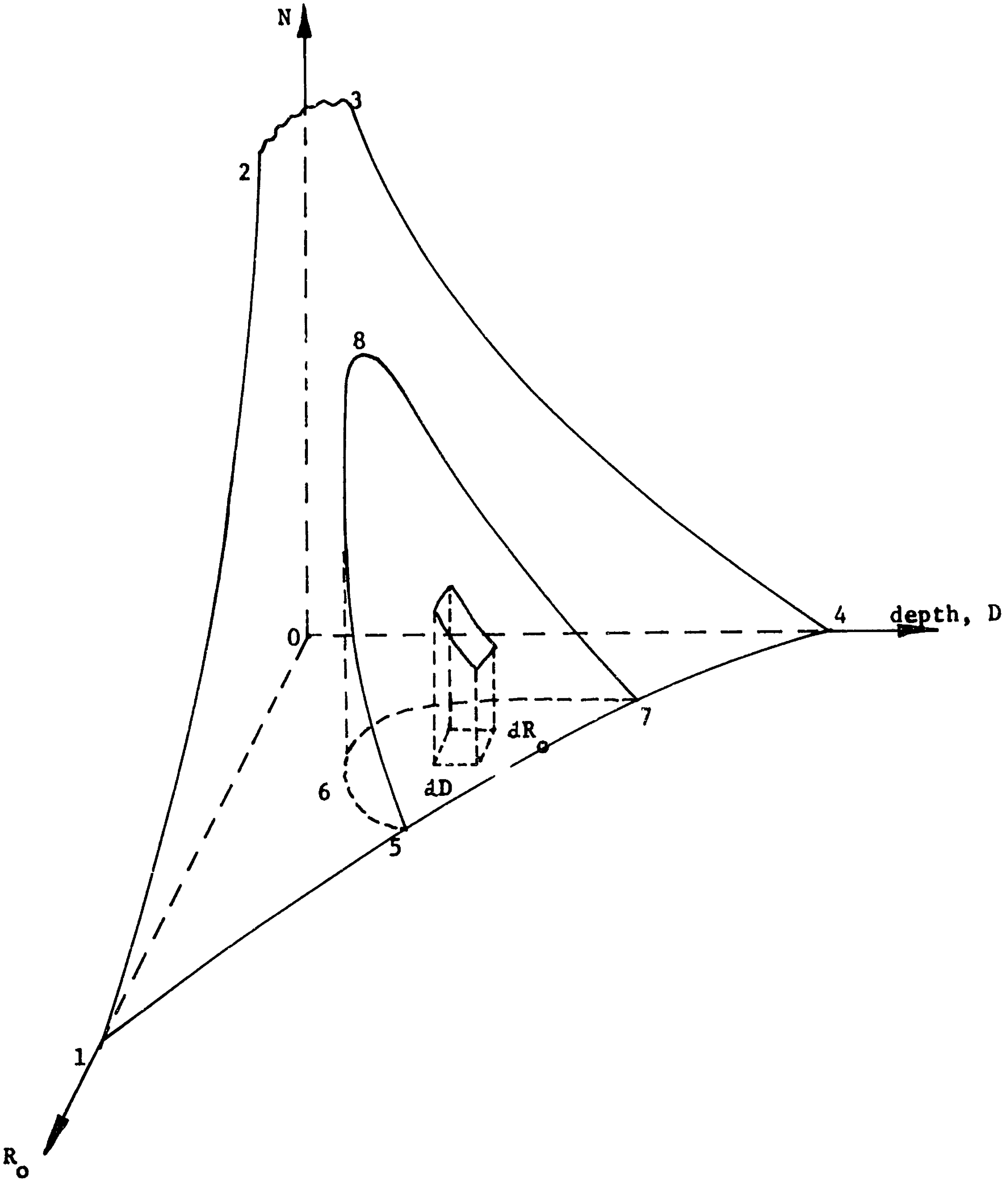

Fig. 28e: Active site population on a given surface having a prescribed cavity size distribution.

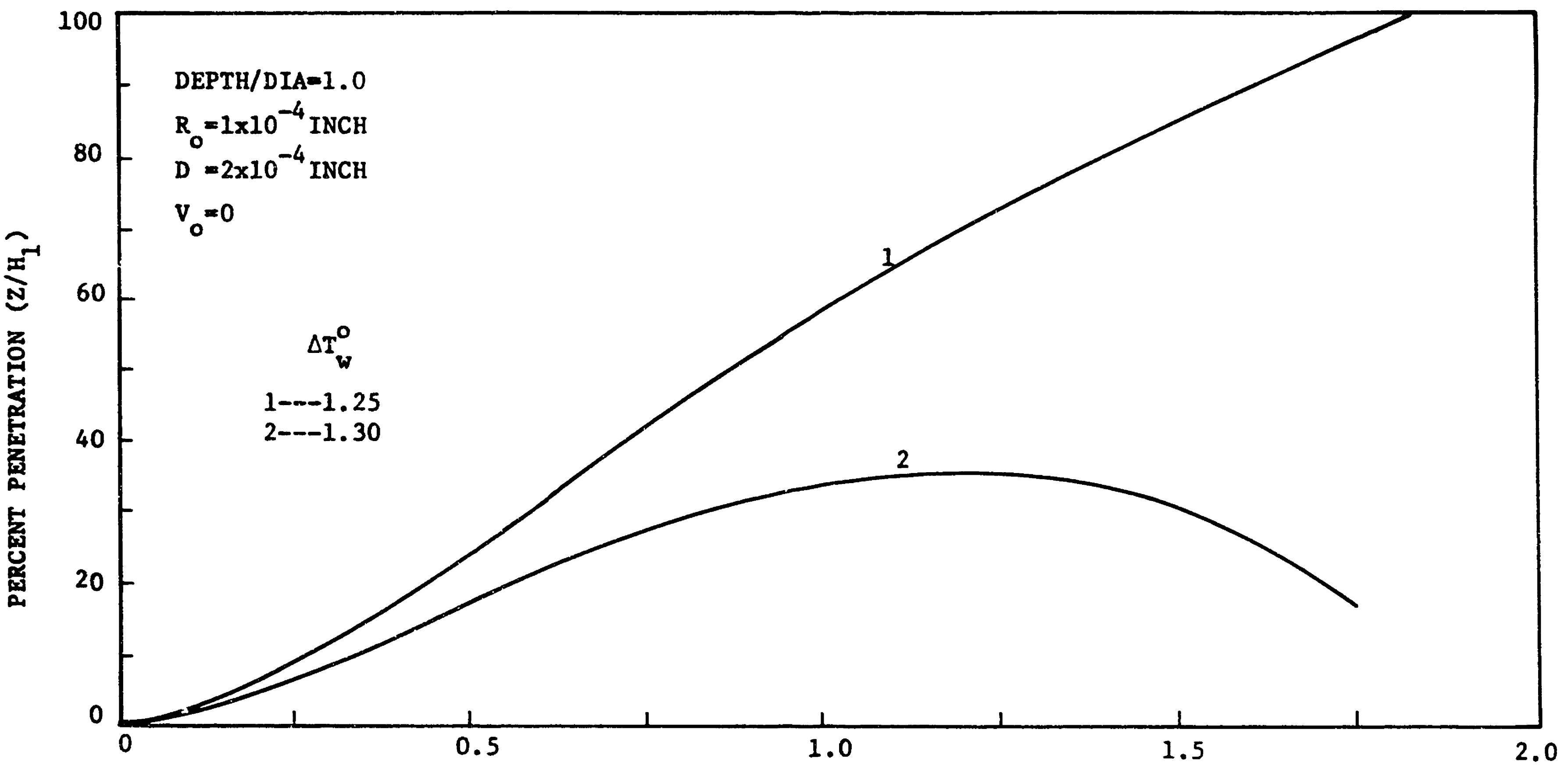

Fig. 29a: Effect of cavity size (R_o and D) on cavity stability in boiling with water.

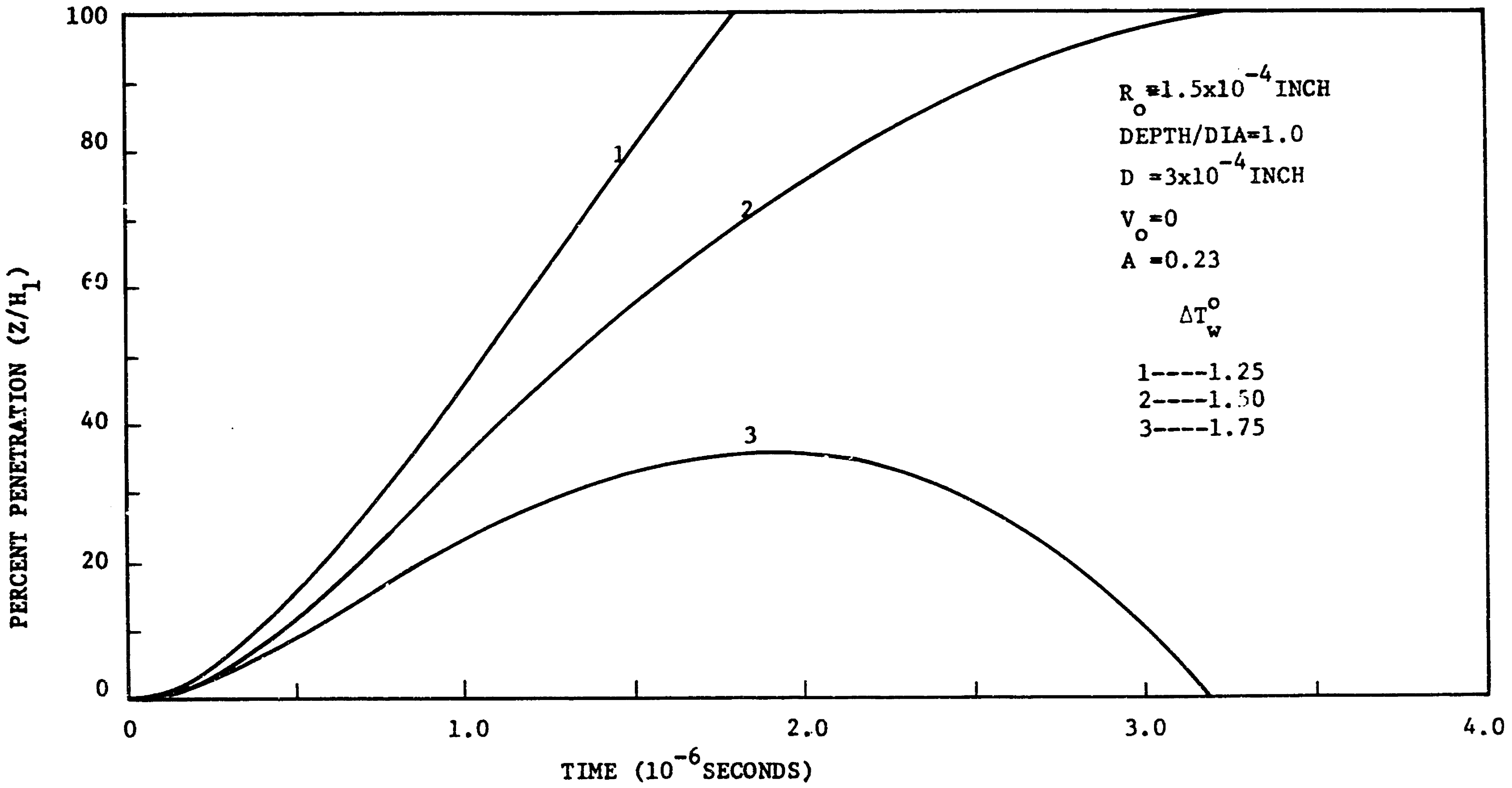

Fig. 29b: Effect of cavity size (R_o and D) on cavity stability in boiling with water.

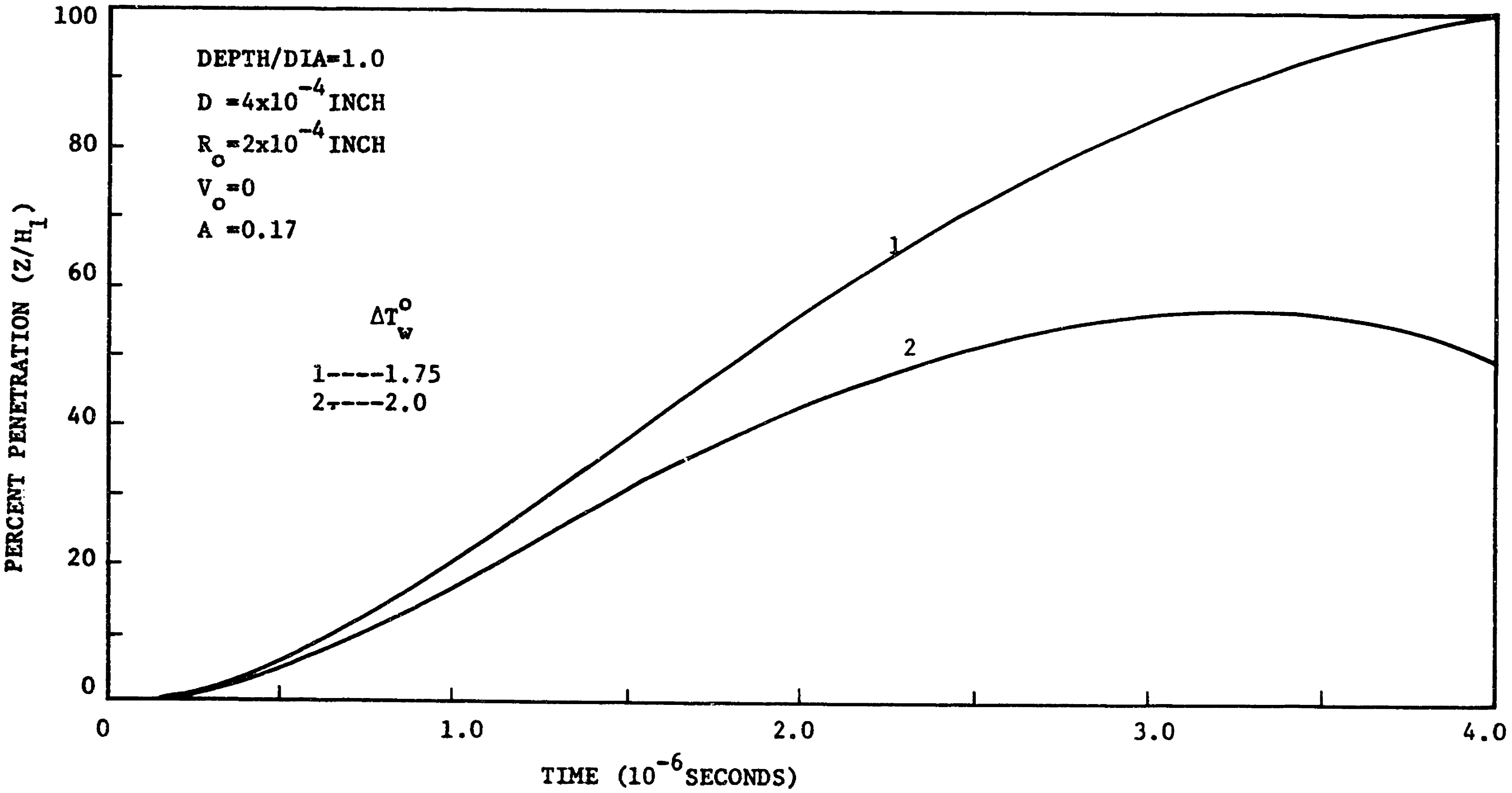

Fig. 29c: Effect of cavity size (R_o and D) on cavity stability in boiling with water.

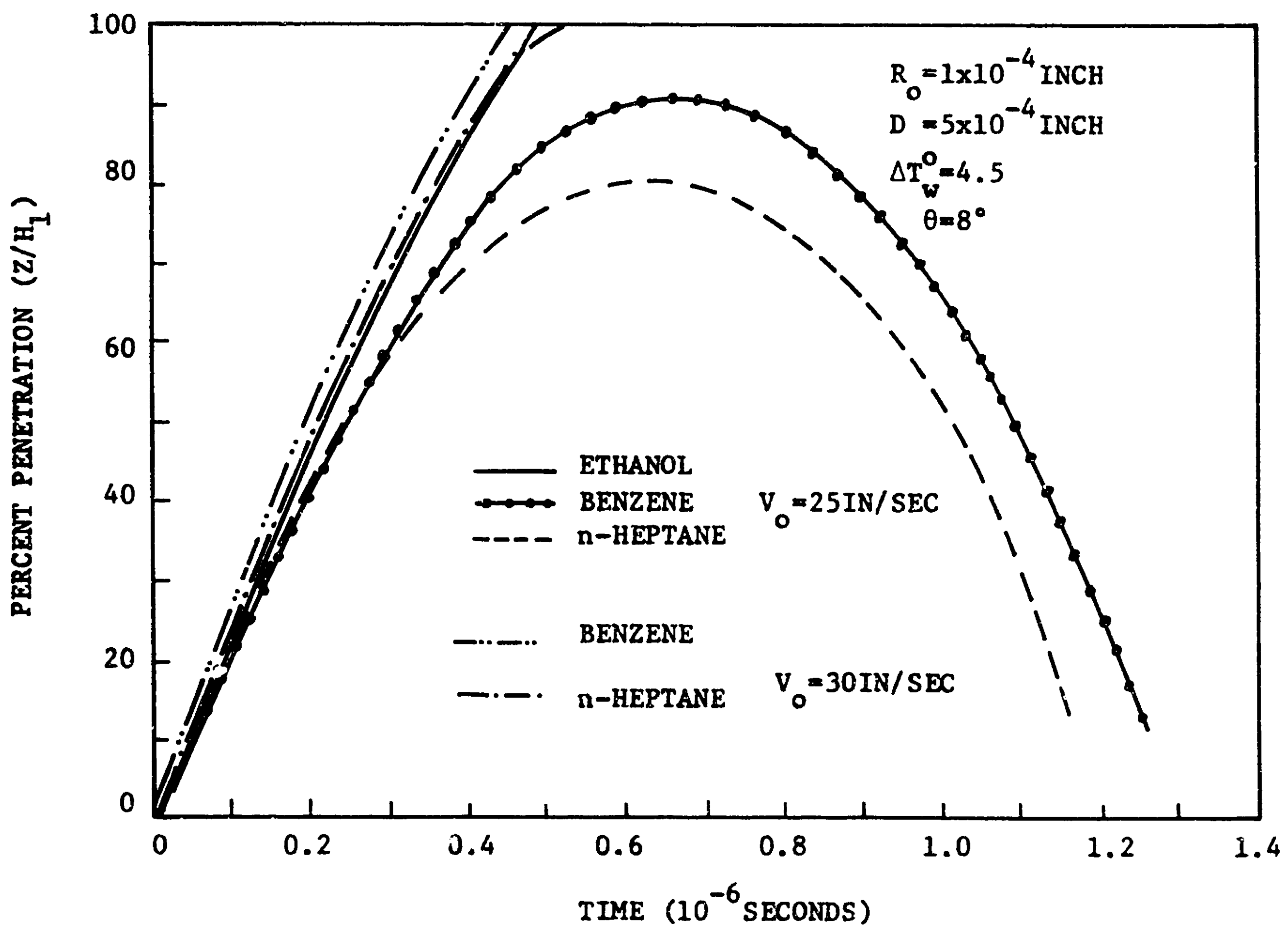

Fig. 30: Effect of initial velocity on the relative behavior of organics.

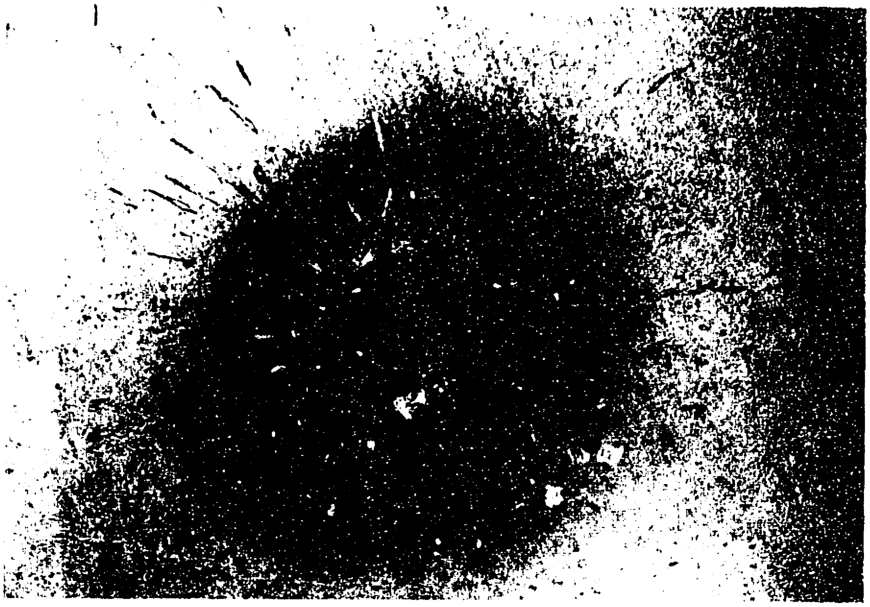

a. Magnification = x1000, R_o = 3.5 x 10^{-4}" , D = 24 x 10^{-4}"

b. Magnification = x1000, R_o = 1.5 x 10^{-4}" , D = 20 x 10^{-4}"

Fig. 31: Photomicrographs of laser cavities before boiling.

c. Magnification =x1000, R_o = 2.5 x 10^{-4}"
D = 24 x 10^{-4}"

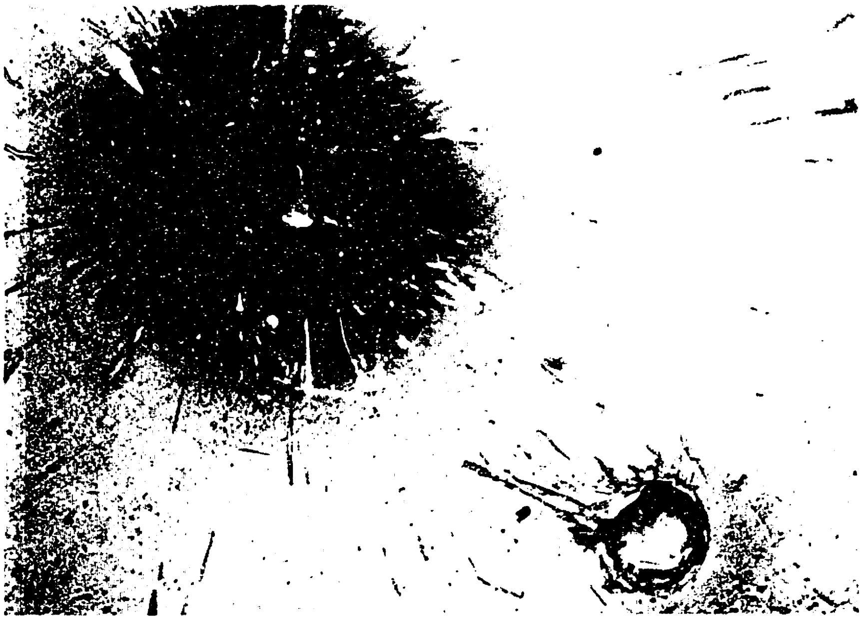

d. Magnification = x1000
Upper cavity: R_o = 2 x 10^{-4}" , D = 24 x 10^{-4}"
Lower cavity: R_o = 2 x 10^{-4}" , D = 6 x 10^{-4}"

Fig. 32: Photomicrographs of laser cavities before boiling.

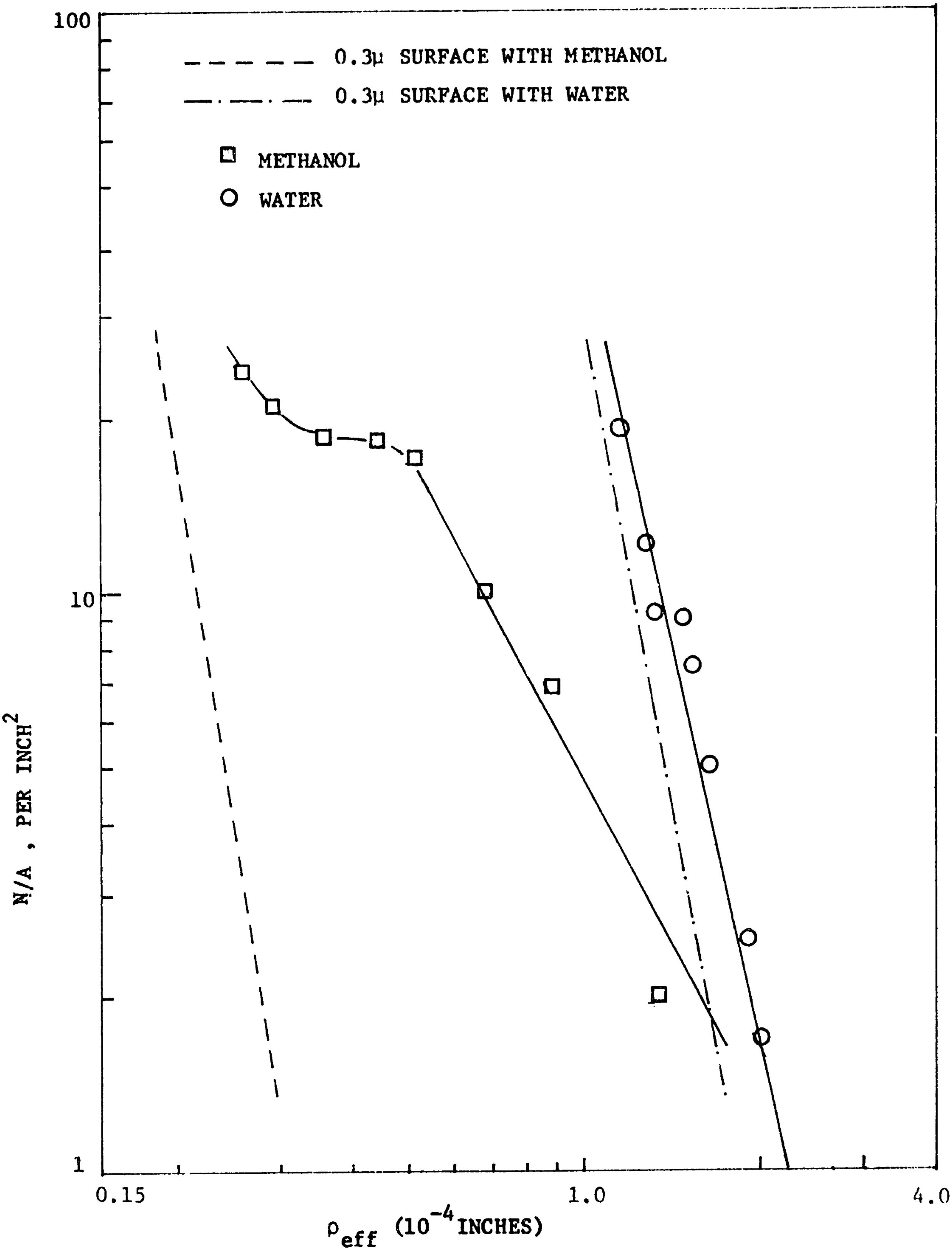

Fig. 33: N/A vs. ρ_{eff} characteristics of the boiling Surface I, having laser drilled cavities.

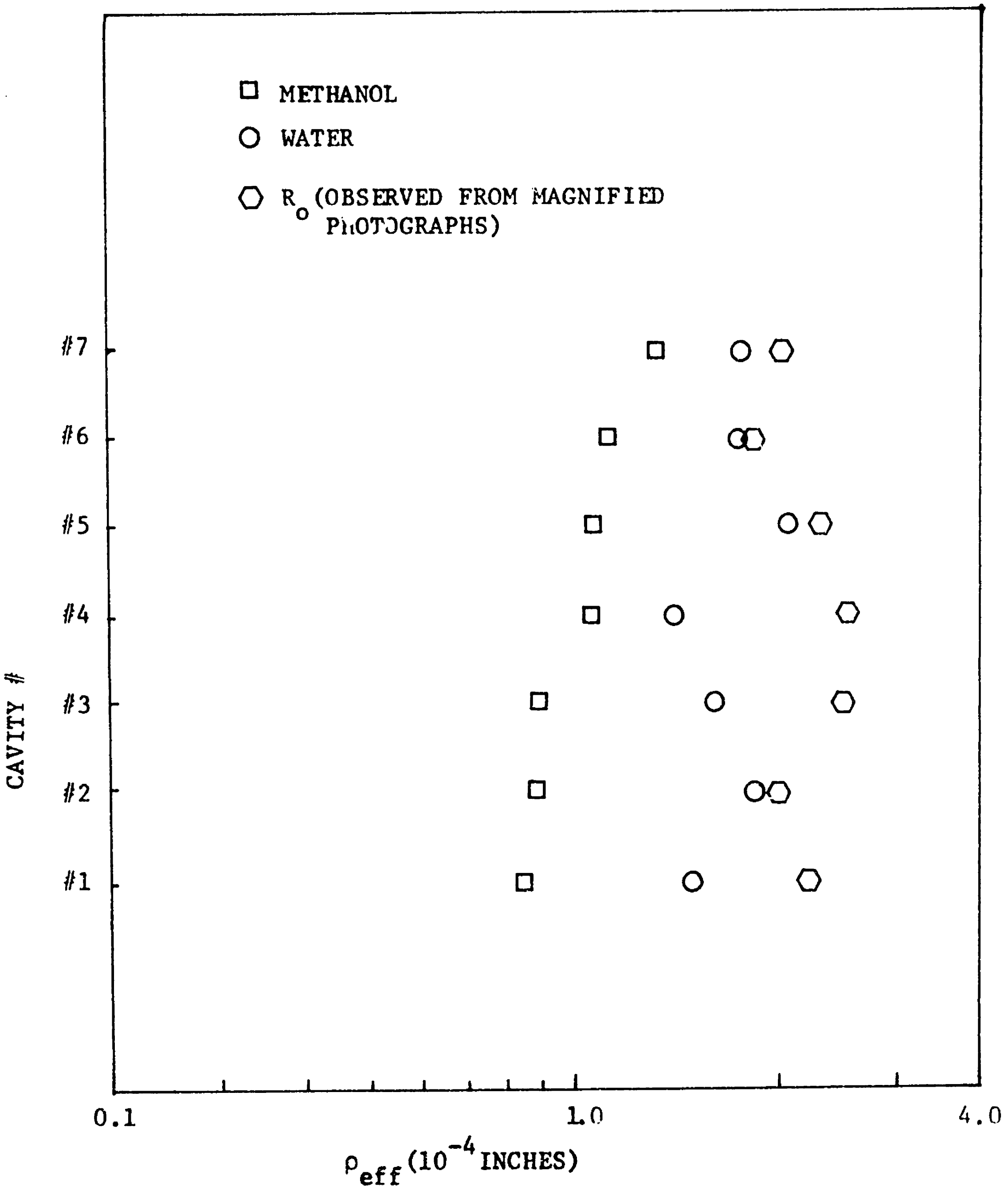

Fig. 34: Boiling data for the individual laser cavities with methanol and water.

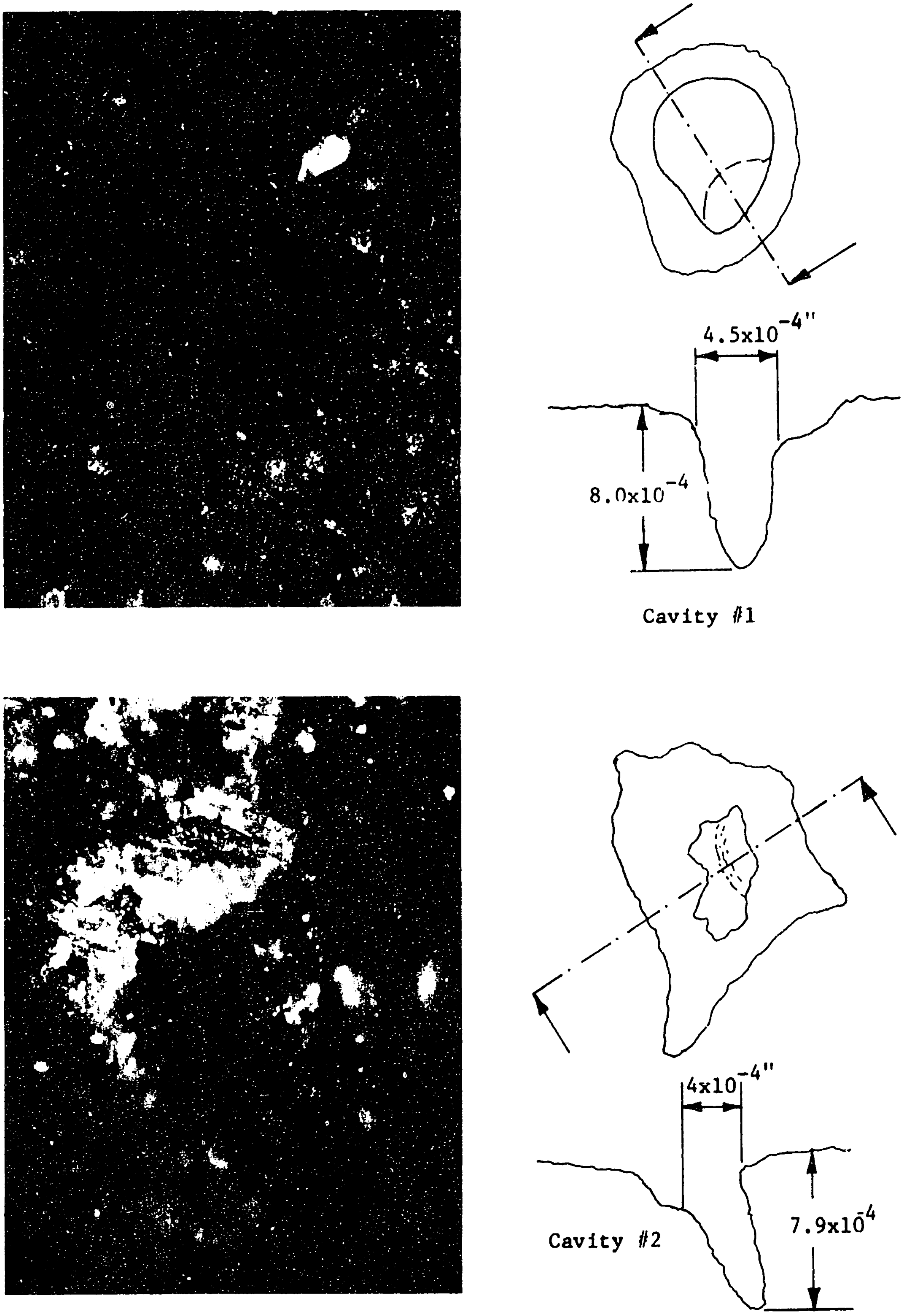

Fig. 35a: Photomicrographs of laser cavities on laser Surface I at magnification x1000.

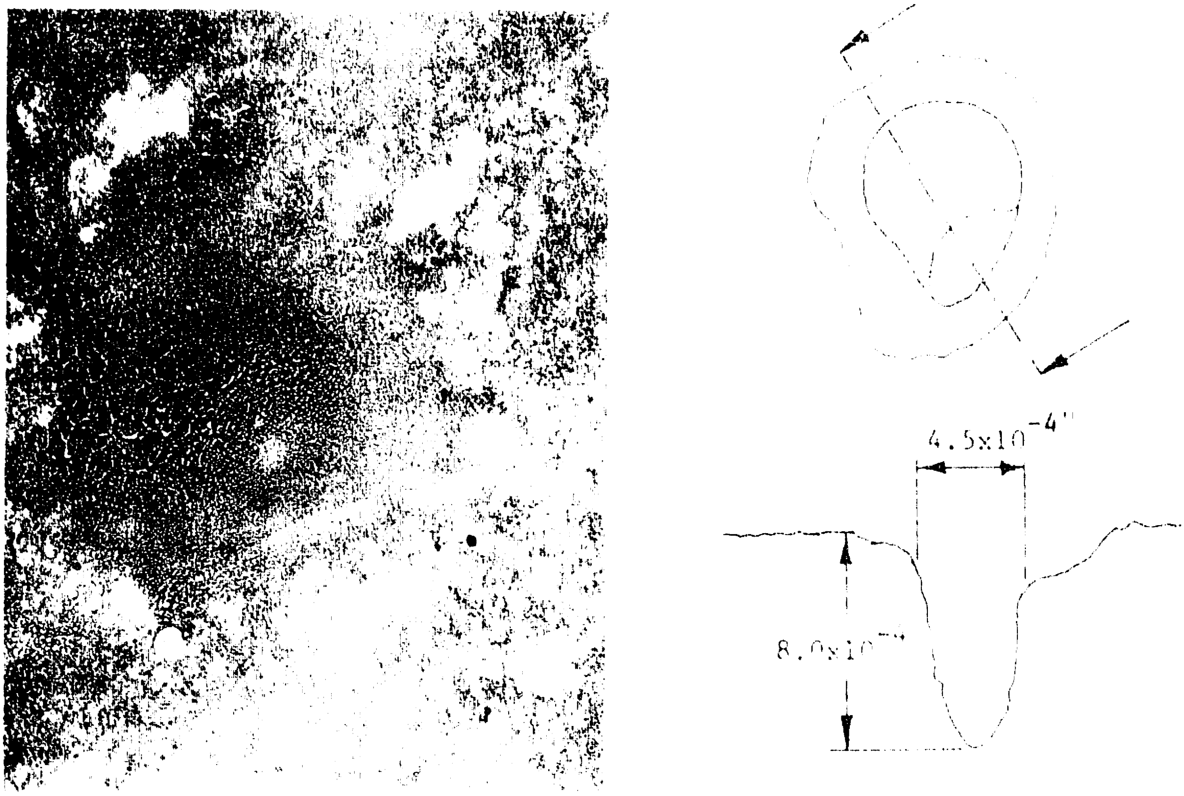

Cavity #1

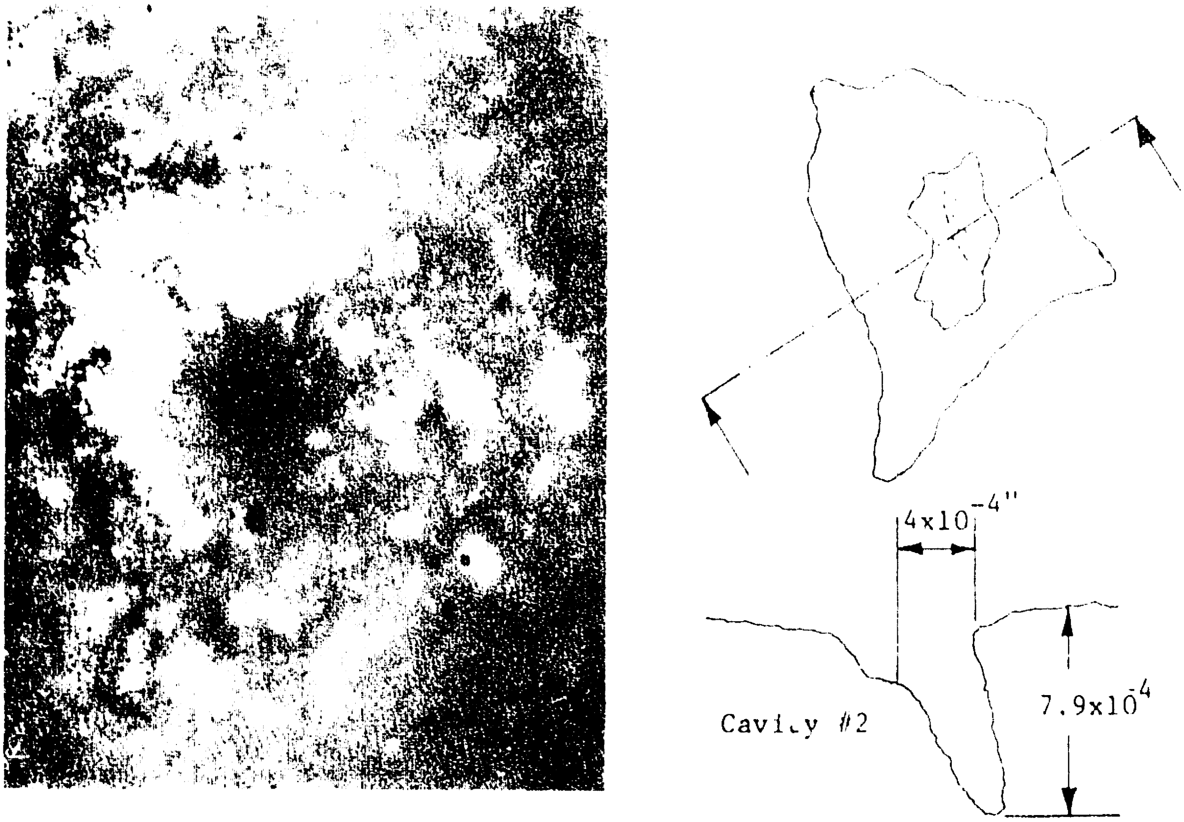

Cavity #2

Fig. 35a: Photomicrographs of laser cavities on laser Surface I at magnification x1000.

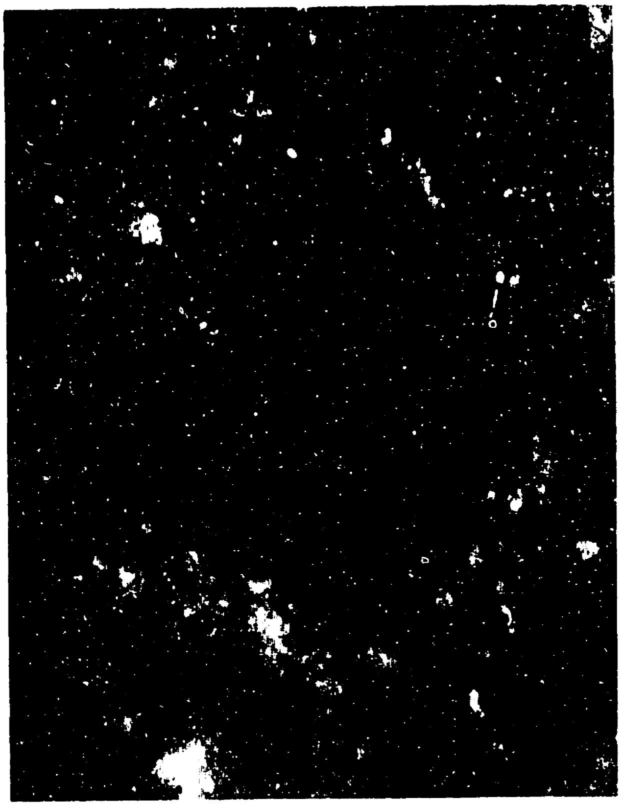

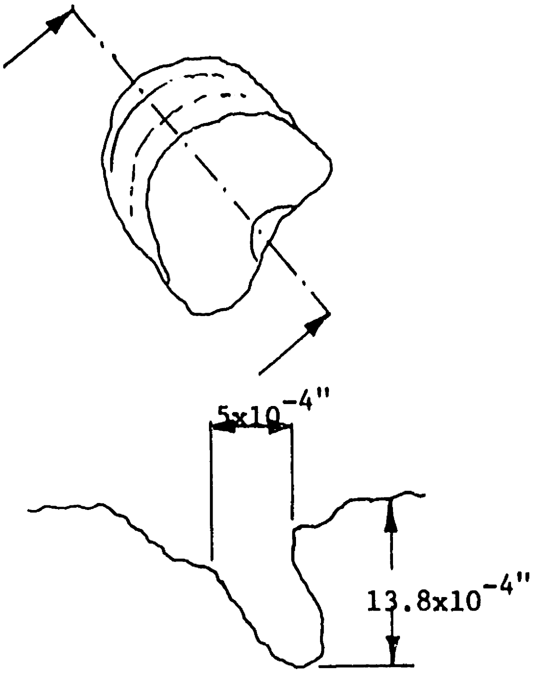

Cavity #3

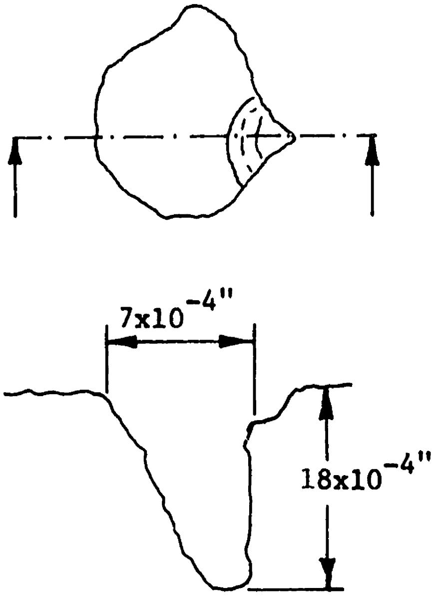

Cavity #4

Fig. 35b: Photomicrographs of laser cavities on laser cavities on laser Surface I, at magnification x1000.

Cavity #3

Cavity #4

Fig. 35b: Photomicrographs of laser cavities on laser cavities on laser Surface I, at magnification x1000.

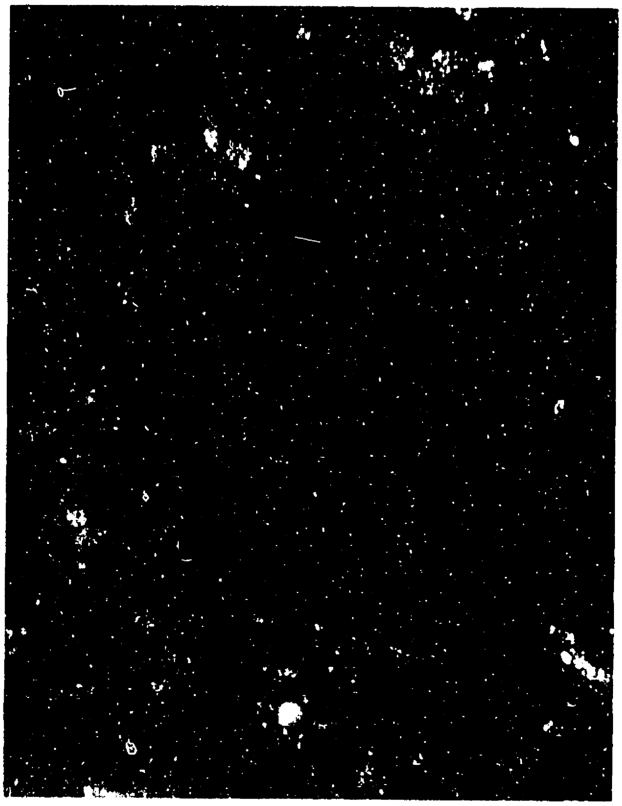

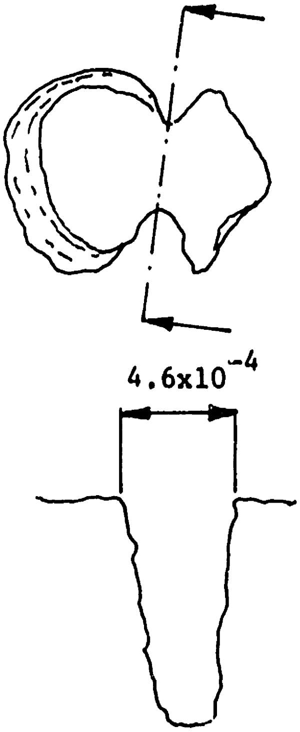

Cavity #5

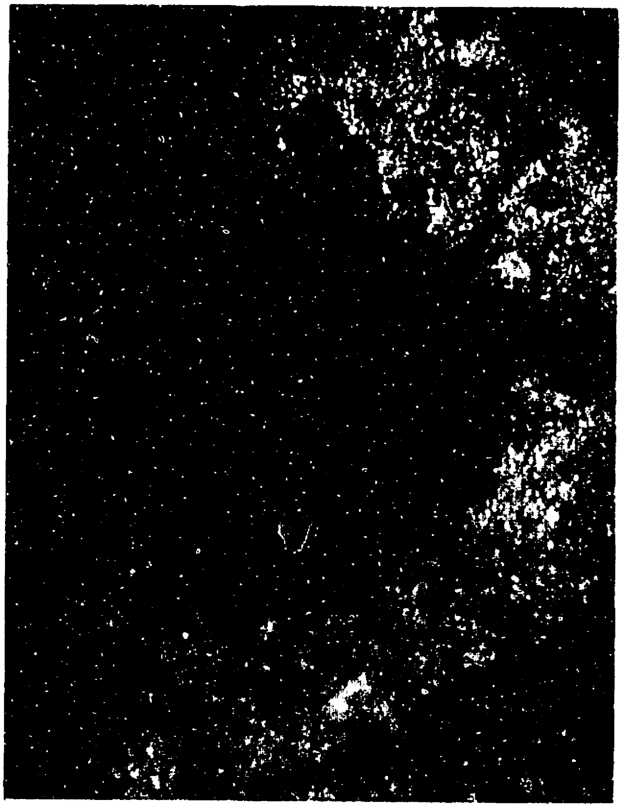

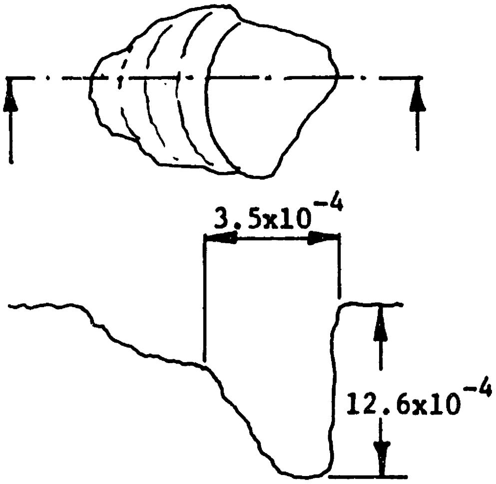

Cavity #6

Fig. 35c: Photomicrographs of laser cavities on laser Surface I at magnification x1000.

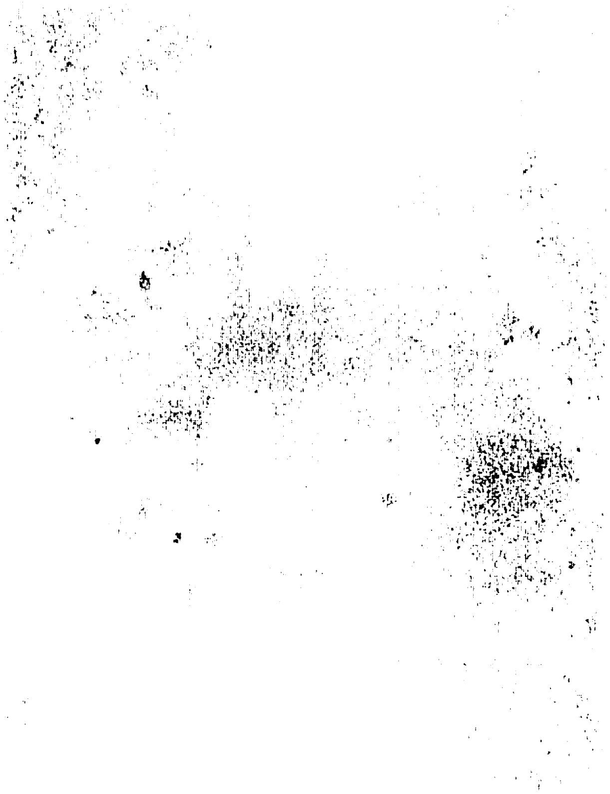

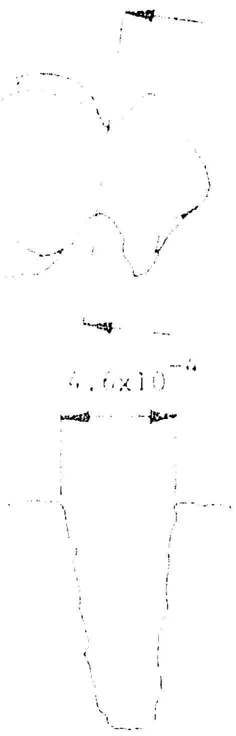

Cavity #5

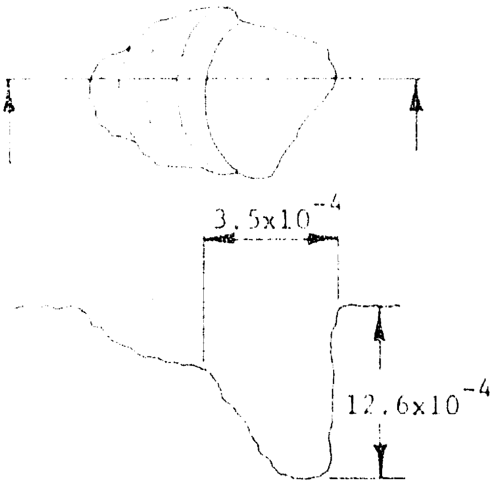

Cavity #6

Fig. 35c: Photomicrographs of laser cavities on laser Surface I at magnification x1000.

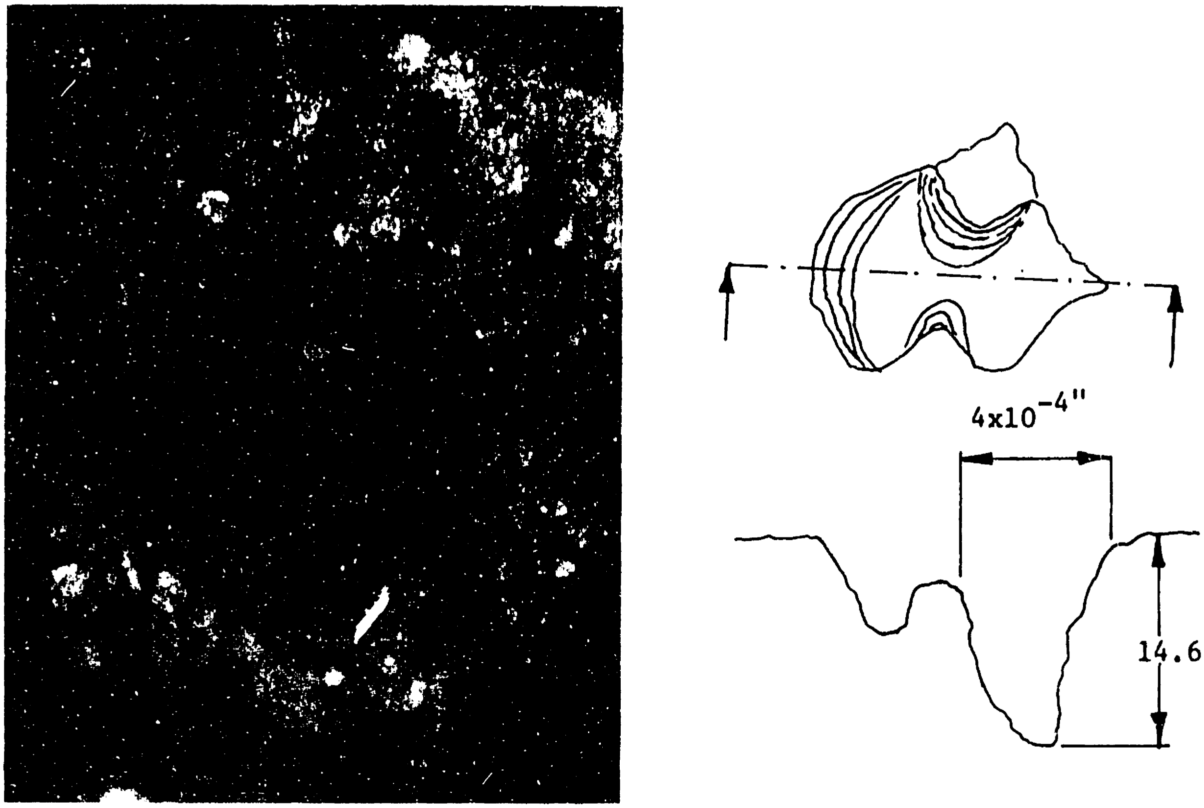

Fig. 35d: Photomicrograph of laser cavity #7 on laser Surface I at magnification x1000.

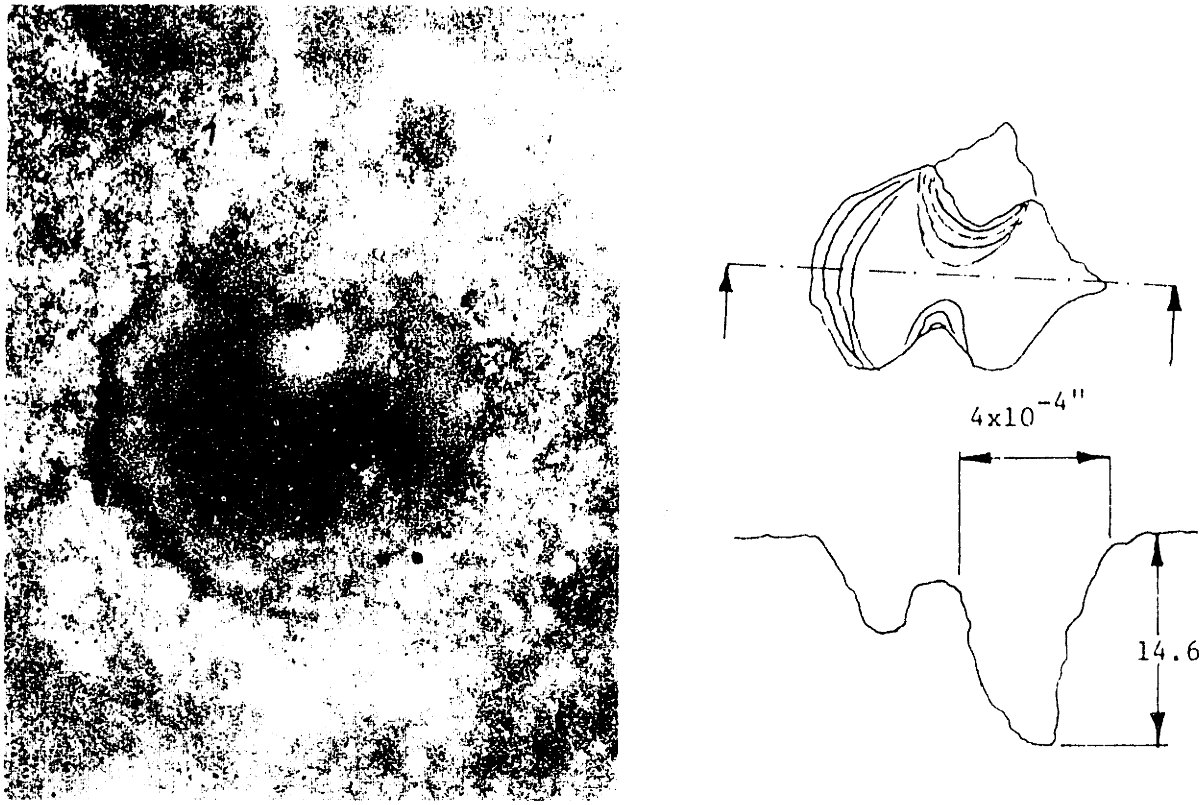

Fig. 35d: Photomicrograph of laser cavity #7 on laser Surface I at magnification x1000.

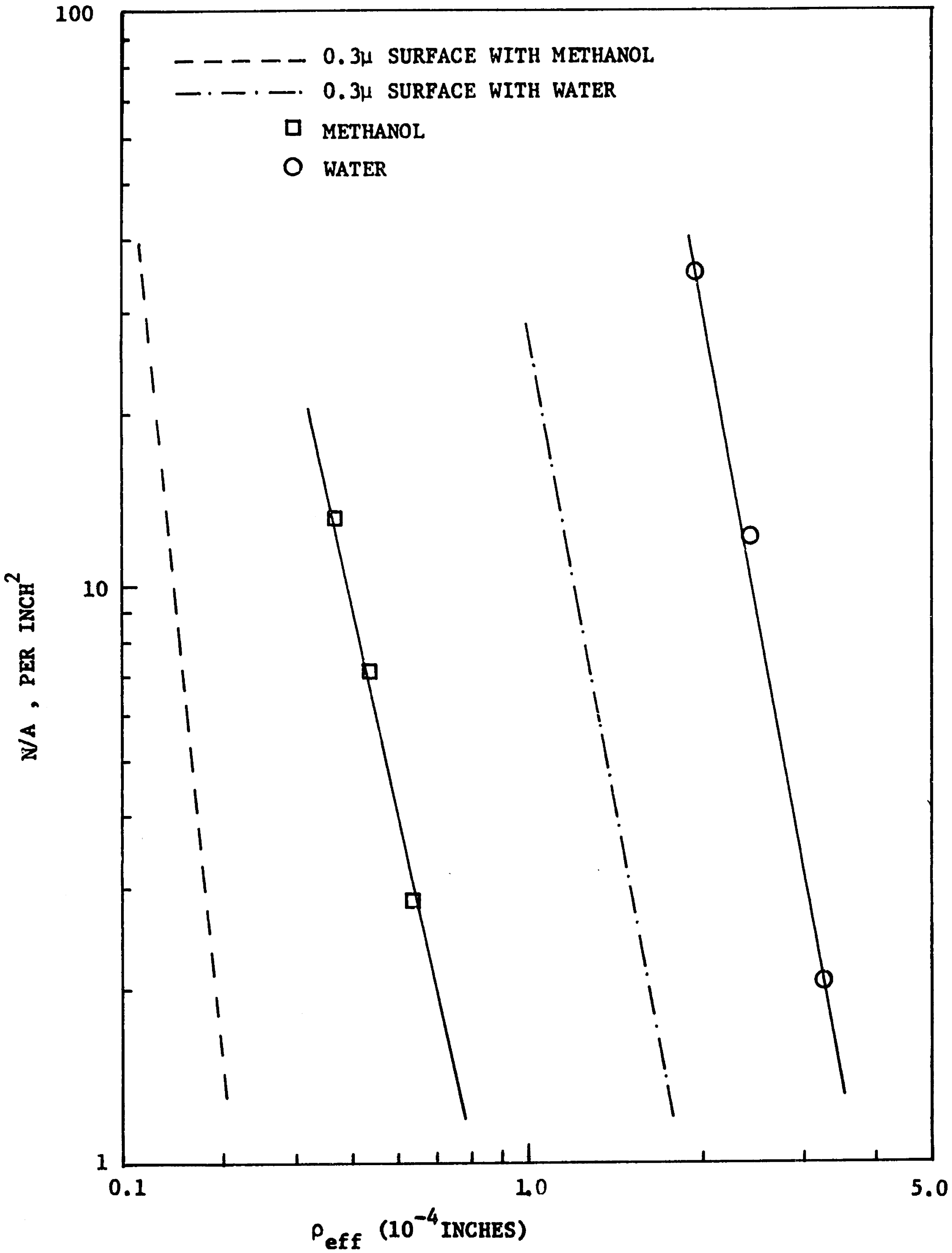

Fig. 36a: Cumulative site density vs. effective cavity size for Surface II, having laser drilled cavities.

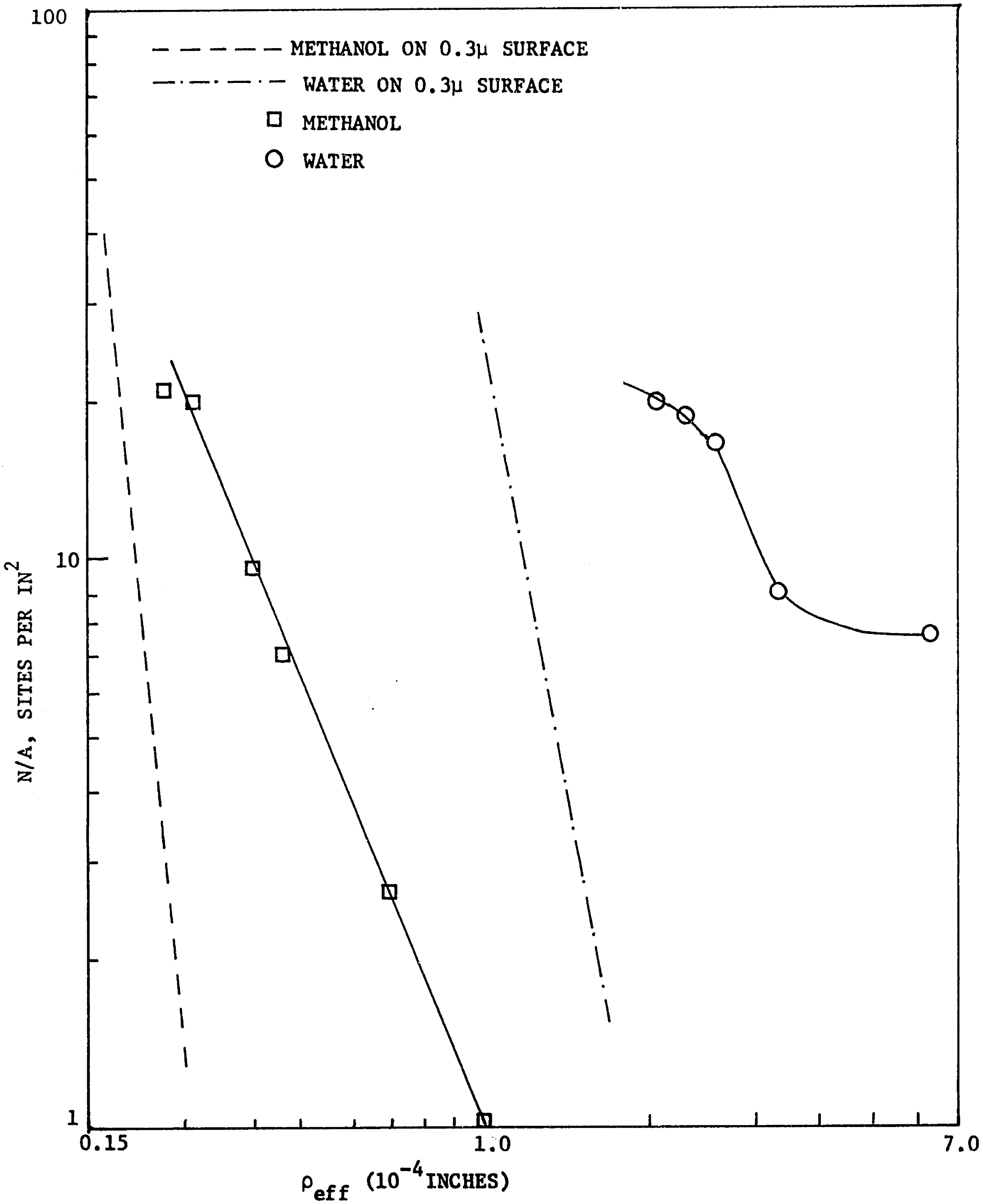

Fig. 36b: N/A vs. ρ_{eff} characteristics of the boiling Surface III, having laser drilled cavities.

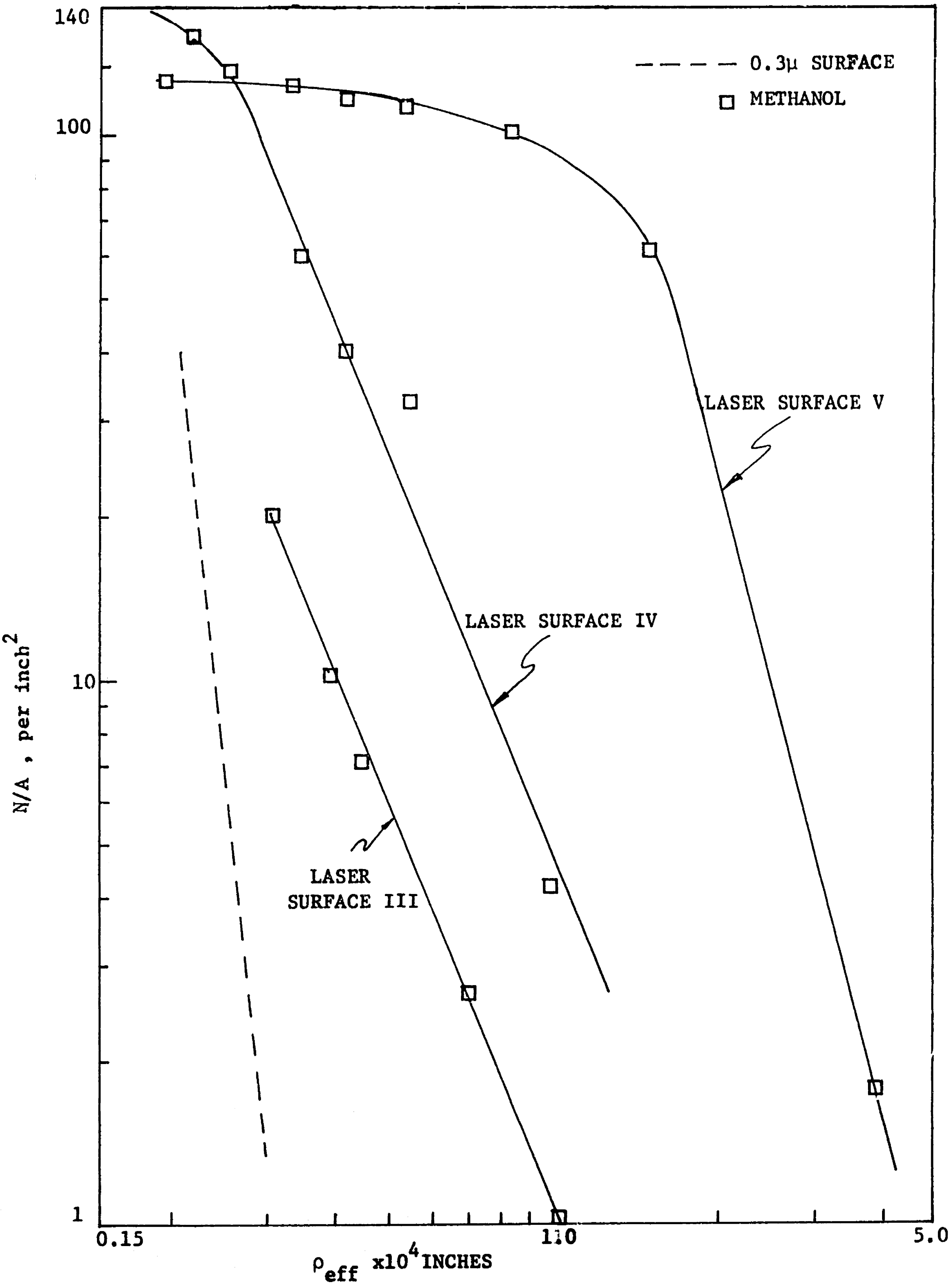

Fig. 37: Cumulative site density vs. effective cavity size for Surfaces III, IV,V,having laser drilled cavities in boiling with methanol.

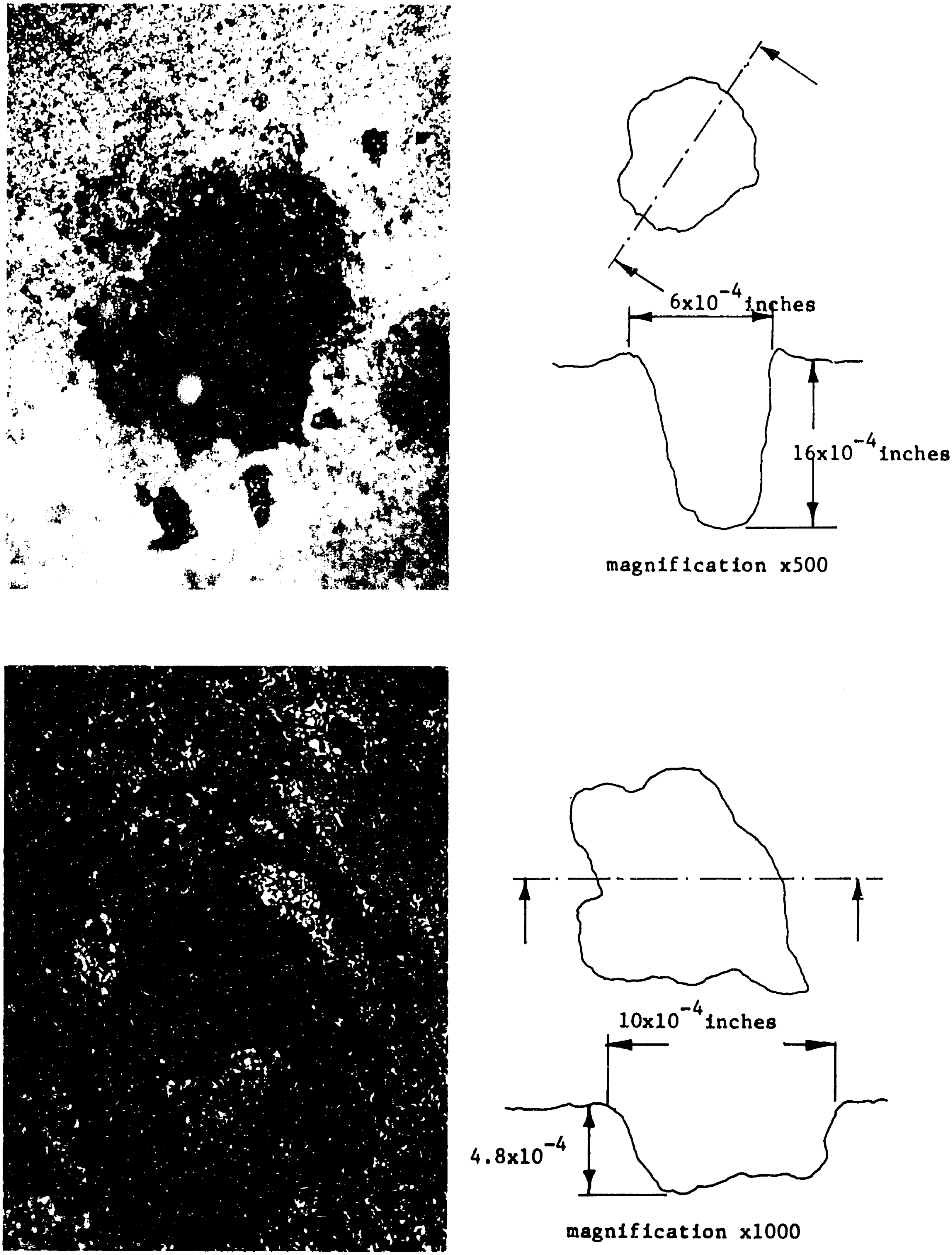

Fig. 38: Photomicrographs of two typical cavities on Surface II and III.

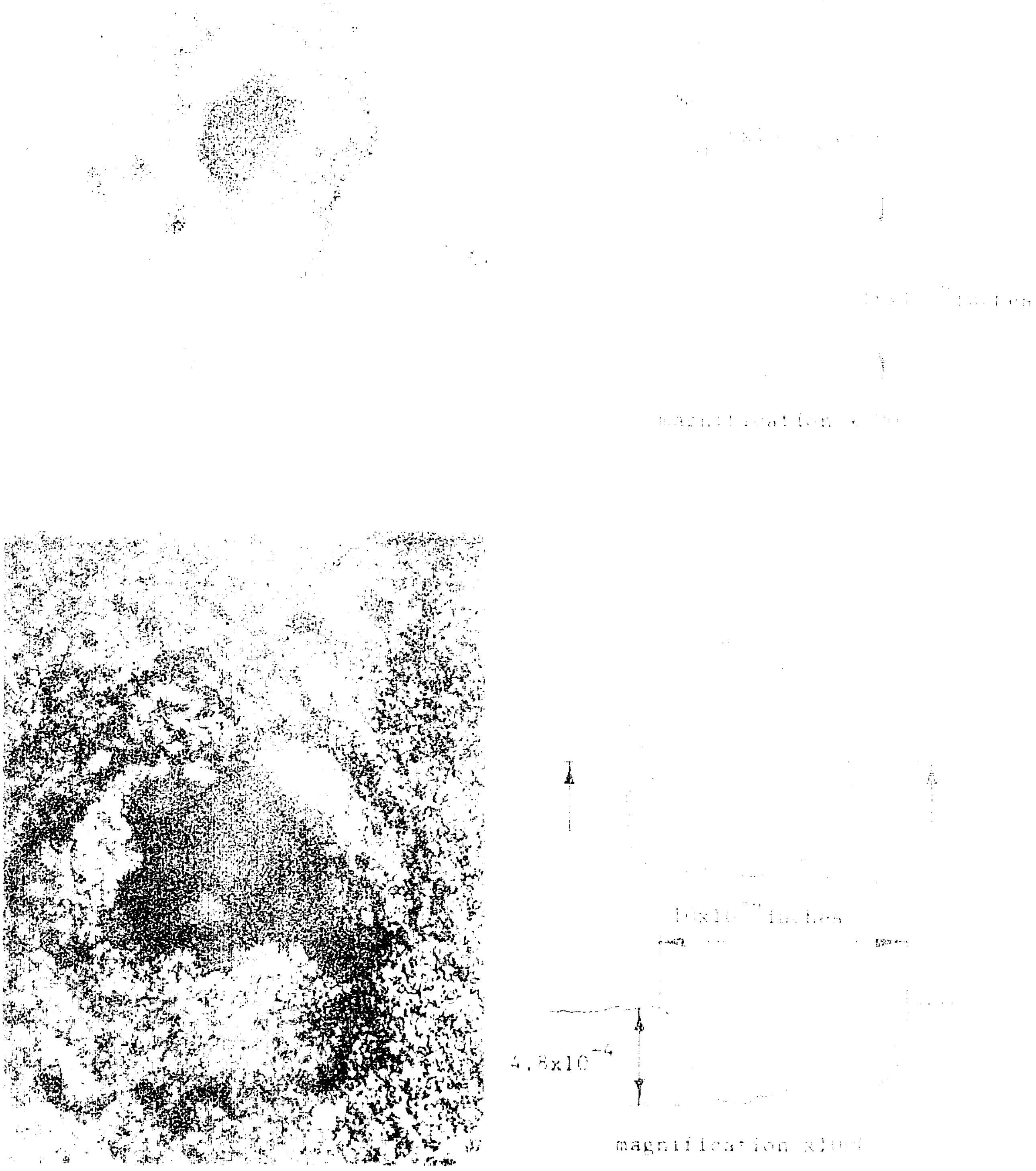

Fig. 38: Photomicrographs of two typical cavities on Surface II and III.

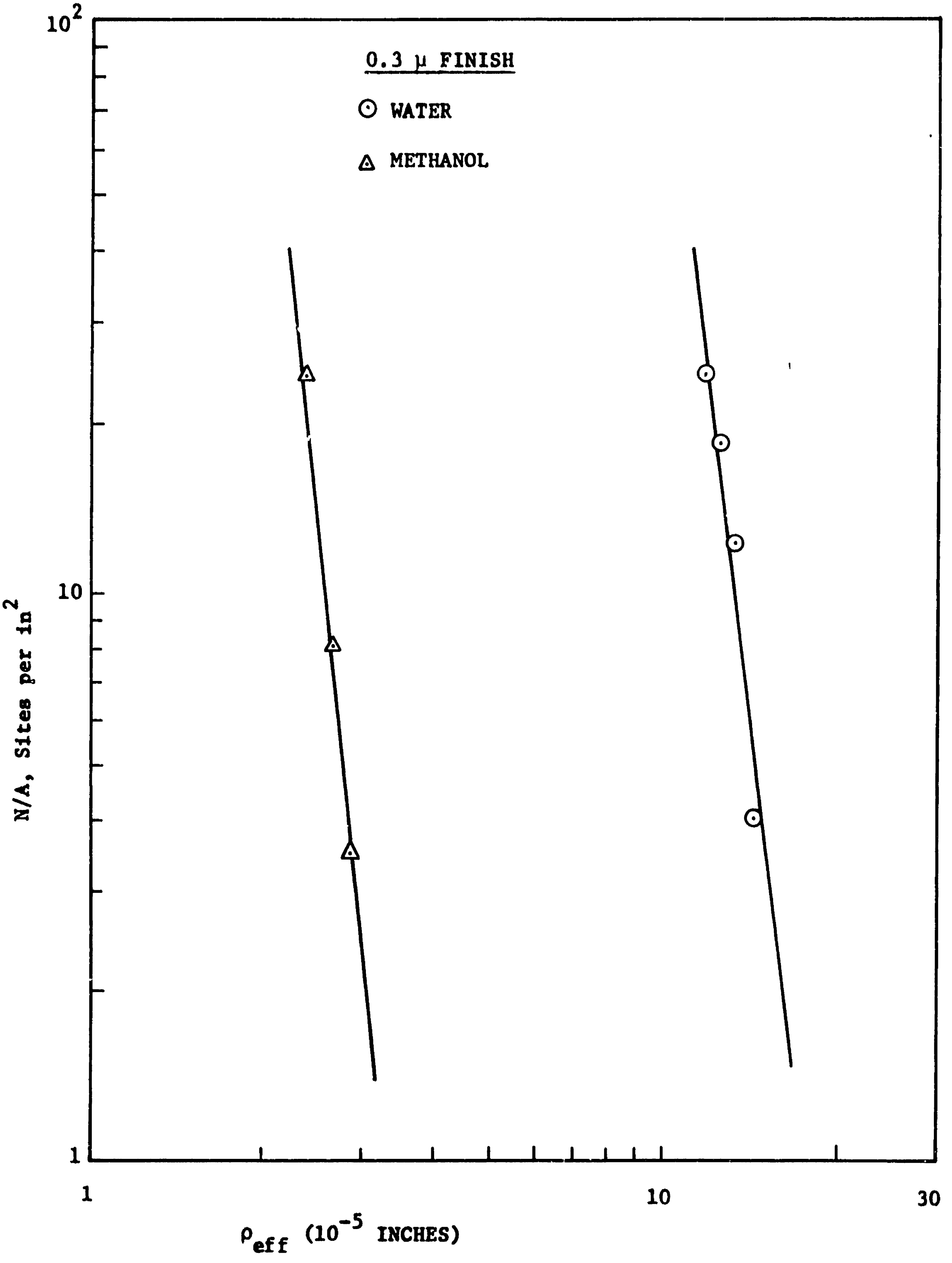

Fig. 39a: Cumulative site density distribution for water and methanol.

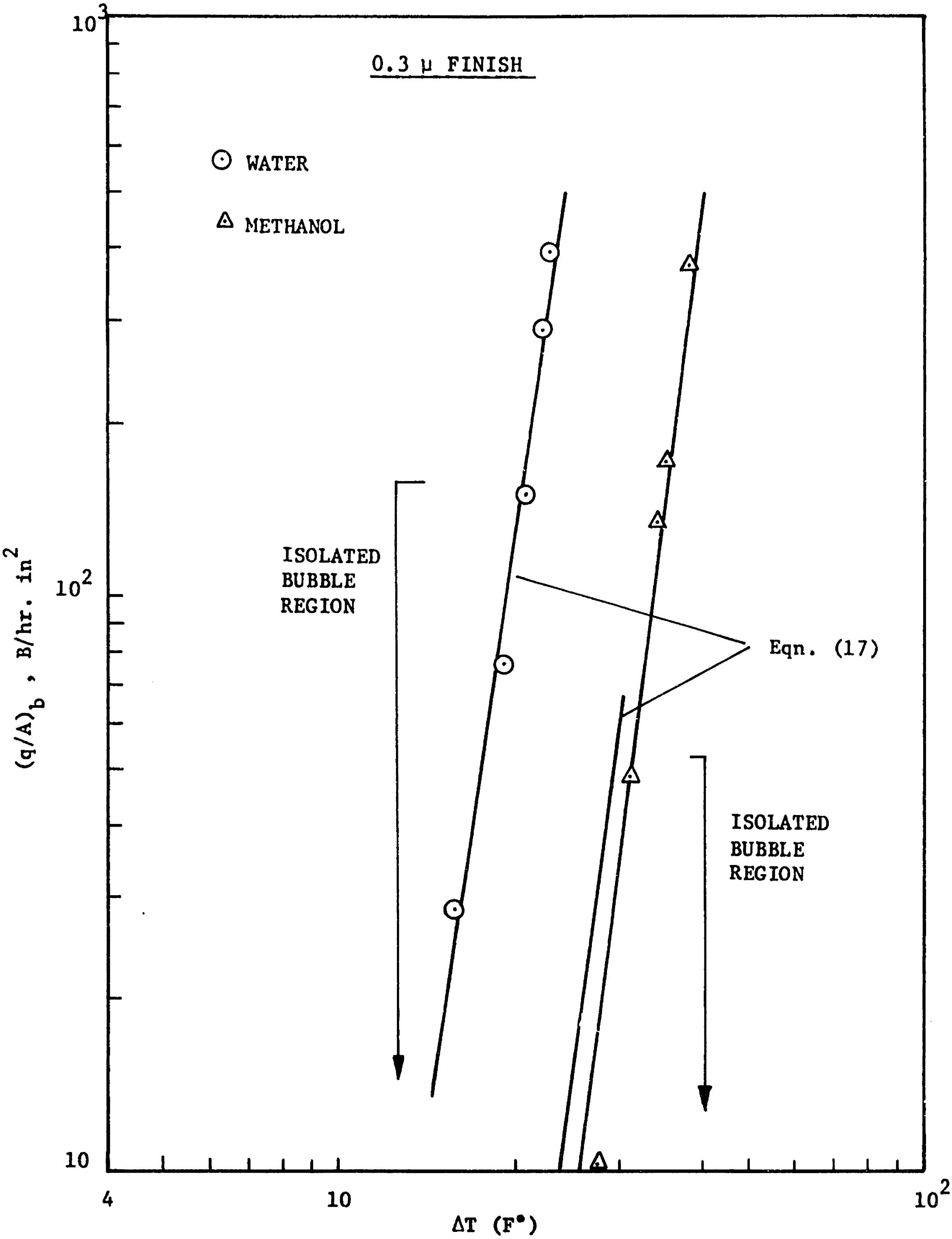

Fig. 39b: Comparison of the predicted and measured boiling heat flux.

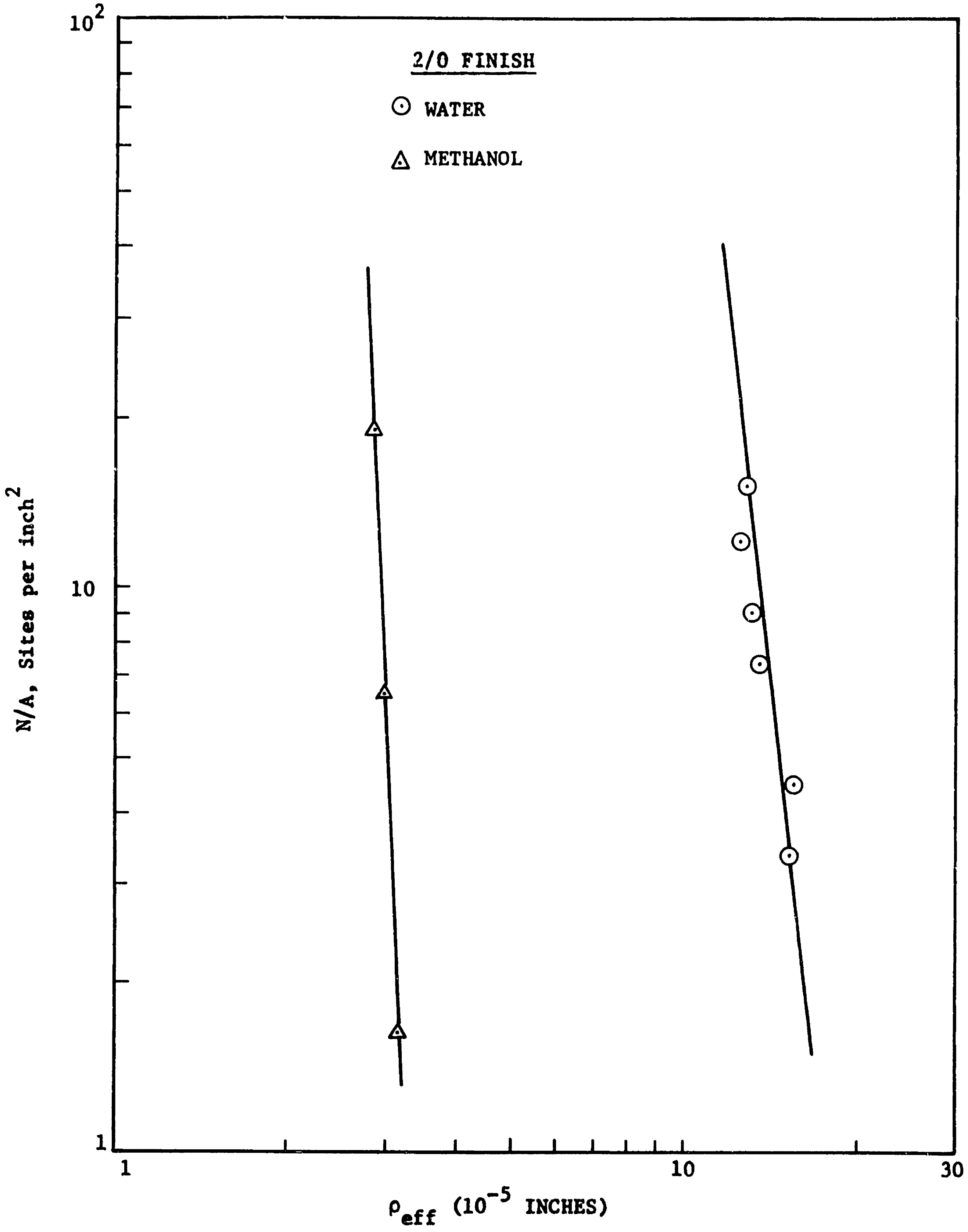

Fig. 40a: Cumulative site density distribution for water and methanol.

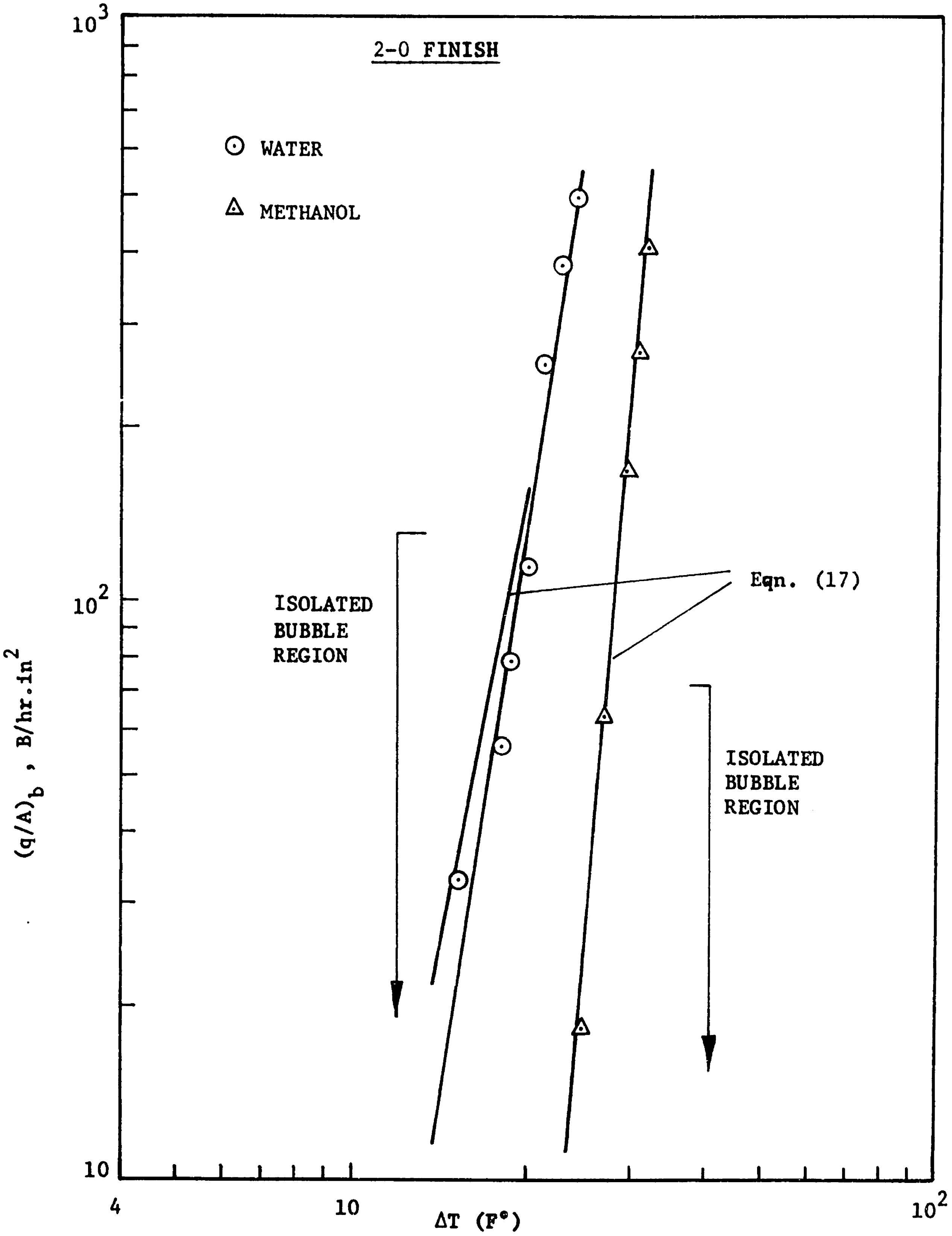

Fig. 40b: Comparison of the measured and predicted boiling heat flux.

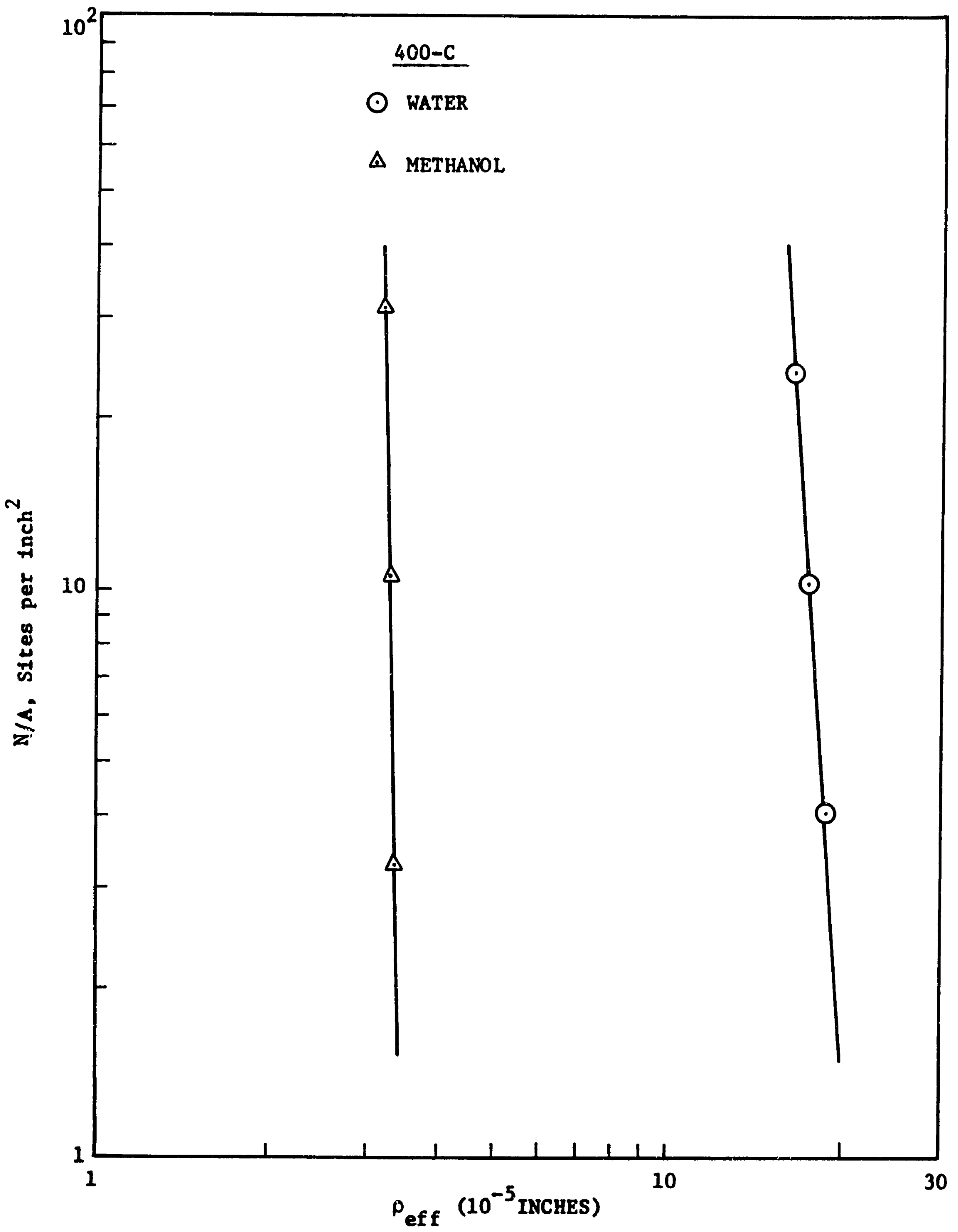

Fig. 41a: Cumulative site density distribution for water and methanol.

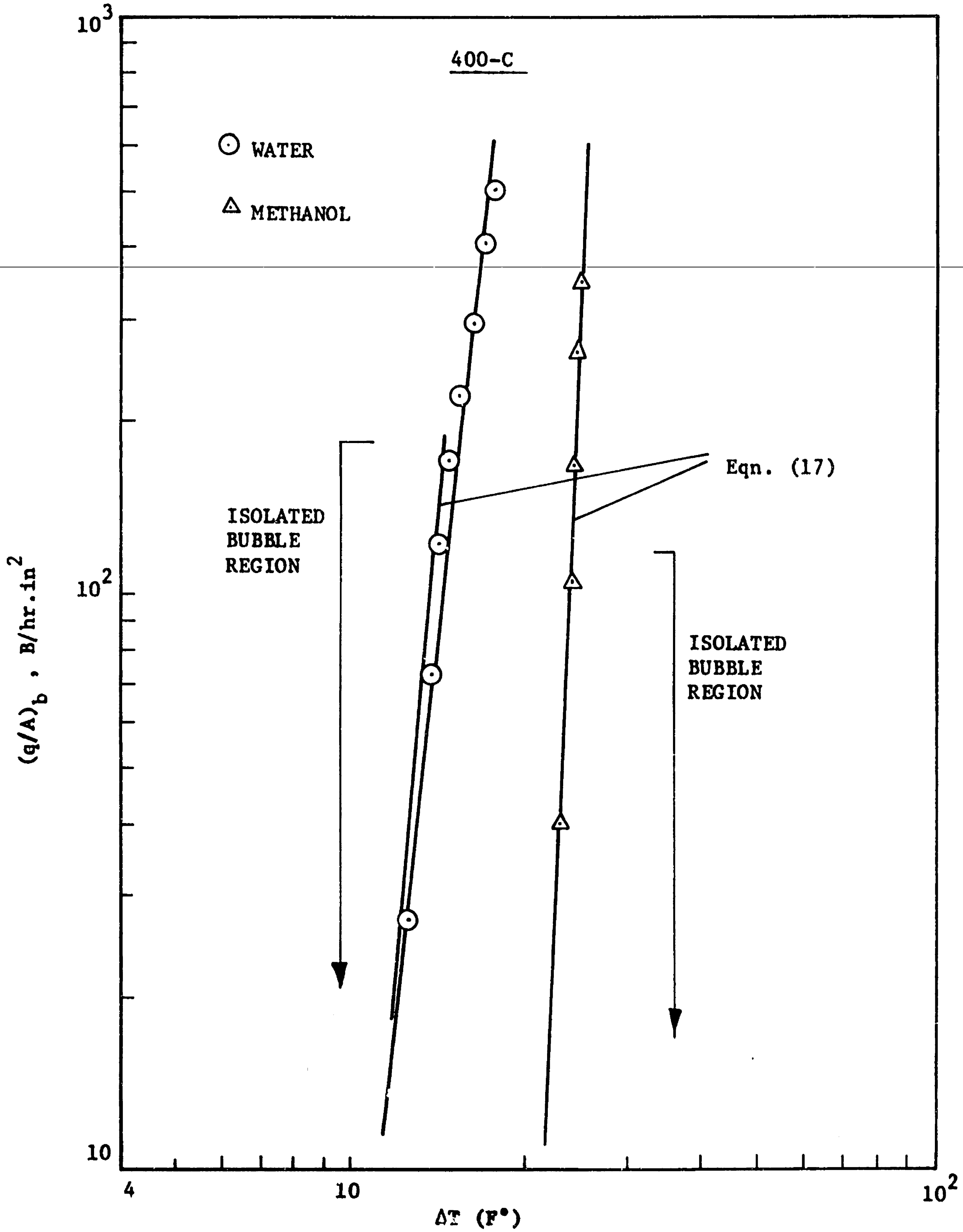

Fig. 41b: Comparison of the predicted and measured boiling heat-flux.

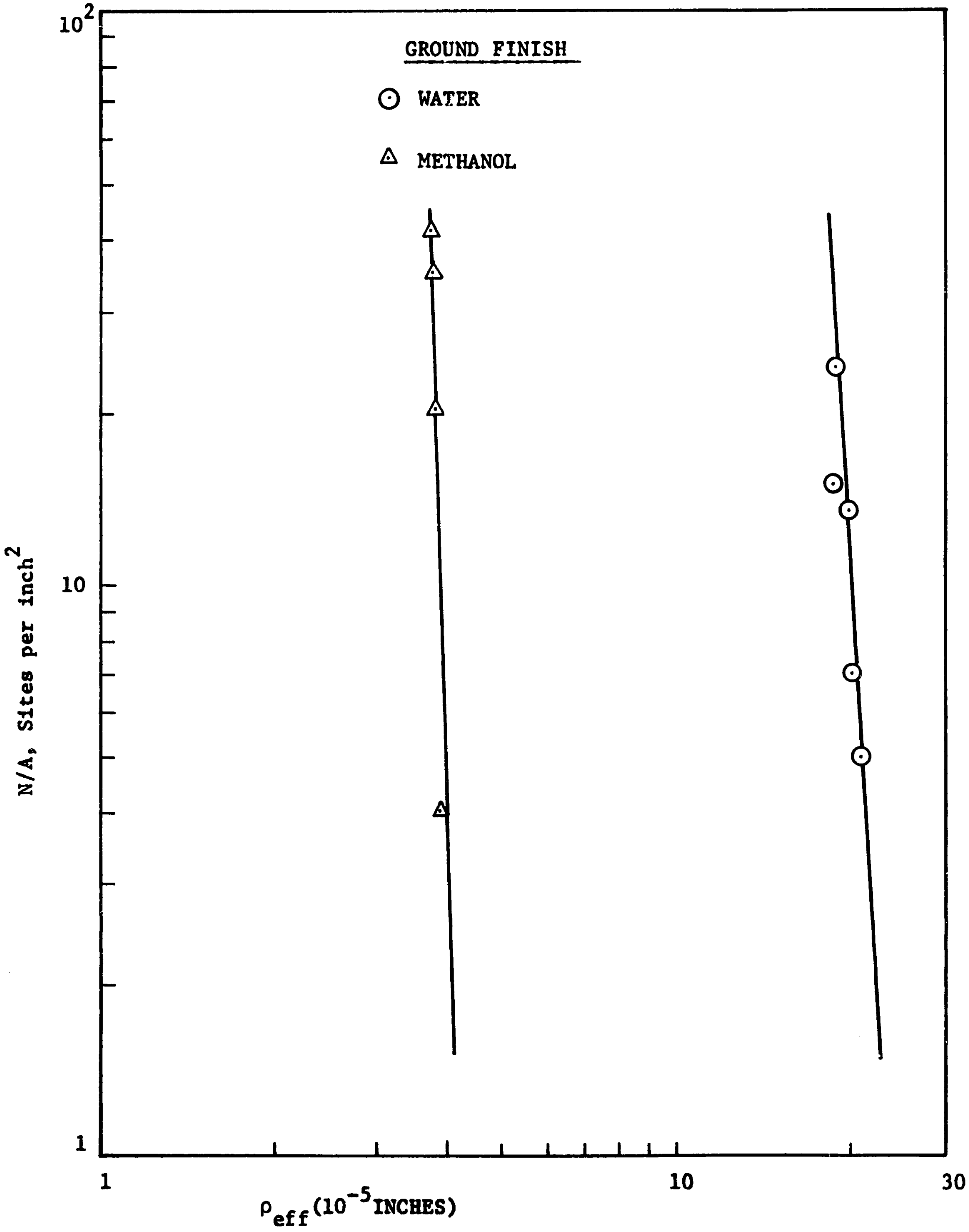

Fig. 42a: Cumulative site density distribution for water and methanol.

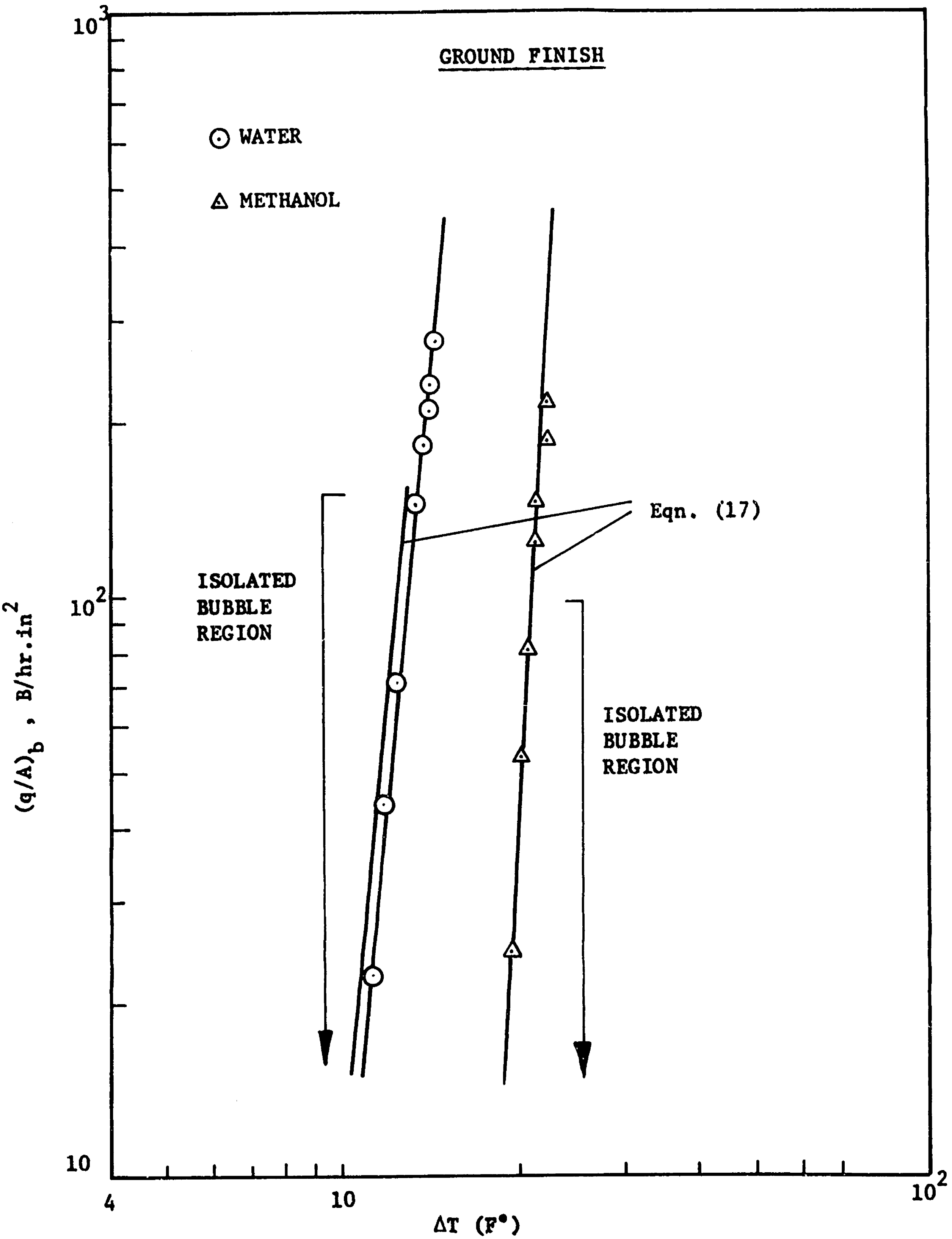

Fig. 42b: Comparison of the predicted and measured boiling heat-flux.

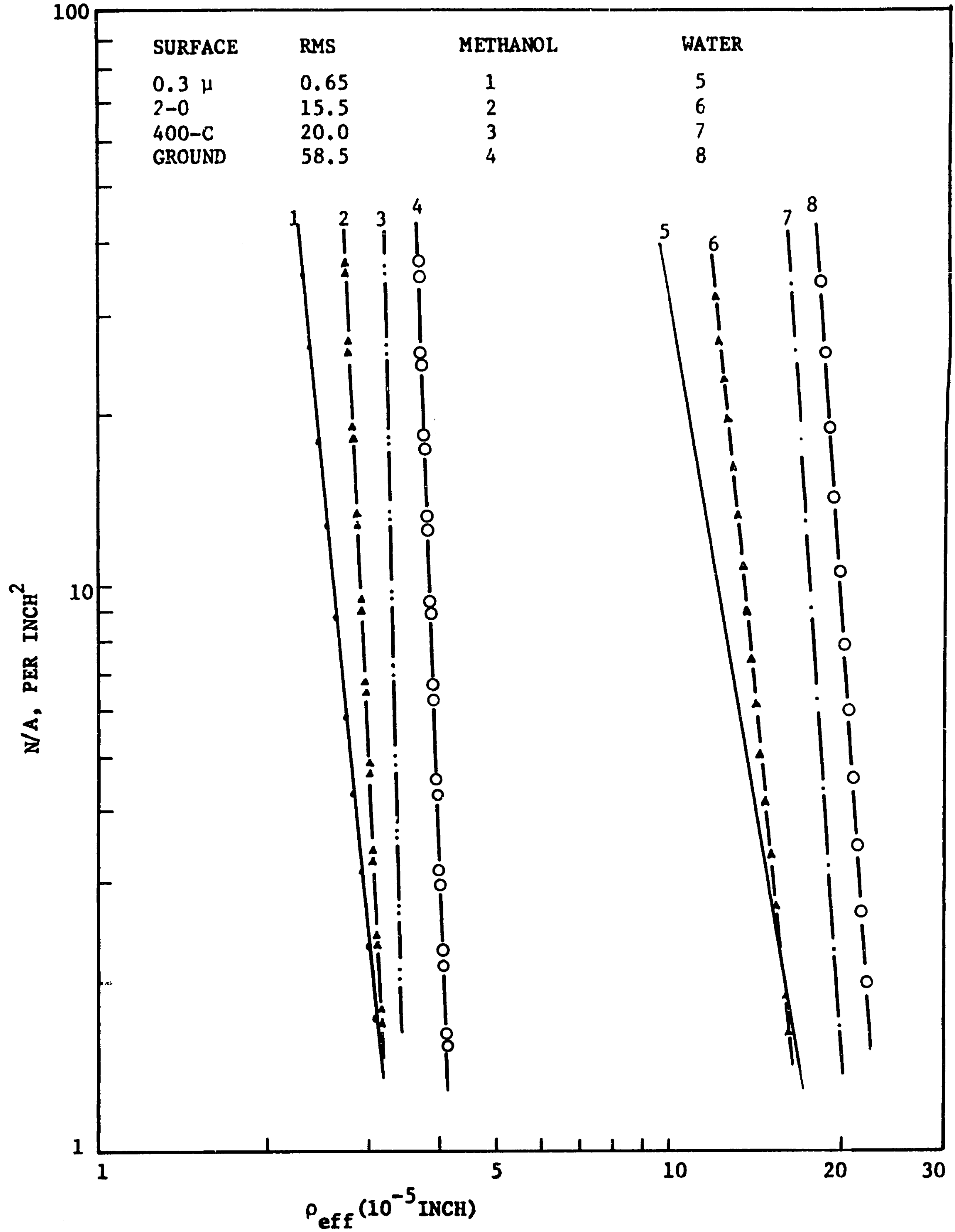

Fig. 43: Cumulative site density curves for water and methanol.

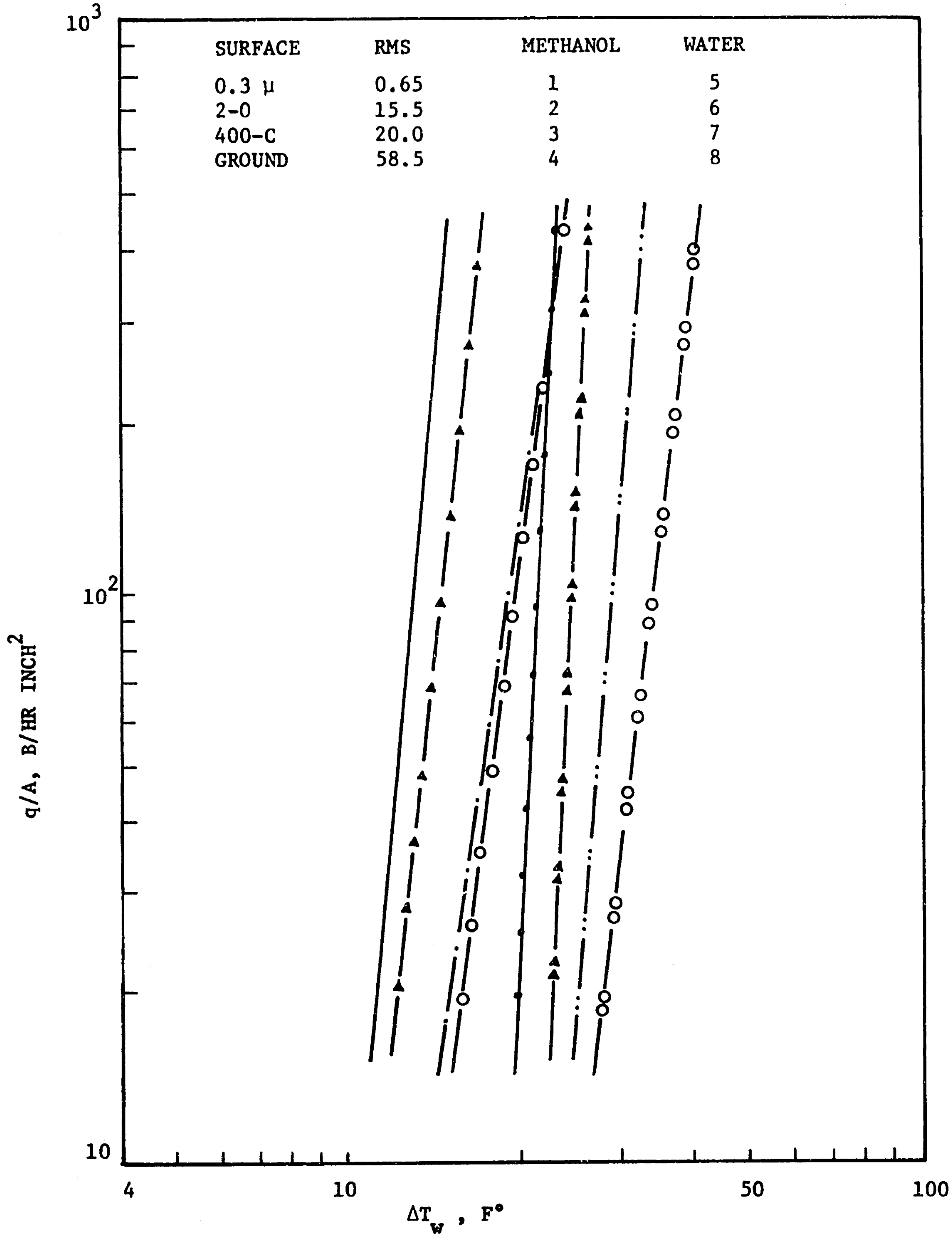

Fig. 44: Boiling curves for water and methanol.

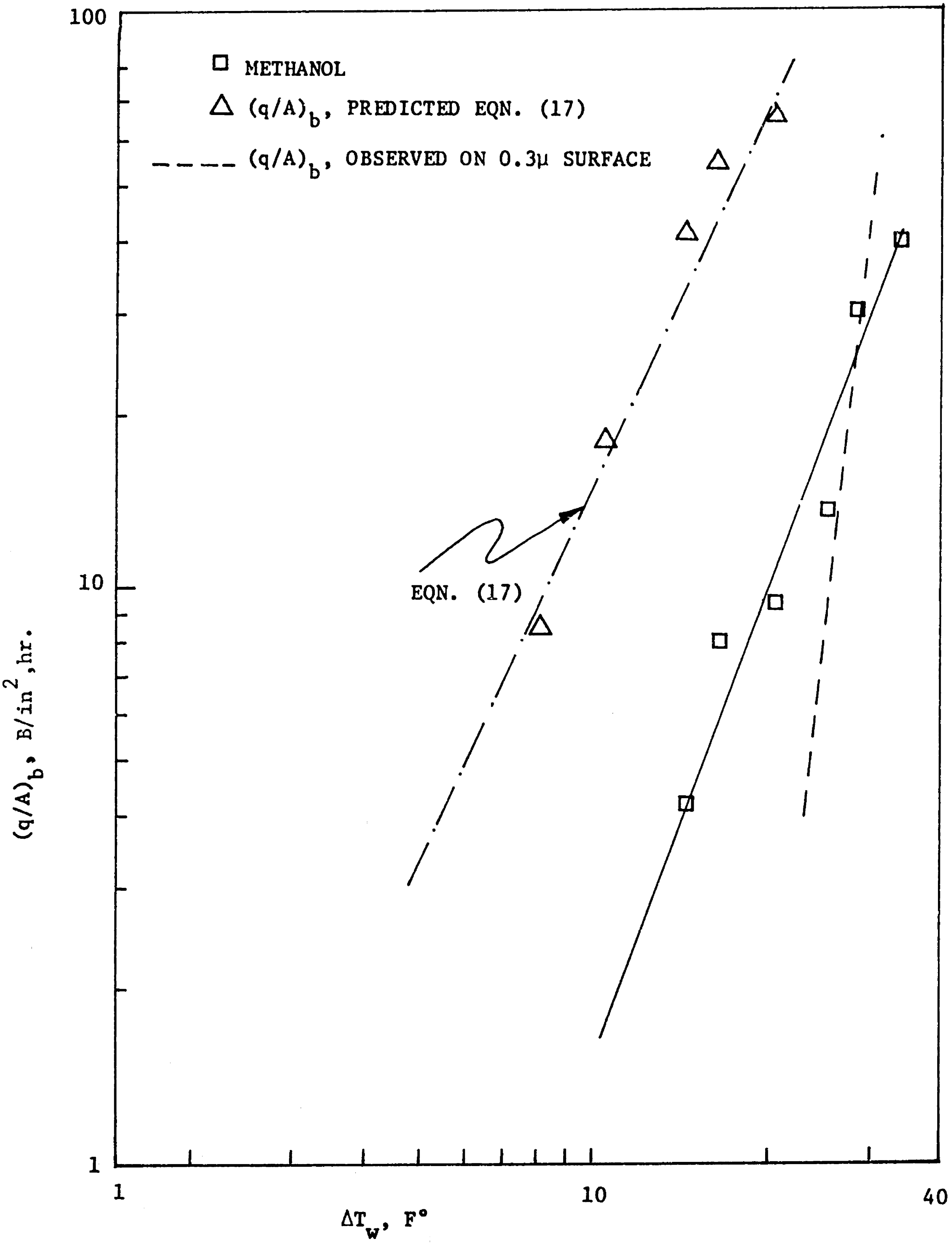

Fig. 45a: Boiling curve for methanol on laser Surface I.

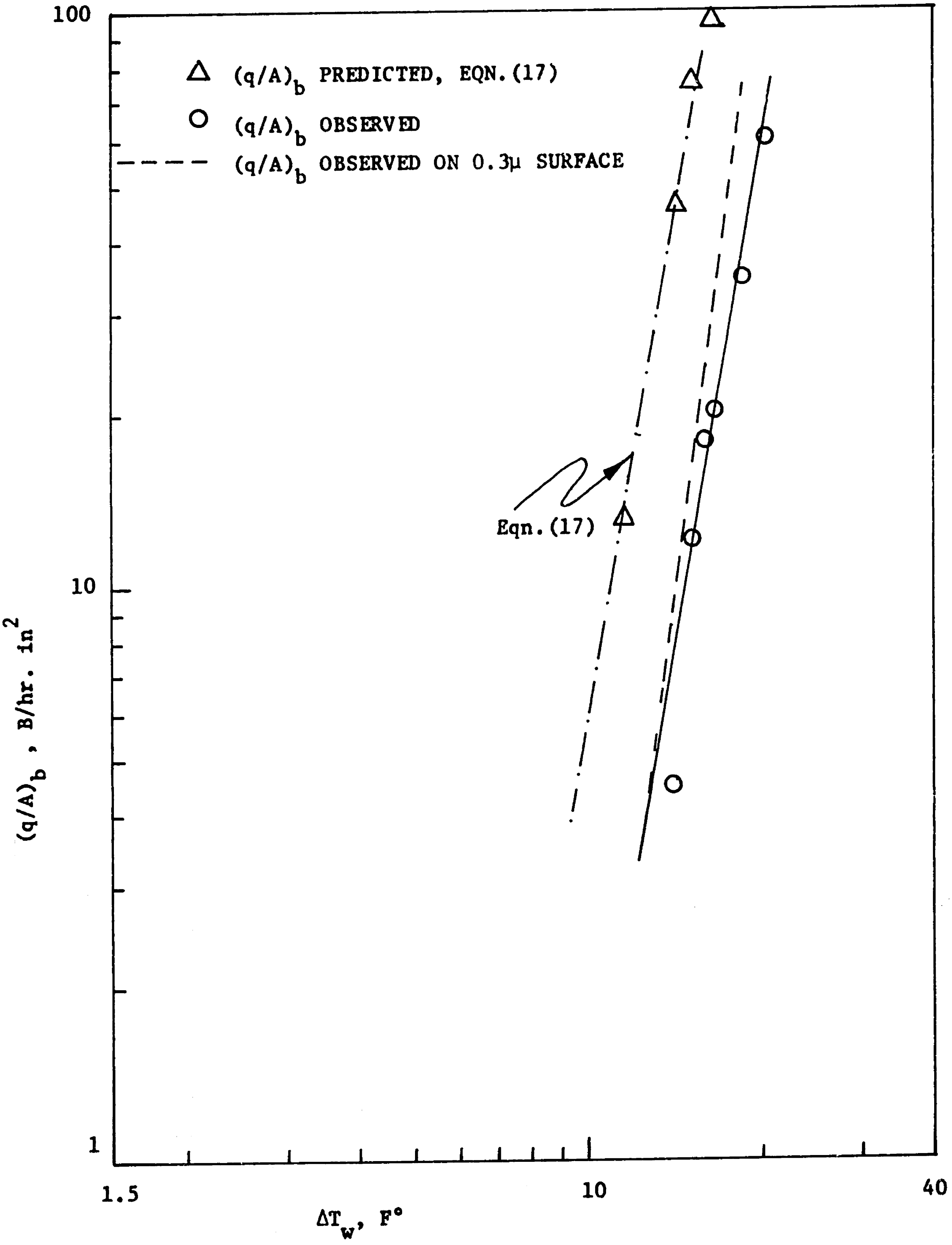

Fig. 45b: Boiling curve for water on laser Surface I.

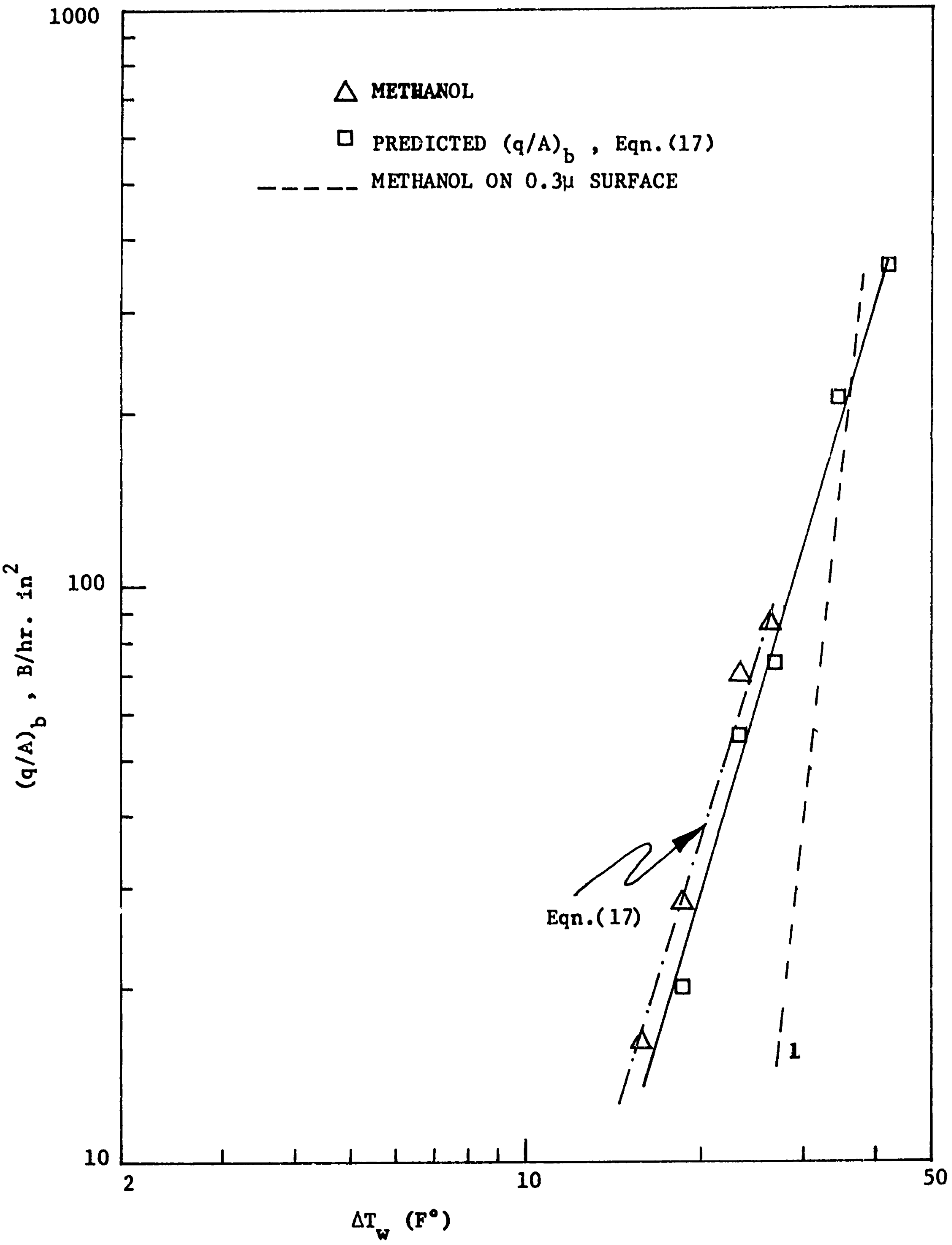

Fig. 46a: Boiling curve for methanol for laser Surface III.

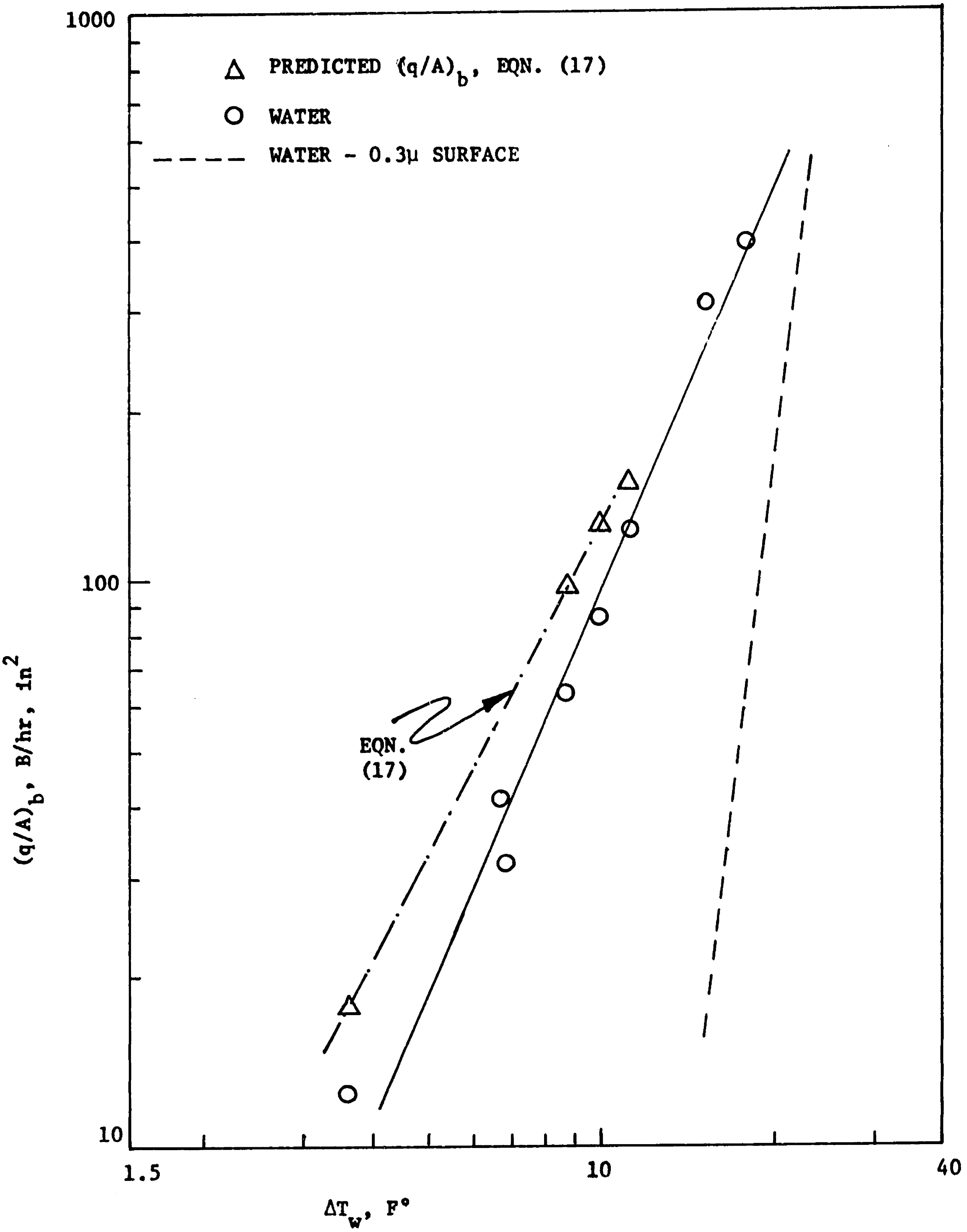

Fig. 46b: Boiling curve for water on laser Surface III.

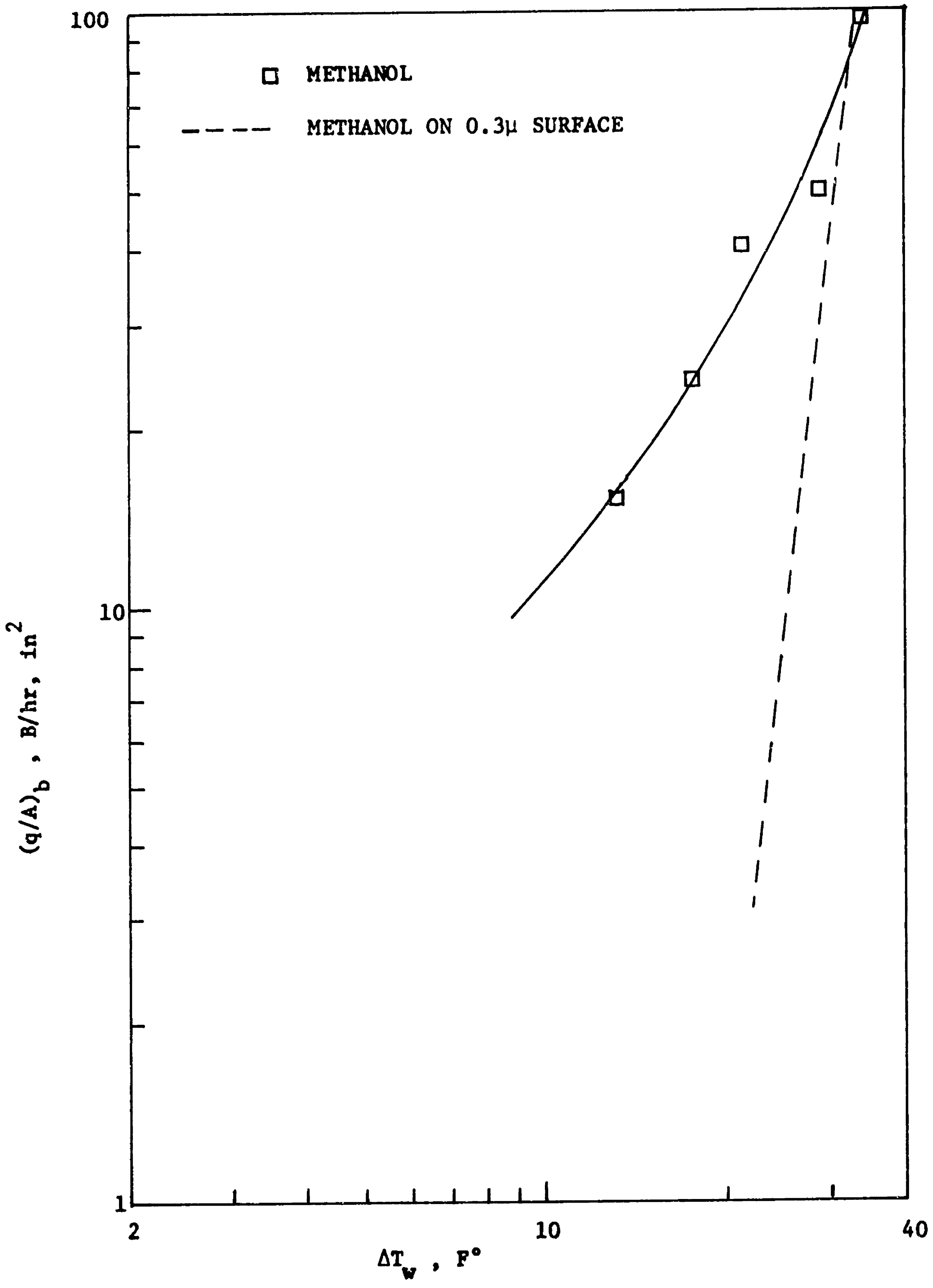

Fig. 47: Boiling curve for methanol on laser surface IV.

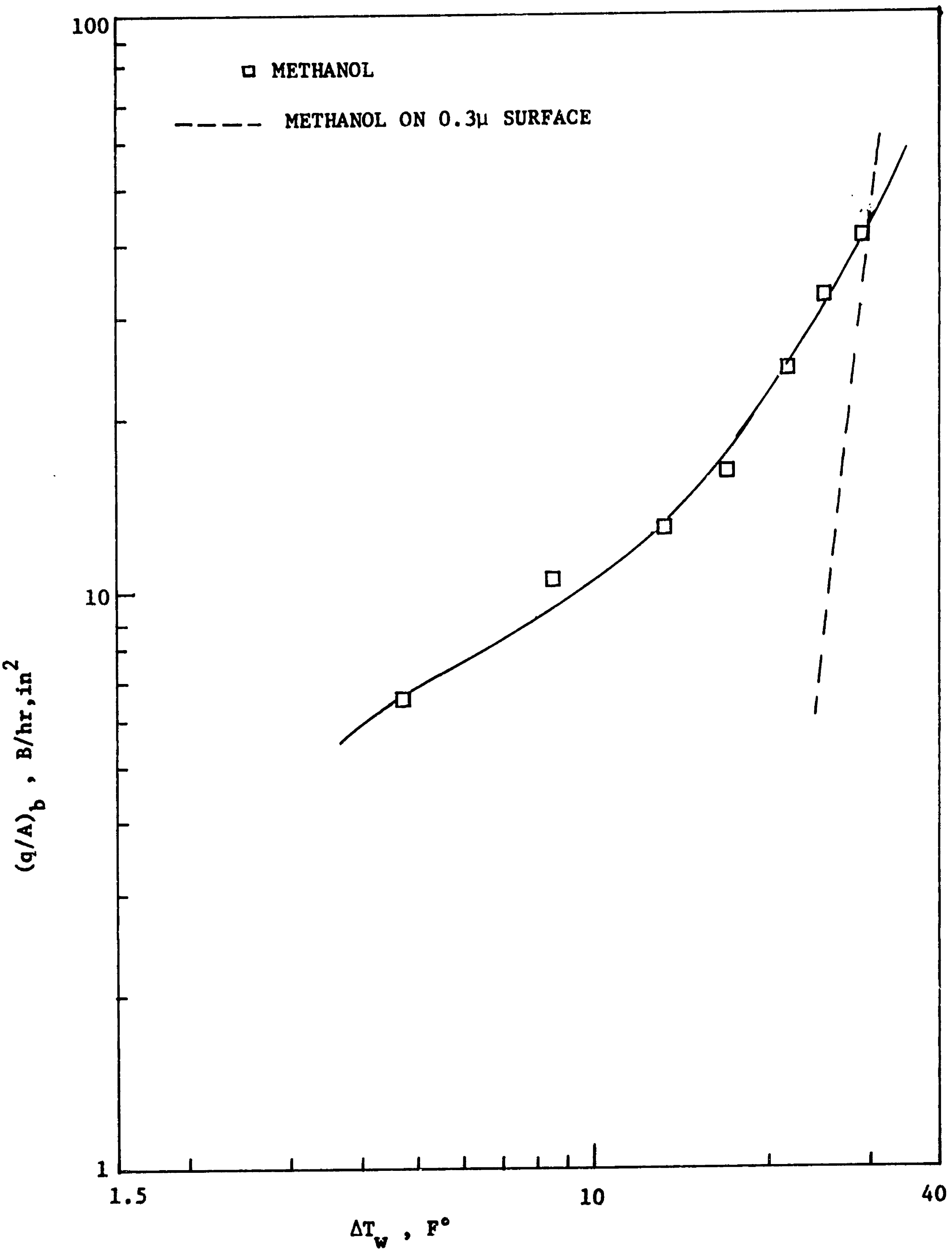

Fig. 48: Boiling Curve for Methanol on Laser Surface V.

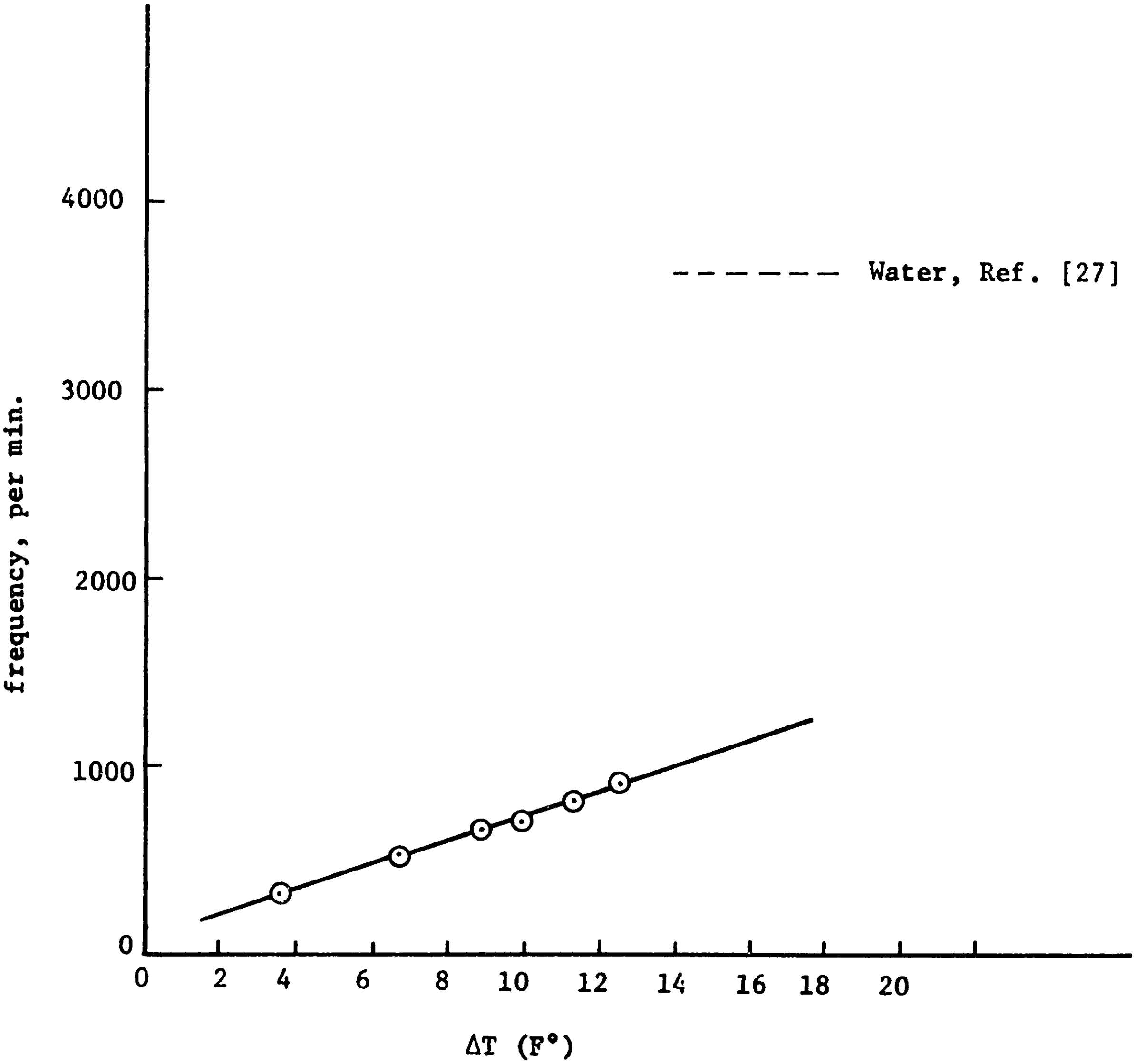

Fig. 49: Frequency of bubble departures vs. superheat from laser cavities in boiling with water on laser Surface III.

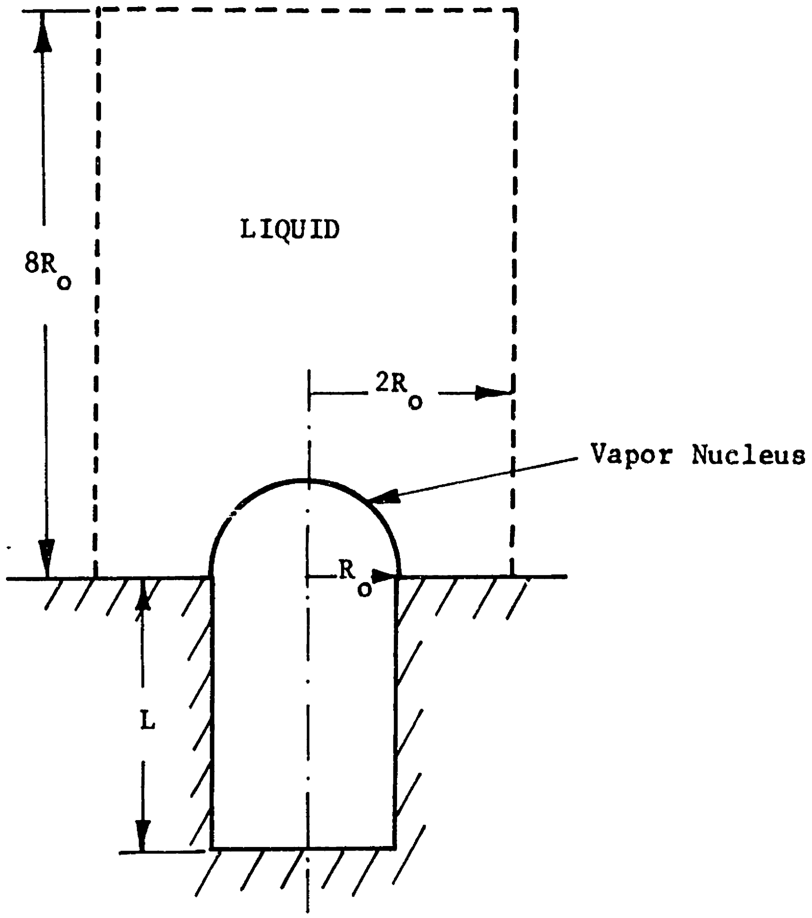

Fig. 50a

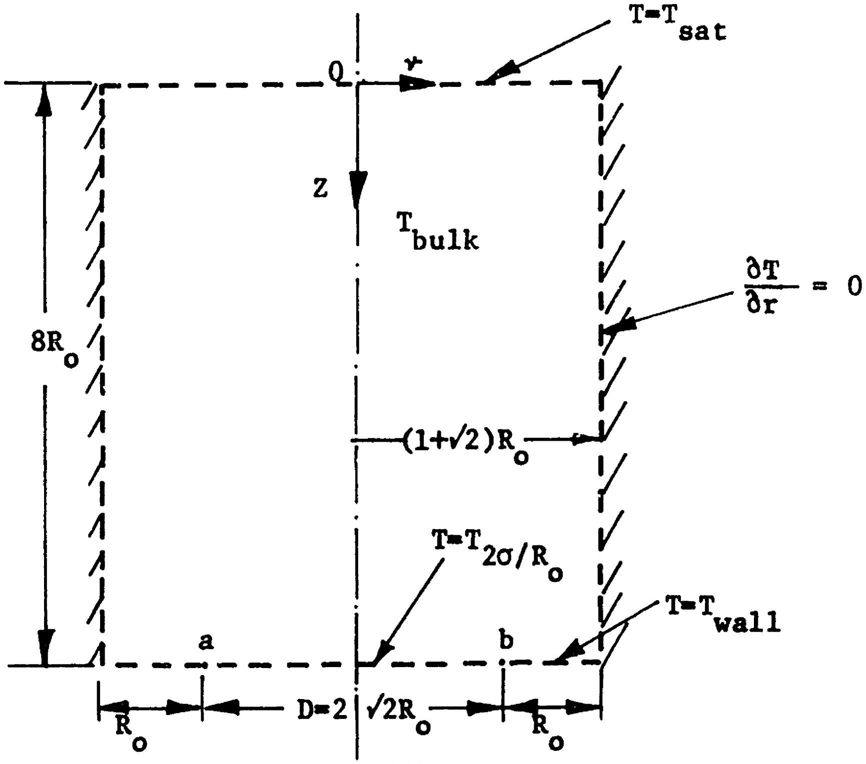

Fig. 50b

Fig. 50: Sketch of Theoretical Model for Prediction of Waiting time, t_w.

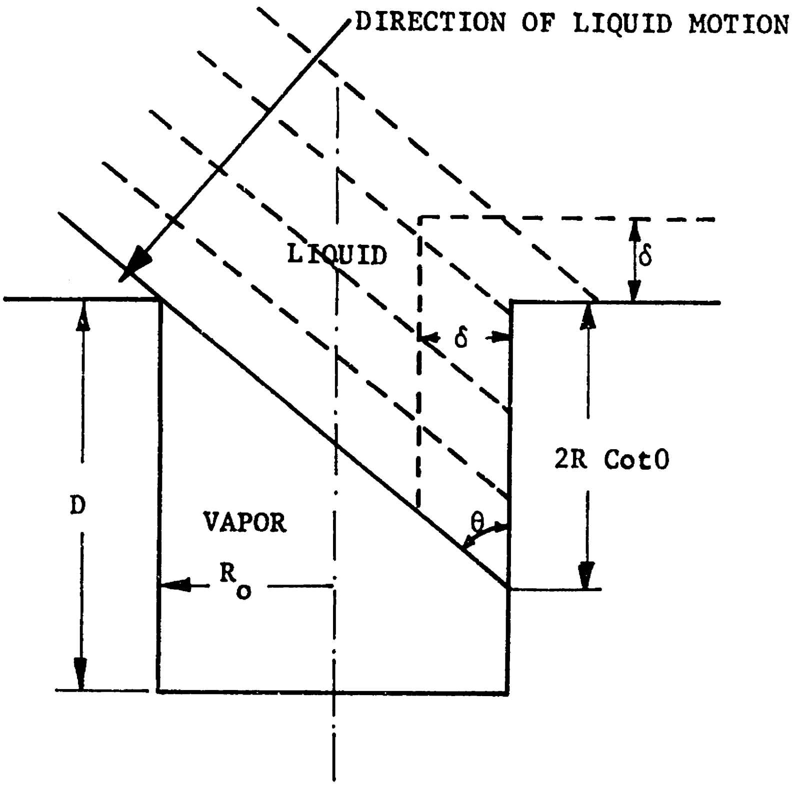

Fig. 51: Sketch of the postulated model to evaluate the initial liquid temperature.

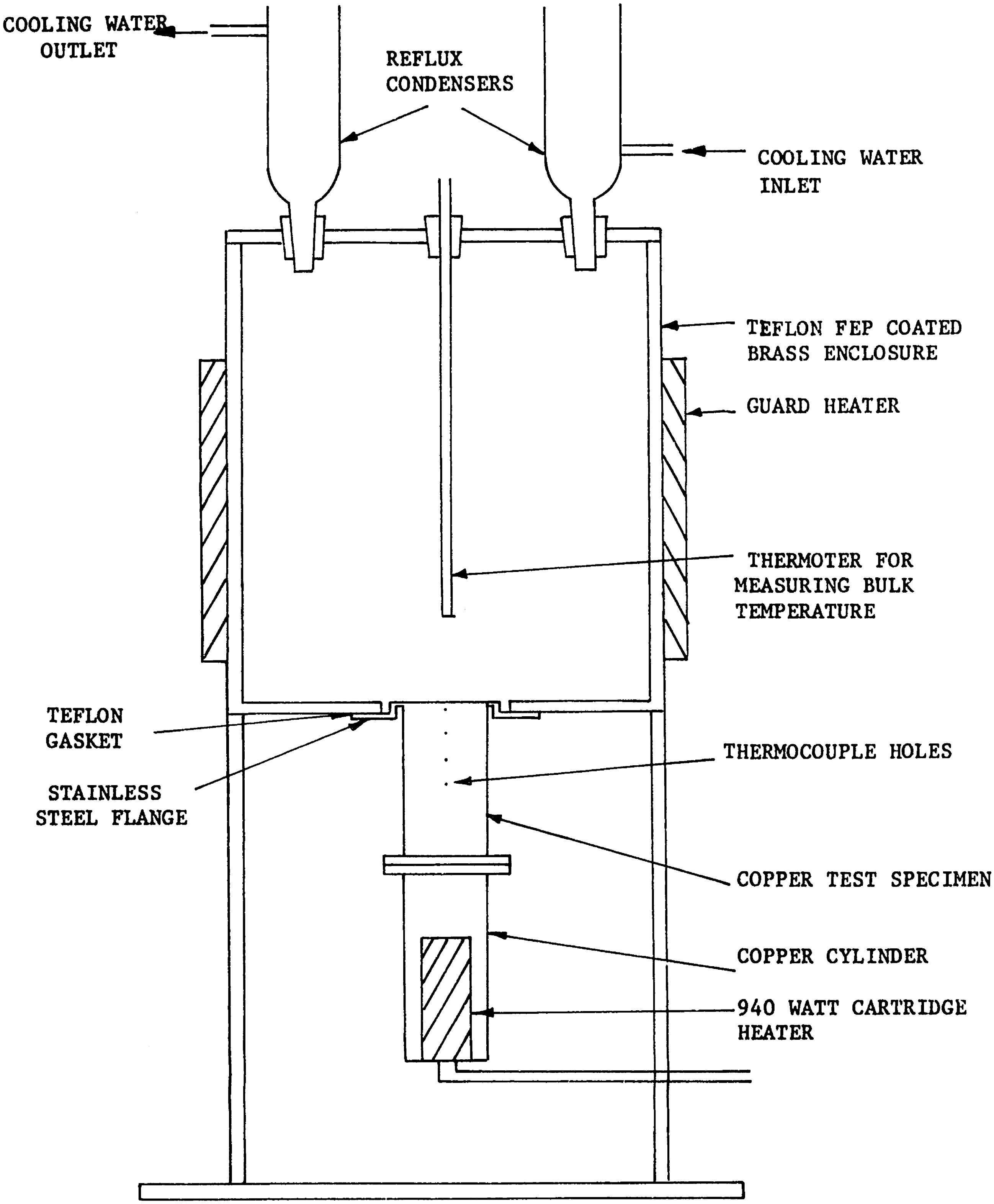

Fig. 52: Sketch of the boiling apparatus.

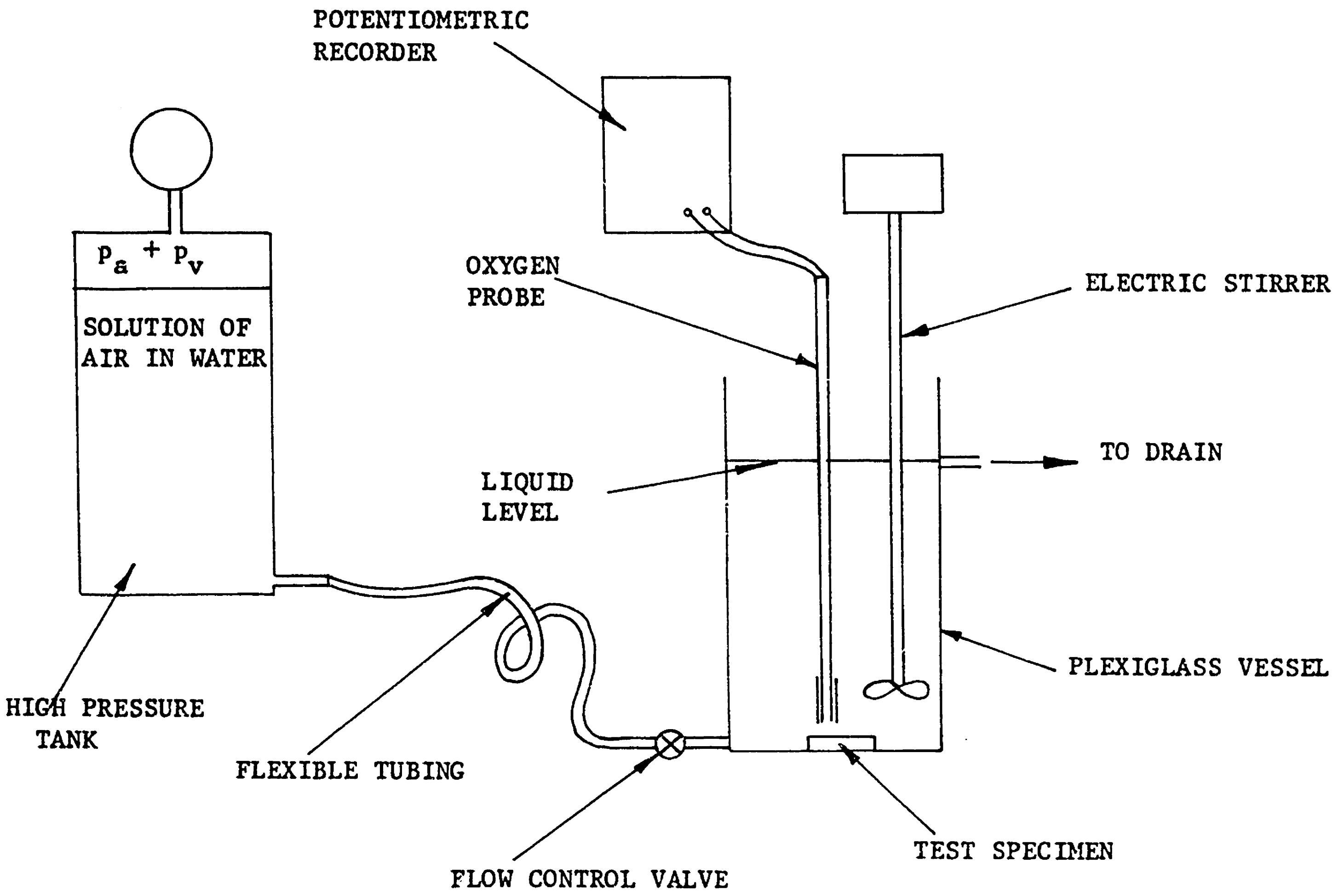

Fig. 53: Sketch of the open system gas diffusion apparatus.

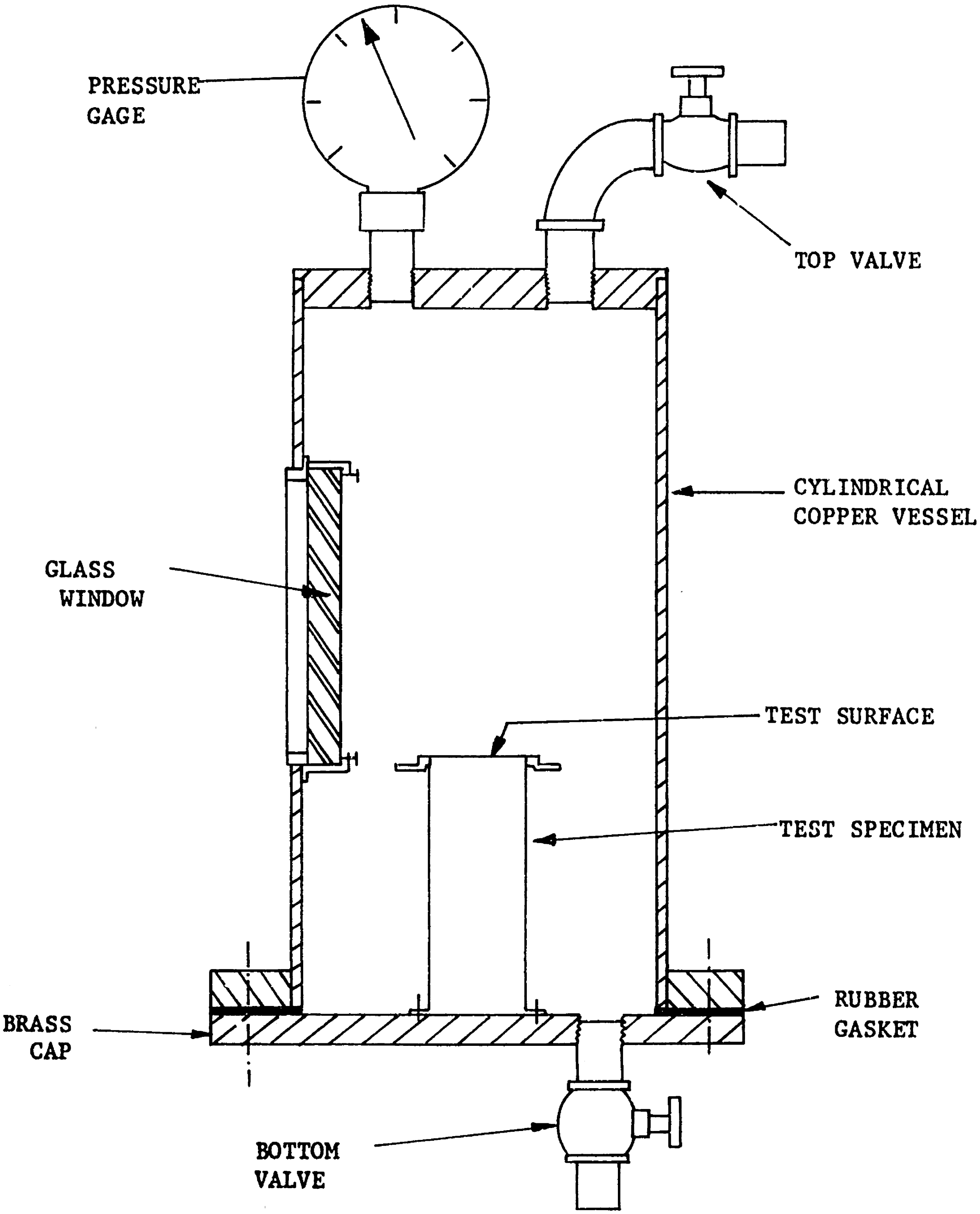

Fig. 54: Sketch of the closed system gas diffusion apparatus.

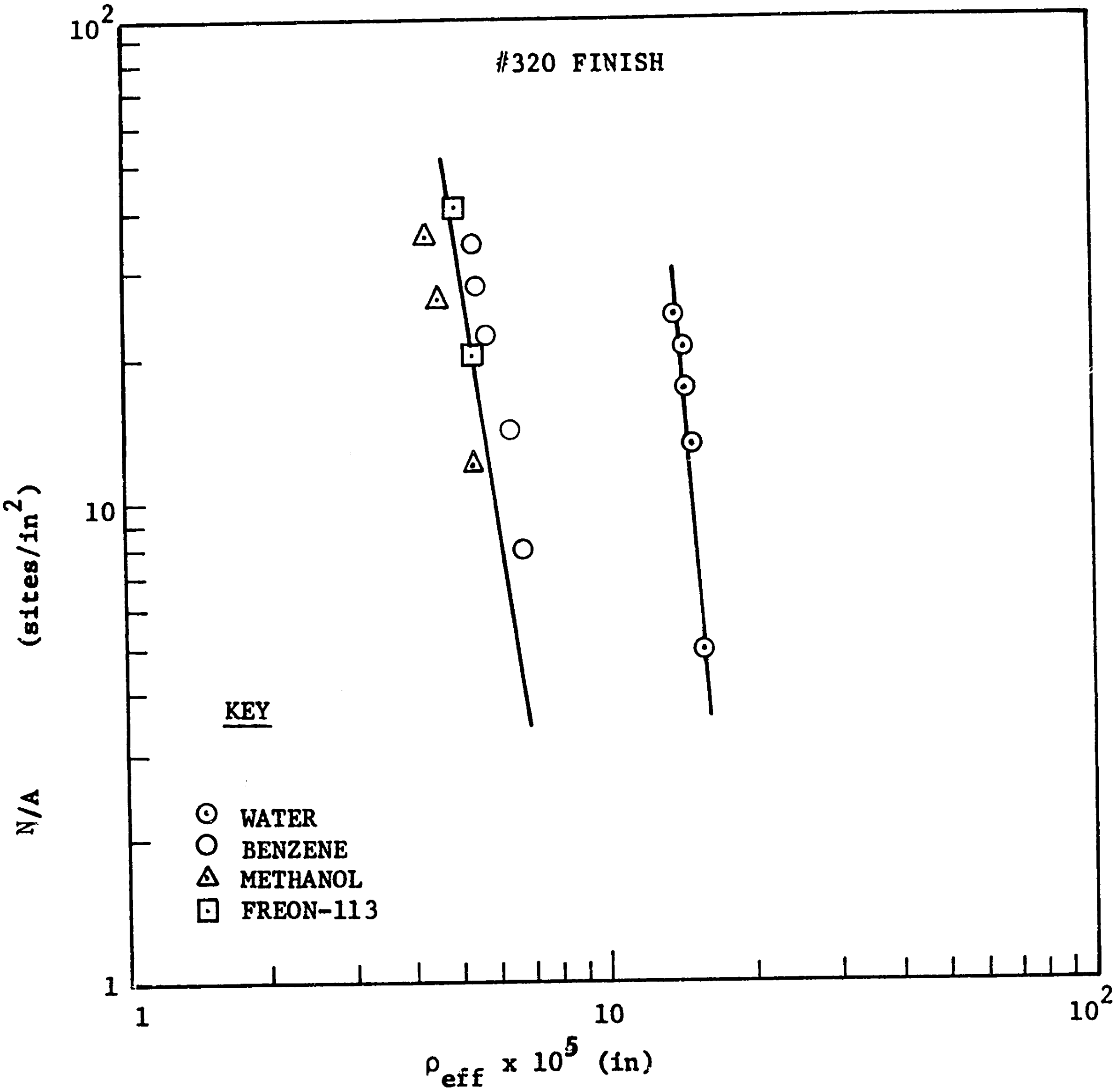

Fig. 55a: Cumulative site density distribution for water and organics, Ref. [18].

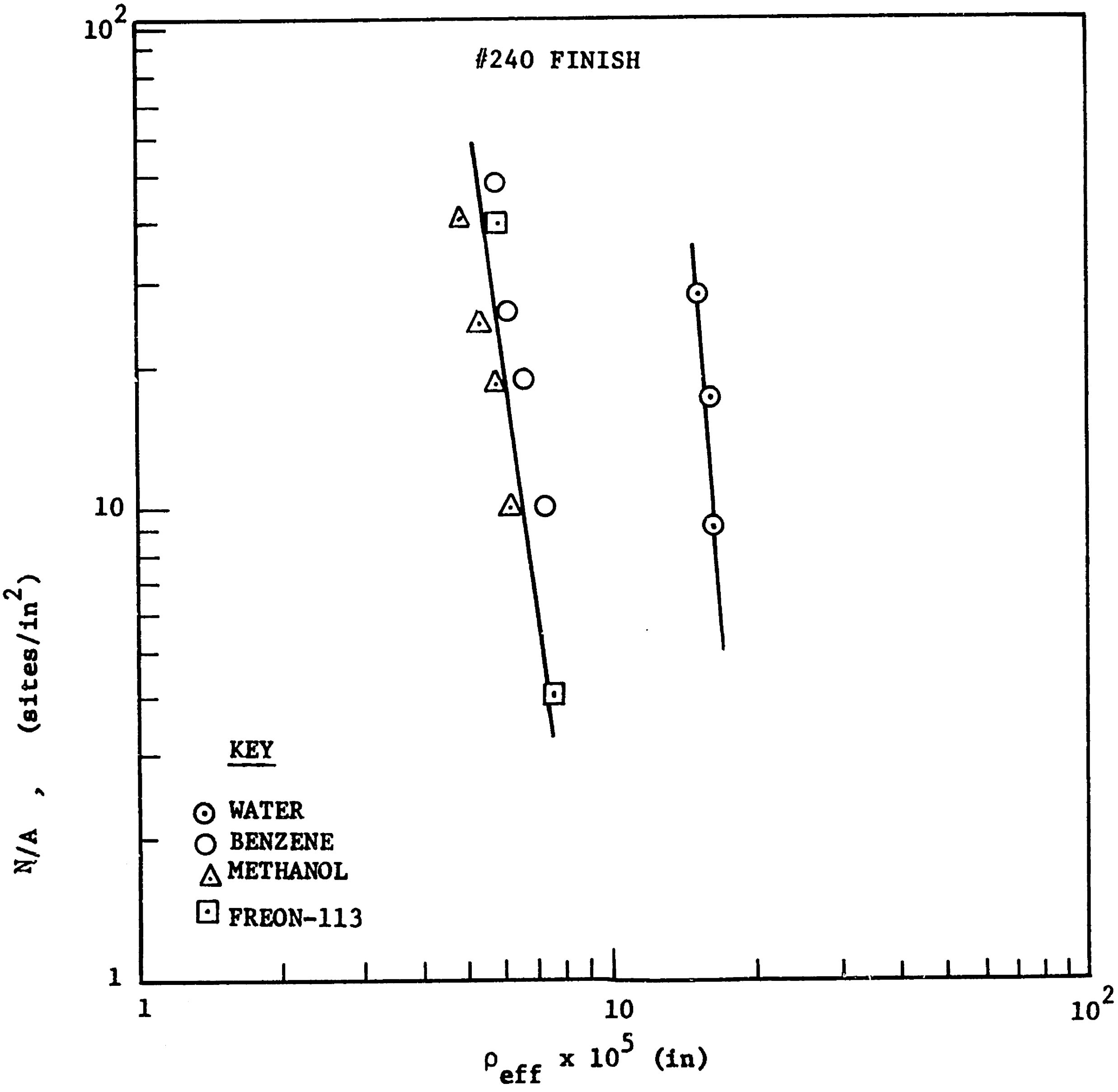

Fig. 55b: Cumulative site density distribution for water and organics, Ref. [18].

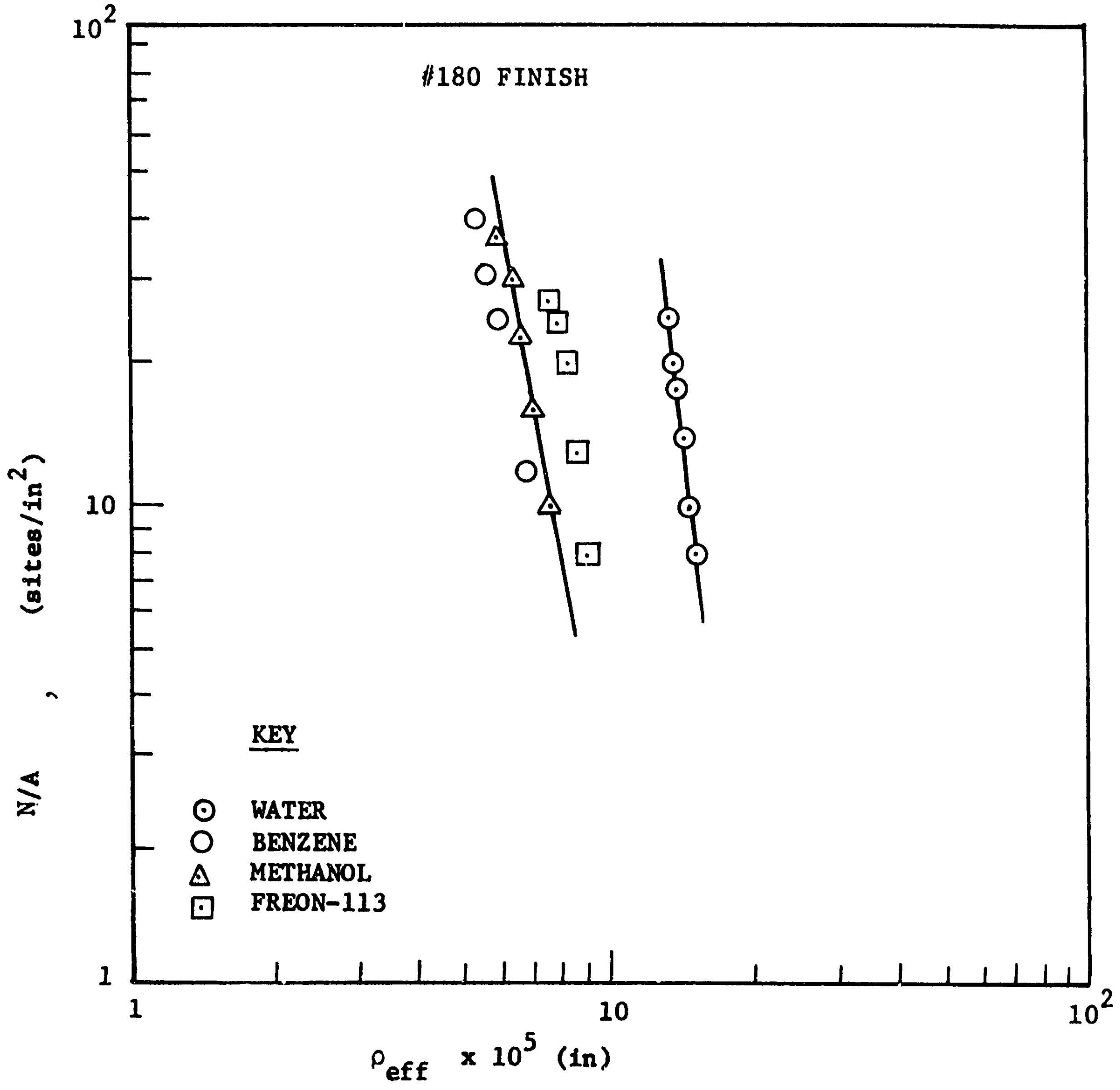

Fig. 55c: Cumulative site density distribution for water and organics, Ref. [18].

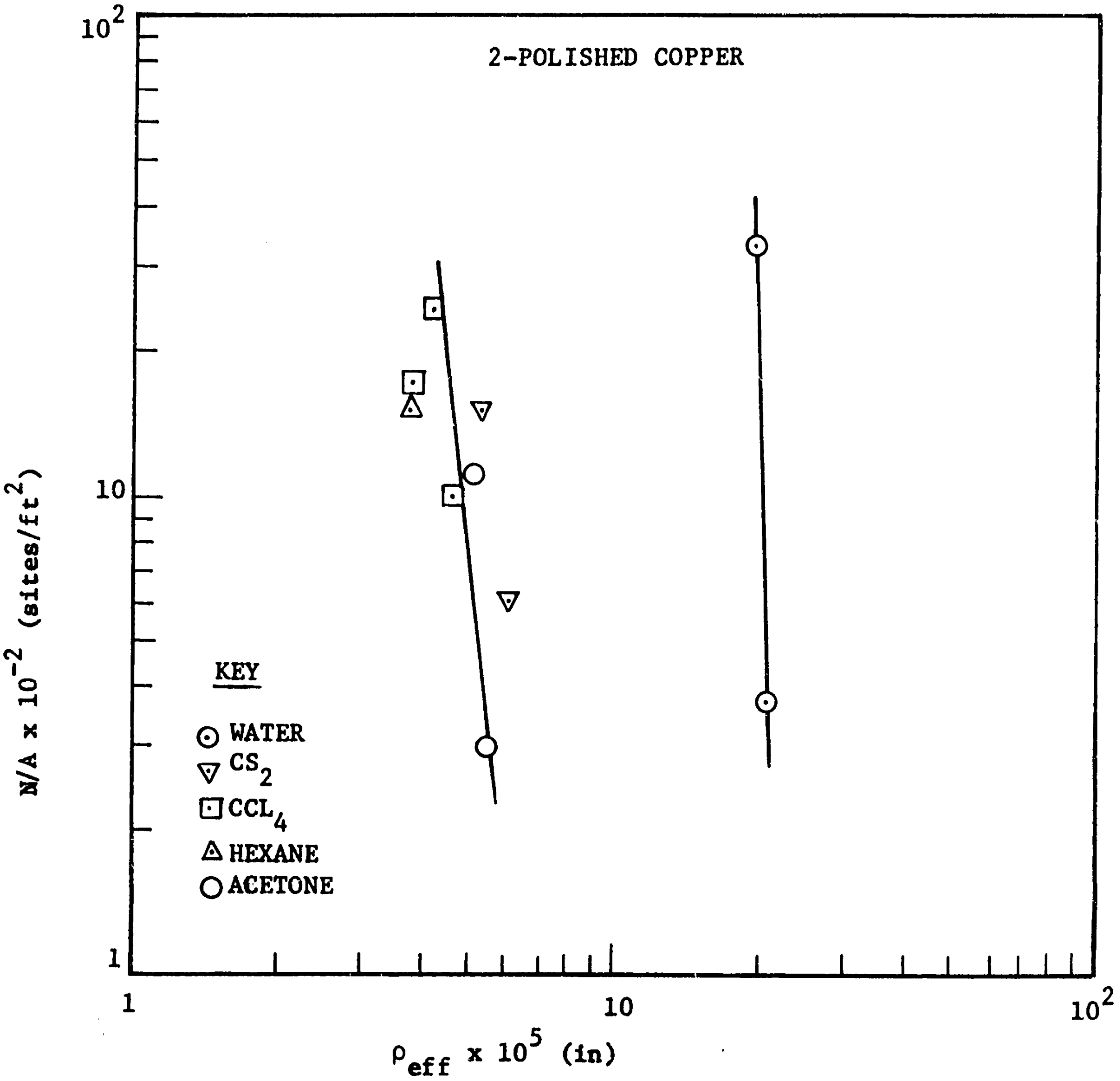

Fig. 55d: Cumulative site density distribution for water and organics, Ref. [4].

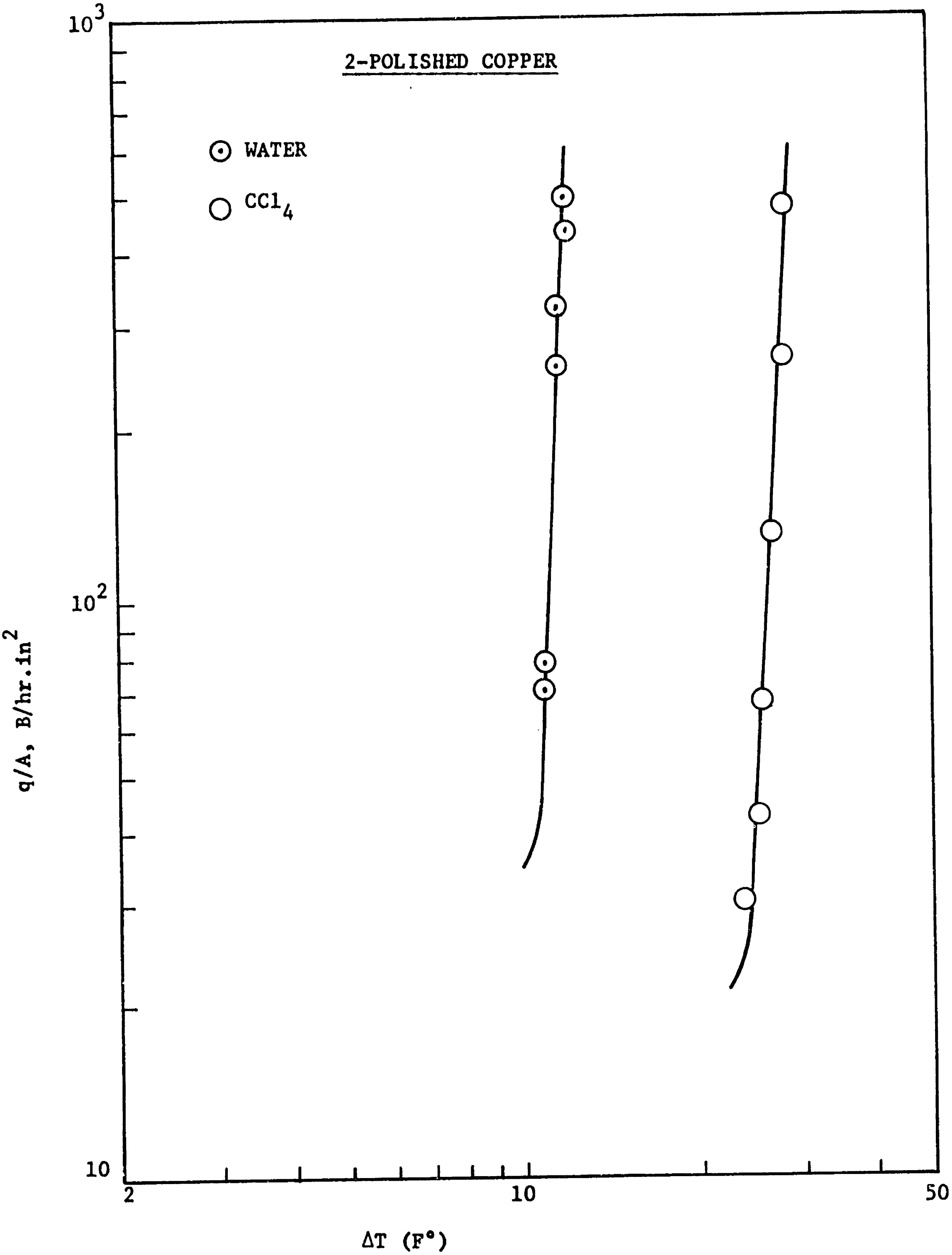

Fig. 56a: Boiling curves for water and CCl_4, Ref. [4].

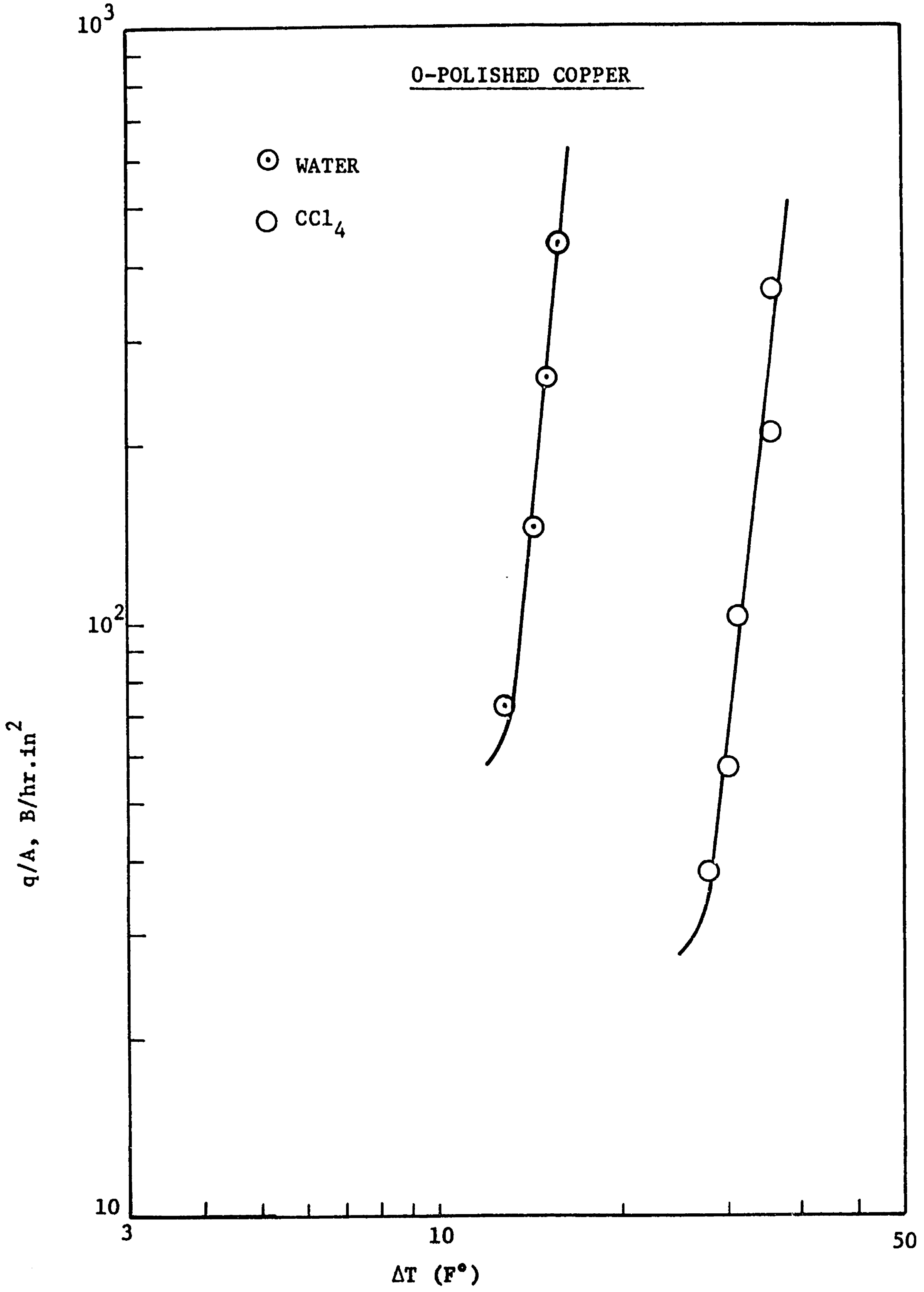

Fig. 56b: Boiling curves for water and CCl_4, Ref. [4].

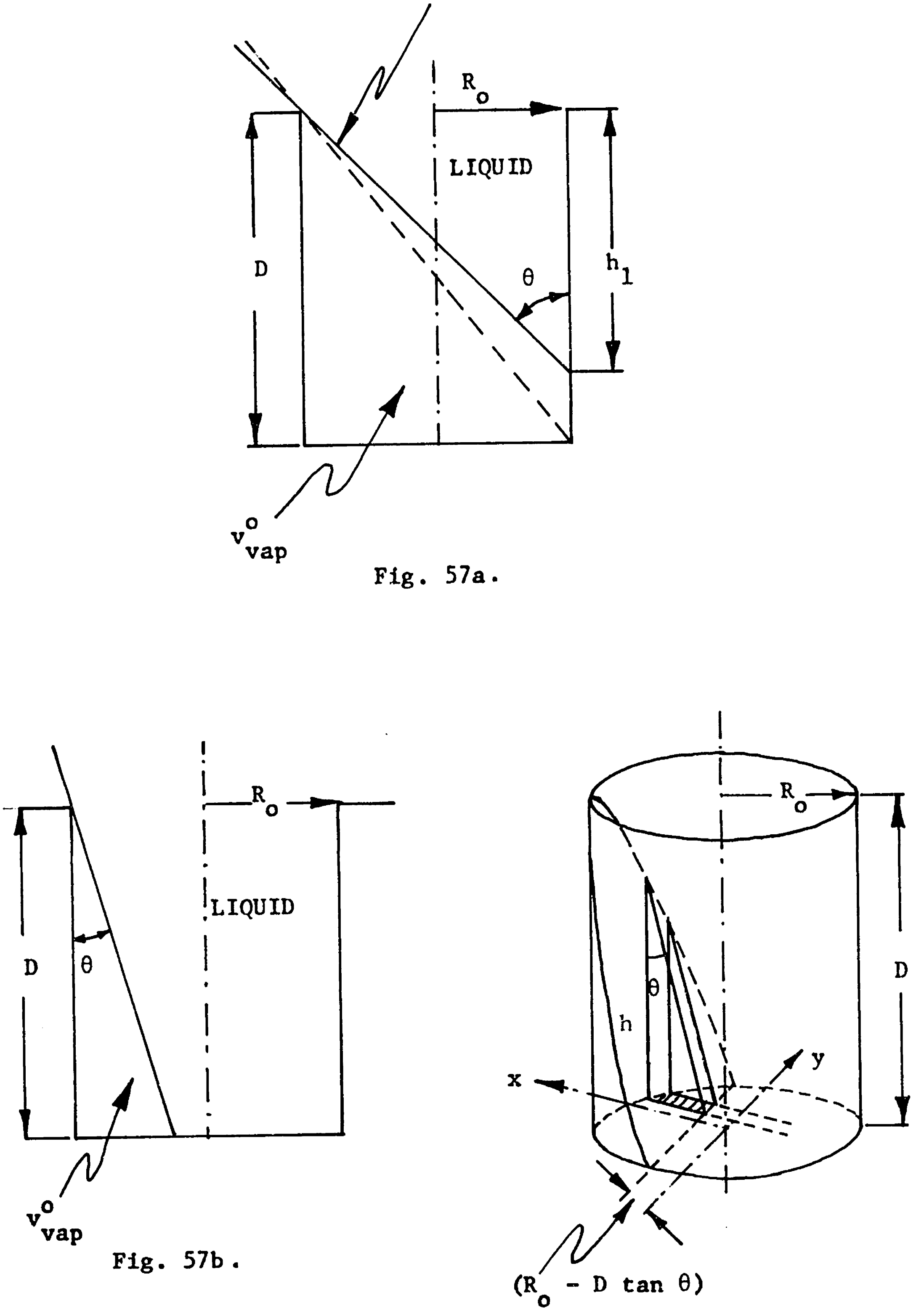

Fig. 57a.

Fig. 57b.

Fig. 57c.

Fig. 57: Sketch for the calculation of v^o_{vap}

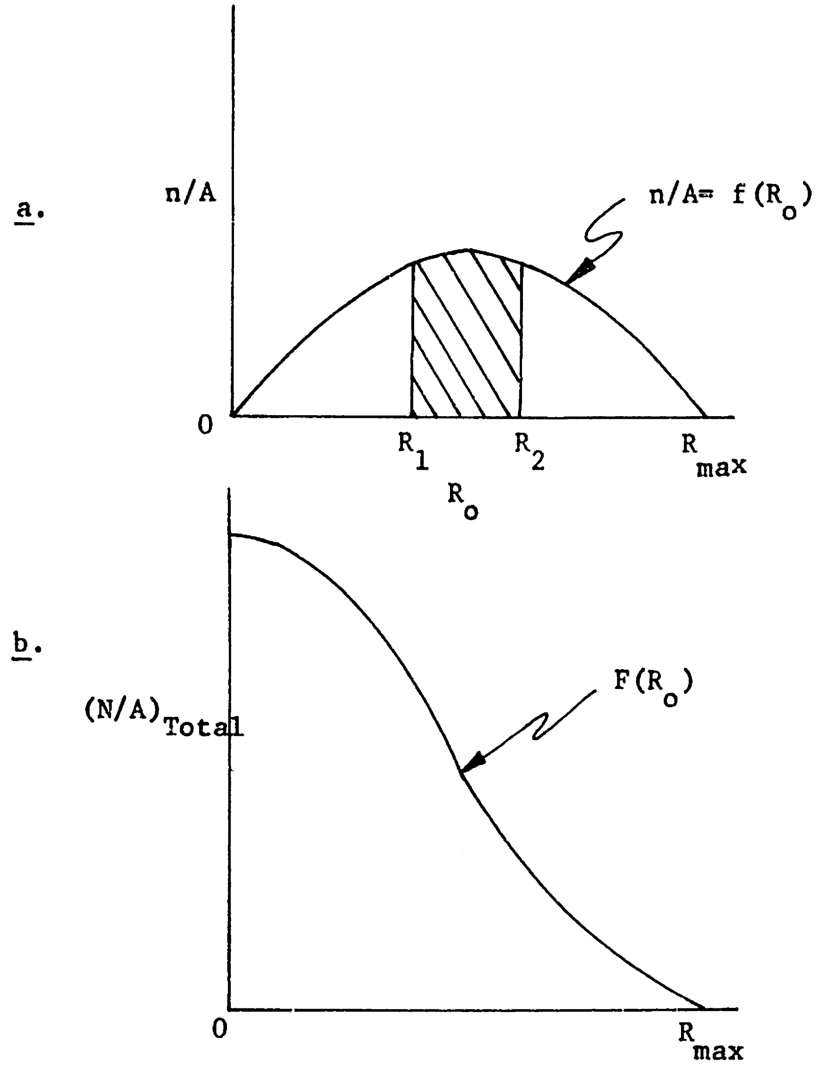

Fig. 58: a. Cavity size(R_o) distribution, and b. cumulative site density vs. size(R_o) for a typical boiling surface.

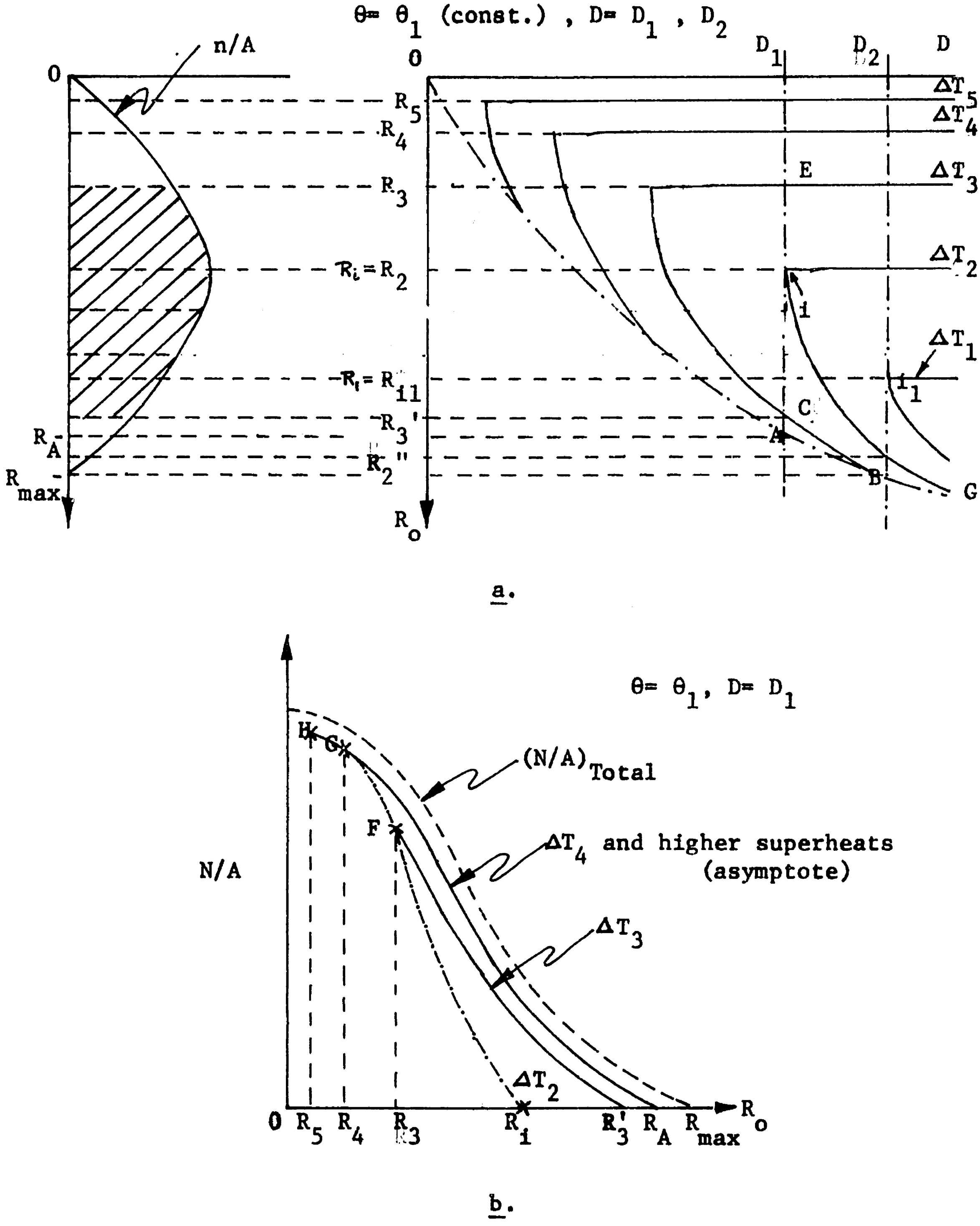

Fig. 59: Effect of varying the wall superheat on the population of active sites in boiling on a surface having a prescribed site distribution.

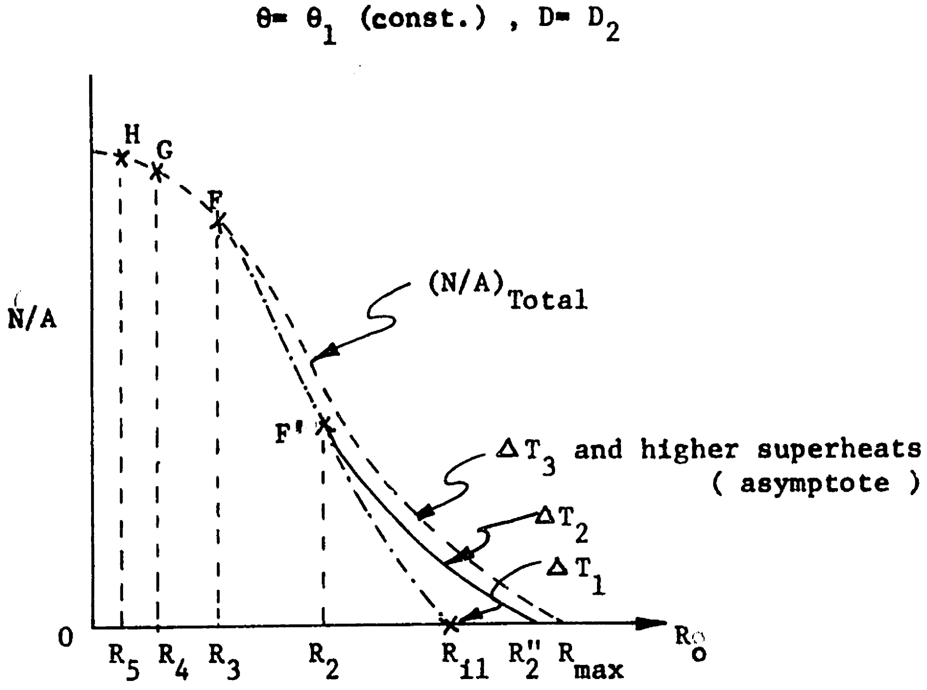

Fig. 59c: Effect of varying the wall superheat on the population of active sites (D= D$_2$).

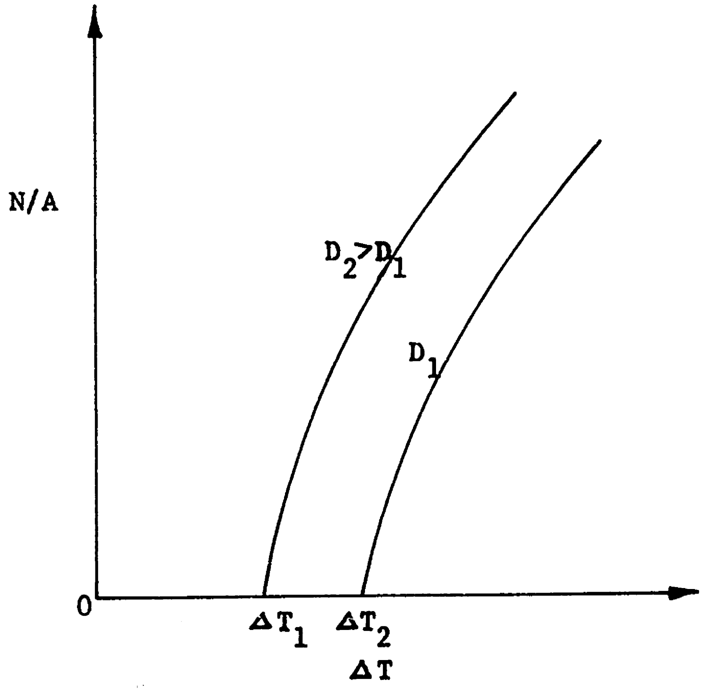

Fig. 59d: Effect of the wall superheat and cavity depth on the cumulative active site population.

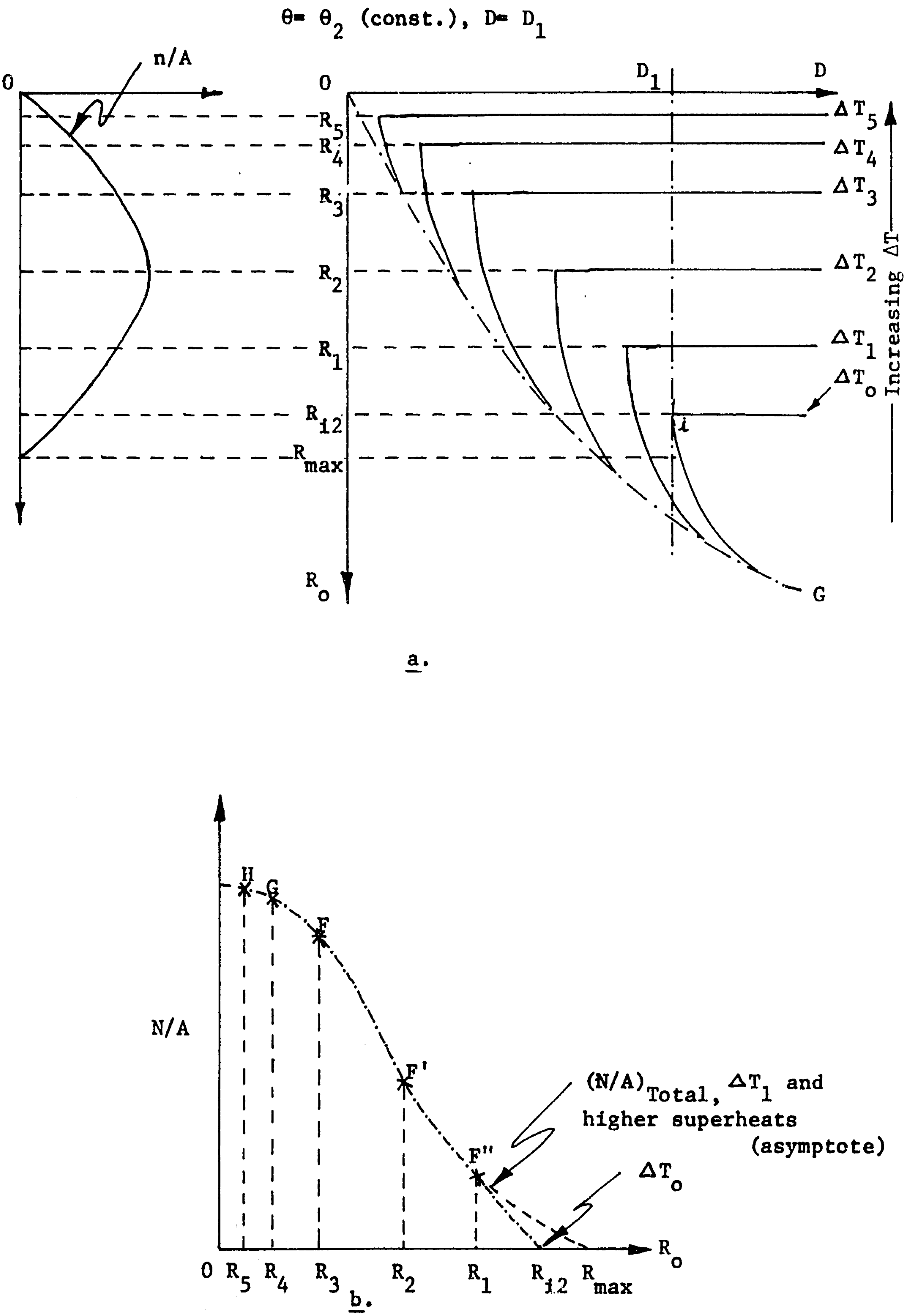

Fig. 60: Effect of the wall superheat on the population of active sites.

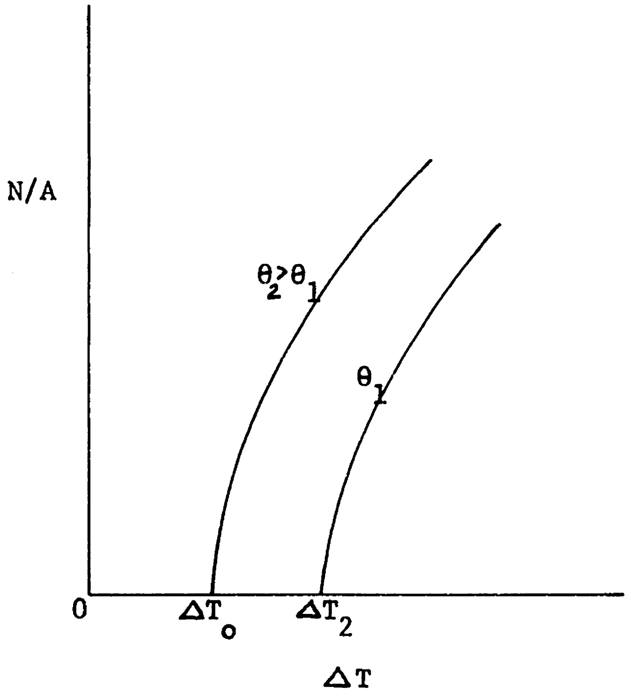

Fig. 60c: Effect of wall superheat and contact angle on the cumulative population of active sites.

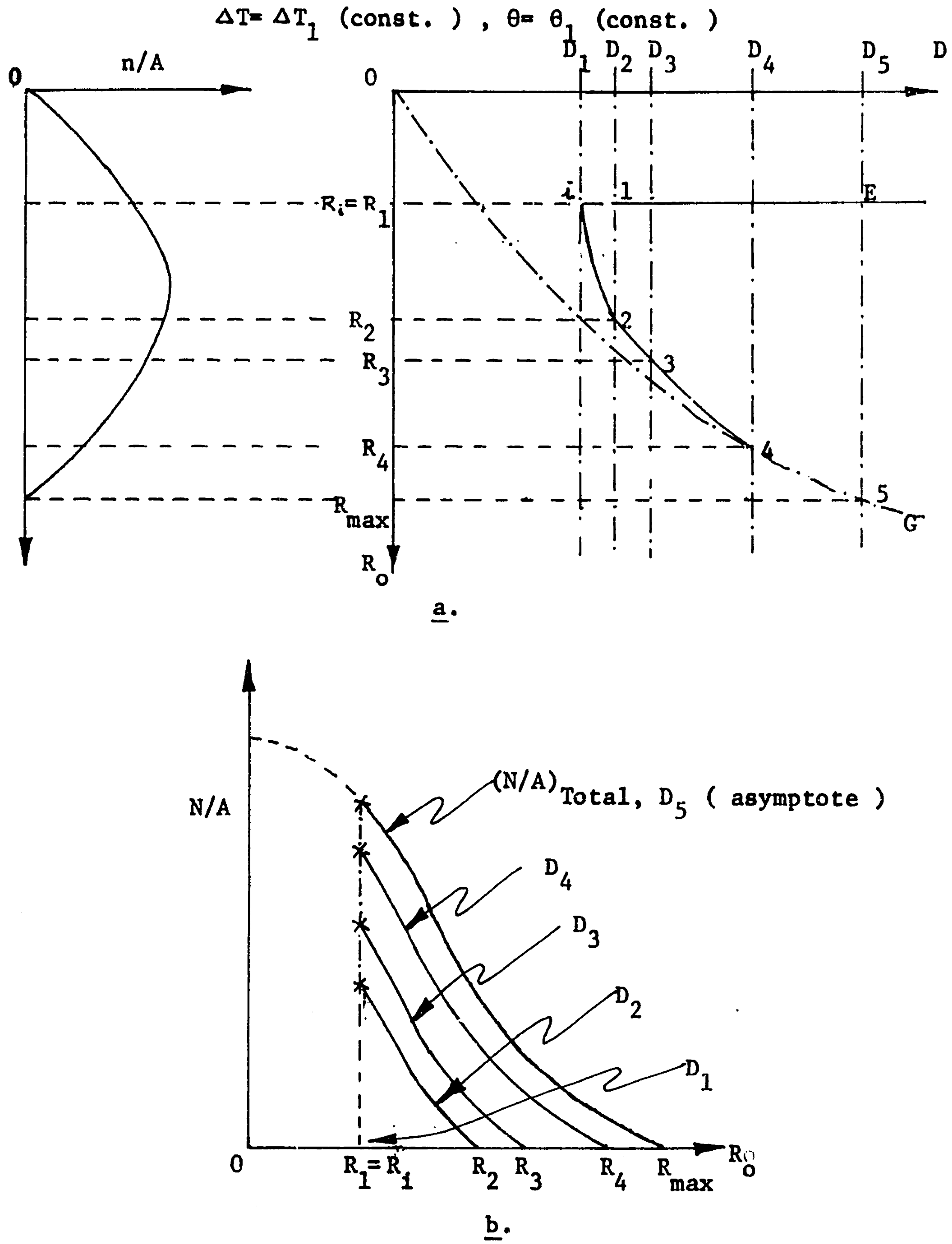

Fig. 61: Effect of cavity depth on the population distribution of active sites.

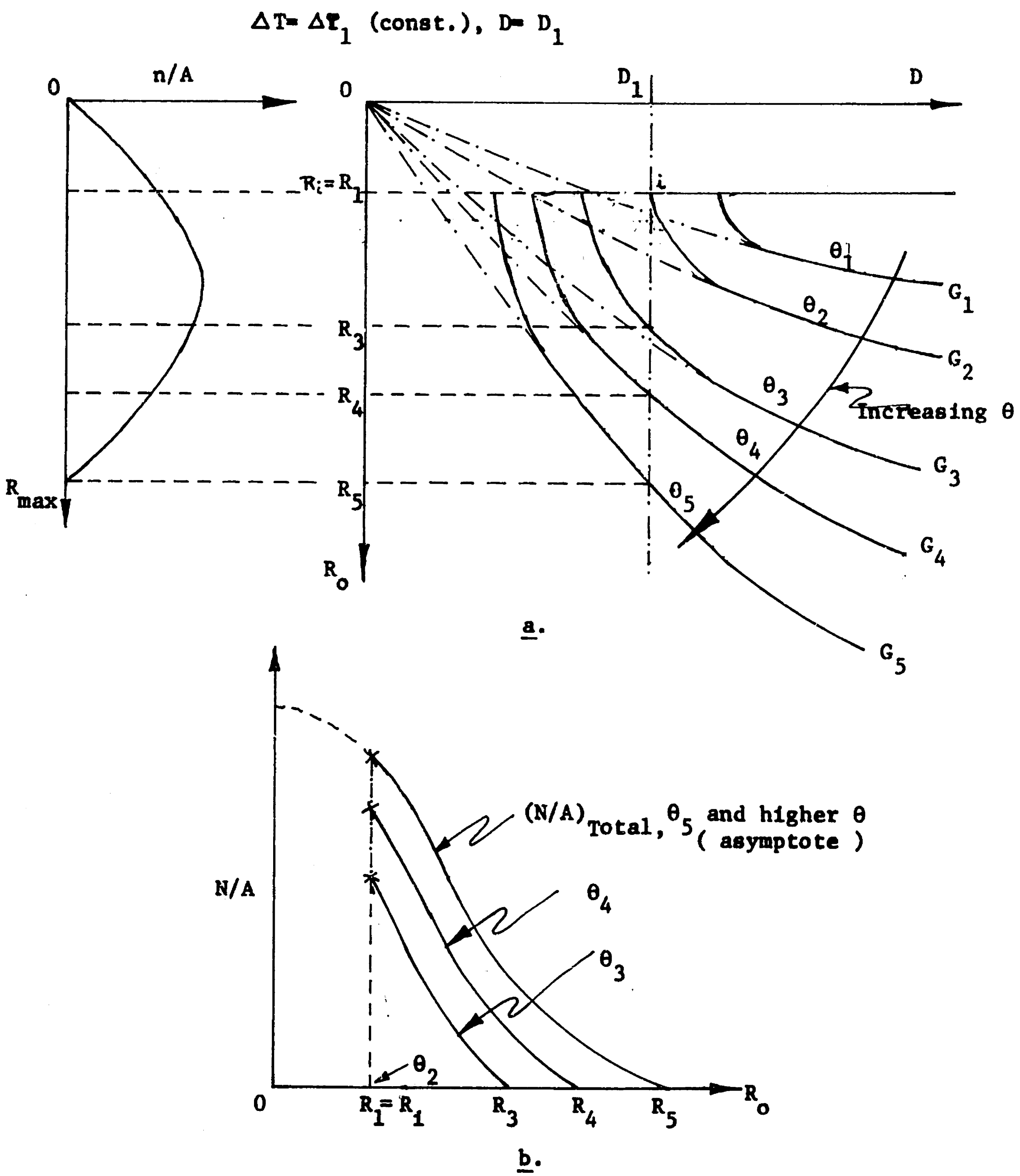

Fig. 62: Effect of contact angle on the population distribution of active sites.